

TECHNISCHE UNIVERSITÄT MÜNCHEN

TUM School of Natural Sciences

Magnon Spin Transport in Magnetically Ordered Insulators

Janine Gückelhorn

Vollständiger Abdruck der von der TUM School of Natural Sciences der
Technischen Universität München zur Erlangung des akademischen Grades einer

Doktorin der Naturwissenschaften

genehmigten Dissertation.

Vorsitz: Prof. Dr. Johannes Knolle

Prüfer der Dissertation: 1. Prof. Dr. Rudolf Gross

2. Prof. Dr. Christian Back

Die Dissertation wurde am 16.08.2023 bei der Technischen Universität München
eingereicht und durch die TUM School of Natural Sciences am 08.12.2023
angenommen.

Janine Gückelhorn

Magnon Spin Transport in Magnetically Ordered Insulators

Dissertation, August 3, 2023

Reviewers: Prof. Dr. Rudolf Gross and Prof. Dr. Christian Back

Technische Universität München

TUM School of Natural Sciences

Walther-Meißner-Institut für Tieftemperaturforschung

der Bayerischen Akademie der Wissenschaften

Walther-Meißner-Straße 8

85748 Garching

Abstract

Present day spintronic devices are based on the generation, transport and manipulation of spin-polarized charge currents. In the last decade, however, a promising candidate for the storage and transport of information at low dissipation level has gained increasing attention: pure spin currents. The latter represent the flow of pure angular momentum without any accompanying net charge current. Pure spin currents offer two intriguing aspects: First, they can be transported in electrically insulating materials, e.g. via quantized spin waves in magnetically ordered insulators, referred to as magnons. Second, pure spin currents can be generated and detected by charge currents in electrically conducting materials without magnetic order and finite spin-orbit coupling via the spin Hall effect. This effect allows the electrical injection and detection of pure spin currents in bilayers consisting of a non-magnetic heavy metal with strong spin-orbit coupling and a magnetically ordered insulator. In such heterostructures, magnon spin transport can be investigated and even manipulated for different device geometries and external conditions. However, due to the quasiparticle nature of spin waves, in particular due to the fact that angular momentum carried by pure spin currents is not conserved but may relax, the control of magnonic spin currents has become an essential but challenging task.

The aim of this thesis is to establish and study more efficient methods for the control/manipulation of pure spin currents in magnetically ordered insulators. The control of magnonic spin currents is achieved by various approaches. In transistor inspired three-terminal devices with three heavy metal electrodes, where the middle electrode, called the modulator, can influence the diffusive incoherent magnon transport between the two outer electrodes via an applied charge current, a nonlinear increase in the magnon conductivity has been reported. Here, we demonstrate that the two common measurement schemes used to investigate the magnon transport properties are both well suited to investigate pure spin currents in such geometries. One measurement method is based on a dc charge current applied to an outer electrode utilizing the current reversal method, while the other method relies on an ac stimulus in combination with lock-in detection. Firstly, a comparison of these two measurement methods reveals a nonlinear contribution to the detected signal from the injection process. Secondly, a twofold increase of the magnon conductivity and a linear magnetic field dependence of the threshold current, indicating the onset of the magnetic damping compensation, is obtained by reducing the effective

magnetization. Subsequently, we could show that large modulator currents impact the device performance. In particular, our results suggest a deterioration of the Pt/YIG interface at the modulator electrode.

Another approach is based on the coherent control of antiferromagnetic magnon excitations by an external magnetic field. Here, we included a discussion on the role of low-energy magnons and the spin injection and detection process. As a key result, we could demonstrate nonreciprocal magnon spin transport in an antiferromagnet.

Kurzfassung

Die heutigen spintronischen Bauelemente basieren auf der Erzeugung, dem Transport und der Manipulation von spinpolarisierten Ladungsströmen. In den letzten zehn Jahren hat jedoch ein weiterer, vielversprechender Ansatz für die Speicherung und den Transport von Information bei geringer Verlustleistung zunehmend an Aufmerksamkeit gewonnen: reine Spinströme. Letztere stellen den Fluss von reinem Drehimpuls ohne begleitenden Ladungsstrom dar. Reine Spinströme bieten zwei faszinierende Aspekte: Erstens können sie in elektrisch isolierenden Materialien übertragen werden, z. B. über quantisierte Spinwellen in magnetisch geordneten Isolatoren, die als Magnonen bezeichnet werden. Zweitens können reine Spinströme durch Ladungsströme in elektrisch leitenden Materialien mit endlicher Spin-Bahn Kopplung und ohne magnetische Ordnung über den Spin-Hall-Effekt erzeugt werden. Dieser Effekt ermöglicht die elektrische Injektion und Detektion von reinen Spinströmen in Doppelschichten, die aus einem nichtmagnetischen Schwermetall mit starker Spin-Bahn-Wechselwirkung und einem magnetisch geordneten Isolator bestehen. In solchen Heterostrukturen kann der Magnonenspintransport untersucht und sogar unter Verwendung von verschiedenen Bauelementgeometrien und äußeren Bedingungen manipuliert werden. Aufgrund der Quasiteilchennatur der Spinwellen, insbesondere der Tatsache, dass der von Spinströmen transportierte Drehimpuls nicht erhalten bleibt sondern relaxiert, ist die Kontrolle der magnonischen Spinströme zu einer wesentlichen, aber schwierigen Aufgabe geworden.

Das Ziel dieser Arbeit ist es, effizientere Methoden für die Kontrolle/Manipulation von reinen Spinströmen in magnetisch geordneten Isolatoren zu etablieren. Die Kontrolle der magnonischen Spinströme wurde durch verschiedene Ansätze erreicht. In von Transistoren inspirierten Dreitor-Bauelementen mit drei Schwermetallelektroden, bei denen die mittlere Elektrode, der sogenannte Modulator, den diffusiven inkohärenten Magnonentransport zwischen den beiden äußeren Elektroden durch einen angelegten Ladungsstrom beeinflussen kann, wurde eine nichtlineare Erhöhung der Magnonenleitfähigkeit berichtet. Hier zeigen wir, dass die beiden üblichen Messverfahren, die zur Untersuchung der Magnonentransporteigenschaften verwendet werden, beide gut geeignet sind, um reine Spinströme in solchen Geometrien zu untersuchen. Während die eine Messmethode auf dem Anlegen eines Gleichstroms an eine der äußeren Elektroden unter Verwendung des Stromumkehrverfahren basiert, beruht die andere Methode auf einer Anre-

gung durch Wechselstrom in Kombination mit der Lock-in-Detektion. Erstens ergab ein Vergleich dieser beiden Messmethoden einen nichtlinearen Beitrag zum nachgewiesenen Signal durch den Injektionsprozess. Zweitens wird eine zweifache Erhöhung der Magnonenleitfähigkeit und eine lineare Abhängigkeit des Schwellwertstroms, der das Einsetzen der magnetischen Dämpfungskompensation anzeigt, durch die Verringerung der effektiven Magnetisierung erreicht. Anschließend konnten wir zeigen, dass sich große Modulatorströme auf die Leistung der Bauelemente auswirken. Insbesondere deuten unsere Ergebnisse auf eine Verschlechterung der Pt/YIG-Grenzfläche an der Modulatorelektrode hin.

Ein anderer Ansatz basiert auf der kohärenten Kontrolle antiferromagnetischer Magnon-Anregungen durch ein externes Magnetfeld. Hier haben wir die Rolle der niederenergetischen Magnonen und den Prozess der Spininjektion und -detektion erörtert. Als Schlüsselergebnis konnten wir den nicht-reziproken Magnonenspintransport in einem Antiferromagneten nachweisen.

Contents

1	Introduction	1
2	Theoretical Background: Pure Spin Currents in Magnetically Ordered Insulators	7
2.1	Spin Transport in Metals	8
2.1.1	Spin Currents	9
2.1.2	Spin Diffusion	11
2.2	Pure Spin Current Generation in Normal Metals	13
2.3	Spin Transport Across Metal/Magnetically Ordered Insulator Interfaces	15
2.4	Spin Hall Magnetoresistance	22
2.5	Charge Current Induced Magnon Transport in Magnetically Ordered Insulators	24
2.5.1	Magnon Generation and Detection via Heavy Metal Electrodes	25
2.5.2	Magnon Transport	28
3	Experimental Details	35
3.1	Material Systems	35
3.1.1	Ferrimagnetic Insulator - Yttrium Iron Garnet	35
3.1.2	Antiferromagnetic Insulator - Hematite	36
3.2	Sample Fabrication and Layout	39
3.3	Experimental Setup	42
4	Manipulation of Magnon Spin Transport in Three-terminal YIG/Pt Nanostructures	45
4.1	Theoretical Concepts	47
4.1.1	Damping Compensation	47
4.1.2	Low Bias Regime	52
4.1.3	Critical Current Regime	55
4.2	Quantitative Comparison of the Dc and Ac Detection Technique	61
4.2.1	Dc-detection Technique	62
4.2.2	Ac-detection Technique	64
4.2.3	SHE Induced Magnon Spin Signal	66
4.2.4	Thermally Generated Magnon Spin Signal	74

4.3	Reduced Effective Magnetization	76
4.3.1	Film Characterization	77
4.3.2	Magnon Transport in Two-terminal Devices	79
4.3.3	Manipulation of the Magnon Transport	81
4.3.4	Critical Current Regime	85
4.4	Impact of Large Modulator Current Exposure	87
4.4.1	Spin Hall Magnetoresistance	90
4.4.2	Low Modulator Current Regime	93
4.4.3	Critical Modulator Current Regime	96
4.4.4	Overcritical Modulator Current Regime	100
4.5	Summary	102
5	Magnon Spin Transport in the Antiferromagnet Hematite	107
5.1	Theoretical Concepts	109
5.1.1	Pseudospin Concept	110
5.1.2	Pseudospin Dynamics and Diffusive Transport	114
5.1.3	Magnon Hanle Effect	118
5.1.4	Nonreciprocal Magnon Hanle Effect	123
5.1.5	Influence of Low-energy Magnons	128
5.1.6	Spin Injection and Detection	132
5.2	Influence of Dimensionality on the Magnon Spin Transport	135
5.2.1	Experimental Details	136
5.2.2	Thin Hematite Film	137
5.2.3	Thick Hematite Film	139
5.3	Nonreciprocal Magnon Spin Transport	145
5.3.1	Characterization of Hematite Thin Films	146
5.3.2	Antisymmetric Magnon Spin Signal in Thick Hematite Films	148
5.3.3	Antisymmetric Magnon Spin Signal in Thin Hematite Films	157
5.4	Summary	160
6	Summary and Outlook	163
6.1	Manipulation of Magnon Spin Transport in Three-terminal Hematite/Pt Nanostructures	165
6.2	Influence of Anisotropy on the Magnon Spin Transport in YIG	170
6.3	NV-Magnetometry Measurements on Three-Terminal MOI/Pt Nanos- tructures	174
	List of Publications	177
	Bibliography	179

Introduction

Nowadays, the data storage and processing capacity has to be constantly increased to keep up with the growing amount of data generation, facilitating our everyday life such as the storing and carrying of information. Over the past decades, the performance of integrated circuits has continuously improved, as Moore's law suggests [1, 2]. This is mainly due to the improvements in the field of fabrication technology allowing the downscaling of complementary metal-oxide-semiconductors (CMOS) technologies. However, further downscaling is challenging as transistors reach sizes of a few atomic layers, where quantum effects become relevant [3]. This leads to an increased standby power dissipation due to increasing leakage currents, for example via quantum tunneling [4–6]. Other challenges are the increasing dynamic power dissipation as well as pushing the heat production to its thermal limits by increasing operation frequencies. In other words, the drastic increase in data storage and processing capacity is accompanied by a significant increase in energy consumption [7]. Although there are variants of semiconductors that try to overcome these challenges, like fin-type field-effect transistors [8, 9] or carbon nanotube field-effect transistor [10, 11], future technologies which may provide performance beyond CMOS technology become more urgent [12–14].

One of the most promising alternatives represents the field of spintronics [7, 15–18]. In this field, the electron spin degree of freedom is exploited for information storage and processing. The spin property is an intrinsic form of angular momentum giving rise to many fascinating transport phenomena. Regarding data storage, a major advantage of electron spins in magnetically ordered materials such as ferromagnets is their non-volatile storage character. In contrast to CMOS technology, where information is stored in the charge degree of freedom and leakage currents can lead to a loss of the stored charge, the magnetization associated with ordered electron spins exhibits an infinite endurance [19]. After the observations of Gerlach and Stern in 1922 that a beam of silver atoms splits in an external inhomogeneous magnetic field [20, 21], the idea of electron spin was first proposed in 1928 [22]. However, it took some time before significant progress in using the spin degree of freedom has been made due to technological limitations and a lack of understanding. In the 1950s, initially only the spin degree of freedom was exploited, for example in hard disk drivers, where magnetically ordered thin films are used for data storage. A major breakthrough was the discovery of the giant magnetoresistance effect in

1988 [23–25] that allowed the electrical readout of the state of the magnetic system. Together with the tunneling magnetoresistance [26–30] an enhanced sensitivity in magnetic field sensors has been achieved. More importantly, these effects provided the means to keep up with the growing demand of data storage capacity. Another milestone in the history of spintronics was the proposal of a spin transistor by Datta and Das in 1990 [31, 32]. Although an efficient experimental realization is still missing, the proposal triggered a broad range of spintronic based devices and concepts. First concepts and applications relied on spin-polarized charge transport and therefore suffered from the same problems as conventional CMOS technologies. In recent years there have been great advancements towards energy-efficient storage devices in the field of spintronics. Nevertheless, many interesting challenges still remain open.

One of these advancements is the usage of pure spin currents, which only carry spin angular momentum without an accompanying charge current [33–36]. An efficient transport of pure spin currents over long distances is realized in magnetically ordered insulators. In such systems, the spin angular momentum is carried by the quantized, bosonic excitations of the spin system, referred to as magnons (quantized spin waves). The subfield of magnonics [37] focuses on phenomena based on these quasiparticles and a key research field addresses the excitation, detection and control of spin waves. In order to integrate magnon-based devices in present day electronic technologies an electrical readout is desirable. Obviously, this requires the coupling of the spin and charge degree of freedom. Nonmagnetic metals containing heavy elements and thereby feature a large spin-orbit coupling allow for the generation and detection of pure spin currents via electrical charge currents. A central role for this charge-to-spin conversion and its reversed process plays the (inverse) spin Hall effect (SHE) [38, 39]. The latter enables interesting phenomena in heterostructures consisting of heavy metals (HMs) and magnetically ordered insulators (MOIs). In such heterostructures, the excitation of auto-oscillations has been demonstrated [40–42]. Furthermore, two or more separated HM electrodes deposited on MOIs allow for spin transport experiments [43, 44]. In these experiments, a charge current applied to one electrode generates spin currents in the MOI via the SHE, while a second electrode acts as detector, where the spin is converted back to a charge via the inverse SHE. A third HM electrode placed between the two other electrodes can be used to control the magnon transport [44, 45]. Although ferro-/ferrimagnetic and antiferromagnetic ordered insulators feature rather different spin wave dynamics, both systems can carry pure spin currents via magnons. In particular, while ferromagnets host magnons with one chirality and thus spin of only one direction, the two magnetic sublattices in antiferromagnets lead to two magnon modes with opposite chirality (spin-up and spin-down magnons). Due to this property many

phenomena are predicted in antiferromagnetic ordered spin systems in complete analogy to electronic systems (e.g. normal metals) with equal density of spin-up and spin-down electrons [46–52].

In this thesis, we aim to gain a deeper understanding of the control of spin currents in ferro-/ferrimagnetic as well as antiferromagnetic systems focusing on incoherent, diffusive magnon transport, which can be seen somewhat similar to the well-known electronic case. In the following, we provide an overview of the topics covered in this thesis.

The underlying theoretical concepts relevant for this thesis are presented in Chapter 2. We start by discussing the spin transport in metals, followed by introducing the pure spin current generation in non-magnetic metals. In order to understand the magnon excitation and detection in MOIs via HM electrodes the spin transfer across a HM/MOI interface is of particular relevance. Based on this interfacial spin transport, we introduce the spin Hall magnetoresistance (SMR), an important measure for the interface quality, and finally discuss the magnon transport in a MOI induced and detected utilizing a two-terminal HM/MOI device.

In Chapter 3, we present the experimental techniques/methods used in our measurements. After introducing the two material systems used in our experiments, the ferrimagnetic insulator yttrium iron garnet ($\text{Y}_3\text{Fe}_5\text{O}_{12}$, YIG) and the antiferromagnetic insulator hematite ($\alpha\text{-Fe}_2\text{O}_3$), we present the fabrication process of our multi-terminal devices. Furthermore, we discuss the utilized experimental setups.

Chapter 4 focuses on the manipulation of the magnon transport in YIG via nanostructured three-terminal devices, where a charge current applied to the so-called modulator electrode between the two outer electrodes can be represented as a change of the effective magnon conductivity in the transport channel. In particular, we investigate the influence of different external and material parameters on the transport regime captured by nonlinear magnetization dynamics.

First, the two main measurement methods to access the magnon transport properties are introduced and compared to each other. They rely on a dc and an ac stimulus applied to the injector electrode and are used throughout this work. We show that both methods are both well suited to investigate incoherent magnon transport in these three-terminal devices. By comparing our theoretical model with our experimental data, we find indications for nonlinear contributions to the detected signal from the injector current and not only the applied modulator current. The results presented in this part have been published in J. Gückelhorn, T. Wimmer, S. Geprägs, H. Huebl, R. Gross, and M. Althammer, *Quantitative comparison of magnon transport experiments in three-terminal YIG/Pt nanostructures acquired via dc and ac detection techniques*, [Applied Physics Letters](#) **117**, 182401 (2020).

In the second part, we investigate the diffusive magnon transport in biaxially strained

YIG thin films. Such films exhibit a significant perpendicular magnetic anisotropy and a reduced saturation magnetization resulting in a reduced effective magnetization. We first use two-terminal nanostructures to demonstrate that these films exhibit transport properties, in particular a low Gilbert damping, comparable to lattice-matched grown YIG films. We then utilize three-terminal devices to study the influence of the reduced effective magnetization on the magnetic field dependence of the threshold current, which defines the onset of a zero-effective damping state. A linear dependence of the latter on the applied magnetic field corroborates our present understanding that this threshold effect scales with the effective magnetization of the material. The results of our detailed investigation can be found in J. Gückelhorn, T. Wimmer, M. Müller, S. Geprägs, H. Huebl, R. Gross, and M. Althammer, *Magnon transport in $Y_3Fe_5O_{12}/Pt$ nanostructures with reduced effective magnetization*, *Physical Review B* **104**, L180410 (2021).

Finally, we study the influence of large modulator currents on the magnon conductivity. To this end, we successively apply larger current densities to the modulator electrode of multiple devices until we reach a complete blocking of the magnon transport. This is caused by locally induced Joule heating that generates temperatures close to the Curie temperature of YIG leading to a transition to its paramagnetic phase. We also quantitatively analyze the evolution of the SMR, the modulator efficiency, and the threshold current as a function of maximum modulator current exposure, followed by a detailed discussion of possible origins of the observed changes.

The second major topic presented in Chapter 5 addresses the magnonic spin transport in antiferromagnetic hematite thin films. Here, we investigate the underlying physics of the recently found magnon Hanle effect, which could be described in terms of a magnon pseudospin model, in more detail. We expand this theoretical model allowing us a clear discussion of our experimental results.

We first investigate the effect of dimensionality of the hematite film on the detector signal due to magnon spin transport by studying hematite films of different thicknesses. As up to now, only ultra-thin hematite films, slightly thicker than 10 nm, have been studied. Interestingly, thicker hematite layers (~ 100 nm) exhibit a large positive offset signal for small magnetic field values. According to our model, we can attribute this observation to finite-spin low-energy magnons, which do not directly contribute to the pseudospin dynamics, but rather contribute as a constant background. Moreover, we directly take into account the spin injection and detection process. The expanded theory as well as our experimental results have been published in J. Gückelhorn, A. Kamra, T. Wimmer, M. Opel, S. Geprägs, R. Gross, H. Huebl, and M. Althammer, *Influence of low-energy magnons on magnon Hanle experiments in easy-plane antiferromagnets*, *Physical Review B* **105**, 094440 (2022).

In the second part, we report on a nonreciprocal response observed in hematite. By interchanging the roles of injector and detector in a two-terminal device, we find an electrically-induced direction-dependent magnon spin transport and magnon Hanle effect. The degree of nonreciprocity is found to vary with the equilibrium Néel vector and thus, can be tuned via an applied magnetic field. This finding can be understood in terms of different pseudofields or pseudospin precession rates, experienced by magnons propagating in opposite directions in the transport channel. This provides a clear evidence for the presence of inversion symmetry breaking at the hematite/substrate system and demonstrates the existence of an emergent magnon pseudospin-orbit interaction. A detailed discussion of our results can also be found in J. Gückelhorn, S. de-la-Peña, M. Scheufele, M. Grammer, M. Opel, S. Geprägs, J. C. Cuevas, R. Gross, H. Huebl, A. Kamra, and M. Althammer, *Observation of the Nonreciprocal Magnon Hanle Effect*, [Physical Review Letters](#) **130**, 216703 (2023).

To conclude this thesis, we summarize the main results in Chapter 6. Furthermore, we give an outlook to current and future experiments, which could answer open questions and provide a better understanding of the underlying mechanisms in the field of all-electrical excited and detected diffusive magnon spin transport. We address recent experiments on the manipulation of the magnonic spin transport in the antiferromagnet hematite. Moreover, we discuss first experiments on the influence of anisotropy on the magnon transport in differently oriented YIG thin films. Last but not least, we present possibilities to investigate the dynamics in three-terminal devices, in particular below the modulator electrode.

Theoretical Background: Pure Spin Currents in Magnetically Ordered Insulators

Present day electronics and information technology are mainly based on electrons exploiting their charge property. The field of spintronics, however, searches for efficient ways to use the spin property of electrons opening up new interesting possibilities. The angular momentum of an electron manifests itself as a tiny magnetic moment. The transport of (spin) angular momentum is the basis for a variety of phenomena such as magnetoresistance effects like giant magnetoresistance [23–25] or tunnel magnetoresistance [26–30], effects based on spin-transfer-torque [40–42, 53–55] and effects based on topological properties of spin textures, e.g. the topological Hall effect [56–62]. In contrast to the charge of an electron, angular momentum is usually not a conserved quantity due to finite spin-orbit coupling and transfer to other localized or mobile entities, such as phonons. This means that (spin) angular momentum is only conserved in good approximation over a characteristic time and length scale, referred to as spin relaxation time and spin decay length l_s ¹. This makes the construction of efficient devices challenging. On the other hand, however, the transfer of angular momentum between two different entities allows the design of new devices. Promising candidates are based on heterostructures consisting of heavy metals (HMs) with large spin-orbit coupling and magnetically ordered insulators (MOIs), where spin-flip scattering processes at the interface enable spin angular momentum transfer to the MOI exciting magnons. In magnetic materials, the exchange interaction results in an ordering of the localized spins. While ferromagnets feature a parallel ordering of neighboring spins, latter orient themselves in an antiparallel fashion in antiferromagnets. In a mean-field approach, this exchange interaction in magnetic materials can be represented by a molecular field or exchange field $\mu_0 \mathbf{H}_{\text{ex}}$, respectively, which is on the order of 100 T - 1000 T. Due to this strong interaction, it would cost very high energy to flip a single spin and

¹When we refer to the spin as a non-conserved quantity, this does not imply that the spin spontaneously disappears. In a closed system, both charge and spin are conserved quantities, however these quantities can be transferred between subsystems, i.e. they do not have to be conserved in a subsystem. In contrast to charge, where the density can only be changed through the inflow or outflow of charges through the surface of the volume, the spin can transfer angular momentum to other subsystems, such as phonons by interacting with the lattice.

therefore this is an unfavorable configuration. A more likely process that costs much lower energy, but is associated with the same change in angular momentum, is to delocalize one spin-flip over a large number of spins. This wave-like excitations of the whole spin lattice can be illustrated as a slight tilting of the spins with respect to each other. These collective excitations of the spin lattice are capable of transporting spin without moving charge carriers and are referred to as spin waves. In analogy to photons, the quantized excitations of an electromagnetic field, the spin waves are treated as quantized excitations of the magnetic order in a magnetic crystal, which are known as magnons. In particular, this means that pure spin currents can be carried via fermions as well as bosons. In the case of fermions, this could be electrons, neutrons, or protons, while for bosons typical examples of angular momentum carriers are photons or quasiparticle excitations in solid state systems, such as phonons, magnons or excitons. A fundamental difference between these two types of particles is their underlying quantum statistics. Fermions obey the Fermi-Dirac statistics [63, 64], while bosons follow the Bose-Einstein statistics [65, 66]. These properties of pure spin currents make them an interesting system to study.

This chapter intends to provide the basic theoretical concepts in order to understand the results in the following chapters in regard to pure spin current injection and detection as well as spin and magnon transport. In Sec. 2.1, we summarize the basics of electronic spin currents and discuss their diffusive transport in metals. This is followed by illustrating the generation and detection process of pure spin currents via a charge current in metals, including the introduction of the spin Hall effect (SHE) in Sec. 2.2. In Sec. 2.3, we introduce bilayers consisting of HMs and MOIs and the spin transport across the corresponding interface. Based on this, we exemplify the concept of spin Hall magnetoresistance (SMR), which represents a measure for the spin transfer efficiency, in Sec. 2.4. Last but not least, we present an approach allowing us to investigate the diffusive magnon transport in MOIs in Sec. 2.5. Two spatially separated HM electrodes enable an electrical and thermal excitation of this pure spin current and its electrical detection. The following introduction to the basic theoretical concepts follows the approaches in Refs. [67, 68]. Main parts of text and figures in this Chapter are reused from T. Wimmer, *Control and Manipulation of Magnonic Spin Currents in Magnetic Insulators*, [Dissertation, Technical University of Munich \(2021\)](#).

2.1 Spin Transport in Metals

First, we introduce the concept of spin currents and their transport in general, before we focus on pure spin currents. Spin currents can be treated in a similar fashion as

charge and heat currents, which means we relate quantities such as currents and driving forces using transport coefficient. However, in contrast to charge or heat current, spin current is no scalar quantity as it has to describe the flow direction as well as the spin orientation, which leads to some differences as discussed in the following.

2.1.1 Spin Currents

Starting with a general description, we introduce the particle current density $\mathbf{j} = n\langle\mathbf{v}\rangle$ with n the particle density and $\langle\mathbf{v}\rangle$ the corresponding expectation value of the particle velocity operator \mathbf{v} . Multiplying \mathbf{j} with the quantity transported by the particles, leads to the required charge, heat and spin current densities. As the transported charge q as well as heat Q are scalar quantities, this simply results in

$$\mathbf{j}_c = q\mathbf{j} = qn\langle\mathbf{v}\rangle \quad (2.1a)$$

$$\mathbf{j}_h = Q\mathbf{j} = Qn\langle\mathbf{v}\rangle \quad (2.1b)$$

for the charge (\mathbf{j}_c) and heat (\mathbf{j}_h) current density. As mentioned before the transported angular momentum is no scalar quantity and thus, the spin current density is obtained by the dyadic product of the particle current density \mathbf{j} and the transported spin $\hat{\mathbf{s}}$ per particle according to [69, 70]

$$\underline{\mathbf{j}}_s = \langle\hat{\mathbf{s}} \otimes \mathbf{j}\rangle = \frac{\hbar}{2}n\langle\hat{\boldsymbol{\sigma}} \otimes \mathbf{v}\rangle = \begin{pmatrix} \mathbf{j}_{s,x} & \mathbf{j}_{s,y} & \mathbf{j}_{s,z} \end{pmatrix}^\top = \begin{pmatrix} \mathbf{j}_s^x & \mathbf{j}_s^y & \mathbf{j}_s^z \end{pmatrix}. \quad (2.2)$$

The spin current density is represented by a second rank tensor indicated by the underline and as before the thermodynamic expectation value for a non-equilibrium state is denoted as $\langle\dots\rangle$. In Eq. (2.2), we used $\hat{\mathbf{s}} = \frac{\hbar}{2}\hat{\boldsymbol{\sigma}}$, where $\hat{\boldsymbol{\sigma}}$ correspond to the vector of the Pauli matrices [71, 72] and assumed that each particle, in our case electrons, transports a spin angular momentum of $\hbar/2$. Note that the row vectors $\mathbf{j}_{s,j} = \frac{\hbar}{2}n\langle\hat{\sigma}_i\mathbf{v}^\top\rangle$ describe the flow direction of the spin current featuring a fixed polarization $\hat{\sigma}_i$, while the column vectors $\mathbf{j}_s^j = \frac{\hbar}{2}n\langle\hat{\sigma}\mathbf{v}_i\rangle$ denote the spin polarization direction for a fixed current flow direction given by the velocity component v_j with $i, j = x, y, z$.

Since we consider a spin- $\frac{1}{2}$ system, we can express the spin current only in terms of two eigenstates, since the spin state manifests itself along a certain quantization axis when experimental measurements are performed. Thus, we can simplify the following derivations. Without the loss of generality, we choose the z -axis and the associated spin-up and spin-down states expressed as $|\uparrow\rangle$ and $|\downarrow\rangle$,

respectively². The expectation value as defined in Eq. (2.2) for these two spin states can be written as $\mathbf{j}_{s,z}^{|\uparrow\rangle} = \frac{\hbar}{2}n \langle \uparrow | \hat{\sigma}_z \mathbf{v}^\top | \uparrow \rangle = \frac{\hbar}{2}n \langle \mathbf{v}^\top \rangle^\uparrow \equiv \mathbf{j}_s^\uparrow$ and $\mathbf{j}_{s,z}^{|\downarrow\rangle} = \frac{\hbar}{2}n \langle \downarrow | \hat{\sigma}_z \mathbf{v}^\top | \downarrow \rangle = -\frac{\hbar}{2}n \langle \mathbf{v}^\top \rangle^\downarrow \equiv \mathbf{j}_s^\downarrow$, respectively. In this case, $\langle \mathbf{v}^\top \rangle^\uparrow$ and $\langle \mathbf{v}^\top \rangle^\downarrow$ denote the expectation values of the particle velocities for spin-up and spin-down states³. We see that the associated particle current density transports spin angular momentum of either $\hbar/2$ or $-\hbar/2$, which we would expect when considering only one certain spin direction. Using these results, we can define the total spin current along our arbitrary chosen quantization direction within the two-fluid model as

$$\mathbf{j}_s = \mathbf{j}_s^\uparrow + \mathbf{j}_s^\downarrow = \frac{\hbar}{2}n(\langle \mathbf{v} \rangle^\uparrow - \langle \mathbf{v} \rangle^\downarrow) = -\frac{\hbar}{2e}(\mathbf{j}_c^\uparrow - \mathbf{j}_c^\downarrow) \quad (2.3)$$

by summing up spin-up and -down currents. In the last step, we related the spin currents to electrical currents using the relation $\mathbf{j}^{\uparrow,\downarrow} = n \langle \mathbf{v} \rangle^{\uparrow,\downarrow} = \mathbf{j}_c^{\uparrow,\downarrow}/q$ with $q = -e$ for electrons. For simplicity, we dropped the transposition of the velocity vector, which makes \mathbf{j}_s a conventional 3-dimensional column vector. The two-fluid model allows to view the spin-up and -down states as separate currents⁴. For this reason, we can define two separate chemical potentials μ^\uparrow and μ^\downarrow for spin-up and -down states, respectively, and express the charge current as $\mathbf{j}_c^{\uparrow,\downarrow} = -(-\sigma_e/e)\nabla\mu^{\uparrow,\downarrow}$ with σ_e the electrical conductivity using Fick's law [73]. Introducing the spin chemical potential or spin accumulation $\mu_s = \mu^\uparrow - \mu^\downarrow$, representing the excess of spin-up states, we obtain [74]

$$\mathbf{j}_s = -\frac{\hbar}{2e} \frac{\sigma_e}{e} \nabla \mu_s. \quad (2.4)$$

According to Eq. (2.4), we can express the metallic spin conductivity as $\sigma_s = \hbar/(2e^2) \cdot \sigma_e$.

In the two-fluid model, pure spin currents might be considered as the opposing flow of spin-up and -down electrons with equal current densities. Due to the opposite propagation direction of the electrons, the net charge current flow is compensated and only angular momentum is transported. The microscopic description of pure

²An arbitrary spin state $|\chi\rangle$ can be represented by a linear combination of the eigenstates according to $|\chi\rangle = \alpha|\uparrow\rangle + \beta|\downarrow\rangle$, where the projection of $|\chi\rangle$ along $|\uparrow\rangle$ ($|\downarrow\rangle$) can be written as a scalar quantity α (β).

³Note that for an explicit calculation of the expectation value of the velocity operator, the exact information about the (non-equilibrium) spatial wavefunction of the system under consideration is demanded. This task is omitted in this derivation for the sake of a general description.

⁴Note that the two-fluid model can only be applied if the two spin systems (spin-up and -down) do not interact with each other. Assuming a finite interaction would result in a thermal equilibrium between the two spin systems and thus equal chemical potentials, which in turn would lead to a relaxation of the spin polarization.

spin currents, however, is not well reflected in this rather simplified picture. In general, the transport of a quantity is a non-equilibrium phenomenon, which is driven by a generalized force acting on the system. In our case, this means that instead of a directed flow of electrons, one has to consider a random walk caused by a spatially inhomogeneous spin distribution. Assuming that the electron density is conserved in the material, a finite excess spin density evolves within the electron system, i.e. the spin current does not carry any charge. The direction of the spin density is described by the gradient in Eq. (2.4).

2.1.2 Spin Diffusion

The spin transport is diffusive in nature. In general, charge carriers elastically scatter maintaining their spin state before undergoing spin-flip scattering after an angular momentum relaxation time τ_e . The spin diffusion constant can be defined as $D = v_F^2 \tau_e$ with v_F the Fermi-velocity and the spin diffusion length increases with time. In a simplified picture, similar to charge carrier transport, one could assume that spin-up and down electrons perform random walk due to scattering with the step size l the free mean path and τ the momentum relaxation time, which is a good (one dimensional) first approximation to what happens in metals (and semiconductors). In contrast to charge carriers, for spins one has to additionally consider that spins flip with a certain probability [75].

As demonstrated in Eq. (2.4), spin currents are driven by external forces which result e.g. from a gradient of the spin chemical potential (cf. Eq. (2.4)) or a temperature gradient. In the following, we discuss the spatial and temporal behavior of spin currents driven by a gradient of the spin chemical potential μ_s .

In order to arrive at a differential equation for the spatial dependence of μ_s , we first introduce the spin density $\rho_s = \rho^\uparrow - \rho^\downarrow$ with ρ^\uparrow and ρ^\downarrow the spin densities for spin-up and -down electron states, respectively⁵. We start by introducing the continuity equation for the spin density, which can be written as [76]

$$\frac{\partial \rho_s}{\partial t} + \nabla \cdot \mathbf{j}_s = -\Gamma_s \rho_s, \quad (2.5)$$

where $\Gamma_s = 1/\tau_s$ is the spin relaxation rate accounting for the finite lifetime τ_s of either spin-up or -down states due to spin-flip scattering events. In contrast to electrically well insulated charge carrier systems, where loss processes can be neglected, the right-hand side of Eq. (2.5) is non-zero. The term on the right-hand side results from the non-conservation of the non-equilibrium spin density ρ_s , which

⁵In general, the spin density ρ_s is a vectorial quantity. For simplicity, however, we again only consider the spin density along an arbitrary quantization axis, which allows a description in the two-fluid model.

is primarily due to two loss mechanisms: a mixing of the two spin channels and the loss of angular momentum to, for example, the phonon system. This means, the relaxation of the total number of excess spin has to be considered. Next, we calculate the spin density via

$$\rho_s = \frac{\hbar}{2} n_s = \frac{\hbar}{2} \int_0^\infty D(\epsilon) \left[n_F(\epsilon, \mu^\uparrow, T) - n_F(\epsilon, \mu^\downarrow, T) \right] d\epsilon \quad (2.6)$$

with $n_s = n^\uparrow - n^\downarrow$ the difference between the electron density of spin-up and -down states, where we assumed that each electron carries a spin angular momentum of $\hbar/2$. Here, we integrate over the electron density of states for one spin direction $D(\epsilon)$ multiplied by the Fermi-Dirac distribution functions $n_F(\epsilon, \mu^{\uparrow,\downarrow}, T) = [\exp((\epsilon - \mu^{\uparrow,\downarrow})/(k_B T)) + 1]^{-1}$ for the electronic spin-up and spin-down states with a single particle energy ϵ at a certain temperature T . When μ_s is finite, a difference between the spin-up and spin-down densities arises. Without loss of generality, we choose $T = 0$ to evaluate ρ_s via Eq. (2.6). This is possible as the electron density has to be a conserved quantity for any temperature. For $T = 0$, the Fermi-Dirac distribution simplifies to a step function according to $n_F(\epsilon, \mu^{\uparrow,\downarrow}, T) = \Theta(\epsilon - \mu^{\uparrow,\downarrow})$, where $\Theta(x)$ corresponds to the Heaviside function, and we obtain

$$\begin{aligned} \rho_s &= \frac{\hbar}{2} \int_0^\infty D(\epsilon) \left[\Theta(\mu^\uparrow - \epsilon) - \Theta(\mu^\downarrow - \epsilon) \right] d\epsilon \\ &= \frac{\hbar}{2} \int_{\mu^\downarrow}^{\epsilon_F} D(\epsilon) d\epsilon + \frac{\hbar}{2} \int_{\epsilon_F}^{\mu^\uparrow} D(\epsilon) d\epsilon. \end{aligned} \quad (2.7)$$

Here, we introduced the Fermi energy $\epsilon_F = (\mu^\uparrow + \mu^\downarrow)/2$. To further simplify the expression in Eq. (2.7), we assume that the spin chemical potential is sufficiently small so that the density of states $D(\epsilon)$ can be considered constant over the energy range $\mu^\downarrow < \epsilon < \mu^\uparrow$. Thus, the spin density is given by

$$\rho_s = \frac{\hbar}{2} [D(\epsilon_F)(\epsilon_F - \mu^\downarrow) + D(\epsilon_F)(\mu^\uparrow - \epsilon_F)] = \frac{\hbar}{2} D(\epsilon_F) \mu_s = \frac{\partial \rho_s}{\partial \mu_s} \mu_s, \quad (2.8)$$

where we rewrote the prefactor of μ_s in a more general way in the last term and thus do not premise a certain approximation for the calculation of the spin density. This linear dependence of ρ_s on the spin chemical potential, allows us to write down a rather simple differential equation for μ_s . Substituting Eqs. (2.4) and (2.8) into the continuity Equation (2.5), we finally obtain [77–79]

$$\frac{\partial \mu_s}{\partial t} - D_s \nabla^2 \mu_s = -\frac{\mu_s}{\tau_s} \quad (2.9)$$

with $D_s = \hbar/(2e) \cdot \sigma_e/e \left(\frac{\partial \rho_s}{\partial \mu_s} \right)^{-1} = \sigma_s \left(\frac{\partial \rho_s}{\partial \mu_s} \right)^{-1}$ the spin diffusion constant⁶, where we used $\sigma_s = \hbar/(2e^2) \sigma_e$ as introduced above. The spin relaxation length, up to which the spin number is mostly conserved, is defined as $l_s = \sqrt{D_s \tau_s}$ ⁷ and features typical values in the range of a few nm up to a few μm ⁸.

2.2 Pure Spin Current Generation in Normal Metals

Having introduced spin currents and their transport, we now discuss the conversion process from charge current to spin current and vice versa. In order to generate pure spin currents in metallic systems, spin-up and -down state electrons have to be transported in opposite directions. Various phenomena based on electrical conductors with a finite spin-orbit coupling (SOC) enable such effects and can transform an applied charge current into a pure spin current. We can differentiate between the spin Hall effect (SHE) in normal metals [38, 39, 80, 81], the Rashba-Edelstein effect in two-dimensional electron systems [82–86] and depending on the symmetry the anomalous Hall effect [87–89] as well as the planar Hall effect [88, 89] in magnetically ordered materials. In the following, we concentrate on the SHE, which is the basis of all our experiments.

The spin Hall effect was first theoretically predicted by Dyakonov and Perel [38] and later reformulated by Hirsch [39]. Experimentally, the first evidence has been observed in the semiconductor GaAs in optical experiments [90]. Since then the SHE was observed in multiple materials and, in particular, heavy metals (HM)⁹ such as platinum (Pt), tantalum (Ta) or tungsten (W), have proven to be reliable materials in the field of charge to spin current conversion. In this thesis, we exclusively use Pt as a non-magnetic spin Hall active metal.

When a charge current $j_c = \sigma_e \nabla \mu_e / e$ with μ_e the electrochemical potential is driven through a normal metal with large enough SOC, the electrons get scattered in

⁶Note that this expression for the spin diffusion constant corresponds to the general expression $D = v_F^2 \tau_e$ defined at the beginning of the section. In order to arrive at this result, we utilize the conductivity $\sigma_e = \tau_e n_e e^2 / m_e$ according to the Drude model and $\rho_s = \hbar/2 \cdot n_s$. The obtained derivation $\partial n_s / \partial \mu_s$ can be approximated with $\hbar/2 \cdot D(\epsilon_F) \epsilon_F$ with $\epsilon_F = 1/2 \cdot m_e v_F^2$, leading to the general expression.

⁷The spin relaxation time indicates the decay length of the spin polarization and has to be contrasted from the spin diffusion length. However, in literature these two definitions have been mixed up and the spin relaxation/decay length is often called the 'spin diffusion' length. Often one speaks of the spin diffusion length for the case of purely diffusive motion, while the term spin relaxation length is used for more general cases, such as drift or magnetic field influenced decay of the spin density [75].

⁸In experiments, the values of l_s for one material can vary very strongly in some cases due to external factors, like the measurement method, or intrinsic differences in the crystalline quality and impurities, making a proper comparison rather difficult.

⁹Since the underlying physical mechanisms are based on SOC, which increases proportionally to Z^4 , normal metals with large nuclear charge numbers Z are particularly suitable.

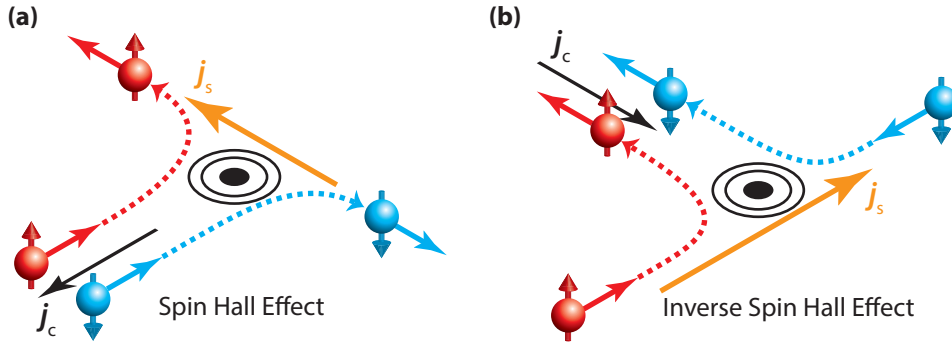


Fig. 2.1 – Illustration of the **(a)** spin Hall effect (SHE) as well as the **(b)** inverse spin Hall effect (ISHE). **(a)** In heavy metals with strong SOC conduction electrons scatter in different directions dependent on their spin state, where the scattering center is represented by the black circles. Due to the SHE, an applied charge current j_c leads to a transverse pure spin current j_s . **(b)** The ISHE describes the reciprocal process converting a spin current j_s into a charge current j_c . The figure has been taken from Ref. [68].

different directions depending on their spin state due to extrinsic impurity scattering and intrinsic bandstructure effects. As depicted in Fig. 2.1(a), this results in a transverse flow of spin-up and -down electrons in opposite directions, which in turn leads to a transverse spin current j_s with spin polarization s ¹⁰. Mathematically, this conversion process can be described by [38, 39, 80, 81]

$$j_s = \frac{\hbar}{2e} \theta_{\text{SH}} j_c \times s, \quad (2.10)$$

where phenomenologically θ_{SH} denotes the dimensionless spin Hall angle, which is a measure for the efficiency of the charge to spin current conversion¹¹. The spin Hall angle of Pt, for example, has a value of $\theta_{\text{SH}} = 0.11$ [92]. In a normal metal the quantization axis of the spin states and thus s is arbitrary. However, according to Eq. (2.10), the spin polarization has to yield an orthogonal relation to the directions of the charge as well as the spin current. As depicted in Fig. 2.1(b), the reciprocal effect, where a spin current is converted into a charge current, exists. Due to the

¹⁰The name SHE might be a bit misleading for the description of this phenomena. In contrast, to Hall effects, which in general describe the generation of a transverse current due to a longitudinal current for the same transport quantity, the SHE considers a charge current as the longitudinal component, which is transformed into a transverse current carrying spin. Note that the SHE originates from SOC that is fundamentally different to conventional effects.

¹¹Conventionally, the spin Hall angle is defined as $\tan \theta_{\text{SH}}$ [91]. However, in general for the conversion of a longitudinal charge current to a transverse spin current the approximation $\tan \theta_{\text{SH}} \approx \theta_{\text{SH}} \ll 1$ is utilized in literature.

Onsager reciprocity, exactly the same physics as for the SHE, lead to the so-called inverse spin Hall effect (ISHE) according to

$$\mathbf{j}_c = -\theta_{\text{SH}} \frac{2e}{\hbar} \mathbf{s} \times \mathbf{j}_s. \quad (2.11)$$

This means electrical conductors with no magnetic order, but with strong SOC allow for a charge current based generation and detection of pure spin currents, which is essential for the implementation in nowadays electronic devices.

2.3 Spin Transport Across Metal/Magnetically Ordered Insulator Interfaces

In this section, we expand our consideration of a heavy metal to a HM combined with a magnetically ordered insulator (MOI). In particular, we look into the pure spin current transport across a HM/MOI interface. Such bilayer systems open up new interesting physics and offer advantages compared to conventional electronics, like the suppression of typically unwanted current shunting. Before we dive deeper into the topic, we clarify some expressions. In general, the interactions between spin currents in a HM and the magnetic order in a MOI are captured by spin-transfer torques [93]. However, the wording spin-orbit torque (SOT) is more appropriate as the pure spin current in the HM originates from SOC and hence the torque caused in the MOI results from spin-orbit coupling [94].

In the following, we employ the results on spin transport across a HM/MOI interface by Bender and Tserkovnyak [95]. A typical bilayer structure is sketched in Fig. 2.2 with an incident spin current density polarized along \mathbf{s} in the HM. Furthermore, $\mathbf{n} = \mathbf{N}/N$ is the unit vector in the adjacent MOI with the magnetic order parameter N . We discuss the interactions between these two quantities, \mathbf{s} and \mathbf{n} , and their effect on the spin transport across the interface. In order to take temperature effects into account, we ascribe the temperatures T_e and T_m to the electron system in the HM and the magnonic system in the MOI, respectively. Moreover, we introduce the interfacial spin chemical potential μ_s^0 and the interfacial magnon chemical potential μ_m^0 , which describe the chemical potentials in the HM and MOI, respectively, directly at the location of the interface¹². According to

¹²The spin/magnon chemical potential can be derived from the spin/magnon diffusion Equation (2.9)/(2.34) using appropriate boundary conditions.

Ref. [95], the interfacial spin current across the interface (along \hat{y}) for arbitrary orientations of \mathbf{s} and \mathbf{n} can be determined by¹³

$$\begin{aligned} \mathbf{j}_{\text{s,int}}^y &= \frac{1}{4\pi} \left(\tilde{g}_i^{\uparrow\downarrow} + \tilde{g}_r^{\uparrow\downarrow} \mathbf{n} \times \right) \left(\mathbf{n} \times \mu_s^0 \mathbf{s} - \hbar \dot{\mathbf{n}} \right) \\ &+ \left[g(\mu_m^0 - \mu_s^0 \mathbf{s} \cdot \mathbf{n}) + S(T_m - T_e) \right] \mathbf{n}. \end{aligned} \quad (2.12)$$

It is important to mention that the vector $\mathbf{j}_{\text{s,int}}^y$ accounts for the amount and spin orientation of pure spin currents across the HM/MOI interface. In particular, as introduced in Eq. (2.2), $\mathbf{j}_{\text{s,int}}^y$ denotes the spin polarization direction with a fixed spin current direction along \hat{y} ¹⁴. Here, we describe the corresponding spin current vector as $\mathbf{j}_{\text{s,int}} = j_{\text{s,int}_i}^y \hat{y}$ with $j_{\text{s,int}_i}^y$ corresponding to the vector components $i \in x, y, z$ of Eq. (2.12). Furthermore, $\tilde{g}_i^{\uparrow\downarrow}$ and $\tilde{g}_r^{\uparrow\downarrow}$ are the effective spin mixing conductance parameters, g denotes the spin conductance and S corresponds to the spin Seebeck coefficient. All these four interfacial spin transfer coefficients can be calculated from the real and imaginary parts of the spin mixing conductance $g^{\uparrow\downarrow}$. We first concentrate on the latter quantity, before we discuss the other four coefficients. The spin mixing conductance is a measure for the proportion of electron spins capable of transferring spin angular momentum to the magnetic order \mathbf{n} across the HM/MOI interface and is given by [96–98]

$$g^{\uparrow\downarrow} = g_r^{\uparrow\downarrow} + i g_i^{\uparrow\downarrow} = \frac{1}{A} \sum_{nm} \left(\delta_{nm} - r_{nm}^{\uparrow} \left(r_{nm}^{\downarrow} \right)^* \right). \quad (2.13)$$

The real ($g_r^{\uparrow\downarrow}$) and imaginary ($g_i^{\uparrow\downarrow}$) part of the spin mixing conductance can be interpreted in analogy to electrical transport, where the complex electrical interface impedance is described by a real component, the resistance, and an imaginary component, the reactance. We discuss the physical interpretation later in this Section, after we have introduced all the quantities. As shown in Eq. (2.13), $g^{\uparrow\downarrow}$ is described by the interfacial reflection amplitudes r_{nm}^{\uparrow} (r_{nm}^{\downarrow}) of electronic spin-up (-down) wavefunctions accounting for the scattering from energy mode m to n . Moreover, $\sum_{nm} \delta_{nm} = M$ refers to the total number of open transport quantum channels across the interface at the Fermi energy. The exact number of channels depends on the available conduction electron modes, which are determined by the geometry of the HM in our case [99]. The quantized conductance value for each

¹³The slight difference compared to Equation (4) in Ref. [95] stems from the consideration that the actual spin direction is opposed to the associated magnetic moment in our case and thus the spin polarization \mathbf{s} features an opposed sign in Eq. (2.12).

¹⁴Describing the spin current across an interface, the spin current density, in contrast to our description within the two-fluid model in Sec. 2.1, has again to be expressed by a vector with its direction defining the polarization direction of the spin current, since only one particular direction of the particle flow, here the one across the interface, is of interest.

channel for one spin direction is given by the conductance quantum $G_0 = e^2/h$ [100]. The sum is normalized to the respective area A (and thus $g^{\uparrow\downarrow}$ has units of $1/m^2$). It is important to mention that this theoretical derivation of $g^{\uparrow\downarrow}$ based on interfacial scattering in Refs. [96–98] considers a HM on top of a conducting magnet and thus conduction electrons are present in the magnetic layer, which is in contrast to magnetic insulators investigated in this thesis. However, the formalism is still applicable in our case for the interfacial scattering of conduction electrons in the HM, because the spin-mixing conductance is predominantly determined by the local magnetic moments or exchange fields, respectively, at the interface [101–103]. Note that in the case of a conducting magnet, the term $-\sum_{nm} t_{nm}^{\uparrow} (t_{nm}^{\downarrow})^*$ has to be added to Eq. (2.13), where $t_{nm}^{\uparrow} (t_{nm}^{\downarrow})$ is the transmission coefficient for spin-up (-down) electrons transmitted from the conducting magnet layer in mode m to the HM in mode n [96–98]. Considering MOIs in this work, the transmission coefficients are vanishing. We want to raise awareness that this is also valid for conducting magnets when the magnetic film is thicker than the spin coherence length $\lambda_{sc} = \pi / |k_F^{\uparrow} - k_F^{\downarrow}|$ with $k_F^{\uparrow} (k_F^{\downarrow})$ the Fermi wavevector for spin-up (-down) states [98].

For temperatures $T \approx 0$, where we can assume a perfect alignment of the magnetic order \mathbf{n} along a certain axis, it is sufficient to consider the spin mixing conductance $g^{\uparrow\downarrow}$. However, for $T > 0$, we obtain fluctuations of the magnetic order leading to deviations from the average relative orientation of \mathbf{s} and \mathbf{n} and the spin mixing conductance has to be corrected for contributions originating from a temperature difference between the electronic system in the HM and the magnon system in the MOI. This includes temperature associated with magnon bandstructure effects via the magnon density of states $D(\epsilon_m)$ and the Bose-Einstein distribution function $n_B(\epsilon_m, \mu_m, T) = (\exp[(\epsilon_m - \mu_m)/(k_B T)] - 1)^{-1}$ with the single particle magnon energy ϵ_m , which is determined by the dispersion relation and the temperature T . Moreover, we introduced the magnon chemical potential μ_m , which accounts for non-equilibrium magnetic excitations of the magnetic order such as magnons¹⁵. Taking these effects into account, we arrive at the effective spin mixing conductance, which is given by [95]

$$\tilde{g}_r^{\uparrow\downarrow} = \left(1 - 2\frac{n_m}{s}\right) g_r^{\uparrow\downarrow} + \frac{2g_r^{\uparrow\downarrow}}{s} \frac{\partial}{\partial \mu_m} M_{\uparrow\downarrow}, \quad (2.14)$$

$$\tilde{g}_i^{\uparrow\downarrow} = \left(1 - \frac{n_m}{s}\right) g_i^{\uparrow\downarrow} \quad (2.15)$$

¹⁵The introduction of a finite chemical potential μ_m into the equilibrium Bose-Einstein distribution function for magnons requires a very efficient and fast local equilibration of the magnon system, otherwise the assumption of an equilibrium-type distribution function is not valid, as in an actual thermal equilibrium μ_m vanishes as the particle number is not conserved [95].

with

$$M_{\uparrow\downarrow} = \int_0^\infty d\epsilon_m D(\epsilon_m) (\epsilon_m - \mu_s) [n_B(\epsilon_m, \mu_m, T_m) - n_B(\epsilon_m, \mu_s, T_e)] . \quad (2.16)$$

Here, n_m/s accounts for the ratio between the thermal magnon density n_m and the equilibrium spin density $s = S/a^3$, where S is the total spin number in a unit cell with the volume a^3 .

Apart from corrections to the zero temperature spin mixing conductance $g^{\uparrow\downarrow}$, we also define the purely temperature-induced interfacial spin transfer coefficients g the spin conductance and S the spin Seebeck coefficient, which are determined by [95]

$$g = \frac{g_r^{\uparrow\downarrow}}{\pi s} \frac{\partial}{\partial \mu_m} M_{\uparrow\uparrow} , \quad (2.17)$$

$$S = \frac{g_r^{\uparrow\downarrow}}{\pi s} \frac{\partial}{\partial T_m} M_{\uparrow\uparrow} \quad (2.18)$$

with

$$M_{\uparrow\uparrow} = \int_0^\infty d\epsilon_m D(\epsilon_m) \epsilon_m [n_B(\epsilon_m, \mu_m, T_m) - n_B(\epsilon_m, 0, T_e)] . \quad (2.19)$$

From this description it is evident that Eqs. (2.17) and (2.18) correspond to purely thermally activated coefficients, because they vanish for $T = T_e = T_m = 0$. In contrast, the effective spin mixing conductance introduced in Eqs. (2.14) and (2.15) remains finite at $T = 0$ and reduces to the spin mixing conductance given in Eq. (2.13). In the following, we discuss the individual terms of Eq. (2.12) and their underlying physics in more detail. In particular, we focus on two configurations: $\mathbf{n} \perp \mathbf{s}$ and $\mathbf{n} \parallel \mathbf{s}$.

First, we consider a simplified expression assuming $T = T_e = T_m = 0$ and $\dot{\mathbf{n}} = 0$, i.e. no coherent precession. Thus, the two parameters g and S vanish, since they represent purely thermally activated coefficients as shown above. For $\mathbf{n} \perp \mathbf{s}$, Eq. (2.12) reduces to

$$\mathbf{j}_{\text{s,int}}^y(T=0) = \frac{1}{4\pi} \left(g_i^{\uparrow\downarrow} + g_r^{\uparrow\downarrow} \mathbf{n} \times \right) (\mu_s^0 \mathbf{s} \times \mathbf{n}) \quad (2.20)$$

with the imaginary $g_i^{\uparrow\downarrow}$ and real $g_r^{\uparrow\downarrow}$ part of the conventional spin mixing conductance $g^{\uparrow\downarrow} = g_r^{\uparrow\downarrow} + i g_i^{\uparrow\downarrow}$ [96–98]. The spin mixing conductance can be interpreted as a measure of the number of spin-flip scattering events at a HM/MOI interface for an ensemble of electron spins when $\mathbf{n} \perp \mathbf{s}$ [104, 105]. Such a scattering process transfers spin angular momentum to the magnetic order of the MOI due to angular momentum conservation, which results in a torque acting on the magnetic order

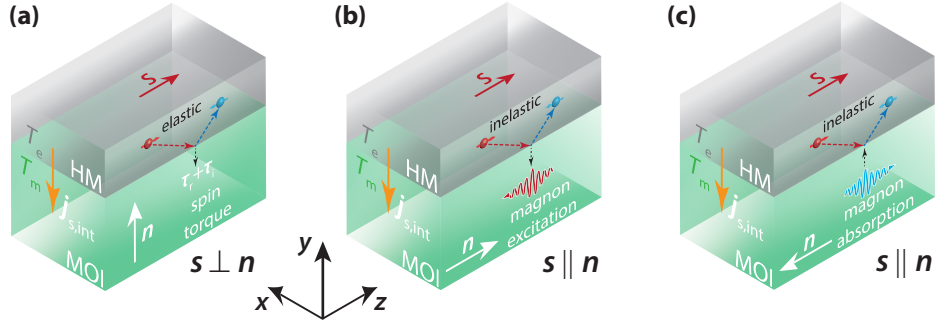


Fig. 2.2 – Spin-flip scattering processes at a HM/MOI interface. For an interfacial spin current $\mathbf{j}_{s, \text{int}}$ the orientation of the spin accumulation in the HM given by \mathbf{s} and the direction of the magnetic order parameter \mathbf{n} in the MOI are relevant. The electrons in the HM as well as the MOI possess a finite temperature T_e and T_m , respectively. (a) For $\mathbf{s} \perp \mathbf{n}$, the electrons scatter elastically at the interface flipping their spin. Their spin angular momentum is transferred to the MOI, leading to the torques τ_r and τ_i described by Eq. (2.12) acting on \mathbf{n} . (b), (c) For $\mathbf{s} \parallel \mathbf{n}$, the electrons are inelastically scattered at the interface and flip their spin due to an interaction with the thermal magnon spectrum in the MOI. For (b) a parallel configuration of \mathbf{s} and \mathbf{n} magnons are excited, while they are absorbed by the electrons for (c) an antiparallel configuration. The figure has been taken from Ref. [68].

vector \mathbf{n} . This means the factor provides information on the interfacial spin torque transparency [93, 101, 106–108]. Note that other possible interfacial processes that preserve spin during a scattering event do not transfer any angular momentum to the MOI, i.e. the interfacial reflection amplitudes in Eq. (2.13) exhibit a value of 1 and therefore are not of relevance for the spin mixing conductance [96].

When we now consider a finite temperature for the configuration $\mathbf{n} \perp \mathbf{s}$, the interfacial spin current can be described by the first line in Eq. (2.12) related to $\mathbf{n} \times \mu_s^0$, since the other terms vanish for $\mathbf{n} \perp \mathbf{s}$. The physical principle behind these contributions are depicted in Fig. 2.2(a), where electrons carrying the pure spin current scatter elastically at the HM/MOI interface and flip their spin. The spin flip, in turn, induces an excess spin angular momentum of \hbar , which is transferred via a torque $\boldsymbol{\tau} = \boldsymbol{\tau}_r + \boldsymbol{\tau}_i$ onto the magnetic order parameter \mathbf{n} . We can distinguish between the so-called damping-like torque $\boldsymbol{\tau}_r \propto \tilde{g}_r^{\uparrow\downarrow} \mathbf{n} \times (\mathbf{n} \times \mathbf{s})$ and the field-like torque $\boldsymbol{\tau}_i \propto \tilde{g}_i^{\uparrow\downarrow} (\mathbf{n} \times \mathbf{s})$ ¹⁶. While $\boldsymbol{\tau}_r$ can be associated with the real part of the spin mixing conductance $g_r^{\uparrow\downarrow}$, $\boldsymbol{\tau}_i$ is related to its imaginary part $g_i^{\uparrow\downarrow}$. Since $g^{\uparrow\downarrow}$ analogue to the electrical transport is composed of a real and imaginary part, we can relate the phenomenon to the complex electrical interface impedance as detailed here within a classical picture.

¹⁶The naming scheme evolved from the equivalent vector symmetries known from the Landau-Lifshitz-Gilbert equation [109, 110].

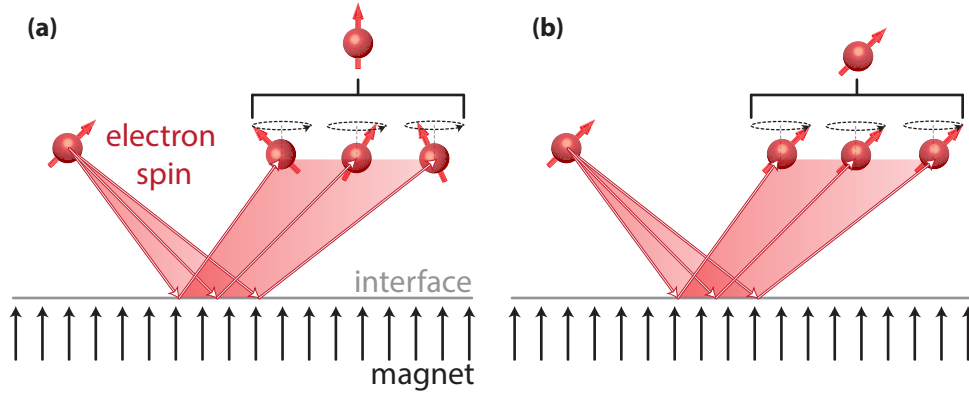


Fig. 2.3 – Classical picture of the spin torques contributions at a HM/MOI interface for the configuration $\mathbf{n} \perp \mathbf{s}$. **(a)** The first contribution τ_r , which is related to the real part of the spin mixing conductance $g_i^{\uparrow\downarrow}$, originates from the precession of the at the interface scattered electron spins in the exchange field of the magnet, resulting in a dephasing of the spins. **(b)** The second contribution to the torque τ_i is associated with $g_i^{\uparrow\downarrow}$ and results from an incomplete dephasing of the electron spins. Thus, these electrons, in contrast to the ones in panel (a), feature a finite spin moment along the transverse direction. The figure has been taken from Ref. [68].

In the case of the damping-like torque, the electron spin \mathbf{s} precesses in the exchange field of \mathbf{n} leading to a dephasing of the scattered quantity [93, 106]. This means the phase of the corresponding precession is rather random, since the scattered conduction electrons in the HM can feature any wavevectors allowed by the Fermi surface and therefore the superposition of all electron scattering events results in a loss of the transverse spin momentum as illustrated in Fig. 2.3(a). The latter is transferred to the magnetic order of the MOI via the torque τ_r (see Fig. 2.2(a)). Comparing this with the more familiar case of electronic transport, we can associate the dissipation of the spin magnetic moment to the real part of the electrical interface impedance, the resistance. Both quantities, the real part of the spin mixing conductance and the electrical resistance, capture the dissipation of spin angular momentum or moving electrical charge, respectively. As depicted in Fig. 2.3(b) for the field-like torque τ_i , the electron spin also precesses in the exchange field of \mathbf{n} , however, the dephasing is not completed and thus the scattered electrons retain a finite spin momentum along the original transverse direction \mathbf{s} . In this case, the torque is exerted directly on \mathbf{n} . The lack of dephasing and the resulting dissipationless spin precession can be related to the imaginary part of the electrical impedance, the reactance. In other words, both $\tilde{g}_i^{\uparrow\downarrow}$ and the reactance quantify the dissipationless part of the spin or charge transport, respectively. The last term in this configuration related to the time derivative $\dot{\mathbf{n}}$ accounts for the

spin pumping contributions stemming from a coherent precession of the magnetic order [98, 111–116].

Last but not least, we discuss the contributions to the interfacial spin current, which become relevant when $\mathbf{n} \parallel \mathbf{s}$. For this configuration, we have to consider the second line of Eq. (2.12), where the purely thermally activated coefficients, g the spin conductance and S the spin Seebeck coefficient become relevant. In general, for $\mathbf{n} \parallel \mathbf{s}$, the incident spin current polarization \mathbf{s} cannot exert a static torque on \mathbf{n} . However, a coupling to magnetic fluctuations is possible as they represent an effective (transient) misalignment of \mathbf{s} and \mathbf{n} , which allows for a finite torque. The resulting spin transfer across the interface relies on the two mechanisms already captured in the relations above. On the one hand, it is driven by the chemical potential difference $\Delta\mu = \mu_m - \mu_s$ (cf. Eq. (2.17)), and on the other hand by the finite interfacial temperature difference δT (cf. Eq. (2.18)).

The contribution proportional to g in Eq. (2.12) captures inelastic spin-flip scattering events of the spin polarized electrons [95], as illustrated in Fig. 2.2(b) and (c). In this case, the scattered electrons release some of their energy and transfer their spin angular momentum to the MOI exciting (panel (b)) or absorbing (panel (c)) a magnon in the thermal spectrum therein depending on the relative orientation between \mathbf{s} and \mathbf{n} . In the first case when \mathbf{s} is parallel to \mathbf{n} , this leads to a non-equilibrium magnon accumulation at the HM/MOI interface. In contrast, for the second case when \mathbf{s} is antiparallel to \mathbf{n} , a non-equilibrium depletion is obtained. This magnon accumulation/depletion can be characterized by an interfacial magnon chemical potential μ_m^0 . We see that this phenomena only occurs at finite temperatures, since the spin-flip scattering process is only possible when the electronic spin can interact with a thermally excited magnon state in the MOI. The last term related to S , also only occurs for finite temperatures and as already mentioned is driven by a temperature difference between the magnon system with temperature T_m and the electron system with temperature T_e . It is important to mention that this effect is independent of the relative orientation between \mathbf{s} and \mathbf{n} . Instead, the spin polarization \mathbf{s} is determined by the magnetic order parameter \mathbf{n} . This temperature driven spin current across a HM/MOI interface is in general known as the spin Seebeck effect (SSE) [117, 118].

The spin transport across HM/MOI interfaces is the basis of several phenomena such as the spin Hall magnetoresistance [69, 92, 119] and all-electrical magnon transport experiments [43, 120], which we exploit in this thesis. In particular, the detection of these interfacial spin currents in such experiments allows to separate the effects from other spurious signals, as the process can be tuned by the relative orientation between \mathbf{s} and \mathbf{n} .

2.4 Spin Hall Magnetoresistance

First, we focus on the spin Hall magnetoresistance (SMR), which was observed for the first time in the discussed HM/MOI bilayers [119]. The effect appears as a modulation of the resistance in the HM depending on the orientation of the magnetic order parameter \mathbf{n} in the MOI. As already mentioned, the SMR originates from pure spin current transport across the HM/MOI interface, which is detailed in the following.

The underlying physics of the SMR are sketched in Fig. 2.4. In experiments, a charge current is applied to the HM layer determining the charge \mathbf{j}_c and spin \mathbf{j}_s flow direction and thus also the spin polarization s . Within our chosen coordinate system, the charge current is driven along \hat{x} leading to a spin current along the y -direction with $s \parallel \hat{z}$ due to the SHE (cf. Eq. (2.10)). The interfacial spin current is described by Eq. (2.12) and depending on the relative orientation of \mathbf{n} and s different contributions dominate. Here, we only focus on the main results, while detailed calculations are presented in Refs. [69, 70]. To keep the discussion of the SMR simple, we neglect finite temperature effects [69, 121] and provide a qualitative picture of the effect. For $T = 0$, we can utilize Eq. (2.20), where the spin conductance and the spin Seebeck coefficient vanish ($g = S = 0$) and the effective spin mixing conductance reduces to $g^{\uparrow\downarrow}$. As discussed in the previous section, $\mathbf{j}_{s, \text{int}}^z(T = 0)$ is zero for the configuration $\mathbf{n} \parallel s$ (cf. Fig. 2.4(a)), while we obtain a finite value for $\mathbf{n} \perp s$ (cf. Fig. 2.4(b)). This difference influences the transverse and longitudinal electrical resistivity ρ of the HM layer. Since the latter is the relevant quantity in this thesis, we only focus on the longitudinal resistivity modulation.

The situation for $\mathbf{n} \parallel s$ is depicted in Fig. 2.4(a). Since the SHE-induced spin current \mathbf{j}_s cannot enter the MOI applying open circuit conditions, a spin accumulation μ_s^0 builds up at the interface. This in turn, gives rise to a gradient $-\nabla\mu_s$, which drives an opposing spin current $\mathbf{j}_{s, \text{back}}$ along \hat{y} as described in Eq. (2.4). This means there is no net spin current (steady state condition), as $\mathbf{j}_{s, \text{tot}} = \mathbf{j}_s + \mathbf{j}_{s, \text{back}} = 0$ and thus a similar resistivity behavior as that of a bare HM layer is obtained for $T = 0$. An analogous picture is found for charge transport, where a charge carrier accumulation at an interface leads to the generation of an electric field, which in turn drives an opposing drift current, so that there is no net charge current. In contrast for $\mathbf{n} \perp s$, the applied charge current is dissipated/absorbed partially by the MOI via the spin torque on \mathbf{n} , as illustrated in Fig. 2.4(b). Due to the resulting dephasing of the spins and the loss of transverse spin momentum in the HM, the opposing spin current $\mathbf{j}_{s, \text{back}}$ is smaller compared to the other configuration, which

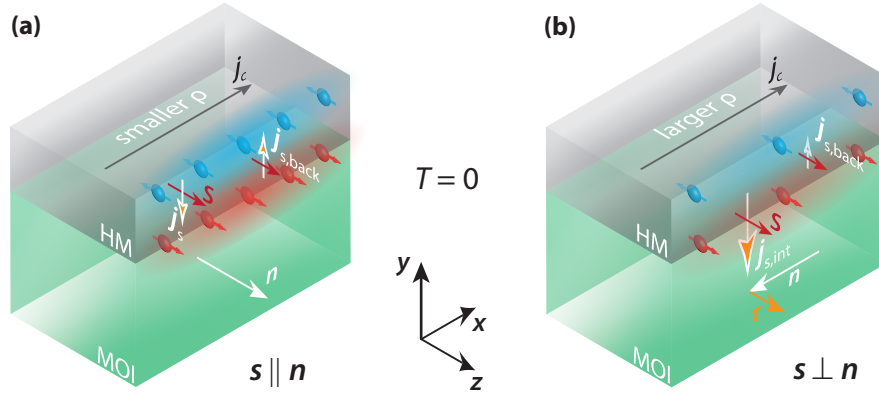


Fig. 2.4 – Influence of the magnetic order n in the MOI on the electrical resistivity ρ in the attached HM at $T = 0$. **(a)** For $n \parallel s$, a similar situation as for a bare HM layer is present. The SHE-induced spin current j_s cannot enter the MOI resulting in an antiparallel oriented, diffusive spin current $j_{s,back}$ described via Eq. (2.4) in the steady state. For a finite temperature only a small spin current flows across the interface and a magnon accumulation underneath the HM builds up due to the spin conductance g . **(b)** For $n \perp s$, spin current flow across the interface is enabled exerting a torque τ onto n in the MOI. As the backflow drift current $j_{s,back}$ only compensates a fraction of the incident spin current, the spin accumulation at the interface is reduced compared to panel (a). This in turn leads to a larger ρ . The figure has been taken from Ref. [68].

results in a larger resistance of the HM layer compared to that of a bare HM layer, where this spin dissipation channel is unavailable.

In order to express the longitudinal resistivity, we switch to a more general nomenclature and redefine the coordinate system in Fig. 2.4. Here, \hat{x} corresponds to the charge current direction j , \hat{y} is the surface normal and \hat{z} is defined as the transverse direction $t = \hat{y} \times j$. Thus, the longitudinal resistivity ρ_{long} of the HM as a function of the magnetic order parameter n is given by [119]

$$\rho_{\text{long}} = \rho_0 + \Delta\rho(1 - n_t^2), \quad (2.21)$$

where $n_t = n \cdot t$ is the projection of n onto t . Furthermore, ρ_0 denotes the resistivity of a bare HM layer and $\Delta\rho = \rho_{\parallel} - \rho_{\perp}$ is the SMR-induced resistivity change where ρ_{\parallel} and ρ_{\perp} correspond to the HM resistances obtained for the configurations $n \parallel j$ and $n \perp j$, respectively. Note that $\rho_0 = \rho_{\perp}$ in our case for $T = 0$. Finally, we can express the relative SMR amplitude assuming $g_r^{\uparrow\downarrow} \gg g_i^{\uparrow\downarrow}$ as [69, 70]

$$\frac{\Delta\rho}{\rho_0} = \frac{\theta_{\text{SH}}^2(2l_s^2\rho_e)(t_{\text{HM}})^{-1}g_r^{\uparrow\downarrow}\tanh^2\left(\frac{t_{\text{HM}}}{2l_s}\right)}{\frac{\hbar}{e^2} + 2l_s\rho_e g_r^{\uparrow\downarrow}\coth\left(\frac{t_{\text{HM}}}{l_s}\right)}. \quad (2.22)$$

Here, l_s is the spin diffusion length and $\rho_e = 1/\sigma_e$ defines the electrical resistivity. The SMR ratio $\Delta\rho/\rho_0$ calculated from several microscopic parameters allows us to extract important quantities under certain conditions. For example, measuring the SMR as a function of the HM thickness t_{HM} enables the extraction of the magnitude of the spin Hall angle $|\theta_{\text{SH}}|$ and l_s , when the spin mixing conductance is known [92, 122]. On the other hand, when these HM parameters are well known, like for the material of our choice, Pt [122], the SMR provides a great tool to determine $g_r^{\uparrow\downarrow}$. In this work, we use the SMR exclusively as a characterization tool for yttrium iron garnet/platinum interfaces, where the imaginary part of the spin mixing conductance is about 2 orders of magnitude smaller than its real part and thus the above assumption $g_r^{\uparrow\downarrow} \gg g_i^{\uparrow\downarrow}$ holds [92, 101, 123]. However, this assumption is not valid for all material systems. In Ref. [124] an europium-based MOI/Pt bilayer was investigated even suggesting that $g_r^{\uparrow\downarrow} \ll g_i^{\uparrow\downarrow}$.

Overall, the description of the SMR effect at $T = 0$ represents an excellent approximation also for finite temperatures [92]. Although $g > 0$ for finite temperatures and thus a finite interfacial spin current transport for $\mathbf{n} \parallel \mathbf{s}$ is obtained, it is reasonable to assume $g \ll g^{\uparrow\downarrow}$ even at room temperature due to its strong temperature dependence ($g \propto T^{3/2}$) [76].

2.5 Charge Current Induced Magnon Transport in Magnetically Ordered Insulators

In this Section, we introduce the physical principles of all-electrical magnonic spin transport experiments. Such experiments are based on spin-to-charge conversion processes (Sec. 2.2) as well as interfacial spin current transport (Sec. 2.3). In contrast to the introduction of the SMR in the previous section, where we considered $T = 0$, we here have to account for finite temperatures as they enable a finite spin injection into the MOI for $\mathbf{n} \parallel \mathbf{s}$. As we have seen in Eq. (2.12), the spin injection via a spin accumulation at a HM/MOI interface depends on the relative orientation between the injected spin \mathbf{s} and the magnetic order \mathbf{n} as well as on the temperature difference between the HM and MOI system. In order to account for this, we can introduce the interfacial magnon flux $j_{\text{m, int}} = \mathbf{j}_{\text{s, int}}^y \cdot (-\mathbf{n})$ ¹⁷ for $T > 0$ and obtain [95]

$$j_{\text{m, int}} = -g(\mu_{\text{m}}^0 - \mu_{\text{s}}^0 \mathbf{s} \cdot \mathbf{n}) - S(T_{\text{m}} - T_{\text{e}}). \quad (2.23)$$

¹⁷According to our considerations magnons are excited in the MOI, instead of depleted, when \mathbf{s} and \mathbf{n} are oriented antiparallel. The minus sign between $j_{\text{m, int}}$ and $\mathbf{j}_{\text{s, int}}^y$ stems from this fact. This means the magnon current carries magnetic moment along $-\mathbf{n}$.

This interfacial magnon current is composed of two contributions. On the one hand, spin injection is possible via the spin conductance g depending on the relative orientation between s and n , which we refer to as SHE-induced/electrically induced magnon injection in the following. On the other hand, the thermally induced magnon injection characterized by the spin Seebeck coefficient is enabled for arbitrary directions. We discuss these two contribution in the context of all-electrical magnon transport experiments in HM/MOI bilayers in more detail and in addition provide more details on the diffusive magnon transport in the MOI.

2.5.1 Magnon Generation and Detection via Heavy Metal Electrodes

The presented concept of all-electrical magnon spin transport experiments was initially introduced theoretically by Zhang and Zhang [125, 126]. The first experimental realization followed a few years later by Cornelissen *et al.* [43] and shortly after by Goennenwein *et al.* [120]. These experiments utilize two spatially separated HM electrodes attached to a MOI as sketched in Fig. 2.5. For convenience, the left electrode, the injector, electrically injects magnons via the SHE, while the right electrode, the detector, allows for an electrical detection via the ISHE. When a charge current j_c is applied along the injector electrode, a spin current j_s flowing towards the HM/MOI interface is generated according to Eq. (2.10). Determined by the device geometry and the direction of j_c , the spin polarized electrons approach the interface with a fixed direction of spin polarization s .

First focusing on the SHE-induced magnons according to the first term in Eq. (2.23), the spin current couples to the thermally occupied magnon states of the MOI via g for $s \parallel n$ (cf. Fig. 2.5(a)). In order to allow for a general description, which also includes multi-sublattice magnetic insulators with ferri- or antiferromagnetic order, we consider two magnon modes with opposite chiralities introduced as α - and β -mode. The opposing magnetic sublattices in ferri- or antiferromagnets give rise to magnons with different chiralities and thus magnon polarizations [127–133]. However, in most conventional ferrimagnets, like for example yttrium iron garnet studied in this thesis, the magnetic structure can be treated as a single sublattice and thus as a quasi-ferromagnetic system. For a ferromagnetic order, it is sufficient to consider only one thermally occupied magnon mode, for example magnons are only part of the α -mode. In general, the α -mode corresponds to magnon excitations in which the magnetic moments are oriented opposite to n ¹⁸, while β -mode excitations are directed along n [36]. This means for a parallel orientation of n and s , α -modes are excited and β -modes are depleted, while the two modes interchange

¹⁸Note that the spin magnetic moment is oriented opposite to the spin direction s as electrons feature a negative charge ($-e$) resulting in a negative gyromagnetic ratio γ .

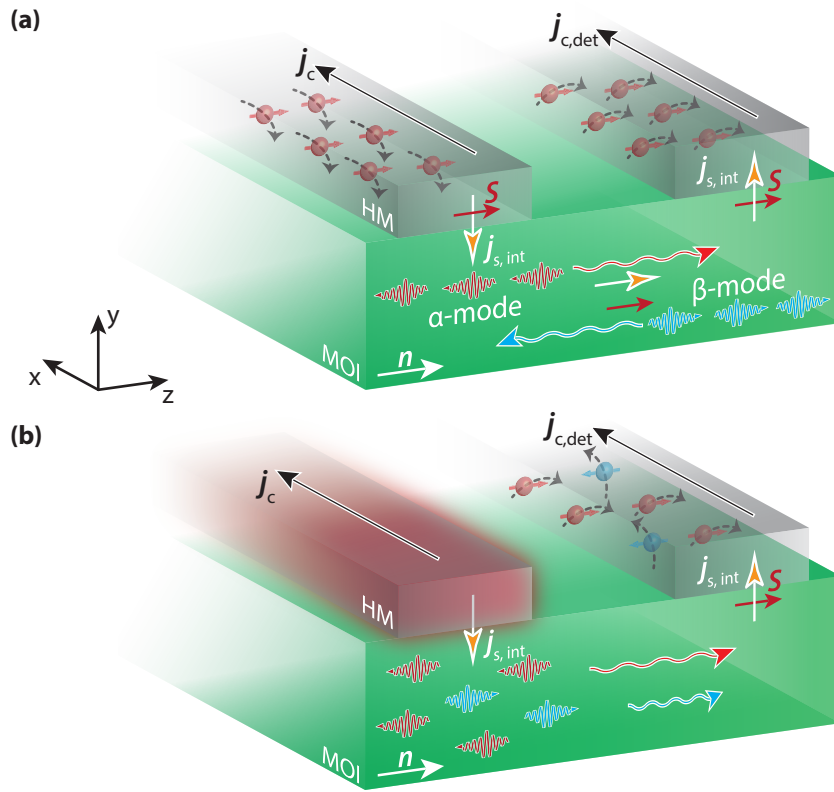


Fig. 2.5 – All-electrical magnon transport scheme of a two-terminal HM/MOI heterostructure. Two electrically isolated HM electrodes are attached to a MOI with the ordering parameter n . **(a)** A charge current j_c applied to the left electrode, referred to as injector, leads to a spin current j_s with spin polarization s inducing an electron spin accumulation at the HM/MOI interface. Due to the parallel orientation of s and n , thermally occupied α -modes are excited, while β -modes are depleted. The resulting diffusive magnon spin current in the MOI with both modes contributing positively is then converted back into a charge current $j_{c,det}$ via the inverse process at the second electrode, the detector, where the charge current can be detected as an open circuit voltage. **(b)** The charge current driven through the injector additionally leads to current-induced Joule heating injecting magnons thermally in the area beneath the HM electrode. In this case, both modes are excited simultaneously in the MOI and an effective magnon spin current due to thermally generated magnons can only be detected via the ISHE at the second electrode if a finite imbalance of the occupation of the α - and β -mode is present. In the simplified case of a ferromagnet, only one mode has to be considered. The figure has been taken from Ref. [68].

their roles for an antiparallel configuration of \mathbf{n} and \mathbf{s} . In addition to a reversal of \mathbf{n} , a reversal of the charge current j_c can also lead to a change in the type of magnons accumulated or depleted below the injector due to the SHE symmetry. As indicated in Fig. 2.5(a), the simultaneous excitation of one polarization of magnons and the depletion of oppositely polarized magnons add up and contribute to the magnon spin current with the same sign [134]. The spatially confined magnon injection gives rise to a localized non-equilibrium magnon accumulation μ_m and leads to a diffusive magnon current transport [43]. The magnon spin current flows to the detector, where it is converted back to a spin accumulation μ_s and induces a spin current j_s according to Eq. (2.4). In the HM electrode, j_s is then transformed into a charge current $j_{c,\text{det}}$ via the ISHE (cf. Eq. (2.11)), which is directed along the same direction as the applied charge current at the injector. Under open circuit conditions, this current can be measured as a voltage drop V_{det} across the HM detector electrode. Since the spin-to-charge or charge-to-spin conversion are exploited at the injector as well as at the detector, the symmetry of the SHE is applied twice in these magnon transport experiments. In angle-dependent measurements, where the orientation of \mathbf{n} is varied with respect to \mathbf{s} , a 180° -symmetric modulation of the detected voltage is expected, since the the injected and detected spin direction \mathbf{s} or \mathbf{j}_c , respectively, determines the sign of the signal and this process is independent of whether \mathbf{s} is parallel or antiparallel to \mathbf{n} .

The second effect allowing for magnon injection depicted in Fig. 2.5(b) originates from Joule heating. Due to the finite resistance of the HM strip, a charge current applied to the injector is always accompanied by Joule heating. This effect is captured in Eq. (2.23) via the spin Seebeck coefficient S and a finite temperature difference between T_m and T_e at the interface induced by the charge current heating. Moreover, Eq. (2.23) shows that the thermal injection of magnons is independent of \mathbf{s} . Consequently, the magnon polarization is exclusively determined by the orientation of \mathbf{n} and both the α - and β -mode are excited simultaneously. The efficiency of this process depends on the thermal occupation of the two modes in the system [129, 130]. Considering a collinear easy-axis antiferromagnet, the oppositely polarized magnon modes are degenerate and the two contributions compensate each other resulting in an effective thermally excited spin of zero. One can think of different possibilities to lift this compensation effect and locally increase the magnon chemical potential, which enables a finite magnon spin transport. In these easy-axis antiferromagnets it has been demonstrated that the degeneracy is lifted when an external magnetic field is applied along the easy-axis [132, 135] or perpendicular to the sublattice magnetizations leading to a deviation from the collinear arrangement [134]. In more complex antiferromagnets, such as easy-plane antiferromagnets, the degeneracy can also be lifted by the Dzyaloshinskii-Moriya

interaction [136, 137], dipolar interactions or certain anisotropies [48, 128, 138]. For a ferromagnetic order, we only have to account for one magnon mode, i.e. there is always a finite excess spin accumulation along \mathbf{n} and therefore a finite magnon spin transport due to thermally injected magnons. Several experimental studies showed that thermally induced magnon transport is mainly driven by gradients in the magnon chemical potential μ_m and the magnon temperature T_m [139–141]. A more detailed description of the magnon transport can be found in Sec. 2.5.2. The thermal contribution of the magnon transport is measured at the detector as a superposition of these two effects. Another effect of the current heating is the variation of the temperature profile across the whole device due to pure heat currents. This might induce an interfacial temperature difference between T_m and T_e at the detector position leading to a spin Seebeck current across the interface according to Eq. (2.12). However, this effect was estimated to have a minor effect on the transport signal [141]. Overall, the signal due to thermally injected magnons exhibits a 360° -symmetric angle dependence, since the thermal magnon polarization is determined by the direction of \mathbf{n} and only the ISHE symmetry at the detector gives rise to an angular modulation. Due to different symmetries of the detected voltage, thermally and electrically induced magnons can be easily distinguished.

2.5.2 Magnon Transport

Up to now, we mainly focused on the electrical injection and detection mechanisms in the HM and the transport across the HM/MOI interfaces. In order to provide a full picture of all-electrical magnon transport experiments, we discuss the magnon transport properties in the following.

Most importantly, we have to take into account the transport of a large magnon ensemble with broad spectral range. The incoherent excitation process leads to a non-equilibrium magnon accumulation μ_m , which exhibits a broad range of mean free paths, instead of enabling a magnon transport of a certain frequency and wavevector. The spatial and temporal dynamics of non-equilibrium distribution functions is well described in the theoretical framework of the Boltzmann transport theory [76, 126, 126]. First, we consider the rather simple case of magnon transport in a ferromagnetic insulator (FMI) with a single parabolic magnon band using the dispersion relation $\epsilon_m(\mathbf{k}) = \hbar\omega_m(\mathbf{k}) = \epsilon_0 + J_s k^2$, where ϵ_0 denotes the magnon gap energy and J_s is the exchange stiffness parameter. Utilizing the Boltzmann equation

of motion, the magnons can be described by the position vector \mathbf{r} , wavevector \mathbf{k} and time t dependent distribution function $f(\mathbf{r}, \mathbf{k}, t)$, which can be written as¹⁹

$$\frac{\partial f}{\partial t} + \frac{1}{\hbar} \frac{\partial \epsilon_m(\mathbf{k})}{\partial \mathbf{k}} \cdot \nabla_{\mathbf{r}} f = \Gamma_{\text{scat}} + \Gamma_{\text{int}}. \quad (2.24)$$

Here, Γ_{scat} denotes the relaxation rate due to magnon scattering, while Γ_{int} accounts for the relaxation (or injection) rate due to interfacial effects. However, the latter describing contributions from the HM/MOI interface according to Eq. (2.12) is treated only as a small perturbation of the system in the following. Accounting for multiple scattering processes, we can utilize the relaxation time approximation for the scattering rate given by

$$\Gamma_{\text{scatt}} = - \sum_i \frac{f - \bar{f}_i}{\tau_i}, \quad (2.25)$$

where \bar{f}_i is the quasi-equilibrium distribution function the magnon subsystem i relaxes into and τ_i defines the corresponding relaxation time. The index sums over the different characteristic scattering processes leading to the relaxation of the system with $i \in \{\text{mm}, \text{mp}, \text{el}, \text{mr}\}$. According to Ref. [95], we distinguish between processes that conserve the number of magnons, like magnon-magnon scattering ($i = \text{mm}$), magnon-phonon scattering ($i = \text{mp}$) as well as elastic magnon-defect scattering ($i = \text{el}$), and magnon non-conserving processes, which are captured by $i = \text{mr}$. Latter is, for example, taken into account by the magnetic Gilbert damping α_G and correspond to magnon scattering with a phonon bath. Similar to the spin of electrons, the number of magnons is not a conserved transport quantity. In the following, we assume $\tau_{\text{mr}} \gg \tau_{\text{mm}}, \tau_{\text{mp}}$, which is a good approximation for FMIs that are relevant for this type of magnon transport so far. In particular, for the ferro-/ferrimagnet yttrium iron garnet, which is investigated in this thesis, τ_{mr} was calculated to be 2-3 orders of magnitude larger than magnon conserving scattering times [76]. These calculations show that magnon conserving processes dominate the magnon scattering in the system. Moreover, each of the quasi-equilibrium distributions \bar{f}_i can be expressed by a Bose-Einstein distribution function $n_B = (\epsilon_m, \mu_m, T) = (\exp[(\epsilon_m(\mathbf{k}) - \mu_m)/(k_B T)] - 1)^{-1}$.

¹⁹Note that the 'field-term' $1/\hbar \nabla_{\mathbf{r}} \epsilon_m(\mathbf{k}) \cdot \nabla_{\mathbf{k}} f(\mathbf{r}, \mathbf{k}, t)$ of the Boltzmann equation [73] is neglected, since we work with spatially homogeneous magnetic fields in our experiment and thus expect $\nabla_{\mathbf{r}} \epsilon_m(\mathbf{k}) = 0$.

For the four characteristic scattering processes the quasi-equilibrium distributions read as

$$\bar{f}_{\text{mm}} = n_{\text{B}}(\epsilon_{\text{m}}, \mu_{\text{m}}, T_{\text{m}}), \quad (2.26\text{a})$$

$$\bar{f}_{\text{mp}} = n_{\text{B}}(\epsilon_{\text{m}}, \mu_{\text{m}}, T_{\text{p}}), \quad (2.26\text{b})$$

$$\bar{f}_{\text{el}} = n_{\text{B}}(\epsilon_{\text{m}}, \mu_{\text{m}}, T_{\text{m}}), \quad (2.26\text{c})$$

$$\bar{f}_{\text{mr}} = n_{\text{B}}(\epsilon_{\text{m}}, 0, T_{\text{p}}), \quad (2.26\text{d})$$

where the magnon conserving relaxation mechanisms ($i \in \{\text{mm}, \text{mp}, \text{el}\}$) do not affect the magnon accumulation and thus $\mu_{\text{m}} \neq 0$. In contrast, the magnon accumulation relaxes for the magnon non-conserving scattering processes ($i \in \{\text{mr}\}$) resulting in $\mu_{\text{m}} = 0$. Furthermore, we can assign characteristic temperatures to the quasi-equilibrium distributions \bar{f}_i depending on the scattering process. Since $i \in \{\text{mm}, \text{el}\}$ represents magnon relaxation processes within the magnon system, the magnon temperature T_{m} can be substituted into \bar{f}_i . Furthermore, the phonon temperature T_{p} can be used for the other two scattering mechanisms with $i \in \{\text{mr}, \text{mp}\}$ as magnons relax into the phonon bath. In general, the magnon temperature equilibration to the phonon bath takes place on a length scale of about 1 nm [76, 142]. Therefore, it is reasonable to assume that magnons are equilibrated with the phonons at all times and thus $T = T_{\text{m}} = T_{\text{p}}$. With these considerations, we can solve Eq. (2.24) under steady state conditions. To this end, we assume a linearized solution for the distribution function according to $f(\mathbf{r}, \mathbf{k}, t) = g(\mathbf{k}) + n_{\text{B}}(\epsilon_{\text{m}}(\mathbf{k}), \mu_{\text{m}}(\mathbf{r}), T(\mathbf{r}))$, where $g(\mathbf{k})$ represents the non-equilibrium wavevector distribution of the magnons and the Bose-Einstein distribution function considers a space-dependent magnon chemical potential $\mu_{\text{m}}(\mathbf{r})$ and temperature $T(\mathbf{r})$. Substituting this ansatz into Eq. (2.24), we obtain

$$g(\mathbf{k}) = \tau_{\text{m}} \left(-\frac{\partial n_{\text{B}}(\epsilon_{\text{m}}(\mathbf{k}), \mu_{\text{m}}, T)}{\partial \epsilon_{\text{m}}(\mathbf{k})} \right) \frac{1}{\hbar} \frac{\partial \epsilon_{\text{m}}(\mathbf{k})}{\partial \mathbf{k}} \times \left[-\nabla \mu_{\text{m}}(\mathbf{r}) - \frac{\epsilon_{\text{m}}(\mathbf{k}) - \mu_{\text{m}}}{T} \nabla T(\mathbf{r}) \right] \quad (2.27)$$

with $(\tau_{\text{m}})^{-1} = \sum_i (\tau_i)^{-1}$ the total magnon scattering time²⁰. Utilizing Eq. (2.27), we can express the corresponding spin current density with the assumption that every magnon carries a spin momentum of \hbar as

$$\mathbf{j}_{\text{m}} = \hbar \int \frac{d\mathbf{k}}{(2\pi)^3} g(\mathbf{k}) \frac{1}{\hbar} \frac{\partial \epsilon_{\text{m}}(\mathbf{k})}{\partial \mathbf{k}}. \quad (2.28)$$

²⁰For the evaluation the approximation $\tau_{\text{mr}} \gg \tau_{\text{m}}$ was used, which represents a reasonable assumption as discussed above.

Furthermore, each magnon carries an energy of $\epsilon_m(\mathbf{k}) - \mu_m$, which enables the definition of the heat current density in a similar fashion according to

$$\mathbf{j}_h = \int \frac{d\mathbf{k}}{(2\pi)^3} g(\mathbf{k}) (\epsilon_m(\mathbf{k}) - \mu_m) \frac{1}{\hbar} \frac{\partial \epsilon_m(\mathbf{k})}{\partial \mathbf{k}}. \quad (2.29)$$

As already stated in the previous section, the magnon spin (\mathbf{j}_m) and heat (\mathbf{j}_h) currents for the magnon transport in FMIs are driven by $\nabla\mu_m$ and ∇T . We can write down the transport equations of the magnon system in a more general form:

$$\begin{pmatrix} \mathbf{j}_m \\ \mathbf{j}_h \end{pmatrix} = - \begin{pmatrix} \sigma_m & \hbar L/T \\ L & \kappa_m \end{pmatrix} \begin{pmatrix} \nabla\mu_m \\ \nabla T \end{pmatrix}. \quad (2.30)$$

Here, the 2×2 matrix contains the linear response transport coefficients, which can be derived by evaluating the \mathbf{k} -dependent integration in Eqs. (2.28) and (2.29) in linear response. In Eq. (2.30), σ_m is the magnon conductivity, κ_m represent the magnon heat conductivity and L denotes the bulk spin Seebeck coefficient²¹. Note that the magnon conductivity introduced in Eq. (2.30) exhibits a noticeable similarity with the Drude model [144, 145]. As calculated in Ref. [68], the magnon conductivity can be expressed as

$$\sigma_m = 3\hbar \frac{n_m \tau_m}{m_m} \quad (2.31)$$

with n_m the thermal magnon density and $m_m = \hbar^2/(2J_s)$ the effective magnon mass. The electrical conductivity introduced within the Drude model, on the other hand, reads $\sigma_e = e^2 n_e \tau_e / m_e$, where n_e is the electron density, τ_e the electron scattering time and m_e the electron mass²². Due to the cross terms in Eq. (2.30), both μ_m and T contribute to \mathbf{j}_m and \mathbf{j}_h . However, in the case of SHE-induced signals temperature driven magnon spin currents were found to contribute only as a minor correction to the signal [76, 133]. In contrast, the thermally induced magnon transport signal is affected significantly by temperature gradients via the bulk spin Seebeck coefficient L [140, 141]. At this point, we omit a further discussion of heat currents and temperature driven effects and focus on magnon chemical potential gradient $\nabla\mu_m$

²¹The bulk spin Seebeck coefficient L should not be confused with the interfacial spin Seebeck coefficient S introduced in Eq. (2.12). While latter accounts for the spin transfer efficiency across a HM/MOI interface due to a finite temperature difference, L represents the response function to temperature and magnon chemical potential gradients for magnon and heat currents in a MOI, respectively [143].

²²Note that the transport quantities \hbar and e in these two relations describing the magnon and electron conductivity, respectively, appear with different powers due to the different definitions of their associated current density. While the magnon current density reads $\mathbf{j}_m = -\sigma_m \nabla\mu_m$, the electrical current density is defined as $\mathbf{j}_c = -(-\sigma_e/e) \nabla\mu$.

driven effects. Throughout this thesis, we consider that the magnon spin current j_m is only driven by $\nabla\mu_m$.

In an analog manner as for spin currents (cf. Sec. 2.1.2), we derive the magnon spin diffusion equation exploiting the continuity equation for j_m , which is given by

$$\frac{\partial\rho_m}{\partial t} + \nabla \cdot \mathbf{j}_m = -\Gamma_{mr} \rho_m, \quad (2.32)$$

with Γ_{mr} the magnon relaxation rate and ρ_m the non-equilibrium magnon spin density. Similar as for electron spin, the non-vanishing term on the right hand side of Eq. (2.32) accounts for the non-conserved character of magnons. Evaluating ρ_m in linear response leads to

$$\begin{aligned} \rho_m &= \hbar\Delta n_m = \hbar \int_0^\infty d\epsilon_m g(\epsilon_m) [n_B(\epsilon_m, \mu_m, T) - n_B(\epsilon_m, 0, T)] \\ &\approx \hbar \frac{\zeta(1/2)}{\Lambda^3 k_B T} \mu_m. \end{aligned} \quad (2.33)$$

Here, Δn_m denotes the non-equilibrium magnon number density, while we identify $\partial\rho_m/\partial\mu_m = \hbar\zeta(1/2)/(\Lambda^3 k_B T)$ with $\zeta(x)$ the Riemann-Zeta function and $\Lambda = \sqrt{4\pi J_s/(k_B T)}$ the thermal (de-Broglie) wavelength [76]. Combining Eqs. (2.30), (2.32) and (2.33), we can introduce the magnon spin diffusion equation as

$$\frac{\partial\mu_m}{\partial t} - D_m \nabla^2 \mu_m = -\frac{\mu_m}{\tau_{mr}} \quad (2.34)$$

with $D_m = \sigma_m(\partial\rho_m/\partial\mu_m)^{-1}$ the magnon diffusion constant. Furthermore, the magnon spin lifetime is given by $\tau_{mr} = \Gamma_{mr}^{-1}$ representing the magnon spin non-conserving scattering times in accordance with their introduction above. To this end, we can similar as for the spin diffusion equation define the magnon decay length as $l_m = \sqrt{D_m \tau_{mr}}$ ²³.

In order to highlight the spatial characteristics of diffusive magnon spin transport, we solve Eq. (2.34) analytically, which is only possible in one dimension. Considering the structure introduced in Fig. 2.5, we assume the one dimensional transport along the spatial coordinate z . Hence, we can apply the boundary conditions $\mu_m(z=0) = \mu_m^0$ with μ_m^0 the magnon accumulation at the injector position $z=0$ and $\mu_m(z=d) = 0$, where we assume that the complete magnon accumulation is absorbed at the detector position d [43]. The resulting analytical expression for the magnon spin current reads $j_m(d) = -D_m \frac{\partial\mu_m(d)}{\partial d} = -2D_m \frac{\mu_m^0}{l_m} \exp(d/l_m)/(1 - \exp(2d/l_m))$. In

²³Note that this terminology has to be contrasted with the diffusion of conserved particles, such as gas diffusing into a room. However, since the magnon transport described in Eq. (2.34) is diffusive in nature and captured by the spatial variation of its chemical potential, the magnon propagation or decay length has often been called the magnon ‘‘diffusion length’’ in literature [43, 76, 120].

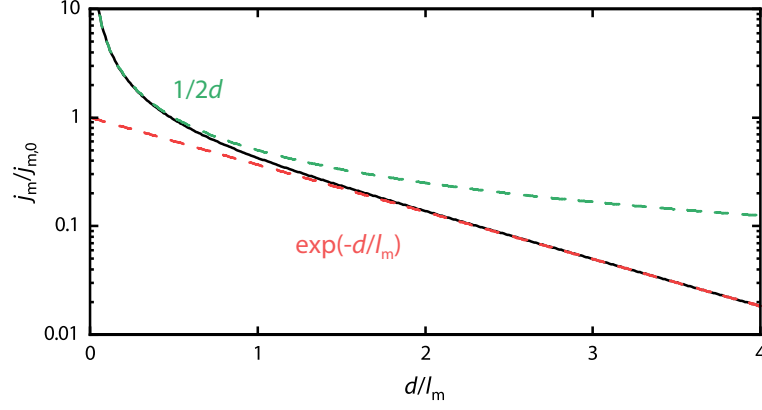


Fig. 2.6 – Calculated evolution of the normalized magnon spin current j_m as a function of the injector-detector distance d . The black line is the analytical solution obtained from Eq. (2.34). For $d \ll l_m$ the signal decay is well described by a $1/(2d)$ relation (green line). In contrast, for $d \gg l_m$ the magnon spin current exhibits an exponential transport scaling as $\exp(-d/l_m)$ (red line).

Fig. 2.6, the normalized magnon spin current j_m is plotted in black as a function of d/l_m . As indicated by the two other dashed lines, we can distinguish between two characteristic magnon spin transport regimes. For $d \ll l_m$, the spatial decay of j_m reduces to a $1/(2d)$ dependence (green line). In this regime, the transport is identical to a diffusion process without relaxation such as diffusive charge transport. Thus, in very good approximation the magnon spin transport can be treated analog to an ohmic-like charge transport, where we assume a linear relation between j_m and $\nabla\mu_m$ via the magnon spin conductance σ_m . For the second regime, we evaluate the other limiting case $d \gg l_m$, where we find an exponential decay of the magnon spin current according to $\exp(-d/l_m)$ (red line). This enables an easy determination of l_m in MOIs via distance-dependent measurements of the magnon spin transport signal using the introduced all-electrical magnon transport devices (cf. Fig. 2.5).

Indeed, this magnon spin transport description can also be applied for antiferromagnetic insulators (AFIs). However, in this case, individually defined magnon spin chemical potentials and temperatures of the two oppositely polarized α - and β -modes have to be taken into account [36]. While this approach works well for easy-axis antiferromagnets, where the magnon transport can be described by the magnon chemical potential [134], it is more complex for non-trivial antiferromagnetic spin textures such as easy-plane antiferromagnets [127]. In such systems, the rotational symmetry about the magnetic order \mathbf{n} is broken due to magnetic interactions. This, in turn, leads to a coupling between the oppositely polarized magnon modes and allows for arbitrary superposition states of the two basis modes. It has been shown that this antiferromagnetic magnon system can be well described by the so-called pseudospin concept [138], which we introduce in Chapter 5.

Experimental Details

In this Chapter, we provide details of the samples investigated in the subsequent Chapters. To allow for a proper understanding and discussion of the presented results below, we first introduce the studied material systems in Sec. 3.1, followed by the description of the nanofabrication process of the samples in Sec. 3.2. In Sec. 3.3, the experimental setup is introduced.

3.1 Material Systems

Throughout this work, two magnetically ordered insulators have been studied, namely the ferrimagnet yttrium iron garnet ($\text{Y}_3\text{Fe}_5\text{O}_{12}$, YIG) and the antiferromagnet hematite ($\alpha\text{-Fe}_2\text{O}_3$). In the following, we summarize their structural and magnetic properties.

3.1.1 Ferrimagnetic Insulator - Yttrium Iron Garnet

The rare-earth iron garnet magnetic insulator $\text{Y}_3\text{Fe}_5\text{O}_{12}$ features a body-centered-cubic (bcc) conventional unit cell with a lattice constant $a = 12.38 \text{ \AA}$ [146, 147]. Overall, the conventional unit cell corresponds to 4 formula units [148] and contains 80 atoms (12 Y^{3+} , 20 Fe^{3+} and 48 O^{2-} ions). While the yttrium Y^{3+} ions are dodecahedrally coordinated, 8 Fe^{3+} ions are octahedrally (FeA) and 12 Fe^{3+} ions are tetrahedrally (FeD) coordinated to the O^{2-} ions. A simulation of the middle layer of the YIG unit cell is shown in Fig. 3.1. The finite net magnetic moment in YIG originates from the Fe^{3+} ions each characterized by a total spin number of $S = 5/2$. In contrast, the yttrium Y^{3+} ions have completely filled shells and therefore the electron configuration carries no net magnetic moment. The latter applies also for the oxygen O^{2-} ions. This results into two magnetic sublattices stemming from the FeA and FeD moments. Within both sublattices the magnetic moments are antiferromagnetically exchange coupled exhibiting exchange energies of $J_{AA} = -0.92 \times 10^{-21} \text{ J}$ and $J_{DD} = -3.24 \times 10^{-21} \text{ J}$ [149]. However, in YIG the inter-sublattice exchange with $J_{AD} = -9.6 \times 10^{-21} \text{ J}$ [149], which is also antiferromagnetic, dominates, leading to a parallel orientation of the intra-sublattice spins. Therefore, the spin structure in YIG can be represented as two antiferromagnetically coupled sublattices (cf. Fig. 3.1). Although the MOI $\text{Y}_3\text{Fe}_5\text{O}_{12}$ is a ferrimagnet, it is usually treated as a single

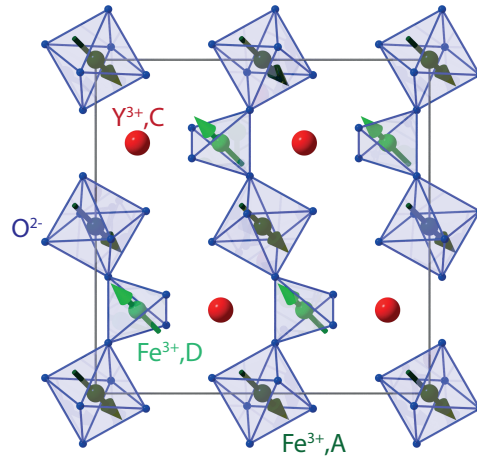


Fig. 3.1 – Middle layer of the cubic unit cell of $\text{Y}_3\text{Fe}_5\text{O}_{12}$. The Y^{3+} ions and O^{2-} ions are represented by red and blue spheres, respectively. The magnetic sublattices composed of octahedrally coordinated Fe^{3+} ions (FeA, light green) and tetrahedrally coordinated Fe^{3+} ions (FeD, dark green) are depicted by spheres, where the spin orientation is indicated via arrows. This simulation has been taken from Ref. [68].

sublattice ferromagnet, due to this strong antiparallel coupling of the sublattices persisting external magnetic fields up to 250 T [150, 151]. The total magnetization \mathbf{M} of the ferromagnet is given by the net magnetization $\mathbf{M}_{\text{Fe, net}} = \mathbf{M}_{\text{FeA}} + \mathbf{M}_{\text{FeD}}$. In addition, the strong antiferromagnetic coupling leads to the large magnetic ordering temperature $T_C = 559$ K (Curie Temperature). The cubic symmetry of the crystal is also reflected in the magnetic anisotropy with the crystalline cubic anisotropy [151] determining the magnetic easy- and hard-axes for the magnetization direction. The corresponding anisotropy field is on the order of a few mT in bulk crystals [152]. Within the thin film limit, an additional shape anisotropy emerges with a magnetic hard-axis pointing out-of-plane, which is present for all studied YIG samples in this work. Featuring low magnetic damping with a magnetic damping coefficient as low as $\alpha_G = 4 \times 10^{-5}$ in bulk crystals [152–154] and a slightly larger value of about 1×10^{-4} in thin films due to surface defects and inhomogeneties [153, 155, 156], YIG is the preferable choice of material for efficient and long-distance spin transport for both incoherently [43, 120] and coherently [157] excited spin waves.

3.1.2 Antiferromagnetic Insulator - Hematite

In the second part of this work, we focus on the antiferromagnetic insulator hematite ($\alpha\text{-Fe}_2\text{O}_3$), which crystallizes in a corundum structure. The simulated crystal structure is shown in Fig. 3.2(a) in side view as well as in top view in Fig. 3.2(b). The

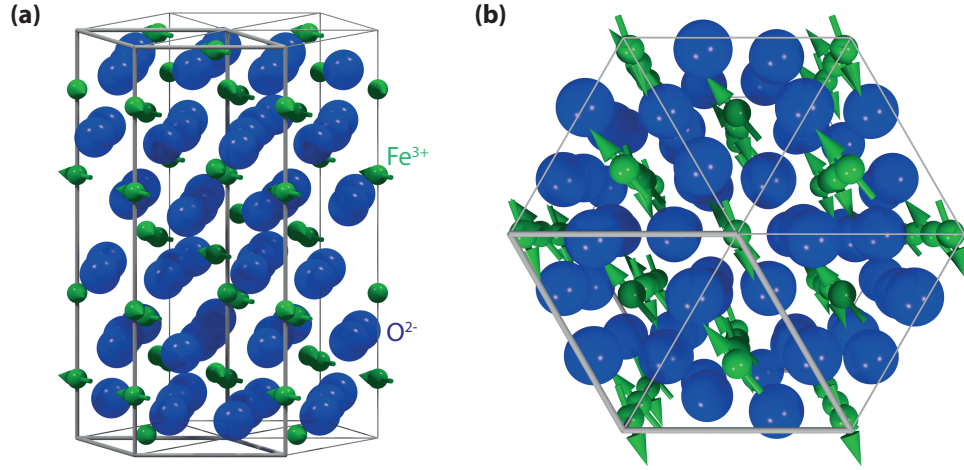


Fig. 3.2 – (a) Side and (b) top view of the corundum crystal structure of $\alpha\text{-Fe}_2\text{O}_3$. The hexagonal conventional cell consists of three trigonal unit cells as emphasized by thick gray connector lines. While the oxygen O^{2-} ions are represented by blue spheres, the magnetic Fe^{3+} ions are depicted as green spheres with arrows that show the spin orientation. The slight canting between the spins of the two sublattices indicate the DMI present in the system. This simulation has been taken from Ref. [68].

conventional unit cell with the lattice constants $a = 5.04 \text{ \AA}$ and $c = 13.77 \text{ \AA}$ [158] contains 6 times the formula unit. As depicted in Fig. 3.2, the oxygen ions (blue spheres) might be described as a hexagonal system, however they are slightly distorted with respect to their neighboring layers in such a way that only every sixth layer along the hexagonal [0001]-direction lies directly on top of each other. The magnetic Fe^{3+} ions with the total spin number $S = 5/2$ in between the oxygen layer are coordinated octahedrally to the O^{2-} ions. Since each iron layer is only occupied up to two-thirds, the symmetry is lowered to a trigonal structure, as indicated by thick connector lines in Fig. 3.2. For $\alpha\text{-Fe}_2\text{O}_3$ the relevant exchange coupling strength is given by the five nearest neighbors of the magnetic Fe^{3+} ions [159], where the antiferromagnetic exchange couplings of the third ($J_3 = -4.69 \times 10^{-22} \text{ J}$) and fourth ($J_4 = -3.17 \times 10^{-22} \text{ J}$) nearest neighbors dominate [159]. This results into a ferromagnetic coupling of the spins of the Fe^{3+} ions within the layer, while the spins exhibit an antiferromagnetic coupling between neighboring layers [160]. The corresponding magnetization orientations of the two sublattices \mathbf{M}_1 and \mathbf{M}_2 in hematite are characterized by the Néel vector $\mathbf{N} = \mathbf{M}_1 - \mathbf{M}_2$ and the corresponding normalized magnetic order vector $\mathbf{n} = \mathbf{N}/N$. The Néel temperature is $T_N = 953 \text{ K}$ in bulk crystals [158]. A second characteristic transition in hematite is characterized by the Morin transition temperature $T_M \approx 263 \text{ K}$ [158, 161], where the spins undergo a reorientation featuring a sign change of the uniaxial magnetic anisotropy. This means hematite undergoes a transition from a magnetic easy (0001)-axis below T_M

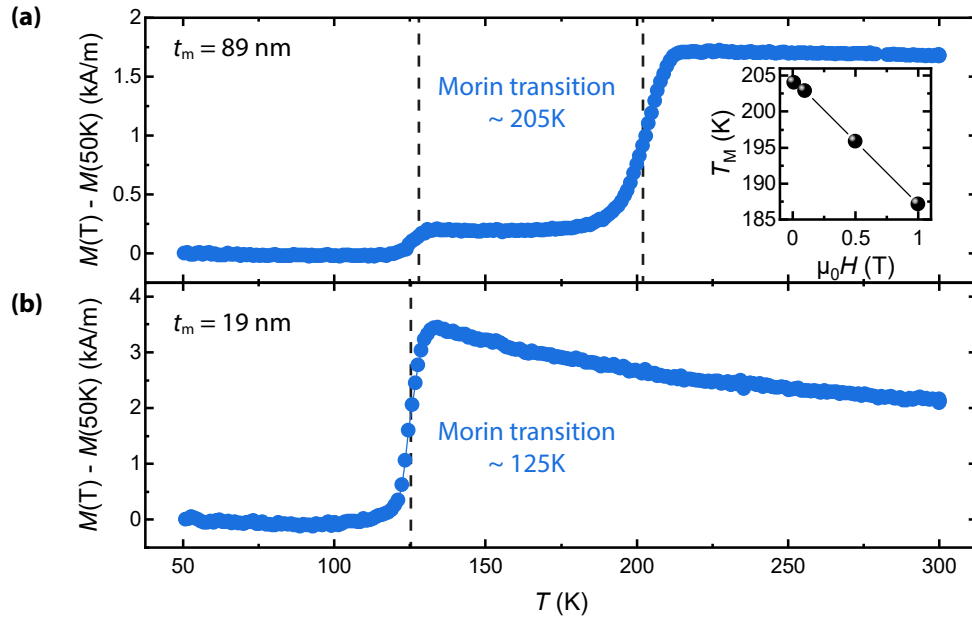


Fig. 3.3 – In-plane magnetization M as a function of the temperature T for a (a) $t_m = 89$ nm and (b) $t_m = 19$ nm thick α - Fe_2O_3 film. For the data obtained at $\mu_0 H = 100$ mT by SQUID magnetometry in zero field cooling (ZFC) configuration, we can unambiguously identify the Morin transition. The inset in panel (a) shows the magnetic field dependence of the Morin transition temperature T_M .

to a magnetic easy (0001)-plane above T_M . In the latter case above T_M , the finite Dzyaloshinskii-Moriya-Interaction (DMI) with the DMI-vector pointing along the (0001)-direction results in a slight canting of the two sublattice magnetizations lying in the (0001)-plane, which leads to a finite net magnetic moment \mathbf{m}_{net} oriented perpendicular to \mathbf{n} . Similar to YIG the crystal symmetry is reflected by the magnetic anisotropy. Since the crystal exhibits a trigonal symmetry, a threefold crystalline anisotropy in the easy-plane phase of hematite is found [162], giving rise to the formation of 120° -domains in the film at zero applied magnetic field.

The Morin transition temperature of our thin films differs from the one in bulk crystals. The growth details are presented in the next Section 3.2. In particular, the hematite thin films investigated in Sec. 5.2 show no Morin transition within the studied temperature range. This means that the films feature an easy-plane phase and an out-of-plane DMI vector over the whole temperature range. As discussed in previous works [68, 127], recent reports indicate a strong decrease and even a complete absence of the Morin transition temperature T_M for thin hematite films due to strain induced changes in the magnetic anisotropy [163, 164]. However, this scenario is rather unlikely in our case, as we find a complete relaxation of our hematite thin films. Another possible explanation for the not observed Morin transition might be an unintended Al doping of the hematite during the growth

process originating from the used sapphire (Al_2O_3) substrates. As demonstrated in Ref. [162], the Morin transition temperature significantly decreases for Al doped hematite. In the thin film limit, even a slight interdiffusion of Al might lead to a strong decrease of T_M . Up to now, this is however a mere speculation and the absence of a Morin transition is not entirely clear. In contrast, we were able to identify the Morin transition when we slightly adjusted the growth process to reduce the oxygen vacancies (cf. Sec. 3.2). In order to determine the Morin transition temperature of the two hematite films with thicknesses of $t_m = 19$ nm and $t_m = 89$ nm studied in Sec. 5.3, we performed SQUID (superconducting quantum interference device) magnetometry measurements. The measured magnetization M as a function of the temperature for the $t_m = 89$ nm and $t_m = 19$ nm thick film is shown in Fig. 3.3(a) and (b), respectively. The magnetic field with a magnitude of 100 mT has been applied in-plane in zero field cooling (ZFC) configuration. Accounting for the diamagnetic background signal stemming from the Al_2O_3 substrate, a temperature independent background linear in magnetic field has been subtracted from both data sets. In both cases, we can unambiguously identify the Morin transition temperature T_M . While we obtain $T_M = 205$ K for the thick film (Fig. 3.3(a)), we find a Morin transition temperature of $T_M = 125$ K for the thinner film. Both values are significantly smaller than the one found in bulk crystals. For the $t_m = 89$ nm thick hematite, we find an additional transition around 125 K indicating two different magnetic phases, which most likely stem from a strained α - Fe_2O_3 layer close to the film/substrate interface. Furthermore, we find the Morin transition to be dependent on the magnetic field as the inset of Fig. 3.3(a) shows. The thick film clearly exhibits a decreasing Morin transition temperature with increasing magnetic field magnitude.

3.2 Sample Fabrication and Layout

The magnon transport experiments presented in Chapter 4 utilize single crystalline YIG thin films grown by pulsed laser deposition (PLD). While the YIG films in Sections 4.2 and 4.4 are grown on (001)-oriented gadolinium gallium garnet ($\text{Gd}_3\text{Ga}_5\text{O}_{12}$, GGG) substrates, the ones in Sec. 4.3 are grown on (111)-oriented yttrium scandium gallium garnet ($\text{Y}_3\text{Sc}_2\text{Ga}_3\text{O}_{12}$, YSGG) substrates. For the experiments in Chapter 5 single crystalline (0001)-oriented α - Fe_2O_3 films are grown by PLD on (0001)-oriented sapphire (Al_2O_3) substrates. For all substrates a Pt layer (~ 180 nm) is sputtered on the unpolished backside before the thin film deposition to enable a homogeneous heat distribution during the deposition. Before the substrates are transferred into the PLD chamber of an ultra high vacuum (UHV) cluster they are cleaned in acetone and isopropanol (IPA) in an ultrasonic bath for at least 2 min

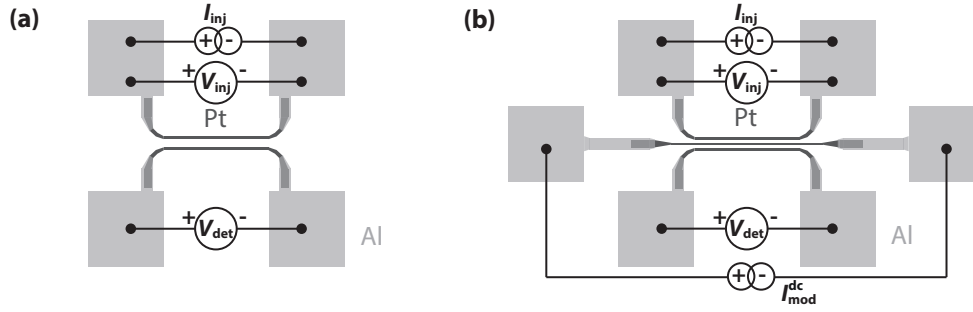


Fig. 3.4 – Sketch of the device with (a) two and (b) three nanostrips. The Pt strips are illustrated in dark gray, while Al bondpads and leads are sketched in light gray. The illustration shows the typical connection scheme for transport measurements.

in each solution. Inside the chamber the backside of the substrate is heated up via an infrared laser, which allows for a stable substrate temperature T_s due to the better absorption of the infrared light at the Pt layer. For the YIG films, a substrate temperature of 450°C is chosen, while the sapphire substrates for the hematite films are heated up to 320°C . In both cases, the growth process takes place in an oxygen atmosphere with a pressure of $p_{\text{O}_2} = 25\ \mu\text{bar}$ to avoid oxygen vacancies. Note that for the hematite films investigated in Sec. 5.3 a RF-atom source is used to inject atomic oxygen into the chamber and further reduce oxygen vacancies. For the film growth a pulsed UV KrF excimer laser with a wavelength of $248\ \text{nm}$ hits the stoichiometric, polycrystalline target material with a laser fluence at the target of $\rho_L = 2.0\ \text{J}/\text{cm}^2$ and a laser frequency of $f = 10\ \text{Hz}$ for YIG and $\rho_L = 2.5\ \text{J}/\text{cm}^2$ and $f = 2\ \text{Hz}$ for hematite. The energy density ρ_L is controlled via an automatic lens system and allows to ionize the target material leading to a pulse plume at the target, which diffuses towards the substrate. For an all-electrical injection and detection of magnon spin currents, we employ two-terminal nanostructures (acting as injector and detector) on the $\alpha\text{-Fe}_2\text{O}_3$ films, while three nanostrips (with an additional modulator in between) are employed on the YIG samples to additionally enable the manipulation of the magnon spin current, as depicted in Fig. 3.4(a) and (b), respectively.

A typical fabrication process can be divided into three steps. In a first step, we deposit $10\ \mu\text{m} \times 10\ \mu\text{m}$ Platinum (Pt) squares (markers) at the corners of the sample. These markers are typically $\sim 45\ \text{nm}$ thick and are utilized for aligning the subsequent parts of the nanostructure. Next, the strips of the heavy non-magnetic material Pt with strong spin-orbit coupling are patterned on the sample. The Pt strips have lengths between $25\ \mu\text{m}$ and $112\ \mu\text{m}$, widths between $100\ \text{nm}$ and $1\ \mu\text{m}$ and a thickness of either $3.5\ \text{nm}$ or $5\ \text{nm}$. Last, we deposit the lead wires and bondpads, which are made of a $\sim 50\ \text{nm}$ Aluminium (Al) layer to electrically contact the nanostrips. We describe the individual fabrication steps in detail below.

	alignment/focus markers
resist layers	<i>PMMA/MA 33%/PMMA-Electra 92</i>
spin coating	4000 rpm, 1 min/4000 rpm, 1 min
bake temperature	170 °C/90 °C
bake time	2 min/2 min
base dose	3.0 C/m ²
development time	90 s
	nanostrips and leads/bondpads²⁴
resist layers	<i>PMMA 600K/PMMA 950K/PMMA-Electra 92</i>
spin coating	4000 rpm, 1 min/4000 rpm, 1 min/4000 rpm, 1 min
bake temperature	170 °C/170 °C/90 °C
bake time	5 min/5 min/2 min
base dose	5.6 C/m ²
development time	120 s

Tab. 3.1 – Resist and lithography parameters for the fabrication of two- and three-terminal devices.

Before every step, the sample is cleaned in acetone and IPA in an ultrasonic bath for at least 2 min at the highest power level for the bare film and 1 min at low power levels after a patterning step in each solution and blown dry with nitrogen. Subsequently, we spin coat the samples with different resist layers depending on the patterning step and bake them out on a hotplate after each coating. The resist types and fabrication parameters are summarized in Tab. 3.1. The structures are patterned via electron beam lithography. Here, the *NanoBeam nB5* system from *NanoBeam Ltd.*, which is operated at a beam voltage of 80 kV, is used. The electron beam is focused on gold nanoparticles for the first step, while the markers are used for the subsequent steps. Since substrate and film are insulating the most upper resist layer in every case is the conductive resist *PMMA-Electra 92* (cf. Tab. 3.1), which avoids surface charging effects that can deteriorate the writing process. After the writing process, we first remove the conductive resist by rinsing the sample for about 20 s in deionized water (H₂O) and blow it dry thereafter. For each resist stack utilized in this work, the samples are then developed in the *AR 600-56* developer from Allresist. After 90 s (for markers) and 2 min (for strips and bondpads) the developing reaction is stopped by rinsing the sample twice in IPA for first 5 s and subsequent 25 s. The metallic films are deposited using DC sputtering, followed by a lift-off procedure. Therefore, the samples are put in an acetone bath heated up to 70 °C for at least 15 min and are gently pipetted thereafter to enhance the lift-off effect. In a last step,

²⁴This resist stack is sometimes also used for the markers.

the sample in the acetone bath is put into an ultrasonic bath at lowest power for 1 min to ensure that all metallic residues are removed.

3.3 Experimental Setup

At the Walther-Meißner-Institut three different superconducting magnet cryostats are available where magnon spin transport measurements can be conducted: (i) a 3D-vector magnet consisting of two superconducting Helmholtz coils and a superconducting solenoid reaching magnetic field strengths up to $\mu_0 H = 2.5$ T in the horizontal plane and up to $\mu_0 H = 6$ T in the vertical direction, (ii) a 1D-magnet with a superconducting Helmholtz coil (split pair) with a magnetic field magnitude up to $\mu_0 H = 7$ T with the possibility to rotate the sample either in-plane (ip) or out-of-plane (oop) using an electronic stepper motor and (iii) a 1D-magnet with a superconducting solenoid with a magnetic field strength as large as $\mu_0 H = 15$ T. Typically, YIG thin films are measured in setup (i) or (ii), while for the α -Fe₂O₃ thin films setup (ii) and (iii) are used. To perform measurements, the samples with the completed nanostructures on top are glued on a chip carrier and wire bonded to the Copper (Cu) pads of the chip carrier. The chip carrier with the sample is then attached to a dipstick, which in turn is installed in a variable temperature inset (VTI) ranging from $2 \text{ K} \leq T \leq 300 \text{ K}$ of one of the superconducting magnet cryostats. The implementation of a new dipstick with a piezoelectric rotation stage also allows to rotate the sample ip for the cryostat achieving magnetic fields up to $\mu_0 H = 15$ T (setup (iii)) [165]. Most common, we perform angle-dependent magnetotransport measurements, i.e. our sample itself is either rotated within a static magnetic field (setup (ii) and (iii)) or the direction of the applied magnetic field $\mu_0 H$ is rotated relative to the sample (setup (i)). In general, these rotations can be done in three different orthogonal planes, however, within this thesis we restrict ourselves and only concentrate on ip rotations around the axis normal of the film plane.

The exact electrical connection scheme of a magnon transport measurement depends on the measurement technique. In general, we distinguish between the dc- and ac-detection technique. In this Section, we focus on the experimental setup and connection scheme, while we describe both methods in detail and provide a quantitative comparison of the dc- and ac-detection technique in Sec. 4.2. First we restrict ourselves to a two-terminal structure (cf. Fig 3.4(a)). For the dc technique, a dc charge current I_{inj} is applied to one of the outer strips, called the injector, with a Keithley 2400 Sourcemeater, which additionally allows us to record the local voltage drop V_{inj} across this strip. Thus, the usage of the dc technique enables the characterization of various magnetoresistance contributions, such as the SMR

(see Sec. 2.4). A Keithley 2182 Nanovoltmeter²⁵ is used to detect the magnon transport signal V_{det} at the second Pt strip, the detector. To distinguish between electrically and thermally induced voltage signals, the current reversal method (see Sec. 4.2.1) is utilized, where dc currents of positive and negative polarity are applied subsequently to the injector and V_{det} is recorded in these different states. The current reversal method specifies how to add or subtract these voltage values to separate electrically and thermally induced voltage signals. Typically, we repeat the current reversal sequence for $n_{\text{rep}} = 5$ times for each external parameter (like magnetic field orientation/ magnitude, temperature, etc.). For an enhanced signal-to-noise ratio, we calculate the SHE-induced and thermally generated voltage signals and take the arithmetic mean over n_{rep} cycles for each setting. In contrast for the ac-readout technique, an ac charge current $I_{\text{inj}}(t) = I_{\text{inj}} \sin(\omega t)$ with angular frequency $\omega = 2\pi f$ and a low frequency of $f = 7.737$ Hz is generated by a Keithley 6221 DC and AC Current Source and applied to the injector. In particular, the frequency f is chosen in such a way that $f \neq n \cdot 50$ Hz with $n \in \mathbb{Z}$ and therefore does not coincide with multiples of the frequency of the ac power outlets. The choice of such a low *quasi-dc* current ensures that we can neglect capacitive/inductive coupling effects between the Pt nanostrips, since they otherwise might overshadow the magnon transport signals. The measured voltage signal V_{det} at the detector is preamplified by a Stanford Research System SR560 low-noise voltage amplifier before being passed to a Zurich Instruments HF2LI 50 MHz or MFLI 500 kHz lock-in amplifier. The digital output of the lock-in amplifier triggers the ac current Keithley 6221 Source and thus synchronizes the current source and the reference signal of the lock-in to avoid a drift of the relative phase between source and reference. For a three-terminal device (cf. Fig. 3.4(b)), a Keithley 2400 Sourcemeter is used to apply an additional dc charge current $I_{\text{mod}}^{\text{dc}}$ to the strip in the center, the modulator, for both techniques. In the case of the dc technique we have to extend the current reversal sequence, i.e. we additionally apply a zero current to the electrode injecting magnons and measure the voltage signal at the detector electrode (cf. Sec. 4.2.1). For the ac technique, the lock-in technique is sufficient for both device geometries to distinguish between SHE-induced and thermally generated voltage signals (cf. Sec. 4.2.2).

²⁵Typical measurements setting for the Keithley 2182: resolution - 7.5 digits, repeating filter count - 30, number of power line cycles - 2.

Manipulation of Magnon Spin Transport in Three-terminal YIG/Pt Nanostructures

In present day technology the fast and reliable transport of information is essential. In the field of spintronics, pure spin currents have drawn much attention due to their potential applications in information processing at a low dissipation level, however their efficient control is a challenging task [33, 166–168]. In magnetically ordered insulators, spin currents are carried by magnons, the elementary excitations of the spin system. These magnonic spin currents opened new opportunities for interesting device concepts based on magnon information processing [37, 44, 169, 170]. For instance, it has been shown that damping compensation via spin transfer torque is an efficient method to optimize the propagation of coherently excited magnons [171–174]. Moreover, a logic majority gate [175] and the first magnon transistor [176] using magnonic crystals [177] have been implemented. While these devices towards magnon logic operations are mainly based on coherently excited magnon transport, recent reports put an increasing interest on the transport of thermally, i.e. incoherently excited magnons as information carriers for logic operations. One promising way towards controlling spin currents relies on spin-transfer torque for spin current generation in bilayer systems consisting of MOIs and HMs with strong spin-orbit coupling. In such bilayer systems incoherent magnons in the MOI can be excited electrically [43, 120, 178] as well as thermally [43, 141, 179], and then detected electrically in the HM via the inverse SHE [35, 39, 180, 181]. A major challenge, however, is that the number of magnons in a spin conductor is not conserved and thus, magnon mediated spin currents only prevail on a characteristic length scale. The latter, sensitively depends on the magnetic Gilbert damping. In this context, the MOI yttrium iron garnet (YIG) is a promising candidate for hosting efficient magnon based spin transport as it features a low Gilbert damping parameter even in nanometer-thin films [149] and a correspondingly large magnon propagation length [43, 182–184]. Devices based on YIG thin films and stripe-shaped HM electrodes have been utilized to show that a superposition of diffusive magnon currents allows for the realization of a majority gate [185]. Later on, transistor-like device concepts were used to demonstrate the manipulation of magnonic spin currents in YIG/Pt bilayers [32, 44, 45, 186]. In this three-electrode arrangement,

a charge current is applied to a Pt strip (injector) injecting magnons into the YIG, which are then detected at a second Pt strip (detector). A charge current applied to the third Pt strip (modulator) placed between the other two Pt electrodes allows one to manipulate the magnon transport from injector to detector [44, 45]. The effect of the modulator can be represented as a change in the effective magnon density and hence conductivity. At a certain threshold current the injected magnons can even counteract the magnetization damping (decay of magnons) resulting in an abrupt increase of the effective magnon conductivity [45].

In this chapter, we investigate the magnon transport in such systems far from equilibrium in more detail. We vary different external parameters and device properties to obtain a detailed understanding of the underlying processes when manipulating the magnon transport in MOIs, which is an important step towards the realization of applications based on pure spin currents. In the first Sec. 4.1 of this Chapter, we introduce the theoretical concepts and summarize the most important findings in transistor-like devices. After introducing the dc-detection technique as well as the ac-readout technique in Sec 4.2, we show that the two most common measurement techniques both efficiently distinguish between electrically and thermally injected magnons. Comparing both techniques, we find distinctive differences between the signals obtained by the two methods above the threshold value. This provides evidence for nonlinear contributions to the detector signal not only from the modulator current, but also from the injector current. Furthermore, we investigate YIG thin films with strongly reduced effective magnetization in Sec. 4.3. Such films exhibit an increased effective magnon conductivity and show a linear dependence of the threshold current on the applied magnetic field due to reduced damping effects. Furthermore, we find that large currents applied to the modulator Pt electrode have a significant impact on the magnon transport. To this end, we shed light on large current exposure to the modulator and its impact on the device performance by investigating the modulation efficiency and threshold currents in Sec. 4.4. We observe a significant decrease in modulation efficiencies and increasing critical currents. Finally, we give a summary of the most important results in Sec. 4.5.

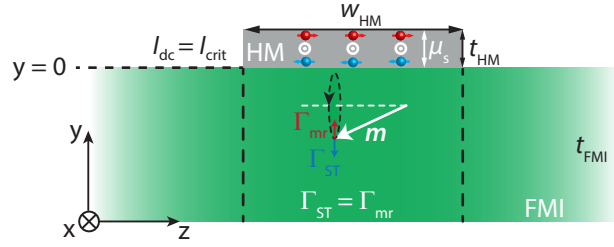


Fig. 4.1 – Cross-sectional view of the bilayer structure consisting of a FMI with thickness t_{FMI} and a HM lead on top with thickness t_{HM} and width w_{HM} to illustrate the process of damping compensation. Due to a dc charge current applied to the HM lead, a spin chemical potential μ_s builds up via the SHE, leading to a spin-transfer torque Γ_{ST} . The latter, acts on the magnetization direction m of the FMI and counteracts the intrinsic damping torque Γ_{mr} . Reaching the critical current $I_{\text{dc}} = I_{\text{crit}}$, leads to an auto-oscillation of the magnetization. The figure is adapted from Ref. [68].

4.1 Theoretical Concepts

After introducing the magnon transport in two-terminal devices in Sec. 2.5.2, we here describe the influence of an additional HM, the modulator, placed in between injector and detector. First, we revisit the theory of the SOT-induced critical current in the context of damping compensation in Sec. 4.1.1. Subsequently, we discuss the phenomenological model, which describes the impact of an additional charge current induced spin injection and the accompanied change in magnon conductivity in a FMI. Here, we distinguish between the low bias regime (Sec. 4.1.2), where the magnon conductivity is described in linear response theory, and the critical current regime (Sec. 4.1.3), where we derive the non-trivial magnon spin conductivity via the approach proposed by S. Takei [187]. These concepts have already been introduced in Ref. [68] and we will summarize the most important points here. Some of the text and figures are taken from T. Wimmer, *Control and Manipulation of Magnonic Spin Currents in Magnetic Insulators*, [Dissertation, Technical University of Munich \(2021\)](#).

4.1.1 Damping Compensation

Using three-terminal nanostructures several works reported on a steep increase in the magnon spin signal, which has been attributed to a very large magnon spin conductivity increase [45, 188]. As shown in Ref. [45], such an enhancement in MOI/HM bilayers can be explained by the presence of a zero effective damping state below the HM electrode. Utilizing the well-established theory of spin Hall oscillators (SHO) [189–191] rationalizes how zero effective damping is achieved. For the rest of the Chapter, we will restrict ourselves to FMIs, as we only investigate

the ferro-/ferrimagnet YIG in the following and an experimental realization of SHOs is still missing for AFIs. As schematically depicted in Fig. 4.1, auto-oscillation of the magnetization \mathbf{m} is present when the spin injection rate at the HM due to the SHE results in an interfacial spin transfer torque $\Gamma_{\text{ST}} \propto I_{\text{dc}}$, which balances the intrinsic damping of the FMI or magnon relaxation rate Γ_{mr} , respectively. Note that without an applied charge current and thus no spin injection rate at the HM the magnetization \mathbf{m} would be aligned along its equilibrium direction. In contrast, when an external perturbation is present, \mathbf{m} precesses around the latter. When the external perturbation is turned off, the magnetization relaxes to its equilibrium direction due to damping processes. However, if we consider a permanent perturbation, as in our case, a steady state is established with a certain opening angle between the magnetization direction and its equilibrium direction, which depends on the strength of the perturbation and the damping.

Starting with the magnon relaxation rate Γ_{mr} of the lowest energy mode ($k = 0$), we obtain the general expression

$$\Gamma_{\text{mr}} = \alpha\gamma\mu_0 \left(H + \frac{M_{\text{eff}}}{2} (N_x + N_z - 2N_y) \right), \quad (4.1)$$

where α is the total magnetic damping constant, $\gamma = g\mu_B/\hbar$ the gyromagnetic ratio with the Landé factor g and Bohr's magneton μ_B , μ_0 the vacuum permeability, H the external magnetic field and $M_{\text{eff}} = M_s - H_k$ the effective magnetization of the FMI with contributions from the saturation magnetization M_s and the perpendicular surface magnetic anisotropy fields H_k . We investigate and discuss the influence of M_{eff} on the magnon transport signal and the threshold value in detail in Sec. 4.3. Furthermore, $N_{x,y,z}$ are the geometry-dependent demagnetization factors. For an out-of-plane magnetized thin film along y and hence $N_x = N_z = 0$ and $N_y = 1$, we find

$$\Gamma_{\text{mr}}^{\text{oop}} = (\alpha_G + \alpha_{\text{sp}}) \gamma\mu_0 (H - M_{\text{eff}}), \quad (4.2)$$

while we obtain for an in-plane magnetized thin film in the x - z -plane ($N_x + N_z = 1$, $N_y = 0$)

$$\Gamma_{\text{mr}}^{\text{ip}} = (\alpha_G + \alpha_{\text{sp}}) \gamma\mu_0 \left(H + \frac{M_{\text{eff}}}{2} \right). \quad (4.3)$$

In both cases, we have set $\alpha = \alpha_G + \alpha_{\text{sp}}$ with α_G the intrinsic Gilbert damping and α_{sp} the Gilbert damping induced by spin pumping due to the adjacent HM layer [192, 193]. In accordance with our measurements presented in the subsequent Sections, we only account for in-plane magnetized thin films. The magnon relaxation

rate Γ_{mr} is identical to the frequency linewidth of the $k = 0$ ferromagnetic resonance mode, which reads

$$\Delta f = \Delta H \left(\frac{\partial \omega_{\text{FMR}}(H)}{\partial H} \right). \quad (4.4)$$

Here, ΔH is the resonance linewidth, which is typically extracted from broadband ferromagnetic resonance (FMR) measurements in this work. Hence, in our experiments we have to account for the FMR frequency

$$\omega_{\text{FMR}}^{\text{ip}}(H) = \gamma \mu_0 \sqrt{H(H + M_{\text{eff}})}, \quad (4.5)$$

which is calculated from the Kittel formula for an in-plane magnetized film. In real experiments an inhomogeneous broadening δH of the FMR linewidth has to be considered and thus we introduce the effective damping parameter

$$\alpha_{\text{eff}} = \alpha_{\text{G}} + \gamma \mu_0 \frac{\delta H}{2\omega_{\text{FMR}}^{\text{ip}}}, \quad (4.6)$$

as demonstrated in Ref. [191]. Substituting α_{G} by α_{eff} in Eq. (4.3) results in

$$\Gamma_{\text{mr}}^{\text{ip}} = \left(\alpha_{\text{sp}} + \alpha_{\text{G}} + \frac{\delta H}{2\sqrt{H(H + M_{\text{eff}})}} \right) \gamma \mu_0 \left(H + \frac{M_{\text{eff}}}{2} \right) \quad (4.7)$$

for the FMI thin film. Including inhomogeneous broadening causes a divergence of the damping rate $\Gamma_{\text{mr}}^{\text{ip}}$ for $H = 0$ for a finite M_{eff} . Moreover, the spin pumping contribution to the damping α_{sp} for the magnon relaxation rate $\Gamma_{\text{mr}}^{\text{ip}}$ due to the HM interface is given by

$$\alpha_{\text{sp}} = g_{\text{eff}} \frac{\hbar \gamma}{4\pi M_s t_{\text{FMI}}} \quad (4.8)$$

with M_s the saturation magnetization, t_{FMI} the thickness of the FMI film, and the effective spin mixing conductance

$$g_{\text{eff}} = \frac{g^{\uparrow\downarrow} \frac{\hbar}{2e^2} \frac{\sigma_{\text{HM}}}{l_s}}{g^{\uparrow\downarrow} + \frac{\hbar}{2e^2} \frac{\sigma_{\text{HM}}}{l_s}} \quad (4.9)$$

to account for the finite interface transparency. Here $g^{\uparrow\downarrow}$ is the normal spin mixing conductance, l_s the spin diffusion length in the HM and σ_{HM} the electrical conductivity of the HM.

As the condition $\Gamma_{\text{mr}}^{\text{ip}} = \Gamma_{\text{ST}}$ has to be satisfied to achieve zero effective damping, we also have to account for the interface injection rate via the SHE. As introduced in Sec. 2.1, a dc current I_{dc} applied to a HM lead results in a spin chemical potential μ_{s} due to the SHE. The created spin-transfer torque Γ_{ST} acts on the precession of the magnetization direction \mathbf{m} as well as on the thermal fluctuations of \mathbf{m} , and hence counteracts the intrinsic damping torque Γ_{mr} (cf. Fig. 4.1)²⁶. The anti-damping spin torque rate in the macrospin approximation is given by [191]

$$\Gamma_{\text{ST}} = \frac{\hbar}{2e} \frac{\gamma}{M_{\text{s}} t_{\text{FMI}} t_{\text{HM}} w_{\text{HM}}} \cdot T \cdot \theta_{\text{SH}} I_{\text{dc}}, \quad (4.10)$$

where θ_{SH} the spin Hall angle of the HM and t_{HM} and w_{HM} the thickness and width of the HM lead, respectively. Furthermore, T denotes the interface spin transparency for spin currents, which is given by

$$T = \frac{g^{\uparrow\downarrow} \tanh(\eta)}{g^{\uparrow\downarrow} \coth(2\eta) + \frac{\hbar}{2e^2} \frac{\sigma_{\text{HM}}}{l_{\text{s}}}}, \quad (4.11)$$

where $\eta = t_{\text{HM}}/(2l_{\text{s}})$ [194]. Note that we approximated $\coth(2\eta) \approx 1$ in Eq. (4.11), as in general the thickness of the HM t_{HM} is larger than $2l_{\text{s}}$. When the condition $\Gamma_{\text{mr}}^{\text{ip}} = \Gamma_{\text{ST}}$ is met, a coherent precession of the magnetization with zero effective damping is present and we can define the critical current as

$$I_{\text{crit}} = \frac{2e}{\hbar} \frac{M_{\text{s}} t_{\text{FMI}} t_{\text{HM}} w_{\text{HM}}}{\gamma T \theta_{\text{SH}}} \left(\alpha_{\text{sp}} + \alpha_{\text{G}} + \frac{\delta H}{2\sqrt{H(H + M_{\text{eff}})}} \right) \gamma \mu_0 \left(H + \frac{M_{\text{eff}}}{2} \right). \quad (4.12)$$

Utilizing Eqs. (4.11) and (4.9), we can rewrite the expression and obtain

$$I_{\text{crit}} = \frac{\hbar}{e} \frac{\sigma_{\text{HM}}}{2l_{\text{s}}} \frac{t_{\text{HM}} w_{\text{HM}}}{\theta_{\text{SH}} \tanh(\eta)} \left(1 + 4\pi M_{\text{s}} t_{\text{FMI}} \frac{\alpha_{\text{eff}}}{\hbar \gamma g_{\text{eff}}} \right) \gamma \mu_0 \left(H + \frac{M_{\text{eff}}}{2} \right), \quad (4.13)$$

which is the same result as already obtained in Ref. [45].

In addition, Wimmer *et al.* [45] showed that the threshold condition calculated from the SHOs theory is identical to the threshold condition calculated from the theory of current-induced magnon Bose-Einstein condensates (BEC) [187, 195, 196], which represents a mere reformulation of the torques in terms of the chemical potentials μ_{s} and μ_{crit} . Note that within the theory this is in particular true for the swasing threshold condition, where spontaneous spin wave emission is suggested for high spin injection rates, proposed by Bender *et al.* [196]. This suggest that the

²⁶This is only true if the spin direction at the interface is parallel to the magnetization direction \mathbf{m} in the FMI. In contrast, an antiparallel alignment results in a spin torque that reinforces the damping.

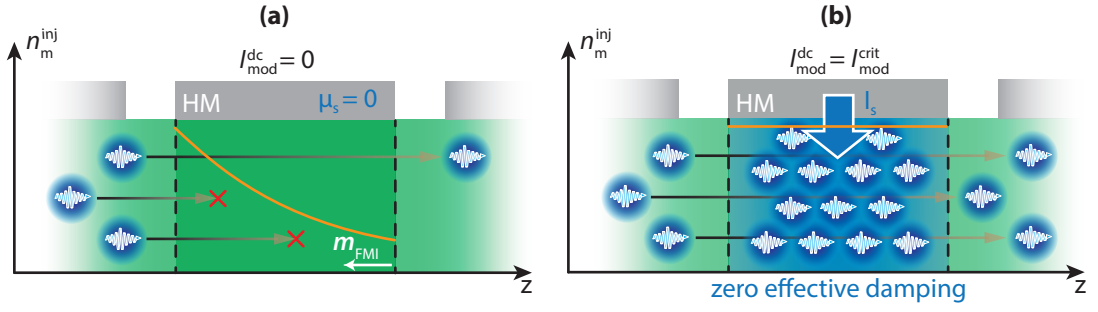


Fig. 4.2 – Illustration of the magnon transport between injector and detector under the influence of a modulator. Magnons (blue wiggly arrows) injected at the injector into the FMI diffuse along the z -direction towards the detector. **(a)** For $I_{\text{mod}}^{\text{dc}} = 0$, the transport is determined by a characteristic spin decay length, as magnon decay events (red crosses) lead to a finite lifetime. The solid orange line depicts the corresponding exponential decay of the injector magnon density n_m^{inj} . **(b)** For $I_{\text{mod}}^{\text{dc}} = I_{\text{mod}}^{\text{crit}}$, the applied modulator current is large enough to compensate the magnetic damping of the FMI film ($\Gamma_{\text{mr}}^{\text{ip}} = \Gamma_{\text{ST}}$). This results in an effectively vanishing magnon decay beneath the modulator, as indicated by the large magnon accumulation. Note that we only consider the magnon transport beneath the modulator. The illustration is adapted from Ref [45].

magnon system beneath the HM undergoes a BEC transition as the steep increase in the magnon transport signal observed in experiments cannot be described by a mere linear (or quadratic) increase in the magnon density n_m . Although the BEC model well describes the critical current dependence as a function of the magnetic field and is compatible with the zero resistance magnon transport beneath the modulator and thus a lossless magnon transport [45], it is not sufficient to verify the formation of a magnon BEC as proposed in Refs. [187, 196]. In particular, magnon transport measurements do not allow predictions on the coherence of the achieved state. For a detailed description and a comprehensive analysis of first experiments investigating the nonlinear magnon transport regime, the reader is referred to Ref. [68].

Based on these theoretical predictions, we can draw a simplified physical picture for the magnon transport in three-terminal structures consisting of three HM strips on top of a FMI and in particular, address the question of how the magnon spin signal injected at the injector and detected at the detector is affected by the dc charge current applied to the modulator (center electrode). Here, we only consider the magnon transport beneath the modulator and neglect the magnon decay before and after the modulator. When no dc current is applied to the modulator ($I_{\text{mod}}^{\text{dc}} = 0$), the magnon density generated at the injector n_m^{inj} decays exponentially, as indicated by the solid orange line in Fig. 4.2(a). For $I_{\text{mod}}^{\text{dc}} = I_{\text{mod}}^{\text{crit}}$ in panel (b), the threshold current for damping compensation is reached and a zero effective damping state

is obtained. In this case, the magnon lifetime diverges and spin transport with an effectively vanishing magnon decay occurs [187].

4.1.2 Low Bias Regime

For a more comprehensive picture, we do not only consider the influence of a HM electrode for $I_{\text{dc}} = I_{\text{crit}}$, but investigate the effect of an external spin current injection into the FMI over a large current range. To this end, we derive a model, which can describe the behavior of the magnon spin transport signal and is based on the influence of a charge current applied to a HM electrode on the magnon conductivity σ_{m} in a FMI. We first introduce the model and then discuss how it can be applied to our experiments. In Sec. 2.5.2, we derived the expression $\sigma_{\text{m}} = 3\hbar n_{\text{m}}\tau_{\text{m}}/m_{\text{m}}$. While the effective magnon mass m_{m} is fixed and determined by the magnon dispersion relation, the magnon density n_{m} as well as the magnon relaxation time τ_{m} can be tuned by an externally applied charge current and the corresponding spin current injection [44, 187]. To discuss this expression, we subdivide the description of the magnon conductivity into different current regimes and follow the approach of T. Wimmer in Ref. [68].

First, we model the magnon conductivity modulation by I_{dc} in the low current regime, which has been first investigated by Cornelissen *et al.* in Ref. [44]. In this regime, the measured signal is well described by a linear and quadratic modulation of the magnon conductivity due to SHE-induced and thermally generated magnons, respectively, according to

$$\sigma_{\text{m}} = \sigma_{\text{m}}^0 + \Delta\sigma_{\text{SHE}}I_{\text{dc}} + \Delta\sigma_{\text{th}}(I_{\text{dc}})^2 \quad (4.14)$$

with σ_{m}^0 the equilibrium magnon conductivity at zero applied current, $\Delta\sigma_{\text{SHE}}$ the SHE-induced magnon conductivity and $\Delta\sigma_{\text{th}}$ the thermally generated magnon conductivity.

In the following, we briefly sketch the derivation of this expression focusing on the change of σ_{m} in a FMI due to the magnon density n_{m} , while we assume τ_{m} to be constant and reuse some of the expressions introduced in Sec. 2.3. Here, we consider a FMI/HM heterostructure as depicted in Fig. 4.1, where the dc current density $j_{\text{dc}} = I_{\text{dc}}/(t_{\text{HM}}w_{\text{HM}})$ in the HM causes a finite spin chemical potential μ_{s}^0 at the FMI/HM interface via the SHE. The interfacial magnon spin current is determined by $\mathbf{j}_{\text{s, int}}^y = [g(\mu_{\text{m}}^0 - \mu_{\text{s}}^0 \mathbf{s} \cdot \mathbf{m}) + S\delta T]\mathbf{m}$ according to Eq. (2.12) with $\mu_{\text{s(m)}}^0 = \mu_{\text{s(m)}}(y = 0)$ the spin (magnon) chemical potential at the interface, \mathbf{m} the magnetization unit vector in the FMI and $\delta T = T_{\text{m}} - T_{\text{e}}$ the interfacial temperature difference between electrons and magnons. The magnon injection into the FMI is

active when $\mathbf{s} \cdot \mathbf{m} > 0$, while magnons are depleted from the FMI when $\mathbf{s} \cdot \mathbf{m} < 0$, i.e the magnon injection/depletion process depends on the relative orientation of the spin polarization \mathbf{s} and the magnetization \mathbf{m} . To obtain the magnon density $n_m(\langle \mu_m^\pm \rangle, T)$, the average magnon chemical potential has to be calculated. To this end, we only assume one spatial dimension, in our case along the y -direction, which results in the spatial distribution of the spin chemical potential $\boldsymbol{\mu}_s = \mu_s \mathbf{s}$ (polarized along \mathbf{s}) as well as the magnon chemical potential $\boldsymbol{\mu}_m = \mu_m \mathbf{m}$ (polarized along \mathbf{m}). Both chemical potentials are determined by the 1D spin diffusion equations

$$\frac{\partial^2 \boldsymbol{\mu}_s}{\partial y^2} = \frac{\boldsymbol{\mu}_s}{l_s^2}, \quad (4.15)$$

$$\frac{\partial^2 \boldsymbol{\mu}_m}{\partial y^2} = \frac{\boldsymbol{\mu}_m}{l_m^2}. \quad (4.16)$$

Note that we furthermore assumed steady state conditions and utilized the decay lengths for spins $l_s = \sqrt{D_s \tau_s}$ and magnons $l_m = \sqrt{D_m \tau_m}$. Applying the boundary conditions of the HM²⁷

$$-\sigma_s \left. \frac{\partial \mu_s(y)}{\partial y} \right|_{y=0} \mathbf{s} - j_s^{\text{SH}} \mathbf{s} = j_{s, \text{int}}^y, \quad (4.17)$$

$$-\sigma_s \left. \frac{\partial \mu_s(y)}{\partial y} \right|_{y=t_{\text{HM}}} \mathbf{s} - j_s^{\text{SH}} \mathbf{s} = 0 \quad (4.18)$$

with $j_s^{\text{SH}} = \frac{\hbar}{2e} \theta_{\text{SH}} j_{\text{dc}}$ the SHE induced spin current (cf. Eq. (2.10)) as well as the boundary conditions of the FMI

$$-\sigma_m \left. \frac{\partial \mu_m(y)}{\partial y} \right|_{y=0} \mathbf{m} = j_{s, \text{int}}^y, \quad (4.19)$$

$$-\sigma_m \left. \frac{\partial \mu_m(y)}{\partial y} \right|_{y=-t_{\text{FMI}}} \mathbf{m} = 0 \quad (4.20)$$

and after some algebra, we obtain the magnon chemical potential as the solution of the diffusion equations, which we in turn average across the thickness of the FMI film resulting in²⁸

$$\langle \mu_m^\pm \rangle = \frac{1}{t_{\text{FMI}}} \int_{-t_{\text{FMI}}}^0 \mu_m^\pm(y) dy = \left(\pm \frac{j_s^{\text{SH}} l_s}{\sigma_s} \tanh(\eta) - \frac{S}{g} \delta T \right) \frac{l_m}{t_{\text{FMI}}} \sinh\left(\frac{t_{\text{FMI}}}{l_m}\right) \quad (4.21)$$

²⁷The spin currents in the HM strip are composed of a diffusive and a SHE-induced spin current according to Eqs. (2.4) and (2.10). Note that the spin current vectors in this case point along the spin polarization direction \mathbf{s} and the current flow direction is defined along the y -direction.

²⁸We used the approximation $\exp(2t_{\text{FMI}}/l_m) \approx 1$, which is valid as the magnon diffusion length l_m in the FMI YIG studied in this chapter is typically a few μm [43], while the YIG film thickness is in general smaller than 20 nm and thus $2t_{\text{FMI}}/l_m \ll 1$.

with $\eta = t_{\text{HM}}/(2l_s)$. While μ_m^+ accounts for the solution of the parallel configuration of \mathbf{s} and \mathbf{m} with $\mathbf{s} \cdot \mathbf{m} = 1$, μ_m^- considers the antiparallel configuration with $\mathbf{s} \cdot \mathbf{m} = -1$. We can further simplify Eq. (4.21) utilizing the approximation $\frac{l_m}{t_{\text{FMI}}} \sinh\left(\frac{t_{\text{FMI}}}{l_m}\right) \approx 1$, where we assumed $t_{\text{FMI}}/l_m \ll 1$ as in general the studied FMI YIG thin films obtain a thickness $t_{\text{FMI}} < 20$ nm, which is much smaller than the expected magnon diffusion length l_m in YIG, where values in the μm regime are expected [43]. Together with $\sigma_s = \frac{\hbar}{2e^2}\sigma_e$ and $j_s^{\text{SH}} = \frac{\hbar}{2e}\theta_{\text{SH}}j_{\text{dc}}$, we can now rewrite the expression for the magnon chemical potential as a function of the experimentally modulated parameter I_{dc} . We obtain

$$\langle \mu_m^\pm \rangle (I_{\text{dc}}) = \pm \frac{e\theta_{\text{SH}}l_s \tanh(\eta)}{\sigma_e t_{\text{HM}} w_{\text{HM}}} I_{\text{dc}} + \frac{S}{g} c I_{\text{dc}}^2, \quad (4.22)$$

where we accounted for the fact that the temperature difference δT is proportional to the Joule heating power $P_J \propto I_{\text{dc}}^2$ [142]. Here, the temperature is expressed as $\delta T = -cI_{\text{dc}}^2$ with c an appropriate conversion factor²⁹. Equation (4.22) shows the expected linear and quadratic contribution in I_{dc} due to the SHE- and thermally induced injection of magnons for the magnon chemical potential in linear response [43, 44]. Now the non-equilibrium magnon density $n_m(\langle \mu_m^\pm \rangle, T)$ can be calculate to

$$\begin{aligned} n_m(\langle \mu_m^\pm \rangle, T) &= \int_0^\infty d\epsilon_m g(\epsilon_m) n_{\text{B}}(\epsilon_m, \langle \mu_m^\pm \rangle, T) \\ &= n_m^0 + \frac{\zeta(1/2)}{\Lambda^3 k_{\text{B}} T} \langle \mu_m^\pm \rangle = n_m^0 + \Delta n_m \end{aligned} \quad (4.23)$$

with the magnon density in thermal equilibrium $n_m^0 = \zeta(3/2)\Lambda^{-3}$ and the non-equilibrium magnon number density $\Delta = \rho_m/\hbar$ (cf. Eq. (2.33)). We find indeed that the magnon chemical potential μ_m is directly proportional to the magnon density n_m and hence $n_m \propto I_{\text{dc}} + I_{\text{dc}}^2$ similar to μ_m [43, 76]. This shows that we have a direct handle on the magnon density via a charge current driven through an adjacent HM. Finally, we arrive at the expression in Eq. (4.14) describing the magnon conductivity

$$\begin{aligned} \sigma_m &= 3\hbar \frac{n_m \tau_m}{m_m} = 3\hbar \frac{\tau_m}{m_m} (n_m^0 + \Delta n_m) \\ &= 3\hbar \frac{\tau_m}{m_m} \left(n_m^0 + \frac{\zeta(1/2)}{\Lambda^3 k_{\text{B}} T} \left(\pm \frac{e\theta_{\text{SH}}l_s \tanh(\eta)}{\sigma_e t_{\text{HM}} w_{\text{HM}}} I_{\text{dc}} + \frac{S}{g} c I_{\text{dc}}^2 \right) \right) \\ &= \sigma_m^0 \pm \Delta \sigma_{\text{SHE}} I_{\text{dc}} + \Delta \sigma_{\text{th}} I_{\text{dc}}^2. \end{aligned} \quad (4.24)$$

²⁹Due to the applied charge current to the HM, we consider $T_e > T_m$ and thus $\delta T < 0$. Assuming $c > 0$, the minus sign in the relation $\delta T = -cI_{\text{dc}}^2$ accounts for the fact that magnons are injected due to current induced heating and thus enhance the magnon chemical potential rather than reduce it.

We see that the magnon density n_m in turn modulates the magnon conductivity in a linear and quadratic fashion and is in contrast to electrical transport not constant.

This description is valid for excitations of linear magnetization dynamics, however it clearly breaks down for higher currents as shown in Refs. [45, 188, 197, 198]. Up to now, the description of the electrically induced magnon conductivity modulation assumes that the dc spin current injection only affects the magnon density n_m , where the current-induced magnon chemical potential μ_m is well below the magnon gap [44]. However, this is only true for the low bias regime and the model is no longer valid when nonlinear contributions are taken into account [199]. In this case, changes in the magnon relaxation time τ_m have also to be taken into account. Note that the clear separation between these two quantities is only valid in the linear regime and generally the modulation of the magnon conductivity via an applied current cannot be narrowed down to changes in either the magnon density n_m or the magnon relaxation time τ_m .

4.1.3 Critical Current Regime

In this section, we introduce a model to describe this nontrivial behavior of the magnon conductivity modulation, in particular the regime of the strong enhancement approaching the damping compensation, based on the theoretical approach by S. Takei [187]. The author considers the formation of a magnon BEC due to a spin chemical potential μ_s in a FMI/HM bilayer, similar to the approach in Ref. [196]. The work presents the calculation of the magnon conductivity σ_m for a three-terminal device on top of a FMI film, where a spin chemical potential in the modulator electrode is induced via the SHE, identical to the investigated structures in this chapter³⁰. The exact expression is not straightforward to evaluate, but the magnon conductivity near the damping compensation shows a divergence of $\sigma_m \propto (\mu_{\text{crit}} - \mu_s)^{-1/2} \propto (1 - I_{\text{mod}}^{\text{dc}}/I_{\text{mod}}^{\text{crit}})^{-1/2}$ when $I_{\text{mod}}^{\text{dc}} \rightarrow I_{\text{mod}}^{\text{crit}}$ at room temperature. While for large temperatures (room temperature and higher) the characteristic exponent is given by $-1/2$, it approaches -1 towards lower temperatures [187]. The model allows us to express the magnon conductivity beneath the modulator as

$$\sigma_m^{\text{mod}} = \sigma_m^0 \left(1 - \frac{I_{\text{mod}}^{\text{dc}}}{I_{\text{mod}}^{\text{crit}}}\right)^{-1/2} + \Delta\sigma_{\text{th}} \left(I_{\text{mod}}^{\text{dc}}\right)^2. \quad (4.25)$$

Note that we added the expected thermally generated magnon contribution due to the spin Seebeck effect from the linear response model (cf. Eq.(4.40)), as Ref. [187]

³⁰While we have derived the critical current (cf. Sec. 4.1.1) and the behavior of the magnon spin transport signal based on the magnon conductivity in the low bias regime (cf. Sec. 4.1.2) due to a dc charge current applied to the modulator in a three-terminal device in a rather general form considering only one HM electrode on top of a FMI, we here consider the whole device under study.

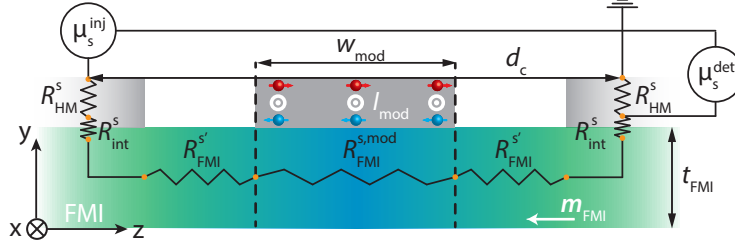


Fig. 4.3 – Sketch of an equivalent spin resistor model for our device design. A spin chemical potential μ_s^{inj} is induced via the SHE at the injector, while the resulting spin chemical potential μ_s^{det} is measured across the detector. The illustration is adapted from Ref. [68].

only accounts for the SHE induced pumping of the magnon system. This means, we assume that the spin Seebeck torque does not result in nonlinear effects in the magnetization dynamics and thus magnon conductivity. This assumption is in agreement with theory works [187, 196], which predict that the spin Seebeck torque by itself cannot achieve magnon condensation or damping compensation, respectively, due to the accompanied temperature rise in the magnon system preventing condensation. Introducing a phenomenological model [68] in the following, we will take into account this theoretical approach.

To this end, we once more assume that the modulation of the magnon conductivity is localized underneath the modulator. According to Ref. [187], we account for the contributions from the regions not covered by the modulator to the total magnon conductivity measured between injector and detector. For a complete description of the magnon conductivity, we adopt an equivalent spin resistor model for our device structure based on the model presented in Ref. [76]. As sketched in Fig. 4.3, the spin chemical potential at the injector μ_s^{inj} induced via the SHE acts as 'spin battery', leading to a spin chemical potential μ_s^{det} , which can be measured across the detector. Based on the spin resistor network (cf. Fig. 4.3), the total magnon conductivity can be written as

$$\sigma_m = \frac{\hbar}{2e^2} \frac{d_c}{A_{\text{FMI}}} \left(2R_{\text{FMI}}^{s'} + R_{\text{FMI}}^{s,\text{mod}}(I_{\text{mod}}^{\text{dc}}) \right)^{-1} \quad (4.26)$$

with $R_{\text{FMI}}^{s,\text{mod}}$ accounting for the $I_{\text{mod}}^{\text{dc}}$ -dependent resistance beneath the modulator and $R_{\text{FMI}}^{s'}$ referring to the spin resistance outside the modulator region. Furthermore, w_{mod} is the modulator electrode width, d_c the center-to-center distance between injector and detector (including the modulator electrode) and $A_{\text{FMI}} = t_{\text{FMI}}l_{\text{HM}}$ is the cross-section of the FMI transport channel with l_{HM} the length of the HM electrode. Note that the prefactor d_c/A_{FMI} considers the conversion into a geometry-independent conductivity rather than a conductance. For

a description exclusively in terms of conductivities, we first rewrite the FMI spin resistances into spin resistivities in Eq. (4.26) with $R_{\text{FMI}}^{s'} = (d_c - w_{\text{mod}}/(2A_{\text{FMI}}))\rho_{\text{FMI}}^{s0}$ and $R_{\text{FMI}}^{s,\text{mod}} = (w_{\text{mod}}/A_{\text{FMI}})\rho_{\text{FMI}}^s(I_{\text{mod}}^{\text{dc}})$ with $\rho_{\text{FMI}}^{s0} = \rho_{\text{FMI}}^s(I_{\text{mod}}^{\text{dc}} = 0)$ and obtain

$$\sigma_m = \frac{\hbar}{2e^2} \left(2\rho_{\text{FMI}}^{s'} + \rho_{\text{FMI}}^{s,\text{mod}}(I_{\text{mod}}) \right)^{-1}. \quad (4.27)$$

The scaled spin resistivities are given by

$$\rho_{\text{FMI}}^{s'} = \frac{d_c - w_{\text{mod}}}{2d_c} \rho_{\text{FMI}}^{s0}, \quad (4.28)$$

$$\rho_{\text{FMI}}^{s,\text{mod}}(I_{\text{mod}}^{\text{dc}}) = \frac{w_{\text{mod}}}{d_c} \rho_{\text{FMI}}^s(I_{\text{mod}}^{\text{dc}}). \quad (4.29)$$

Now, we can define the corresponding scaled magnon conductivities

$$\sigma'_m = \frac{\hbar}{2e^2} \left(\rho_{\text{FMI}}^{s'} \right)^{-1}, \quad (4.30)$$

$$\sigma_m^{\text{mod}}(I_{\text{mod}}^{\text{dc}}) = \frac{\hbar}{2e^2} \left(\rho_{\text{FMI}}^{s,\text{mod}}(I_{\text{mod}}^{\text{dc}}) \right)^{-1}. \quad (4.31)$$

Taking into account the considerations in Ref. [187] according to Eq. (4.25), we finally arrive at

$$\sigma_m(I_{\text{mod}}^{\text{dc}}) = \left\{ 2(\sigma'_m)^{-1} + \left[\sigma_m^{0,\text{mod}} \left(1 - \frac{I_{\text{mod}}^{\text{dc}}}{I_{\text{mod}}^{\text{crit}}} \right)^{-1/2} + \Delta\sigma_{\text{th}} \left(I_{\text{mod}}^{\text{dc}} \right)^2 \right]^{-1} \right\}^{-1}, \quad (4.32)$$

where σ'_m the magnon conductivity of the region not covered by the modulator is considered to be constant and hence unaffected by the modulator current $I_{\text{mod}}^{\text{dc}}$. Moreover, we introduced the scaled equilibrium magnon conductivity beneath the modulator

$$\sigma_m^{0,\text{mod}} = \frac{d_c}{w_{\text{mod}}} \sigma_m^0 \quad (4.33)$$

with σ_m^0 the actual equilibrium magnon conductivity independent of the geometry. We see that we obtain the equilibrium magnon conductivity in limit of $I_{\text{mod}}^{\text{dc}} = 0$

$$\sigma_m^0 \equiv \sigma_m(I_{\text{mod}}^{\text{dc}} = 0) = \left(2(\sigma'_m)^{-1} + (\sigma_m^{0,\text{mod}})^{-1} \right)^{-1} = \left(2\rho_{\text{FMI}}^{s'} + \rho_{\text{FMI}}^{s,\text{mod}0} \right)^{-1} \quad (4.34)$$

with $\rho_{\text{FMI}}^{\text{s,mod}0} = \rho_{\text{FMI}}^{\text{s,mod}}(I_{\text{mod}}^{\text{dc}} = 0)$. Whereas, we obtain the expected vanishing magnon resistivity beneath the modulator $\rho_{\text{FMI}}^{\text{s,mod}}(I_{\text{mod}}^{\text{crit}}) = 0$ when the modulator current approaches the critical current $I_{\text{mod}}^{\text{crit}}$

$$\sigma_{\text{m}}^{\text{crit}} \equiv \sigma_{\text{m}}(I_{\text{mod}}^{\text{dc}} = I_{\text{mod}}^{\text{crit}}) = (2(\sigma'_{\text{m}})^{-1})^{-1} = \left(2\rho_{\text{FMI}}^{\text{s'}}\right)^{-1}, \quad (4.35)$$

where $\sigma_{\text{m}}^{\text{crit}}$ defines the critical magnon conductivity. Furthermore, we define

$$\eta_{\text{crit}} = \frac{\sigma'_{\text{m}}}{\sigma_{\text{m}}^{\text{0,mod}}} = \frac{2w_{\text{mod}}}{d_{\text{c}} - w_{\text{mod}}}, \quad (4.36)$$

which describes the ratio between the unchanged magnon conductance and the modulated magnon conductance. Utilizing Eq. (4.30), (4.28), (4.33) and $(\rho_{\text{FMI}}^{\text{s0}})^{-1} = \sigma_{\text{m}}^{\text{0}}$, we find that the ratio η_{crit} depends exclusively on the device geometry, in particular on the ratio between modulated and unmodulated regions. If experimentally extracted ratios are larger than this geometry defined ratio, this would suggest that the changes of the magnon conductivity are not restricted to the region beneath the modulator as assumed in the derivation of this phenomenological model.

In our experiments, we consider that the magnon spin transport from injector to the detector is exclusively driven by the magnon chemical potential gradient $\nabla\mu_{\text{m}}$ induced at the injector position. As derived in Sec. 2.5.2, this assumption is perfectly valid for the SHE-induced magnon spin transport, where the injection process is characterized by interfacial spin conductance g (cf. Eq. (2.17)) and the temperature driven magnon spin currents only contribute as a neglectable correction to the signal [76]. In contrast, the thermally generated magnon spin current injection is characterized by the interfacial spin Seebeck coefficient (cf. Eq. (2.18)) and its transport is significantly affected by temperature gradients due to Joule heating and the accompanied temperature rise. As this thesis mainly focuses on SHE-induced magnon transport, we will not consider the latter here. Our detection techniques, the dc- as well as the ac-method, enable us to distinguish between magnons stemming from the injector and the modulator. This means the measured magnon transport signal at the detector only accounts for the magnons injected at the injector and thus the detector signal as a function of the dc modulator current $I_{\text{mod}}^{\text{dc}}$ represents a change of the magnon conductivity in the transport channel, in contrast to a mere increase of the magnon spin signal due to a second magnon source. We will discuss this topic in detail in the next Sec. 4.2. Due to our assumption and detection techniques, any change in the magnon spin transport signal induced by the modulator current reflects a change in the magnon conductivity σ_{m} , i.e. we expect that the measured detector voltage $V_{\text{det}}(I_{\text{mod}}^{\text{dc}}) \propto \sigma_{\text{m}}(I_{\text{mod}}^{\text{dc}})$. While the magnon conductivity is given by its equilibrium value $\sigma_{\text{m}}^{\text{0}}$ for $I_{\text{mod}}^{\text{dc}} = 0$, $\sigma_{\text{m}}(I_{\text{mod}}^{\text{dc}})$ is

expected to behave according to Eqs. (4.14) and (4.25) for the low bias and critical current regime, respectively. Following the discussion in Chap. 2, the detector signal contains much more information than only σ_m , e.g., due to several conversion processes at the injector and detector electrode. However, we do not expect that the interfacial as well as the metallic spin conductivities exhibit significant changes due to an applied dc charge current at the modulator and thus we consider the dependence of V_{det} exclusively as a change of σ_m . It is important to mention that due to our experimental configuration, as depicted in Fig. 4.3, the measured signal at the detector V_{det} results from the current applied to the injector I_{inj} , which differs from the conventional definition of a conductivity. In general, the latter is a local quantity, which describes the response function between a local current density and a local driving field, as for example, the electric field in the case of charge transport. Although our configuration does not represent a local correlation between a current and a driving field, we can consider the ratio $V_{\text{det}}/I_{\text{inj}}$ as a formal conductance. At first glance, this seems not to coincide with our discussion, as the ratio has, formally, units of a resistance instead of a conductance. However, as the injector current I_{inj} represents the driving field, which induces the magnon chemical potential gradient $\nabla\mu_m$ and the measured detector voltage V_{det} accounts for the detected magnon spin current $j_m = -\sigma_m\nabla\mu_m$, we expect $V_{\text{det}}/I_{\text{inj}} \propto j_m/\nabla\mu_m \propto \sigma_m$. In this Chapter, we do not normalize the detector voltage signals to the injector current because we kept the injector current constant during our measurements. In order to quantify the low bias and critical current regime in our measurements, we define appropriate fit functions depending on the modulator current regime and measurement method in the following.

First, we consider angle-dependent measurements, where the magnetic field direction with respect to the device is varied, while its magnitude is fixed. To account for the angle-dependent detector voltage signals $V_{\text{det}}(\varphi)$, we have to rephrase Eq. (4.32). As discussed in Sec. 2.3, the SHE-induced magnon injection is only active when the magnetization direction of the FMI \mathbf{m} is parallel to the spin polarization \mathbf{s} and thus its magnitude is proportional to $\sim \cos(\varphi)I_{\text{mod}}^{\text{dc}}$ ³¹. In contrast, thermally generated magnon injection does not scale with the angle of the magnetization

³¹Within our chosen coordinate system (cf. Fig. 4.4), positive (negative) magnetic fields are defined at $\varphi = 0^\circ, 360^\circ$ ($\varphi = 180^\circ$). This means, magnons are injected (depleted) via the SHE when $H \cdot I_{\text{mod}}^{\text{dc}} > 0$ ($H \cdot I_{\text{mod}}^{\text{dc}} < 0$).

orientation φ . Thus, we can rewrite Eq. (4.32) accounting for the angle dependence of the voltage signals according to

$$V_{\text{det}}(\varphi, I_{\text{mod}}^{\text{dc}}) = \cos^2(\varphi) \times \left\{ 2(\Delta V')^{-1} + \left[\Delta V_{\text{mod}}^0 \left(1 - \frac{\cos(\varphi) I_{\text{mod}}^{\text{dc}}}{I_{\text{mod}}^{\text{crit}}} \right)^{-1/2} + \Delta R_{\text{th}} I_{\text{mod}}^{\text{dc}} \right]^2 \right\}^{-1} \quad (4.37)$$

with the coefficients $\Delta V'$, ΔV_{mod}^0 and ΔR_{th} , which are proportional to σ'_m , $\sigma_m^{0, \text{mod}}$ and $\Delta\sigma_{\text{th}}$ and consider the conversion of the different terms into detector voltages. The $\cos^2(\varphi)$ function of Eq. (4.37) accounts for the usual angle dependence originating from the SHE-induced magnon transport between injector and detector (cf. Sec. 2.5.2). Furthermore, we replaced $I_{\text{mod}}^{\text{dc}} \rightarrow \cos(\varphi) I_{\text{mod}}^{\text{dc}}$ in the term related to the SHE-induced magnon injection of Eq. (4.32) to consider the additional SHE symmetry at the modulator. Separating the different angle symmetries in Eq. (4.37), we can define a fit function for the angle-dependent signal

$$V_{\text{det}}(\varphi) = \frac{A \cos^2(\varphi) + B \cos^2(\varphi) \left(1 - \frac{\cos(\varphi) I_{\text{mod}}^{\text{dc}}}{I_{\text{mod}}^{\text{crit}}} \right)^{1/2}}{1 + C \left(1 - \frac{\cos(\varphi) I_{\text{mod}}^{\text{dc}}}{I_{\text{mod}}^{\text{crit}}} \right)^{1/2}}, \quad (4.38)$$

where $A = \Delta V'/2$, $B = (1/2)(\Delta V'/\Delta V_{\text{mod}}^0) \Delta R'_{\text{th}} I_{\text{mod}}^{\text{dc} 2}$ and $C = (1/\Delta V_{\text{mod}}^0)(\Delta V'/2 + \Delta R'_{\text{th}} I_{\text{mod}}^{\text{dc} 2})$. Note that the parameters B and C depend on $I_{\text{mod}}^{\text{dc}}$ due to thermally induced changes in the magnon conductivity. From the angle dependence, we typically extract the voltage amplitudes A_{det} for positive and negative magnetic fields to study the behavior dependent on $I_{\text{mod}}^{\text{dc}}$. Utilizing the corresponding angles $\varphi = 0^\circ, 360^\circ$ and $\varphi = 180^\circ$ for $+\mu_0 H$ and $-\mu_0 H$, respectively, within our chosen coordinate system, we obtain a modulator current-dependent fit function

$$A_{\text{det}} \left(I_{\text{mod}}^{\text{dc}}, \pm \mu_0 H \right) = \frac{A + B \sqrt{1 \mp \frac{I_{\text{mod}}^{\text{dc}}}{I_{\text{mod}}^{\text{crit}}}}}{1 + C \sqrt{1 \mp \frac{I_{\text{mod}}^{\text{dc}}}{I_{\text{mod}}^{\text{crit}}}}}. \quad (4.39)$$

It is important to note that our fits are always restricted to the region up to $I_{\text{mod}}^{\text{dc}} = I_{\text{mod}}^{\text{crit}}$, as the phenomenological model is no longer valid beyond this point.

As derived in Sec. 4.1.2, the conductivity modulation in the low bias regime is sufficiently well described by Eq. (4.24). In this regime the magnon density n_m underneath the modulator is affected by the SHE-induced spin accumulation at the FMI/HM interface as well as by the Joule heating in the HM electrode. In linear

response, we find for the magnon conductivity $\sigma_m \propto I_{\text{mod}}^{\text{dc}} + (I_{\text{mod}}^{\text{dc}})^2$. To verify and investigate the linear and quadratic charge current dependence in the low bias regime, we reformulate the expression in Eq. (4.24) and use the following function to fit our data:

$$A_{\text{det}} \left(I_{\text{mod}}^{\text{dc}} \right) = A_0 + \Delta R_{\text{SHE}} I_{\text{mod}}^{\text{dc}} + \Delta R_{\text{th}} \left(I_{\text{mod}}^{\text{dc}} \right)^2. \quad (4.40)$$

Here, $\Delta R_{\text{SHE}} = (\Delta\sigma_{\text{SHE}}/\sigma_m^0)A_0$ and $\Delta R_{\text{th}} = (\Delta\sigma_{\text{th}}/\sigma_m^0)A_0$ are the linear and quadratic coefficients characterizing the efficiencies of the modulation effects in the low bias regime.

Previous experiments [68, 200] demonstrated that the introduced phenomenological model accurately represents the experimentally measured angle dependence as well as modulator current dependence. For angle-dependent measurements it has been shown that the most prominent modulation of the angle dependence stems from the square root dependencies in Eq. (4.38). Since these terms are directly connected to the SHE-induced injection of magnons [187], this corroborates the presented model that exclusively electrically injected magnons via the SHE contribute to the damping compensation. By implication, this suggests that the thermally generated magnons are not responsible for the damping compensation, but rather hinder the magnon system achieving damping compensation supporting our assumption [187, 196].

4.2 Quantitative Comparison of the Dc and Ac Detection Technique

In this section, we quantitatively compare two measurement schemes, which allow us to characterize the magnon spin transport in two-terminal as well as three-terminal devices. Here, we distinguish between a dc-detection technique utilizing the current reversal method and an ac-readout technique based on lock-in detection. While some works are based on a dc charge current applied to the injector [120, 186, 199], others rely on an ac stimulus applied to the injector [43–45]. Up to now, these two main measurement methods have been used to access and compare the magnon transport properties, although it is not clear whether or not these methods yield exactly the same results, in particular when the transport between injector and detector is manipulated via an additional applied dc charge current. Especially the aspect that it is not always obvious in literature how SHE- and thermally induced signal contributions are considered in the two measurement methods makes an interpretation challenging. With a proper interpretation, we expect both

measurement techniques to result in the same electrically induced signals if (i) the injector current in both cases is small enough that we can neglect nonlinear contributions and stay in the linear transport regime and (ii) the measurement frequency for the ac technique is low compared to characteristic time constants, regarding both the measurement setup and the sample under investigation. In the following, we revisit the sample configuration and introduce both measurement techniques. We present angle-dependent measurements of the SHE and thermally injected magnons for both measurement configurations and compare the results in detail. Furthermore, we verify that both schemes allow us to investigate the modulation of magnon transport induced by an additional dc charge current applied to the center modulator strip.

The vast majority of text and figures in this Section is taken from the article published in J. Gückelhorn, T. Wimmer, S. Geprägs, H. Huebl, R. Gross, and M. Althammer, *Quantitative comparison of magnon transport experiments in three-terminal YIG/Pt nanostructures acquired via dc and ac detection techniques*, [Applied Physics Letters](#) **117**, 182401 (2020).

4.2.1 Dc-detection Technique

We introduce the dc-detection technique for the general case of a three-terminal device, as sketched in Fig. 4.4(a). A charge current I_{inj} is applied to the injector, inducing a magnon accumulation in the YIG film via the SHE and Joule heating. The magnons diffuse away from the injector and towards the detector strip, where they can be detected as a voltage signal V_{det} . A dc charge current $I_{\text{mod}}^{\text{dc}}$ is applied to the modulator electrode allowing for the manipulation of the magnon spin transport between injector and detector via a SHE-induced spin accumulation and Joule heating effects.

Following previous works [44, 45, 76, 199], we express the detector voltage as

$$V_{\text{det}}(I_{\text{inj}}, I_{\text{mod}}^{\text{dc}}) = \sum_{i \in \{\text{inj}, \text{mod}\}} \sum_{j=1}^{\infty} R_{i\text{-det}}^j(I_{\text{mod}}^{\text{dc}}) \cdot [I_i]^j. \quad (4.41)$$

Here, $R_{i\text{-det}}^j(I_{\text{mod}}^{\text{dc}})$ are the transport coefficients accounting for the conversion process at the YIG/Pt interface and the transport in the YIG layer. Note that we only account for changes in R_i^j via $I_{\text{mod}}^{\text{dc}}$. This assumption is only valid for small injector currents I_{inj} [44, 45]. Explicitly accounting for magnons injected at the injector and at the modulator in Eq. (4.41), allows us to verify that both our measurement techniques are able to disentangle the detector voltages generated via I_{inj} and $I_{\text{mod}}^{\text{dc}}$ and thus only consider magnons induced at the injector. In the following, we

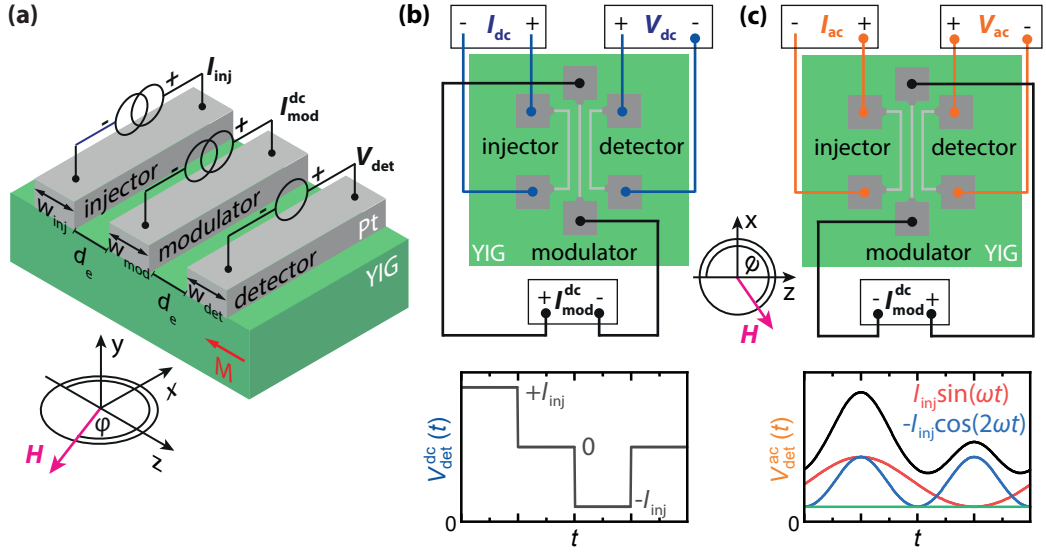


Fig. 4.4 – (a) Schematic depiction of the sample configuration with the electrical wiring scheme and the coordinate system with the in-plane rotation angle φ of the applied magnetic field. (b) Top view of the device with the detailed connection scheme (upper panel) and schematic dependence of the detector voltage V_{det} as a function of time according to Eq. (4.41) (lower panel) for the dc-detection technique. The dc current at the injector is step-wise varied from $+I_{\text{inj}}$ to $-I_{\text{inj}}$ and vice versa. (c) Top view of the device (upper panel) and schematic dependence of V_{det} (lower panel) for the ac-detection technique. The first (red) and second (blue) harmonic signal for $V_{\text{det}}^{\text{ac}}$ is shown as well as a constant offset detector voltage (green). The black line corresponds to their superposition.

will show that for both the advanced current reversal method (dc technique) and the lock-in technique (ac technique) the first sum vanishes (with $i = \text{inj}$) and the voltage signals only contain contributions from $I_{\text{mod}}^{\text{dc}}$ via the transport coefficients $R_{\text{inj-det}}^j(I_{\text{mod}}^{\text{dc}})$.

For the dc-detection technique, we utilize an advanced current reversal scheme, which is sketched in Fig. 4.4(b). We apply a dc charge current sequence $+I_{\text{inj}}, 0, -I_{\text{inj}}, 0$ to the injector, while a constant dc charge current $I_{\text{mod}}^{\text{dc}}$ is applied to the modulator. For each configuration we measure the voltage $V_{\text{det}}^{\text{dc}}$ at the detector (cf. 4.4(b)). From these measurements, we can then define the voltage due to SHE-induced magnons transported from the injector to the detector as

$$\begin{aligned}
 V_{\text{dc}}^{\text{SHE}} &= \frac{1}{2} \left[V_{\text{det}}^{\text{dc}} \left(I_{\text{inj}}, I_{\text{mod}}^{\text{dc}} \right) - V_{\text{det}}^{\text{dc}} \left(-I_{\text{inj}}, I_{\text{mod}}^{\text{dc}} \right) \right] \\
 &= R_{\text{inj-det}}^1 \left(I_{\text{mod}}^{\text{dc}} \right) I_{\text{inj}} + R_{\text{inj-det}}^3 \left(I_{\text{mod}}^{\text{dc}} \right) \left(I_{\text{inj}} \right)^3 + \dots,
 \end{aligned} \tag{4.42}$$

where we assume an odd symmetry with respect to I_{inj} . Furthermore, we utilized Eq. (4.41) to obtain the second line in Eq. (4.42). While the SHE-induced voltage

contributions $V_{\text{dc}}^{\text{SHE}}$ switch sign under a polarity change, thermal voltages are even under current reversal and thus we define

$$\begin{aligned} V_{\text{dc}}^{\text{therm}} &= \frac{1}{2} \left[V_{\text{det}}^{\text{dc}} \left(I_{\text{inj}}, I_{\text{mod}}^{\text{dc}} \right) + V_{\text{det}}^{\text{dc}} \left(-I_{\text{inj}}, I_{\text{mod}}^{\text{dc}} \right) - 2V_{\text{det}}^{\text{dc}} \left(0, I_{\text{mod}}^{\text{dc}} \right) \right] \\ &= R_{\text{inj-det}}^2 \left(I_{\text{mod}}^{\text{dc}} \right) \left(I_{\text{inj}} \right)^2 + \dots, \end{aligned} \quad (4.43)$$

as the voltage due to thermally generated magnons assuming an even symmetry with respect to I_{inj} and utilizing Eq. (4.41). This elaborate scheme allows us to disentangle the dc detector voltages generated via I_{inj} and $I_{\text{mod}}^{\text{dc}}$. This means, $V_{\text{dc}}^{\text{SHE}}$ and $V_{\text{dc}}^{\text{therm}}$ only contain contributions from $I_{\text{mod}}^{\text{dc}}$ via the transport coefficients $R_{\text{inj-det}}^j \left(I_{\text{mod}}^{\text{dc}} \right)$.

For two-terminal devices, we use the standard current reversal technique with $I_{\text{mod}}^{\text{dc}} = 0$. In this case, in Eq. (4.43) in the first line the subtraction of the induced voltage signal for zero applied modulator current is vanishing, i.e. for two-terminal devices it is sufficient to sum the voltage contributions due to positive and negative I_{inj} . In contrast, Eq. (4.42) accounting for SHE injected magnons remains unchanged. Thus, it is sufficient to subsequently apply dc currents with positive ($+I_{\text{inj}}$) and negative ($-I_{\text{inj}}$) polarity. Furthermore, the coefficients R_i^j do no longer account for changes via $I_{\text{mod}}^{\text{dc}}$, but only for the conversion processes involved in the magnon transport from injector to detector.

4.2.2 Ac-detection Technique

For the second method, the ac-readout technique, we again apply a constant dc charge current $I_{\text{mod}}^{\text{dc}}$ to the modulator. However, this time we simultaneously apply an ac charge current $I_{\text{inj}}^{\text{ac}}(t) = I_{\text{inj}} \sin(\omega t)$ to the injector with angular frequency $\omega = 2\pi f$. Via lock-in detection, we record the first and second harmonic signals of $V_{\text{det}}^{\text{ac}}$, as depicted in Fig. 4.4(c). In general, the lock-in detection method allows to measure at the fundamental frequency f and any of its harmonics. The input signal of the lock-in, the n^{th} harmonic voltage signal $V^{n\omega}$ (with $n \in \mathbb{N}$), is split and separately multiplied with an in-phase sinusoidal reference signal ($\propto \sin(n\omega t)$) and its 90° phase shifted signal ($\propto \cos(n\omega t)$). Subsequent, these signals are integrated over a time interval $T \gg 1/\omega$ by low-pass filtering. The output signal $V^{n\omega}$ is given by the two components

$$V_X^{n\omega} = \frac{\sqrt{2}}{T} \int_0^T \sin(n\omega t) V_{\text{det}}^{\text{ac}}(t) dt \quad (4.44)$$

$$V_Y^{n\omega} = \frac{\sqrt{2}}{T} \int_0^T \cos(n\omega t) V_{\text{det}}^{\text{ac}}(t) dt, \quad (4.45)$$

where the subscript X denotes the in-phase and Y the quadrature component. A phase delay ϕ of the signal arriving at the detector leads to finite signals in both components. This finite phase shift ϕ could have various origins, including the experimental setup introduced in Sec. 3.3: (i) different trigger conditions between the ac current source and the lock-in could lead to a phase shift, (ii) a phase delay at the voltage preamplifier is possible, (iii) an inductive crosstalk in our design might occur or (iv) the phase shift is independent of the setup and stems from the magnon transport between injector and detector [68]. The exact identification of the origin of ϕ would be tedious and as it is not relevant for the analysis of the presented data, it is not within the scope of this thesis. To account for the full signal response in only one component, we apply a rotation matrix to our signals and obtain

$$\begin{pmatrix} V_{X'}^{n\omega} \\ V_{Y'}^{n\omega} \end{pmatrix} = \begin{pmatrix} \cos n\phi & \sin n\phi \\ -\sin n\phi & \cos n\phi \end{pmatrix} \begin{pmatrix} V_X^{n\omega} \\ V_Y^{n\omega} \end{pmatrix}. \quad (4.46)$$

The rotated components are denoted as X' and Y' . To make sure that the full signal response is in one of the components (X' or Y'), the phase shift ϕ has to be determined. Therefore, we analyze the first harmonic voltage signal ($n = 1$) obtained by angle-dependent measurements and iteratively apply the rotation matrix to the X and Y components of the signal for different ϕ values until the angle dependence of $V_{Y'}^{1\omega}$ vanishes and the whole signal amplitude is captured by the X' component. The determined ϕ -value is then utilized to analyze the first harmonic signal of follow-up measurements, such as current- or field-dependent measurements. Higher harmonic signals have to be rotated by $n\phi$ to get the signal into one component. Utilizing Eq. (4.41), the full signal response of the first harmonic signal $V_{ac}^{1\omega}$ for a time interval $T \gg 1/\omega$ is given by

$$\begin{aligned} V_{ac}^{1\omega} &= \frac{2}{T} \int_0^T \sin(\omega t) V_{det}^{ac} \left(I_{inj}^{ac}(t), I_{mod}^{dc} \right) dt \\ &= R_{inj-det}^1 \left(I_{mod}^{dc} \right) I_{inj} + \frac{3}{4} R_{inj-det}^3 \left(I_{mod}^{dc} \right) (I_{inj})^3 + \dots, \end{aligned} \quad (4.47)$$

which corresponds to the SHE-induced magnon transport signal. We see that the first harmonic voltage signal is odd with respect to I_{inj} . For the second harmonic signal $V_{ac}^{2\omega}$, we obtain

$$\begin{aligned} V_{ac}^{2\omega} &= -\frac{2}{T} \int_0^T \cos(2\omega t) V_{det}^{ac} \left(I_{inj}^{ac}(t), I_{mod}^{dc} \right) dt \\ &= \frac{1}{2} R_{inj-det}^2 \left(I_{mod}^{dc} \right) (I_{inj})^2 + \dots, \end{aligned} \quad (4.48)$$

Device	t_{YIG} (nm)	t_{Pt} (nm)	$w_{\text{inj}} = w_{\text{det}}$ (nm)	w_{mod} (nm)	d_e (nm)
D300	7.0	3.5	500	300	200
D500	11.4	5	500	500	200

Tab. 4.1 – Device parameters of D300 and D500 investigated in the dc- and ac-experiments.

which corresponds to the thermally generated magnons due to Joule heating in the injector and is even with respect to I_{inj} . Here, we have to account for the -90° phase shift of the signal with respect to the reference signal. The lock-in technique assures that the first and second harmonic signals only contain contributions from the magnon transport between the injector and detector.

4.2.3 SHE Induced Magnon Spin Signal

First, we focus on the voltage signals of the SHE-induced magnons acquired via the dc- and ac-detection technique. If we compare $V_{\text{dc}}^{\text{SHE}}$ (Eq. (4.42)) and $V_{\text{ac}}^{1\omega}$ (Eq. (4.47)), we find that these two quantities should be identical if $R_{\text{inj-det}}^j = 0$ for $j \geq 2$. Thus a quantitative comparison of $V_{\text{dc}}^{\text{SHE}}$ and $V_{\text{ac}}^{1\omega}$ should allow us to obtain information on higher order SHE contributions.

For the experiments, we investigate two three-terminal devices (D300 and D500) on two different YIG thin films. The injector and detector length $l_{\text{inj}} = l_{\text{det}} = 50 \mu\text{m}$ as well as the modulator length $l_{\text{mod}} = 64 \mu\text{m}$ are identical for both devices. The other device parameters slightly differ and are summarized in Tab. 4.1. Note that the measurements for D500 were performed in the same experimental setup, while the dc and ac measurements of D300 were conducted in two different setups. For all measurements we use a peak value of $I_{\text{inj}} = 100 \mu\text{A}$, which corresponds to an injector current density of $J_{\text{inj}} = I_{\text{inj}}/(t_{\text{Pt}}w_{\text{inj}}) \approx 5.7 \times 10^{10} \text{ A/m}^2$ for D300 and $J_{\text{inj}} = 4 \times 10^{10} \text{ A/m}^2$ for D500. In an analogous manner, we can define the modulator current density $J_{\text{mod}} = I_{\text{mod}}^{\text{dc}}/(t_{\text{Pt}}w_{\text{inj}})$.

To characterize the magnon transport in our devices, we plot the detector voltages $V_{\text{dc}}^{\text{SHE}}$ and $V_{\text{ac}}^{1\omega}$ as a function of the magnetic field orientation φ (cf. Fig. 4.4(a)) measured for a fixed magnetic field strength of $\mu_0 H = 50 \text{ mT}$ and a temperature of $T = 280 \text{ K}$. We first focus on D300 with $V_{\text{dc}}^{\text{SHE}}$ for different positive and negative modulator currents $I_{\text{mod}}^{\text{dc}}$ in Fig. 4.5 (a) and (b), respectively, as well as $V_{\text{ac}}^{1\omega}$ in Fig. 4.5(c) for $I_{\text{mod}}^{\text{dc}} \geq 0$ and (d) for $I_{\text{mod}}^{\text{dc}} \leq 0$. For $I_{\text{mod}}^{\text{dc}} = 0$ (light green data points), we observe the distinctive $\cos^2 \varphi$ modulation for magnon transport between the injector and detector without an additional modulator in between for both measurement schemes. Both $V_{\text{dc}}^{\text{SHE}}$ and $V_{\text{ac}}^{1\omega}$ show minima for $\mathbf{H} \parallel \pm \hat{z}$ ($\varphi = 0^\circ, 180^\circ, 360^\circ$), which correspond to maxima in the magnon transport between the injector and detector [43, 120]. For $I_{\text{mod}}^{\text{dc}} > 0$ (cf. Fig. 4.5(a), (c)), both magnon

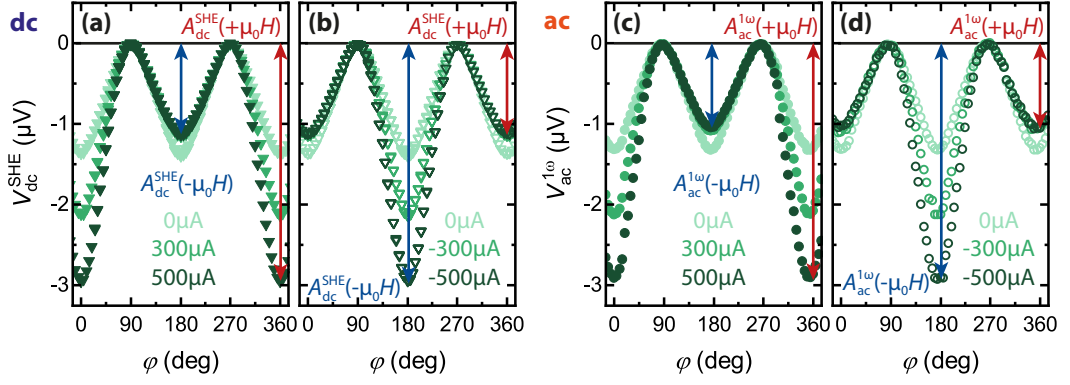


Fig. 4.5 – (a), (b) Detector signal V_{dc}^{SHE} and (c), (d) $V_{ac}^{1\omega}$ of device D300 plotted versus the rotation angle φ of the in-plane magnetic field \mathbf{H} with constant magnitude $\mu_0 H = 50$ mT for various I_{mod}^{dc} . (a), (c) For $I_{mod}^{dc} > 0$, the detector signal is significantly increased at $\varphi = 0^\circ, 360^\circ$ and slightly reduced at $\varphi = 180^\circ$, while (b), (d) for $I_{mod}^{dc} < 0$ the angle dependence is shifted by 180° . The angle dependence and the ranges of V_{dc}^{SHE} and $V_{ac}^{1\omega}$ are in perfect agreement. The voltage amplitudes A_{dc}^{SHE} and $A_{ac}^{1\omega}$ are extracted from the angle dependence of the detector signals as shown by the vertical arrows.

transport signals V_{dc}^{SHE} and $V_{ac}^{1\omega}$ are significantly increased at $\varphi = 0^\circ, 360^\circ$. This enhancement can be explained by an increase in magnon conductivity caused by a magnon accumulation underneath the modulator. On the one hand, the SHE-induced magnon chemical potential and on the other hand thermally generated magnons due to Joule heating are the origin of this enhanced magnon accumulation. The increase in magnon conductivity in turn leads to a larger magnon transport signal at the detector and thus a higher negative voltage signal for V_{dc}^{SHE} and $V_{ac}^{1\omega}$. At $\varphi = 180^\circ$, we obtain a decreased magnon transport signal at the detector for both measurement techniques. In this case, a magnon depletion occurs underneath the modulator due to the annihilation of magnons via the SHE. However, the depletion in V_{dc}^{SHE} and $V_{ac}^{1\omega}$ is rather small compared to the enhancement at $\varphi = 0^\circ, 360^\circ$, as it is counterbalanced by the thermally injected magnons arising due to Joule heating at the modulator. For $I_{mod}^{dc} < 0$, we observe a 180° shifted behavior compared to the data for $I_{mod}^{dc} > 0$, i.e. the magnon transport signals V_{dc}^{SHE} and $V_{ac}^{1\omega}$ are significantly increased at $\varphi = 180^\circ$, while they are slightly decreased at $\varphi = 0^\circ, 360^\circ$. In this configuration, the magnon accumulation underneath the modulator is increased for $\varphi = 180^\circ$ due to the SHE-induced magnon chemical potential and the thermal magnons arising due to Joule heating. In contrast, the decrease at $\varphi = 0^\circ, 360^\circ$ originates from the annihilation of magnons via the SHE, which is however counterbalanced by thermally generated magnons at the modulator. This behavior has already been reported by Wimmer *et al.* in Ref. [45]. Comparing the dc and ac configuration, we find that not just the angle dependence is equivalent, but also the voltage amplitudes V_{dc}^{SHE} and $V_{ac}^{1\omega}$ are

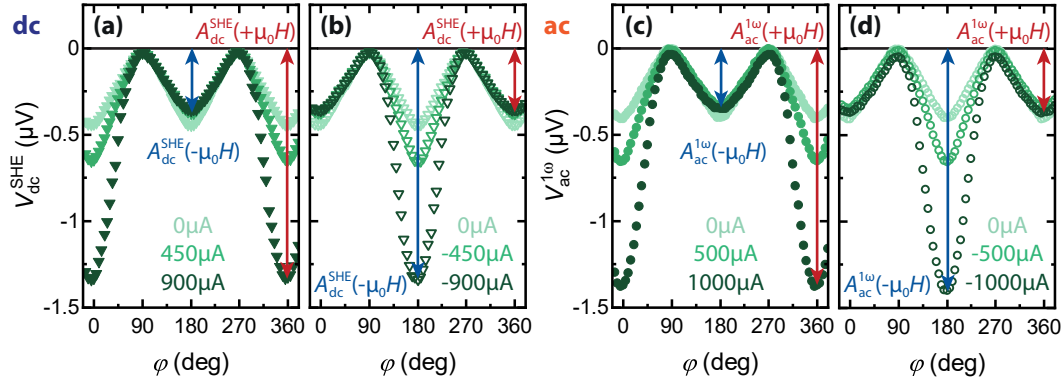


Fig. 4.6 – Detector signals (a), (b) V_{dc}^{SHE} acquired via the dc-detection technique and (c), (d) $V_{ac}^{1\omega}$ the first harmonic signal of the ac-readout technique of SHE injected magnons of D500 as a function of the magnetic field orientation φ with $\mu_0 H = 50$ mT for various modulator currents I_{mod}^{dc} . (a), (c) For $I_{mod}^{dc} > 0$, the magnon spin transport is significantly increased at $\varphi = 0^\circ, 360^\circ$ and reduced at $\varphi = 180^\circ$. (b), (d) For $I_{mod}^{dc} < 0$, we observe a 180° shifted behavior. Similar to Fig. 4.5 the ranges and behavior of the SHE induced magnon spin transport signals V_{dc}^{SHE} and $V_{ac}^{1\omega}$ are in perfect agreement.

in very good agreement. As already mentioned, this is expected if the frequency of the ac signal is low compared to characteristic frequencies set by characteristic time constants and if the injector current amplitude is low enough in both cases to stay in the linear transport regime.

To rule out effects due to different measurement setups, we now present the data of device D500, which was measured in a single setup instead of two different setups. In an analogous manner to Fig. 4.5, we plot the detector signals V_{dc}^{SHE} and $V_{ac}^{1\omega}$ as a function of the magnetic field orientation φ at a magnetic field magnitude of $\mu_0 H = 50$ mT and $T = 280$ K for various modulator currents up to $I_{mod}^{dc} \leq 1000 \mu A$ achieving similar current densities at the modulator as with the device D300³². In Fig. 4.6(a) and (b) the measurement results V_{dc}^{SHE} recorded with the dc method for positive and negative I_{mod}^{dc} , respectively, are shown, while the panels (c) and (d) show the angle dependence of $V_{ac}^{1\omega}$ for $I_{mod}^{dc} \geq 0$ and for $I_{mod}^{dc} \leq 0$. For $I_{mod}^{dc} = 0$ as well as $I_{mod}^{dc} > 0$ and $I_{mod}^{dc} < 0$, we find a similar angle dependence as for D300, however the absolute voltage amplitudes V_{dc}^{SHE} and $V_{ac}^{1\omega}$ are reduced. Since the magnon transport in the MOI exhibits an exponential decay for sufficiently large injector-detector distances [43, 141], we can explain this decrease by the larger separation between injector and detector for D500. The behavior of the angle dependence is based on the same processes already explained for D300. Similar

³²Note that despite the large current densities present in the Pt strips, predominantly in the modulator electrode, we measure a resistance between injector and detector over the whole modulator current range of above 1 GΩ. Since this value is comparable to the input resistance of our measurement setup and is about 5 orders of magnitude larger than the Pt resistance, we do not expect any influence from an enhanced electrical conduction of the YIG film.

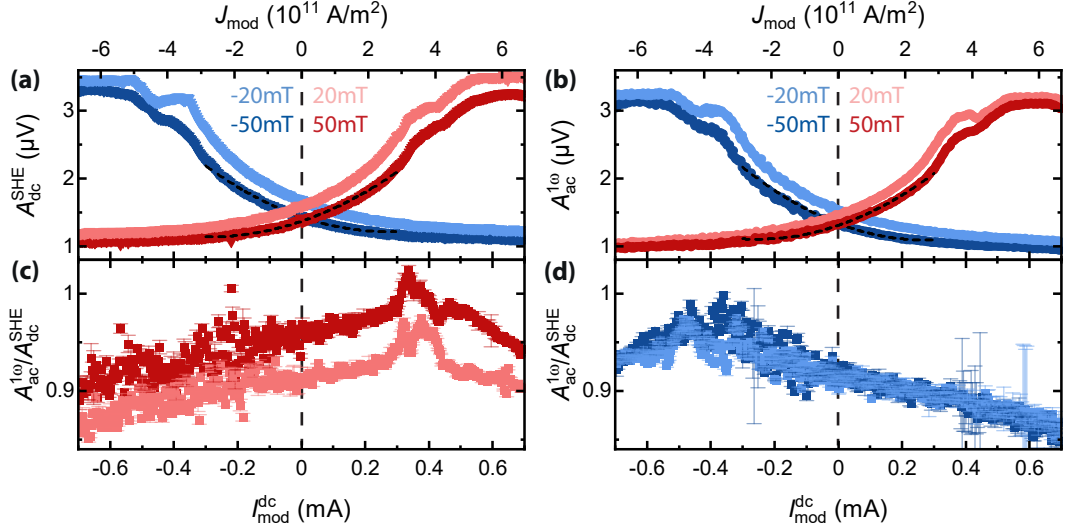


Fig. 4.7 – Extracted amplitudes (a) $A_{dc}^{SHE}(\pm\mu_0H)$ and (b) $A_{ac}^{1\omega}(\pm\mu_0H)$ of the SHE injected magnons of D300 as function of the modulator current I_{mod}^{dc} . The curves and signal amplitudes show similar behaviors for (a) the dc and (b) ac method. The black dashed lines for $\mu_0H = \pm 50$ T are fits to Eq.(4.40) exemplary indicating the $I_{mod}^{dc} + (I_{mod}^{dc})^2$ dependence in the low bias regime ($|I_{mod}^{dc}| \leq 0.3$ mA). (c), (d) Ratio $A_{ac}^{1\omega}/A_{dc}^{SHE}$ of the extracted amplitudes for the ac and dc configuration for (c) positive and (d) negative magnetic field values μ_0H .

to D300, the comparison of the dc and ac technique shows an equivalence of the angle dependence as well as of the voltage amplitudes V_{dc}^{SHE} and $V_{ac}^{1\omega}$, although the applied modulator current magnitudes slightly differ. Our findings are in perfect agreement with the predictions of our detector voltage model, which suggests that V_{dc}^{SHE} and $V_{ac}^{1\omega}$ should be equal when only first and second order transport coefficients contribute ($R_{inj-det}^j \neq 0$ for $j \leq 2$).

For a more elaborate quantitative comparison of the voltage signals detected in the dc and ac measurements, we extract the signal amplitudes $A_{dc}^{SHE}(\pm\mu_0H)$ and $A_{ac}^{1\omega}(\pm\mu_0H)$ of the angle-dependent measurements, as exemplary indicated by arrows in Fig. 4.6 and plot them as a function of the modulator current I_{mod}^{dc} . Note that we analyze A_{dc}^{SHE} and $A_{ac}^{1\omega}$ instead of V_{dc}^{SHE} and $V_{ac}^{1\omega}$, because the voltage measured at $\varphi = 90^\circ, 270^\circ$ is close to zero, which leads to significant contributions of noise. We first focus on the signal amplitudes $A_{dc}^{SHE}(\pm\mu_0H)$ and $A_{ac}^{1\omega}(\pm\mu_0H)$ of the device D300, which are shown in Fig. 4.7(a) and (b) for different magnetic field magnitudes $\mu_0H = \pm 20$ mT, ± 50 mT. At first glance, both the functional dependence on the modulator current and the absolute value of the detector signal show a similar behavior for the dc (Fig. 4.7(a)) and ac (Fig. 4.7(b)) configuration. As discussed in Sec. 4.1.2, the signal amplitudes in the low bias regime ($|I_{mod}^{dc}| \leq 0.3$ mA) can be described by a superposition of a linear (SHE) and quadratic (Joule heating) modulator current dependence [44, 45]. To illustrate this, we exemplary

plot this $I_{\text{mod}}^{\text{dc}} + (I_{\text{mod}}^{\text{dc}})^2$ dependence for $\mu_0 H = \pm 50$ mT as a blacked dashed line in Fig. 4.8(a) and (b). The fits using Eq.(4.40) well model the measured data points in the low bias regime, while for $I_{\text{mod}}^{\text{dc}} > 0.3$ mA for positive magnetic field values and for $I_{\text{mod}}^{\text{dc}} < -0.3$ mA for $\mu_0 H < 0$ we observe a pronounced deviation from this behavior. We can attribute this deviation of the detector signal from the $I_{\text{mod}}^{\text{dc}} + (I_{\text{mod}}^{\text{dc}})^2$ dependence to a zero effective damping state underneath the modulator (cf. Sec. 4.1.1). To show that the extracted amplitudes as a function of the modulator current $I_{\text{mod}}^{\text{dc}}$ for the dc configuration are in accordance with the amplitudes of the ac scheme, we plot the ratio $A_{\text{ac}}^{1\omega}/A_{\text{dc}}^{\text{SHE}}$. Fig. 4.7(c) shows the ratios for positive magnetic field values, while panel (d) shows $A_{\text{ac}}^{1\omega}/A_{\text{dc}}^{\text{SHE}}$ for negative magnetic field values. Focusing on $\mu_0 H > 0$, the curve exhibits a slight increase of $A_{\text{ac}}^{1\omega}/A_{\text{dc}}^{\text{SHE}}$ in the negative and low bias regime ($I_{\text{mod}}^{\text{dc}} \leq 0.3$ mA). According to our angle-dependent measurements and the detector voltage model we would expect a rather constant behavior $A_{\text{ac}}^{1\omega}/A_{\text{dc}}^{\text{SHE}} = 1$, when only linear effects contribute, i.e. $R_{\text{inj-det}}^j(I_{\text{mod}}^{\text{dc}}) = 0$ for $j \geq 2$. The deviation from the expected constant behavior might originate from the two different measurement setups, where the dc and ac measurements were conducted, potentially causing differences in the detector resistances. For $I_{\text{mod}}^{\text{dc}} > 0.3$ mA, we observe one or more peaks and for even higher modulator currents we find a decreasing signal ratio, which is a clear deviation from the behavior in the negative and low bias regime. For the negative field polarities, we extract a decrease of the ratio $A_{\text{ac}}^{1\omega}/A_{\text{dc}}^{\text{SHE}}$ in the low and positive bias regime ($I_{\text{mod}}^{\text{dc}} \geq -0.3$ mA), while we again find a clear deviation from the linear I_{inj} dependence for negative modulator currents $I_{\text{mod}}^{\text{dc}} < -0.3$ mA. Following the arguments of our theoretical model, this behavior indicates a deviation from the linear I_{inj} dependence for $I_{\text{mod}}^{\text{dc}} > 0.3$ mA with $R_{\text{inj-det}}^j(I_{\text{mod}}^{\text{dc}}) \neq 0$ for $j \geq 2$. We attribute this to a new regime established via the damping compensation underneath the modulator. This reflects a typical threshold behavior of nonlinear effects [199]. We see that the ratio $A_{\text{ac}}^{1\omega}/A_{\text{dc}}^{\text{SHE}}$ slightly differs for different magnetic field magnitudes, predominantly in the nonlinear regime. A possible explanation for this complex behavior might be the population of additional damping compensated magnon modes with increasing modulator current $I_{\text{mod}}^{\text{dc}}$.

To investigate this behavior in more detail and to compare how large the influence is when the measurements are conducted in two different setups, we analyze the data of device D500 in a similar manner. Analogous to Figure 4.7, we extract the amplitudes $A_{\text{dc}}^{\text{SHE}}(\pm\mu_0 H)$ and $A_{\text{ac}}^{1\omega}(\pm\mu_0 H)$ of the angle-dependent measurements shown in Fig. 4.6 and plot them as a function of the applied modulator current $I_{\text{mod}}^{\text{dc}}$ for various magnetic field magnitudes in Fig. 4.8(a) and (b) for the dc and ac configuration. In accordance with our previous observations, we find similar behaviors and detector voltage amplitudes for the dc (Fig. 4.8(a)) and ac (Fig. 4.8(b))

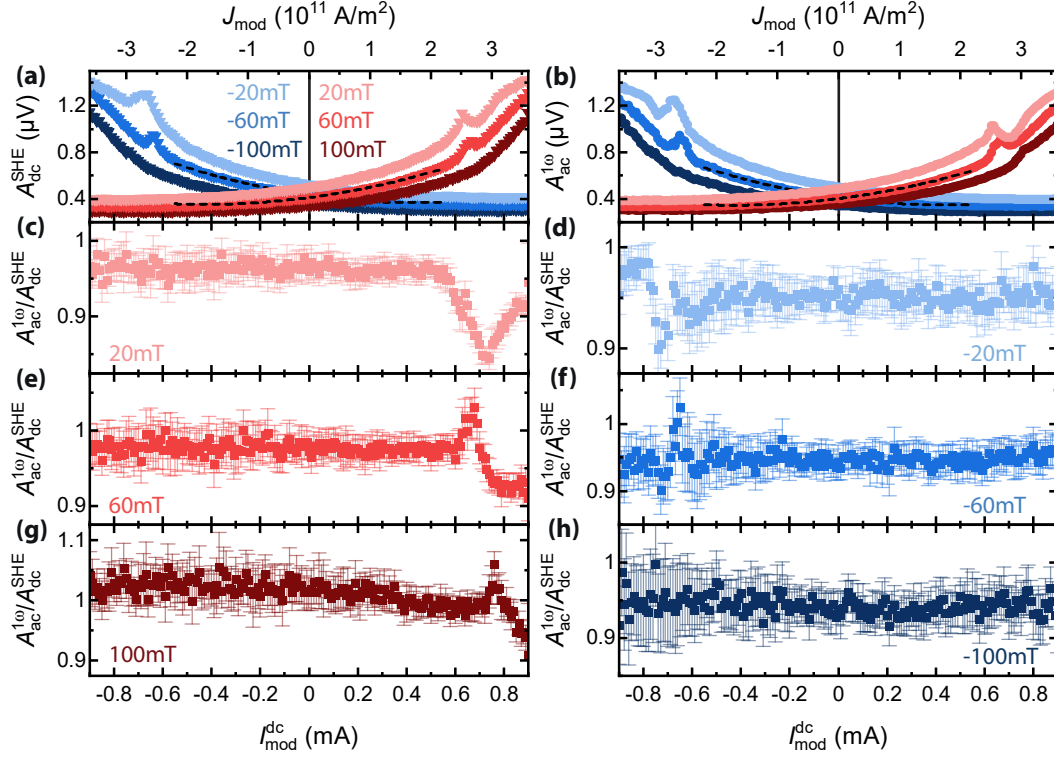


Fig. 4.8 – Extracted amplitudes (a) $A_{dc}^{SHE}(\pm\mu_0H)$ and (b) $A_{ac}^{1\omega}(\pm\mu_0H)$ of the SHE injected magnons of device D500 (as indicated by arrows in Fig. 4.6) plotted versus the dc charge current I_{mod}^{dc} . The signal amplitudes show a similar behavior for the (a) dc and (b) ac measurement method. The black dashed lines for $\mu_0H = \pm 60$ T are fits to Eq.(4.40) exemplary indicating the $I_{mod}^{dc} + (I_{mod}^{dc})^2$ dependence in the low bias regime ($|I_{mod}^{dc}| \leq 0.55$ mA). (c), (d), (e), (f), (g), (h) Ratio $A_{ac}^{1\omega}/A_{dc}^{SHE}$ of the extracted amplitudes for the ac and dc configuration for (c), (e), (g) positive and (d), (f), (h) negative magnetic field magnitudes μ_0H . (c), (e), (g) For $I_{mod}^{dc} \leq 0.55$ mA, the ratio exhibits a nearly constant behavior close to the value 1. A clear deviation from 1 is found for higher modulator currents. (d), (f), (h) For $\mu_0H < 0$, we observe a similar dependence with a threshold behavior for negative modulator current values ($I_{mod}^{dc} < -0.55$ mA).

measurement technique. In the low bias regime of device D500 ($|I_{mod}^{dc}| \leq 0.55$ mA) we observe the predicted superposition of a linear (SHE) and quadratic (Joule heating) dependence. The fits to Eq. (4.40) (black dashed lines) for $\mu_0H = \pm 60$ mT in Fig. 4.8(a) and (b) well reproduce the $I_{mod}^{dc} + (I_{mod}^{dc})^2$ dependence in the low bias regime. We find a clear deviation from this behavior for modulator currents $I_{mod}^{dc} > 0.55$ mA or $I_{mod}^{dc} < -0.55$ mA for positive and negative magnetic field magnitudes, respectively. Similar to device D300, we attribute this threshold behavior to a zero effective damping state [45]. For a quantitative comparison of the absolute amplitude values of the dc and ac configuration, we plot the ratios $A_{ac}^{1\omega}/A_{dc}^{SHE}$ as a function of the modulator current I_{mod}^{dc} in Fig. 4.8(c), (e), (g) for positive and in (d), (f), (h) for negative magnetic field values. For positive field magnitudes in

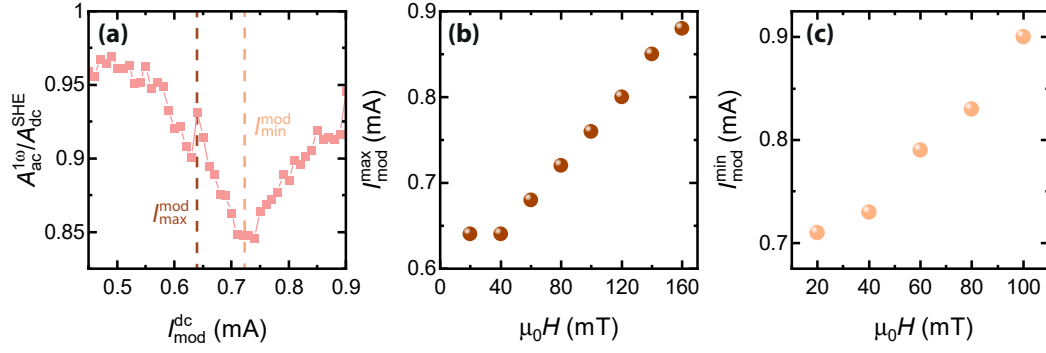


Fig. 4.9 – (a) Detailed view of the ratio $A_{ac}^{1\omega}/A_{dc}^{SHE}$ of D500 for $\mu_0 H = 20$ mT for large dc charge currents I_{mod}^{dc} . (b) Modulator current value of the peak/kink position I_{mod}^{max} as a function of the magnetic field magnitude $\mu_0 H$. I_{mod}^{max} is extracted from the ratios $A_{ac}^{1\omega}/A_{dc}^{SHE}$ as exemplary indicated in (a). (c) Modulator current value of the dip position I_{mod}^{min} versus $\mu_0 H$ extracted from the ratios $A_{ac}^{1\omega}/A_{dc}^{SHE}$ as indicated by the orange dashed line in (a).

the negative and low bias regime ($I_{mod}^{dc} \leq 0.55$ mA), the ratio is nearly constant with a value close to 1, which is in contrast to the behavior of device D300. Since our detector voltage model predicts $A_{ac}^{1\omega}/A_{dc}^{SHE} = 1$ for only linear effects with $R_{inj-det}^j(I_{mod}^{dc}) = 0$ for $j \geq 2$, this observation corroborates our simple model. However, for $I_{mod}^{dc} > 0.55$ mA we extract a clear deviation from 1. While we observe a dip for $\mu_0 H = 20$ mT, we find a peak for $\mu_0 H = 60$ mT and 100 mT. This observation substantiates our considerations that higher orders of I_{inj} contribute in this regime. For negative magnetic field magnitudes, a similar dependence of $A_{ac}^{1\omega}/A_{dc}^{SHE}$ can be extracted, however with a polarity change and thus a threshold for negative modulator currents I_{mod}^{dc} . For $\mu_0 H = -100$ mT (Fig. 4.8(h)), the threshold behavior cannot be observed due to a worse signal-to-noise ratio. Comparing the devices D300 and D500, we see that conducting measurements in two different setups, introduces an uncertainty, which results in a slightly different behavior of the ratio of the detector voltage signals of device D300 compared to D500. Concluding, this means that the comparison of the dc- and ac-detection method is most precise when all measurements can be performed in the same setup.

Similar to our previous observation, the ratios $A_{ac}^{1\omega}/A_{dc}^{SHE}$ of device D500 slightly differ for varying magnetic field magnitudes, predominantly in the nonlinear regime. For a more quantitative analysis of the field dependence, we investigate the behavior within the nonlinear regime in more detail. As exemplary shown for $\mu_0 H = 20$ mT in Fig. 4.9(a), the ratio $A_{ac}^{1\omega}/A_{dc}^{SHE}$ in the nonlinear regime ($I_{mod}^{dc} > 0.55$ mA) exhibits a complex structure. We are able to extract two dominant features, the modulator currents I_{mod}^{max} and I_{mod}^{min} , which are defined as the current values where the ratio in the nonlinear regime reaches its local maximum and minimum, respectively. The

extracted modulator current $I_{\text{mod}}^{\text{max}}$ is plotted as a function of the applied magnetic field magnitude in Fig. 4.9 (b). For $\mu_0 H < 40$ mT, the modulator current has a constant value of $I_{\text{mod}}^{\text{max}} \approx 0.64$ mA, while we find an about linear increase of $I_{\text{mod}}^{\text{max}}$ for larger magnetic field strengths ($\mu_0 H > 40$ mT). The minimum modulator current $I_{\text{mod}}^{\text{min}}$ is plotted as a function of $\mu_0 H$ in Fig. 4.9 (c). It also increases with increasing magnetic field values, however, we obtain $I_{\text{mod}}^{\text{min}}$ values being larger than those of $I_{\text{mod}}^{\text{max}}$ over the whole magnetic field range. Similar results have been found for the critical threshold currents in Ref. [45]. Comparing our results to the theory model considering higher order terms ($R_{\text{inj-det}}^j(I_{\text{mod}}^{\text{dc}}) \neq 0$ for $j \geq 2$), we can use equations (4.42) and (4.47) and obtain the ratio $V_{\text{ac}}^{1\omega}/V_{\text{dc}}^{\text{SHE}} = (R_{\text{inj-det}}^1 I_{\text{inj}} + \frac{3}{4} R_{\text{inj-det}}^3 (I_{\text{inj}})^3) / (R_{\text{inj-det}}^1 I_{\text{inj}} + R_{\text{inj-det}}^3 (I_{\text{inj}})^3)$. Assuming finite transport coefficients $R_{\text{inj-det}}^1, R_{\text{inj-det}}^3 \neq 0$, we obtain a ratio smaller than 1 if $R_{\text{inj-det}}^1$ and $R_{\text{inj-det}}^3$ have the same sign, while the ratio is larger than 1 if the two transport coefficients have opposite signs. As already stated, we can only speculate on the physical origin of the observation. Considering the magnon dispersion relation, one possible explanation might be the excitation of additional damping compensated magnon modes with increasing modulator current $I_{\text{mod}}^{\text{dc}}$ leading to a complex behavior of the amplitudes and ratios. Note that we only take contributions up to the third order in I_{inj} into account, which probably indicate coupling effects between SHE and thermally excited magnons. If we assume such an additional third order contribution in I_{inj} , one would expect within our model to observe a signal in the third harmonic in the ac configuration. However, we could not detect any significant third harmonic signal. Utilizing equations (4.42) and (4.47) again, we can calculate the difference of the two voltages to $V_{\text{dc}}^{\text{SHE}} - V_{\text{ac}}^{1\omega} = 1/4 R_{\text{inj-det}}^3 (I_{\text{inj}})^3$. From the difference between the voltage amplitudes $A_{\text{dc}}^{\text{SHE}}$ and $A_{\text{ac}}^{1\omega}$ we can now estimate a third harmonic signal of the order of several 10 nV, which is unfortunately lower than the noise floor in our lock-in measurements. Thus, improvements in the signal-to-noise ratio is needed, which may allow us the detection of this higher order contribution. Recently, a comprehensive study investigated the nonlinear transport properties of magnons in extended YIG films using two-terminal Pt devices [197, 198]. The authors distinguished between high-energy magnons with a characteristic decay length in the sub-micrometer range and low-energy magnons with a characteristic decay length in the micrometer range. Varying the charge current applied to the injector, they could identify different transport regimes for the low-energy magnons. While for low injector currents, the spin current is a linear function of the electrical current, the spin transport is highly correlated for larger currents on the order of the damping compensation threshold, which is marked by a saturation of the magnon transconductance. For even larger injector currents, where the temperature below the injector approaches the Curie temperature of YIG, it has been found that

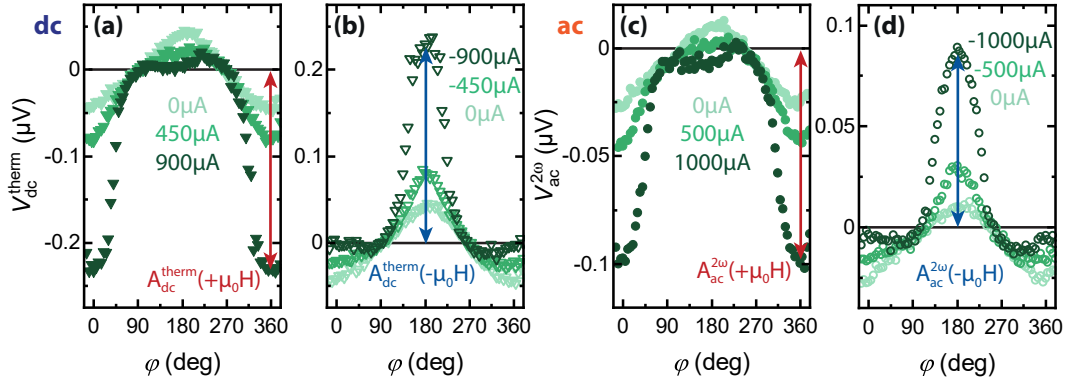


Fig. 4.10 – (a), (b) Detector signals of thermally generated magnons V_{dc}^{therm} and (c), (d) $V_{ac}^{2\omega}$ of D500 plotted versus the magnetic field orientation with $\mu_0 H = 50$ mT for various modulator currents $I_{\text{mod}}^{\text{dc}}$. (a), (c) For $I_{\text{mod}}^{\text{dc}} > 0$, the thermally generated magnon spin signal is increased at $\varphi = 0^\circ, 360^\circ$, while it is decreased at $\varphi = 180^\circ$. (b), (d) For $I_{\text{mod}}^{\text{dc}} < 0$, we observe a 180° shifted behavior. While the angle dependence of V_{dc}^{therm} and $V_{ac}^{2\omega}$ are in good agreement, their absolute amplitude values strongly differ.

the scattering with high-energy magnons dominates and a diffusive transport is observed [197, 198].

4.2.4 Thermally Generated Magnon Spin Signal

We now discuss the magnon transport due to thermally generated magnons. Note that the data is only available for device D500. We start with the angle-dependent data obtained from the detector signals V_{dc}^{therm} and $V_{ac}^{2\omega}$. In Fig. 4.10(a) and (b), we plot the angle-dependent thermal voltage signals for the dc-detection technique and in panel (c) and (d) for the ac-readout technique for the same positive and negative modulator currents $I_{\text{mod}}^{\text{dc}}$, respectively, as for the SHE induced magnons in Fig. 4.6. For $I_{\text{mod}}^{\text{dc}} = 0$ (light green data points), the voltage signals for the thermally generated magnons show the characteristic $\cos \varphi$ modulation in accordance with previous work [43]. It results from the angle dependence of the spin injection/detection at the injector/detector electrode. For $I_{\text{mod}}^{\text{dc}} > 0$ (cf. Fig. 4.10(a) and (c)), we find an increase of the detector signals V_{dc}^{therm} and $V_{ac}^{2\omega}$ at $\varphi = 0^\circ, 360^\circ$ and a decrease at $\varphi = 180^\circ$ as already reported by Wimmer *et al.* in Ref. [45]. This difference is significantly increased for the highest modulator currents $I_{\text{mod}}^{\text{dc}} = 900 \mu\text{A}$ and $1000 \mu\text{A}$. It is important to mention, while an applied dc charge current in the range between $0 \mu\text{A}$ and about up to $200 \mu\text{A}$ only lead to a temperature increase at the electrode of a few Kelvin, our highest applied dc charge currents result in a temperature increase of about 100 K. Note that is only a rough estimation according to local thermometry measurements for a comparable device geometry [45]. In

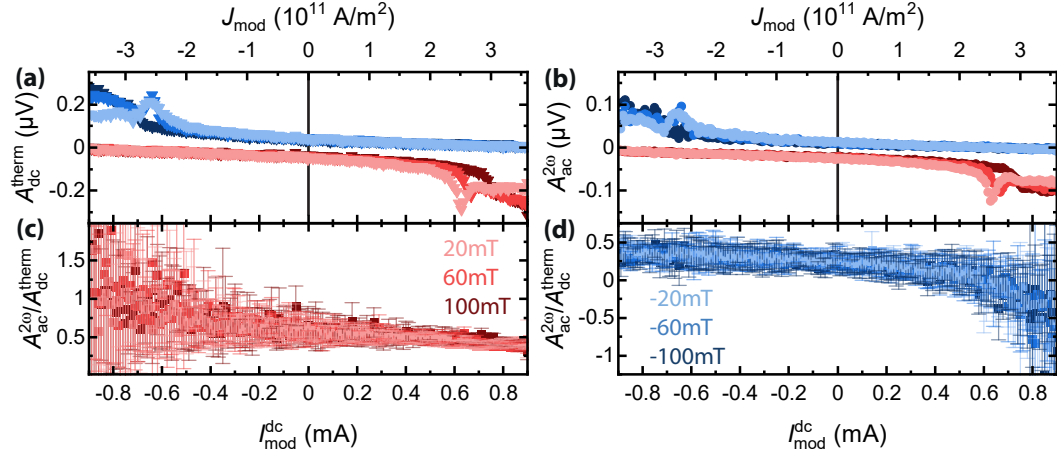


Fig. 4.11 – Extracted amplitudes (a) $A_{dc}^{\text{therm}}(\pm\mu_0H)$ and (b) $A_{dc}^{\text{therm}}(\pm\mu_0H)$ of the thermally generated magnon spin transport signal of device D500 (as indicated in Fig. 4.10) each plotted for different external magnetic field magnitudes versus the dc charge current $I_{\text{mod}}^{\text{dc}}$. (c), (d) Ratio $A_{ac}^{2\omega}/A_{dc}^{\text{therm}}$ of the extracted amplitudes for the dc and ac configuration for (c) positive and (d) negative field values μ_0H . In both cases the ratio exhibits a nearly constant behavior over the whole modulator current range at a value close to 0.5 within the experimental error.

Ref. [45], they measured a temperature increase of 90 K for a maximum modulator current of $800\mu\text{A}$ and a Pt modulator with a width of 500 nm and a thickness of 3.5 nm, which is slightly thinner compared to our case. Performing similar measurements on another YIG/Pt device suggest an increase of the temperature that is larger than twice the measured value for thinner modulator electrodes and thus larger modulator current densities, as detailed in Sec. 4.4.4. We can attribute this enhancement and reduction of the signal to the same mechanisms as in the case for the SHE induced magnons (V_{dc}^{SHE} and $V_{ac}^{1\omega}$). At $\varphi = 0^\circ, 360^\circ$, the magnon conductance is increased due to SHE and thermally injected magnons, while at $\varphi = 180^\circ$ the magnon depletion due to the SHE is counterbalanced by thermal magnons and thus only a small decrease of the signal is observed. For the same reasons, we observe a 180° shifted behavior for negative modulator currents $I_{\text{mod}}^{\text{dc}} < 0$, where the thermally generated magnons V_{dc}^{therm} (Fig. 4.10(b)) and $V_{ac}^{2\omega}$ (Fig. 4.10(d)) are increased at $\varphi = 180^\circ$ and decreased at $\varphi = 0^\circ, 360^\circ$. Comparing the dc- and ac-measurement techniques, we find a similar angle dependence of the detector signal, however with a strongly different absolute magnitude. This difference is in agreement with our detector voltage model (Eqs. (4.43) and (4.48)), as discussed below.

For the quantitative comparison, we extract the amplitudes $A_{dc}^{\text{therm}}(\pm\mu_0H)$ and $A_{ac}^{2\omega}(\pm\mu_0H)$ of the thermally generated magnons as indicated by arrows in Fig. 4.10 and plot them as a function of the modulator current for the same magnetic field

magnitudes $\mu_0 H$ as in the case for the SHE induced magnons $A_{\text{dc}}^{\text{SHE}}$ and $A_{\text{ac}}^{1\omega}$. The extracted amplitudes are shown in Fig. 4.11(a) and (b) for the dc and ac configuration. The qualitative dependence of the signal amplitude on $I_{\text{mod}}^{\text{dc}}$ is identical for $A_{\text{dc}}^{\text{therm}}$ and $A_{\text{ac}}^{2\omega}$ for all magnetic field magnitudes and current ranges. In agreement with previous reports [45], the curves exhibit a significant kink above a certain critical current value. To account for the differences in the absolute amplitude values, we show the calculated ratios $A_{\text{ac}}^{2\omega}/A_{\text{dc}}^{\text{therm}}$ for positive magnetic field values in Fig. 4.11(c) and for $\mu_0 H < 0$ in Fig. 4.11(d). In both cases, the ratio $A_{\text{ac}}^{2\omega}/A_{\text{dc}}^{\text{therm}}$ is nearly constant over the whole modulator current range and exhibits a value of 0.5 within the experimental error for all measured magnetic field magnitudes. The small deviations, most notably in the negative current regime for $\mu_0 H > 0$ (Fig. 4.11(c)) and in the positive current regime for $\mu_0 H < 0$ (Fig. 4.11(d)), can be attributed to the low thermal signal amplitude in our devices, which cause a worse signal-to-noise ratio. Furthermore, differences in the thermal landscape due to a difference in the average applied heating power for the dc and ac configuration may also lead to a deviation. While the ratios $A_{\text{ac}}^{1\omega}/A_{\text{dc}}^{\text{SHE}}$ of SHE induced magnons show a dependence on the magnetic field magnitude, we do not find any magnetic field dependence for $A_{\text{ac}}^{2\omega}/A_{\text{dc}}^{\text{therm}}$. We can explain this by comparing our results to our detector voltage model. Utilizing Eqs. (4.43) and (4.48), we obtain a constant ratio, which yields $A_{\text{ac}}^{2\omega}/A_{\text{dc}}^{\text{therm}} = 0.5$ if only transport coefficients up to the fifth order ($j \leq 5$) contribute. This nicely agrees with our results. However, the quantitative comparison of the thermal signal is not suitable to detect higher order contributions, as deviations originating from transport coefficients higher than the fifth order, are unfortunately lower than the signal-to-noise ratio in our measurement setups.

4.3 Reduced Effective Magnetization

While we observe clear differences between the SHE-induced magnon transport signals for the dc- and ac-detection technique above a certain modulator current, this critical current value does not sensitively depend on the measurement technique. However, other parameters might impact the magnon conductivity underneath the modulator in YIG or FMIs in general. According to the current understanding, this threshold effect, when the injected magnons below the modulator can counteract the magnetization damping, scales with the saturation magnetization and the magnetic anisotropy of the material (cf. Sec. 4.1.1) [45, 196]. In this section, we explore the impact of these parameters and investigate the magnon transport in FMIs with significant perpendicular magnetic anisotropy fields H_k and reduced saturation magnetization M_s .

In general, YIG thin films grown on the lattice matched substrate GGG exhibit a finite in-plane effective magnetization $M_{\text{eff}} = M_s - H_k > 0$, which results in an elliptical magnetization precession trajectory with the long axis aligned in the film plane, as schematically sketched in Fig. 4.12(a). The finite M_{eff} gives rise to nonlinear damping effects via parametric pumping of higher frequency modes [201]. Recently, it has been reported that the ellipticity of the magnetization precession can be minimized,

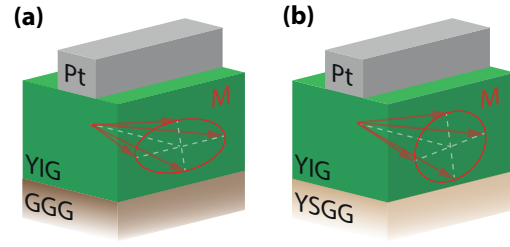


Fig. 4.12 – (a) Sketch of the elliptical magnetization precession in YIG thin films grown on lattice-matched GGG. (b) Minimized ellipticity in biaxially strained YIG thin films grown on YSGG due to the reduced effective magnetization.

suppressing nonlinear damping and thereby achieving spin-orbit torque induced coherent magnetization auto-oscillations even in extended magnetic films [202, 203]. In these experiments, the samples exhibit a large perpendicular anisotropy (PMA) leading to a compensation of the in-plane shape anisotropy and thereby approaching $M_{\text{eff}} = 0$. For our experiments, we also reduce the ellipticity of the magnetization precession by reducing the effective magnetization of YIG. When our samples achieve a compensation of the anisotropy or $M_{\text{eff}} = 0$, respectively, we expect a circular magnetization precession, as sketched in Fig. 4.12(b). Hence, a suppression of nonlinear damping effects is expected leading to an enhanced magnon-based spin conductivity. Our experimental approach utilizes a biaxially strained YIG thin film grown on yttrium scandium gallium garnet (YSGG) approaching strongly reduced effective magnetization. In the following, we investigate the magnetic properties of the strained YIG films and show that they exhibit low Gilbert damping comparable to YIG thin films grown on lattice-matched GGG. Moreover, we investigate the magnon transport in two- and three-terminal devices. Utilizing latter, we find a linear dependence of the critical current on the applied magnetic field. This allows us to corroborate the expected scaling with the effective magnetization of the FMI.

Main parts of this section, figures and text, have been published in J. Gückelhorn, T. Wimmer, M. Müller, S. Geprägs, H. Huebl, R. Gross, and M. Althammer, *Magnon transport in $Y_3Fe_5O_{12}/Pt$ nanostructures with reduced effective magnetization*, *Physical Review B* **104**, L180410 (2021).

4.3.1 Film Characterization

To be able to control M_{eff} in our experiments, we pseudomorphically grow a 12.3 nm thick YIG film onto a YSGG substrate by PLD (cf. Sec. 3.2). The lattice mismatch of

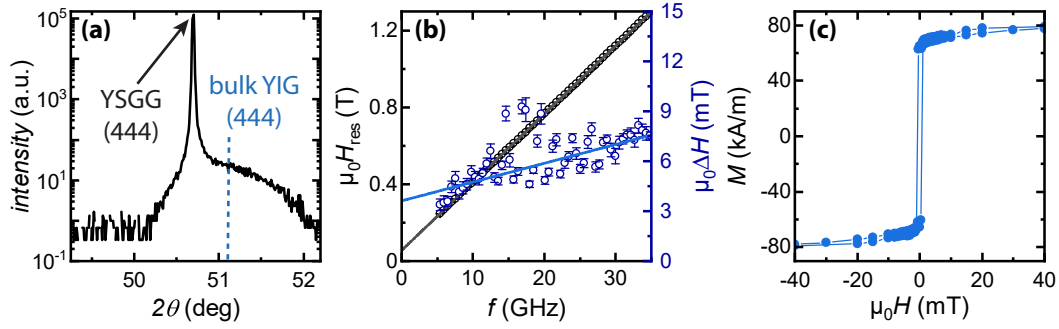


Fig. 4.13 – (a) X-ray diffraction of a 12.3 nm thick YIG film grown on a (111)-oriented YSGG substrate. The blue vertical line marks the calculated 2θ -position of the (444) reflection of bulk YIG. (b) Resonance field H_{res} and linewidth ΔH as a function of frequency extracted from FMR measurements of the 12.3 nm thick YIG film grown on YSGG. (c) In-plane SQUID magnetometry measurements of a 9 nm thick YIG film grown on (111)-oriented YSGG at 300 K. A saturation magnetization $M_s = 80$ kA/m is observed.

0.4 % between YIG and YSGG induces a biaxial in-plane tensile strain in the YIG thin film. Thus, strain-induced magnetoelastic coupling [204] results in large H_k [205]. To confirm this in-plane lattice strain, we perform x-ray diffraction measurements on the thin film. Figure 4.13(a) shows the $2\theta - \omega$ scan with the substrate (444) diffraction peak clearly visible at $2\theta = 50.7^\circ$. The corresponding film peak appears as a broad shoulder in the diffraction pattern and is shifted to larger 2θ values due to the in-plane tensile strain. To emphasize the shift we marked $2\theta = 51.07^\circ$ the calculated position of the (444) reflection of bulk YIG using $\lambda = 1.5406 \text{ \AA}$ and $a = 12.38 \text{ \AA}$ (cf. Sec. 3.1). The large width and low intensity of the film peak originates from the small film thickness. Note that the width of the reflection peak in a $2\theta - \omega$ scan is only infinitely narrow, if the crystal is infinitely large. For thin films, however, we are dominated by a finite coherence length, i.e. the number of crystal planes contributing to the coherent scattering is reduced due to the finite thickness. As the coherence length is reduced, the full width half maximum of the thin film reflection in 2θ scales inversely with the thin film thickness. The broadening, the low intensity and the overlap with the substrate peak make it challenging to conduct more advanced experiments, which would provide more precise results. For instance, an omega rocking curve is rather difficult to measure and interpret due to the problem of unambiguously separating substrate and thin film contributions.

We magnetically characterize the strained YIG film utilizing broadband ferromagnetic resonance (FMR). Therefore, the thin film is placed face down on a coplanar waveguide and the complex transmission parameter S_{21} is measured as a function of the microwave frequency and the magnetic bias field applied in the out-of-plane direction using a vector network analyzer (VNA). From this data, we extract the

resonance field $\mu_0 H_{\text{res}}$ (black data points) and the linewidth $\mu_0 \Delta H$ (blue data points) and plot them against the frequency in Fig. 4.13(b). We determine the effective magnetization $\mu_0 M_{\text{eff}} = (56.0 \pm 0.2) \text{ mT}$ by linear fitting with the Kittel equation $f = \gamma \mu_0 / (2\pi) (H_{\text{res}} - M_{\text{eff}})$. This value is significantly decreased compared to unstrained YIG films of similar thickness, which exhibit an about three times larger effective magnetization value [45]. FMR also allows us to determine the Gilbert damping parameter α_G [206]. By fitting the FMR linewidth ΔH to $\mu_0 \Delta H = \mu_0 \delta H + 4\pi f \alpha_G / \gamma$ (blue line in Fig. 4.13(b)), we obtain the inhomogeneous linewidth $\mu_0 \delta H = (3.6 \pm 0.4) \text{ mT}$ and $\alpha_G = 1.5 \pm 0.2 \times 10^{-3}$. Similar values for α_G were extracted from FMR measurements for epitaxial high-quality YIG thin films grown on lattice-matched GGG substrates under the same conditions [45].

Finally, we perform SQUID (superconducting quantum interference device) magnetometry measurements to obtain the saturation magnetization M_s , which enters the calculation of the critical current dependence as a fixed parameter (see Sec. 4.1.1). For these measurements, we used a second sample, a 9 nm thick YIG film grown on a YSGG substrate under the same conditions as the 12.3 nm thick biaxial strained YIG film investigated in detail in this Section. In Fig. 4.13(c) the obtained magnetization M is shown as a function of the in-plane magnetic field for a temperature of 300 K. We find a saturation magnetization of $M_s = 80 \text{ kA/m}$, which is smaller compared to the value of $M_s = 111 \text{ kA/m}$ observed for YIG thin films grown on lattice-matched GGG under the same conditions [45]. Similar values for thin YIG films grown on YSGG varying from $M_s \approx 85 \text{ kA/m}$ to 136 kA/m were found in Ref. [205]. Recent theoretical studies indicate that PMA can be achieved in YIG films with the proper tensile in-plane biaxial strain [207].

4.3.2 Magnon Transport in Two-terminal Devices

After the film characterization, we deposited 5 nm thick Pt strips on top of the strained YIG film according to the fabrication process described in Sec. 3.2 to allow for an all-electrical generation and detection of pure spin currents and investigation of the magnon transport. First, we investigate the magnon transport using two-strip structures as depicted in Fig. 4.14(a). While the injector strip has a length of $l_{\text{inj}} = 50 \mu\text{m}$ and a width of $w_{\text{inj}} = 500 \text{ nm}$, the detector has a length of either $l_{\text{det}} = 50 \mu\text{m}$ or $64 \mu\text{m}$ and its width w_{det} varies. Furthermore, the center-to-center distance d_c between injector and detector varies. In our experiments, we apply a dc charge current $I_{\text{inj}} = 100 \mu\text{A}$ to the injector electrode, while we use the dc-detection technique to record the voltage signal V_{det} at the detector (cf. Fig. 4.14(a)).

For the characterization of the magnon transport, the voltage signal $V_{\text{det}}^{\text{SHE}}$ is measured as a function of the magnetic field orientation φ for a fixed magnetic field

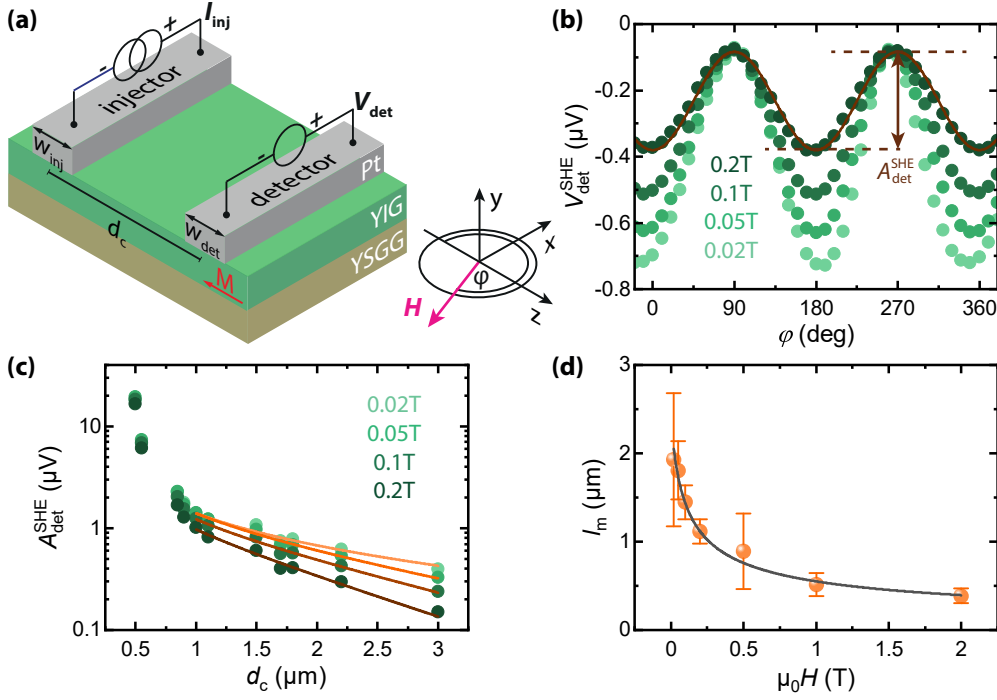


Fig. 4.14 – (a) Sketch of the sample configuration of a two-terminal device with the electrical connection scheme, and the coordinate system with the in-plane rotation angle φ of the applied magnetic field \mathbf{H} . (b) Detector signal V_{det}^{SHE} as a function of the magnetic field orientation φ for different magnetic field strengths $\mu_0 H$. The brown line is a fit to $A_{det}^{SHE} \cos^2(\varphi)$. (c) Voltage amplitude A_{det}^{SHE} , as indicated in (b), plotted versus the injector-detector distance d_c on a logarithmic scale for the same magnetic field magnitudes as in (b). (d) Extracted magnon spin relaxation length l_m from the exponential fits in (c) as a function of $\mu_0 H$. A fit to Eq. (4.50) (gray line) results in a magnon diffusion constant $D = (1.75 \pm 0.05) \times 10^{-4} \text{ m}^2/\text{s}$.

magnitude $\mu_0 H = 50 \text{ mT}$ at a temperature $T = 280 \text{ K}$. The results for a structure with $w_{det} = 500 \text{ nm}$, $l_{det} = 50 \mu\text{m}$ and $d_c = 2.2 \mu\text{m}$ are shown in Fig. 4.14(b). As for YIG films grown on GGG, we observe the characteristic $\cos^2(\varphi)$ angular dependence, which we expect for SHE-induced magnons transported from injector to detector [43, 120]. Therefore, the voltage signal as a function of the angle φ can be fitted with a simple $A_{det}^{SHE} \cos^2(\varphi)$ function as exemplary indicated for $\mu_0 H = 200 \text{ mT}$. The quantity A_{det}^{SHE} , which corresponds to the amplitude of the SHE-generated magnon transport signal, is extracted for several structures and plotted as a function of d_c for different $\mu_0 H$ in Fig. 4.14(c). Overall, we observe a decreasing amplitude signal A_{det}^{SHE} with increasing distance d_c . This expected behavior for magnon transport can be divided into two different distance regimes: for distances shorter than the magnon relaxation length l_m , the signal A_{det}^{SHE} follows a $1/d_c$ dependence, while it exhibits an exponential decay for larger distances, when the magnon relaxation dominates [43, 141]. An exponential fit to the second

regime, allows us to extract the magnon relaxation length. Here, we use a fit of the form $A_{\text{det},0}^{\text{SHE}} e^{-d_c/l_m}$ with $A_{\text{det},0}^{\text{SHE}}$ the amplitude at zero distance for $d_c \geq 1 \mu\text{m}$ (orange lines in Fig. 4.14(c)). In Fig. 4.14(d) the extracted l_m values are plotted versus the magnetic field magnitude $\mu_0 H$. The l_m values are on the order of $1 \mu\text{m}$ and thus in good accordance with values found for YIG thin films grown on lattice-matched GGG [45]. However, the magnon relaxation length is not constant, but decreases with increasing magnetic field strength. We can explain the magnetic field dependence of l_m by recapping the physics leading to it. Therefore, we have to consider the magnon relaxation rate $\Gamma_{\text{mr}}^{\text{ip}}$ for an in-plane magnetized film (cf. Sec. 4.1.1). Taking damping contributions from inhomogeneous broadening δH into account, we see that the damping rate $\Gamma_{\text{mr}}^{\text{ip}}$ in Eq. (4.7) diverges for a finite positive M_{eff} at $\mu_0 H = 0$. However, in the limit of $M_{\text{eff}} = 0$, Eq. (4.7) reduces to

$$\Gamma_{\text{mr}}^{\text{ip}} = \gamma \mu_0 \left(\alpha_G H + \frac{\delta H}{2} \right). \quad (4.49)$$

In this case, the relaxation rate is constant for $\mu_0 H = 0$ and we expect a strictly linear dependence on the magnetic field magnitude. Together with $l_m = \sqrt{D\tau_m}$, where D corresponds to the magnon diffusion constant and the magnon lifetime τ_m can be calculated via $\tau_m = 1/\Gamma_{\text{mr}}^{\text{ip}}$, we can describe the magnetic field dependence of l_m according to

$$l_m = \sqrt{\frac{D}{\gamma \mu_0 \left(\alpha_G H + \frac{\delta H}{2} \right)}}. \quad (4.50)$$

Utilizing the values obtained from the FMR measurements, we can fit our data extracted from the two-terminal transport measurements in Fig. 4.14(d) with Eq. (4.50) obtaining a good agreement between theory and experiment. The only free fit parameter is the magnon diffusion constant D . Neglecting the field dependence of D , we obtain $D = (1.75 \pm 0.05) \times 10^{-4} \text{ m}^2/\text{s}$, which is in accordance with the values found for YIG films on GGG [76]. This supports the quantitative understanding of the phenomenon.

4.3.3 Manipulation of the Magnon Transport

In a next step, we manipulate the magnon transport between injector and detector. To this end, we turn to three-terminal devices with a center Pt strip acting as the modulator as schematically sketched in Fig. 4.15(a). In this configuration, the injector as well as the detector have a length of $l_{\text{inj}} = l_{\text{det}} = 50 \mu\text{m}$ and a width of $w_{\text{inj}} = w_{\text{det}} = 500 \text{ nm}$. The modulator has a length of $l_{\text{mod}} = 64 \mu\text{m}$, while its width w_{mod} and the edge-to-edge distance d_e between strips varies. For the three-

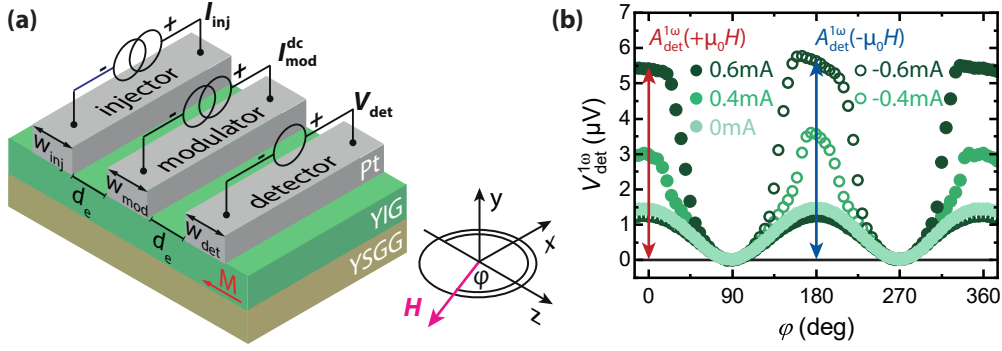


Fig. 4.15 – (a) Sketch of the sample configuration for a three-terminal device with the electrical connection scheme, and the coordinate system with the in-plane rotation angle φ of the applied magnetic field \mathbf{H} . (b) Detector voltage $V_{\text{det}}^{1\omega}$ plotted versus the magnetic field orientation φ for various modulator currents $I_{\text{mod}}^{\text{dc}}$ at a fixed magnetic field magnitude $\mu_0 H = 50$ mT. The voltage amplitude $A_{\text{det}}^{1\omega}$ is extracted from the angle dependence of the detector signals as indicated by the arrows.

strip experiments, we utilize the ac-readout technique and apply a low-frequency charge current with an amplitude of $I_{\text{inj}} = 200 \mu\text{A}$ to the injector. While a constant dc current is fed through the modulator, we record the first harmonic signal $V_{\text{det}}^{1\omega}$ steaming from SHE-induced magnon transport via lock-in detection.

We perform angle-dependent measurements and measure the voltage signal $V_{\text{det}}^{1\omega}$ as a function of the magnetic field orientation φ (cf. Fig. 4.15(a)) for various magnetic field magnitudes and modulator currents $I_{\text{mod}}^{\text{dc}}$ for different structures. In Fig. 4.15(b), we plot typical results for a device with $d_e = 200$ nm and $w_{\text{mod}} = 400$ nm for a magnetic field strength $\mu_0 H = 50$ mT. For $I_{\text{mod}}^{\text{dc}} = 0$ (light green data points), we find the expected $\cos^2(\varphi)$ dependence, which we have already observed in our two-terminal measurements. As reported in Refs. [44, 45] and observed in Sec. 4.2, $V_{\text{det}}^{1\omega}$ is significantly increased at $\varphi = 0^\circ, 360^\circ$ for $I_{\text{mod}}^{\text{dc}} > 0$. Due to the applied dc charge current at the modulator, a SHE-induced magnon chemical potential builds up and magnons are generated thermally due to Joule heating leading to a magnon accumulation underneath the modulator. The latter enhances the magnon conductivity, resulting in a larger voltage signal $V_{\text{det}}^{1\omega}$ ³³. At $\varphi = 180^\circ$, the magnon transport is slightly decreased, as the SHE-induced magnon depletion is nearly compensated by the thermally generated magnons. For $I_{\text{mod}}^{\text{dc}} < 0$, we observe the 180° shifted angle dependence, i.e. the voltage signal $V_{\text{det}}^{1\omega}$ is increased at $\varphi = 180^\circ$ and reduced at $\varphi = 0^\circ, 360^\circ$. At the modulator we have to account for both SHE and Joule heating contribution consistent with the assumption in previous

³³As demonstrated in Sec. 4.2 the used measurement techniques are essential to distinguish between the magnons generated by the modulator and the injector. This means, any change in the first harmonic signal $V_{\text{det}}^{1\omega}$ reflects a change in the magnon conductivity.

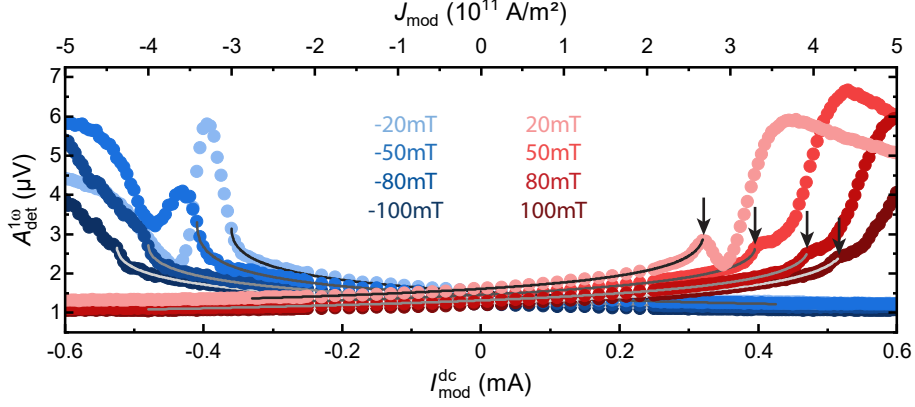


Fig. 4.16 – Voltage amplitude $A_{\text{det}}^{1\omega}$, as indicated in Fig. 4.15, plotted as a function of the modulator current $I_{\text{mod}}^{\text{dc}}$ for different magnetic field magnitudes $\mu_0 H$. The gray lines are fits to Eq. (4.39) for modulator current values below the threshold current ($I_{\text{mod}}^{\text{dc}} < I_{\text{mod}}^{\text{crit}}$).

reports [44, 45, 208]. However, the shape of the peaks changes with increasing modulator current ($|I_{\text{mod}}^{\text{dc}}| > 0$). While we observe a clear $\cos^2(\varphi)$ dependence for $I_{\text{mod}}^{\text{dc}} = 0$, the peak maximum gets rather broad for $I_{\text{mod}}^{\text{dc}} = \pm 0.6$ mA.

Before we discuss possible origins, we perform a more quantitative analysis. To this end, we extract the signal amplitudes $A_{\text{det}}^{1\omega}(+\mu_0 H)$ at $\varphi = 0^\circ$ or 360° , respectively, and $A_{\text{det}}^{1\omega}(-\mu_0 H)$ at $\varphi = 180^\circ$ (cf. Fig. 4.15(b)) and plot them as a function of the modulator current $I_{\text{mod}}^{\text{dc}}$ for different magnetic field strengths $\mu_0 H$ in Fig. 4.16. In the low bias regime for $|I_{\text{mod}}^{\text{dc}}| < 0.25$ mA, we find the expected superposition of a linear and quadratic $I_{\text{mod}}^{\text{dc}}$ dependence corresponding to the SHE-induced and thermally generated magnons [44, 45, 208]. For larger currents $|I_{\text{mod}}^{\text{dc}}| > 0.25$ mA, we observe a clear deviation from this behavior accompanied with a strong increase in the signal amplitude $A_{\text{det}}^{1\omega}$. Analogous to previous reports [45, 208], we can attribute this nonlinear behavior to the presence of a zero effective damping state generated below the modulator via the SHE-mediated spin-orbit torque as derived in Sec. 4.1.1. Thus, the effective magnon conductivity is enhanced, leading to a strong increase of the voltage signal, while the magnon injection rate remains unchanged. Here, we observe a maximum enhancement of $A_{\text{det}}^{1\omega}$ by a factor of 6, which corresponds to a twofold increase compared to previous experiments [45, 208]. We attribute this strong increase to the reduction in M_{eff} (due to the significant perpendicular magnetic anisotropy fields H_k induced via the strain as well as the reduced saturation magnetization M_s) and the associated more circular magnetization precession. Furthermore, we find a rich peak structure in the nonlinear regime $|I_{\text{mod}}^{\text{dc}}| > 0.25$ mA. We observed first onsets of such a peak structure in the previous Sec. 4.2 on unstrained YIG thin films grown on GGG [208]. Different aspects may lead to this voltage amplitude structure. On the one hand, the theoretical work

by Takei [187] predicts that above the threshold value fluctuations of the magnon conductivity occur, which also influence the stability of the magnon conductivity in our three-strip structures. Micromagnetic simulations using the *MuMax3* code [209] for similar device geometries corroborate these predictions showing a strong chaotic behavior, i.e. spin wave bullets form at the threshold current value and their density increases with increasing current [68, 210]. On the other hand, in experiments with metallic CoNi [203] a reduced magnon density was observed and attributed to nonlinear magnon damping as the effective magnetization was small but still finite. For our device, such nonlinear damping processes due to the finite M_{eff} or instabilities in the magnon conductivity due to fluctuations or contributions from both effects may lead to the found peak structure. Furthermore, we show in Sec. 4.4 that large dc currents applied to the modulator electrode, as in this case, have a significant influence on the magnon transport and in particular on the critical current regime. However, more investigations are needed to unambiguously determine the physical origin of these peaks. Additionally to the rich peak structure, we find a distinct asymmetry in the amplitude signal $A_{\text{det}}^{1\omega}$ for positive and negative field polarity. This observation differs from the results obtained for YIG thin films on lattice-matched GGG substrates [45, 208]. Up to now, we can only speculate on the detailed origin of this asymmetry, however it may be related to one or a combination of the following discussed aspects. As the measurements were conducted in setup (i), it is possible that the magnetic field is slightly misaligned due to trapped flux from the 3D-vector magnet, which can reach a few mT. This might impact the amplitudes, in particular measurements that were conducted at low magnetic field magnitudes, where we observe the most pronounced asymmetry. Another aspect that should be taken into account, is the exposure of the modulator to large currents, which is accompanied by high temperatures reaching temperature increases of about 100 K at the electrode [45]. Since the current exposure is typically a few hours long this results in a local Joule heating or thermal annealing, respectively. The annealing process in turn could lead to a change in different device parameters, for example the spin mixing conductance or the spin transfer efficiency. The thermal annealing is also the reason why a hysteresis or rather multiple hysteresis for different fixed modulator currents are rather difficult to perform, while we potentially modify device parameters. We will discuss this effect and the resulting changes in the parameters in detail in Section 4.4. Lastly, effects related to the crystalline-orientation of YIG, such as a change in the magnetic anisotropy may have an impact. While the previously investigated YIG film were (001)-oriented [45, 208], we here have utilized a (111) orientation, which allows us to make use of the crystalline magnetic anisotropy. To the best of our knowledge, a comparison of different crystalline orientations of YIG has not been pursued so far. Therefore, we start to investigate effects stemming

from different crystalline orientations in Section 6.2. The two latter aspects may also cause the differences in the peak structure of the angle-dependent measurements shown in Fig. 4.15(b).

The gray lines in Fig. 4.16 are fits to the phenomenological model introduced in Sec. 4.1.3 based on the theory by Takei [187]. Using Eq. (4.39), we can model the dependence of $A_{\text{det}}^{1\omega}$ caused by the SHE and thermal injection of magnons. Since the model is only valid up to the threshold/critical current value $I_{\text{mod}}^{\text{dc}} = I_{\text{mod}}^{\text{crit}}$, we restrict our fitting procedure to this region. The parameters $\Delta V'$, ΔV_{mod}^0 , $\Delta R'_{\text{th}}$ and $I_{\text{mod}}^{\text{crit}}$ are used as fit parameters. The fits for the different magnetic field strengths reproduce the measured data well. Although this model does not account for the amplitude asymmetry for opposite field polarities, it is well suited to extract the critical current $I_{\text{mod}}^{\text{crit}}$.

In general, in YIG/Pt heterostructures non-equilibrium magnons are injected into the YIG and Cornelissen *et al.* [76] have shown that the electrically driven magnon spin transport is best described by a non-equilibrium magnon chemical potential. To quantify this in our YIG films with reduced M_{eff} , we estimate the spin chemical potential μ_s , which depends on the modulator current and is given by $\mu_s = [e\theta_{\text{SH}}I_{\text{mod}}^{\text{dc}} \tanh(\eta)]/[w_{\text{mod}}\sigma_{\text{Pt}}\eta]$. For the threshold current $I_{\text{mod}}^{\text{crit}}$ extracted at $\mu_0 H = 50$ mT, we added the calculated μ_s to Tab. 4.3. Similar values have been found in Ref. [45] for unstrained YIG films grown on GGG.

4.3.4 Critical Current Regime

To quantitatively compare the strained YIG films with reduced M_{eff} to the conventional YIG thin films grown on GGG, we rely on the magnetic field dependence of $I_{\text{mod}}^{\text{crit}}$, which has been derived in Sec. 4.1.1. In Fig. 4.17(a), the extracted critical currents (indicated by arrows in Fig. 4.16) of the discussed structure (orange data points), called D400 in the following, are plotted as a function of $\mu_0 H$. In addition, we plot $I_{\text{mod}}^{\text{crit}}$ for an unstrained YIG thin film grown on GGG taken from Ref. [45] (black data points). In this case, $I_{\text{mod}}^{\text{crit}}$ shows a constant behavior up to $\mu_0 H \leq 50$ mT, while an increase is observed for $\mu_0 H > 50$ mT. This in contrast to our findings for YIG films with reduced effective magnetization, where we observe a linear increase of the threshold current $I_{\text{mod}}^{\text{crit}}$ with applied magnetic field for $\mu_0 H > 20$ mT. The magnetic field dependence of the critical current $I_{\text{mod}}^{\text{crit}}$ has been associated with damping compensation, which is achieved when $\Gamma_{\text{mr}}^{\text{ip}} = \Gamma_{\text{ST}}$ [45]. In this regime, the threshold current is given by Eq. (4.13). The theory model (dashed line) describes quantitatively well the magnetic field dependence of $I_{\text{mod}}^{\text{crit}}$ taken from Ref. [45]. The small deviation for $\mu_0 H \leq 20$ mT could be attributed to in-plane magnetocrystalline anisotropy fields [45]. However, the data of device D400 is not well represented.

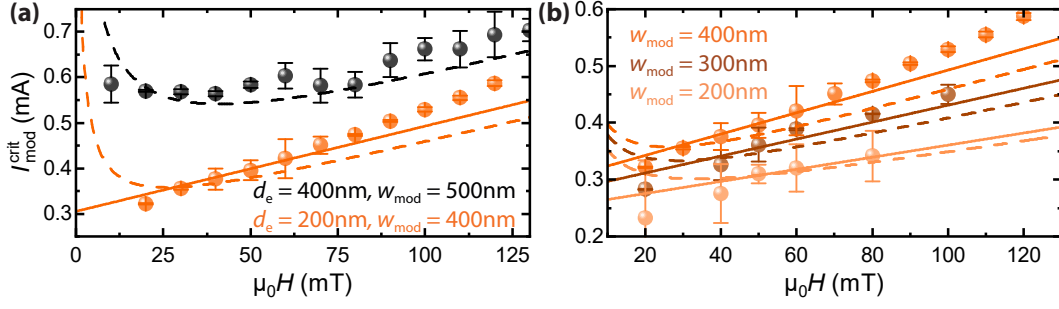


Fig. 4.17 – Extracted critical current $I_{\text{mod}}^{\text{crit}}$ as a function of the magnetic field strength $\mu_0 H$. **(a)** The orange data points (device D400) are extracted from Fig. 4.16 as indicated by the arrows. For comparison, the black data points are taken from Ref. [45], where YIG thin films grown on lattice-matched GGG substrates are investigated. **(b)** Additional data of devices D300 (brown) and D200 (light orange) on the same biaxially strained YIG film compared to device D400. The dashed lines correspond to fits to Eq. (4.13) with a finite M_{eff} , while solid lines are fits to Eq. (4.51) in the limit of $M_{\text{eff}} = 0$.

	Symbol	Value	Unit
Pt strip thickness	t_{Pt}	5	nm
Pt spin diffusion length [92]	l_s	1.5	nm
Pt spin Hall angle [92]	θ_{SH}	0.11	
YIG thickness	t_{YIG}	12.3	nm
gyromagnetic ratio	γ	1.76×10^{11}	rad/Ts
YIG saturation magnetization	M_s	80	kA/m
inhomogeneous broadening	$\mu_0 \delta H$	3.6	mT
Gilbert damping	α_G	1.5×10^{-3}	
YIG effective magnetization	$\mu_0 M_{\text{eff}}$	56	mT

Tab. 4.2 – Values for the parameters used for the fitting curves utilizing Eqs. (4.13) and (4.51) in Fig. 4.17.

While we find a good quantitative agreement for large magnetic field values, we observe a clear deviation for $\mu_0 H < 40$ mT. Similar behaviors can be observed for two more devices on the same YIG thin film with reduced M_{eff} grown on YSGG. The results for D300 with $w_{\text{mod}} = 300$ nm and D200 with $w_{\text{mod}} = 200$ nm are plotted in Fig. 4.17(b) together with the data of the investigated structure D400. While the modulator width of the three structures varies, the edge-to-edge distance of $d_e = 200$ nm is the same. In accordance with D400, the extracted $I_{\text{mod}}^{\text{crit}}$ of D300 and D200 exhibit a linear dependence on $\mu_0 H$ and the fit with Eq. (4.13) (dashed lines) cannot capture the behavior for $\mu_0 H \leq 40$ mT. The fixed film parameters and the device dependent parameters used for the fit procedure can be found in Tab. 4.2 and Tab. 4.3, respectively. The spin mixing conductance $g^{\uparrow\downarrow}$ remains the only free fit parameter and the resulting values are also summarized in Tab. 4.3. However, if we

Symbol	unit	D400	D300	D200
w_{mod}	nm	400	300	200
σ_{Pt}	$10^6 \text{ 1}/(\Omega \text{ m})$	2.15	2.22	2.26
$g^{\uparrow\downarrow}$	$10^{18} \text{ 1}/\text{m}^2$	(17 ± 2)	(11 ± 1)	(6.5 ± 0.2)
$g^{\uparrow\downarrow} (M_{\text{eff}} = 0)$	$10^{18} \text{ 1}/\text{m}^2$	(9.9 ± 0.4)	(7.6 ± 0.3)	(5.2 ± 0.1)
μ_{s}	meV	28.2	33.4	42.1

Tab. 4.3 – Device dependent parameters and experimentally determined interface spin mixing conductance $g^{\uparrow\downarrow}$ extracted from fits in Fig. 4.17 to Eq. (4.13) and Eq. (4.51) in the limit $M_{\text{eff}} = 0$ and the calculated spin chemical potential μ_{s} .

assume $M_{\text{eff}} \approx 0$ Eq. (4.13) reduces to

$$I_{\text{mod}}^{\text{crit}} = \frac{\hbar \sigma_{\text{Pt}}}{e} \frac{t_{\text{Pt}} w_{\text{mod}}}{2l_{\text{s}} \theta_{\text{SH}} \tanh(\eta)} \left(\mu_0 H \left[\gamma + 4\pi M_{\text{s}} t_{\text{YIG}} \frac{\alpha_{\text{G}}}{\hbar g_{\text{eff}}} \right] + 4\pi M_{\text{s}} t_{\text{YIG}} \frac{\mu_0 \frac{\delta H}{2}}{\hbar g_{\text{eff}}} \right), \quad (4.51)$$

lifting the divergence for $H = 0$ and corroborating our observed linear magnetic field dependence of $I_{\text{mod}}^{\text{crit}}$. Assuming $M_{\text{eff}} \approx 0$ (solid lines), describes our observed data in Fig 4.17(a) and (b) quantitatively well over the whole magnetic field range. Moreover, the observed linear dependence on $\mu_0 H$ is in accordance with the results by Evelt *et al.* [202], who studied Bismuth doped YIG thin films also epitaxially strained by a substituted GGG substrate, leading to a PMA, which compensates dipolar effects. Due to the resulting nearly vanishing M_{eff} , a circular magnetization precession is achieved. Furthermore, SOT induced damping compensation is achieved via a charge current applied to a Pt strip, resulting in an emission of coherent spin waves into the extended film. For $M_{\text{eff}} \approx 0$ as well as for a finite M_{eff} , we obtain spin mixing conductance values $g^{\uparrow\downarrow}$ (cf. Tab. 4.3) comparable to YIG/Pt structures on GGG [45]. Small deviations between data and fit still occur and are potentially caused by uncertainties in the fixed parameters, as for example α_{G} and M_{eff} , which have a considerable influence on the slope and intercept. Comparing both fits, the fit in the limit of $M_{\text{eff}} \approx 0$ represents the data better than the measured finite effective magnetization, which supports our assumption of a circular magnetization precession. The real value of M_{eff} , however, will probably be finite. Our results demonstrate that the threshold current clearly depends on the saturation magnetization M_{s} and the anisotropy fields H_{k} . However, to fully capture the field dependence of the critical current, a more sophisticated theoretical model is needed.

4.4 Impact of Large Modulator Current Exposure

In recent measurements, current densities as large as $1 \times 10^{12} \text{ A}/\text{m}^2$ are applied to the modulator electrode. In this section, we investigate the impact of large

Symbol	unit	A	B	C	D
w_{mod}	nm	150	150	250	450
d_e	nm	425	425	375	375
d_c	μm	1.5	1.5	1.5	1.7

Tab. 4.4 – Device parameters w_{mod} the modulator width, d_e the edge-to-edge distance between Pt strips and d_c the center-to-center distance between injector and detector for the four characterized devices A, B, C and D. While the modulator width varies (apart from A and B), we chose similar d_c values for a reasonable comparison of all devices.

modulator current densities on the magnon transport and the device performance in detail. Therefore, we subdivide the modulator current-dependent magnon transport into three regimes: (i) the low modulator current regime, where the magnon spin transport is sufficiently well described by a linear and quadratic modulation of the magnon conductivity (cf. Sec. 4.1.2), (ii) the critical modulator current regime, which comprises the area near and at the current-induced magnetic damping compensation, where the magnon transport is dominated by nonlinear magnon conductivity contributions due to SHE induced pumping (cf. Sec. 4.1.3) and (iii) the overcritical modulator current regime, where we observe a vanishing magnon spin signal as the temperature below the electrode approaches the Curie temperature due to Joule heating. We quantitatively study the evolution of the spin Hall magnetoresistance, the modulation efficiency in the low bias as well as critical current regime and the threshold currents as a function of successively increasing maximum modulator current exposure. This Section extensively reuses parts of text and figures published in T. Wimmer, J. Gückelhorn, M. Opel, S. Geprägs, R. Gross, H. Huebl, and M. Althammer, *Analysis of Critical Behavior and Electrical Annealing of Spin Current-Controlled Magnon Transistor Devices*, In preparation (2023).

For the experiments in this section, we use a $t_{\text{YIG}} = 13$ nm thick, single crystalline (001)-oriented YIG film grown on GGG. To investigate and modulate the magnon spin transport three-terminal nanostructures consisting of $t_{\text{Pt}} = 5$ nm thick Pt strips are patterned on top of the YIG film (cf. Fig. 4.4). Here, we consider four devices, which are indicated by the capital letters A, B, C and D in the following. While the injector and detector width $w_{\text{inj}} = w_{\text{det}} = 500$ nm is the same for all four devices, the modulator widths w_{mod} and distances d_e are summarized in Tab. 4.4. For the magnon transport modulation experiments, we exclusively utilize the ac-detection technique with a low frequency current $I_{\text{inj}}^{\text{ac}}(t) = I_{\text{inj}} \sin(\omega t)$ with a fixed amplitude $I_{\text{inj}} = 200 \mu\text{A}$ applied to the injector. Additionally, we apply a dc charge current $I_{\text{mod}}^{\text{dc}}$ to the modulator and thus tune the magnon conductivity by the additional dc spin injection within the transport path between injector and detector. All measurements

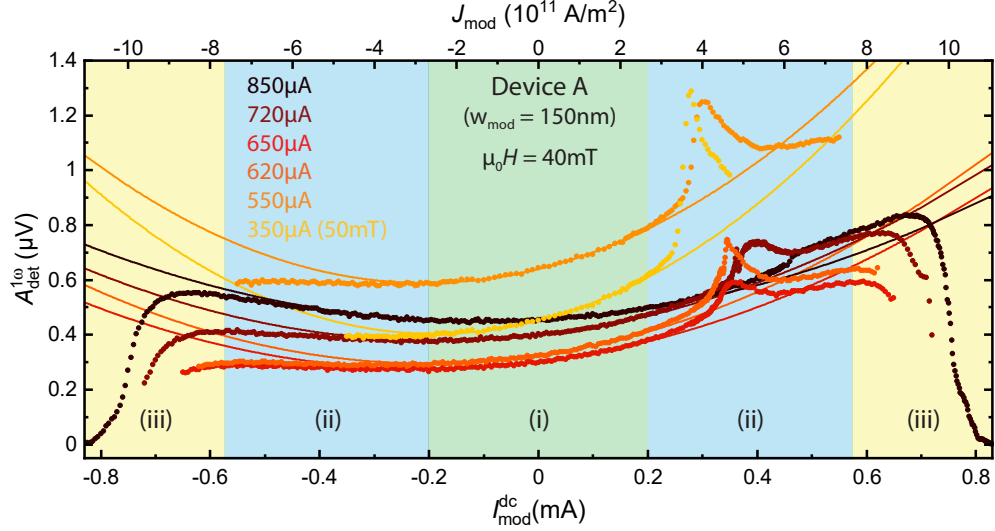


Fig. 4.18 – Electrically induced magnon transport amplitude $A_{\text{det}}^{1\omega}$ as a function of the modulator current $I_{\text{mod}}^{\text{dc}}$ for a successively increased maximum modulator current $I_{\text{mod}}^{\text{max}}$. The measurements were performed for device A with $w_{\text{mod}} = 150$ nm and a magnetic field magnitude $\mu_0 H = 40$ mT (except for the modulator current dependence with $I_{\text{mod}}^{\text{max}} = 350 \mu\text{A}$, which is measured for an applied magnetic field of $\mu_0 H = 50$ mT). The modulator current-dependent signal $A_{\text{det}}^{1\omega}$ is divided into three regimes: (i) the low modulator current regime (green area), (ii) the critical regime (blue area) and (iii) the overcritical regime (yellow area). The solid lines are fits to Eq. (4.40) describing the non-critical magnon conductivity modulation in the low bias regime. The fit range is limited to regime (i) and the fit curves are extrapolated to larger $I_{\text{mod}}^{\text{dc}}$.

are performed in the 3D-vector magnet cryostat (setup (i)) at a base temperature of $T = 280$ K.

To investigate the effect of large modulator currents on the magnon transport efficiency and critical behavior, we run several modulator current sweeps and successively increase the maximum modulator current $I_{\text{mod}}^{\text{max}}$. Here, we measure the detector voltage signal $V_{\text{det}}^{1\omega}$ at a fixed angle $\varphi = 0^\circ$ (cf. Fig. 4.4) and sweep the modulator current $I_{\text{mod}}^{\text{dc}}$ from positive to negative values. In this case, the magnetic field is applied along the z -direction perpendicular to the Pt strips and thus, the magnetization \mathbf{M} collinear to the spin polarization \mathbf{s} corresponding to the maximum magnon transport signal amplitude. In order to account for finite detector voltage signals, which are not related to magnon transport, we subsequently measure the modulator current dependence of $V_{\text{ac}}^{1\omega}$ at $\varphi = 90^\circ$ within the same range as $V_{\text{det}}^{1\omega}(\varphi = 0^\circ)$. The signal amplitude is then given by $A_{\text{det}}^{1\omega} = V_{\text{det}}^{1\omega}(\varphi = 0^\circ) - V_{\text{det}}^{1\omega}(\varphi = 90^\circ)$. In Fig. 4.18, we plot the detector voltage amplitude $A_{\text{det}}^{1\omega}$ as a function of the modulator current for device A and an external magnetic field of $\mu_0 H = 40$ mT³⁴. For the

³⁴The first measurement run with $I_{\text{mod}}^{\text{max}} = 350 \mu\text{A}$ is shown for a slightly different magnetic field $\mu_0 H = 50$ mT, since unfortunately there was no corresponding measurement at 40 mT.

sake of clarity, we split the current dependence in three regimes as indicated in Fig. 4.18: (i) the low modulator current regime characterized by a linear and quadratic magnon conductivity dependence due to SOT-induced magnetization dynamics and Joule heating effects, respectively (green colored region), (ii) the critical modulator current regime around $I_{\text{mod}}^{\text{crit}}$ dominated by nonlinear magnon conductivity contributions (blue colored region) and the overcritical current regime (iii) for $I_{\text{mod}}^{\text{dc}} \gg |I_{\text{mod}}^{\text{crit}}|$ (yellow colored region). To show that the simple parabolic model for linear magnetization dynamics describing regime (i) is no longer valid in regime (ii) and (iii), we fit Eq. (4.40) to the low modulator current regime in Fig. 4.18. The extrapolated fit curves clearly deviate from the behavior observed for larger $I_{\text{mod}}^{\text{dc}}$. More important, we see that the large modulator current exposure exhibits a significant impact on the qualitative behavior of the magnon transport modulation. To discuss this finding in more detail, we first study the evolution of the SMR magnitude for the Pt modulator electrode, where we find a reduction in the SMR and thus the interface transparency due to Joule heating induced changes at the interface after a large modulator current was applied. Next, the different modulator current regimes are discussed. For the low modulator current regime (i), we observe an overall decreasing modulator strength originating predominantly from the decreasing spin mixing conductance. A critical current increase with increasing $I_{\text{mod}}^{\text{max}}$ in the critical modulator current regime (ii) corroborates the finding of a decreasing interface quality. Finally, we can explain the strong decrease and vanishing of the magnon spin amplitude in the overcritical current regime (iii) by a local magnetic phase transition of the YIG below the modulator to its parametric state as thermometry measurements (in Sec. 4.4.4) suggest that the Curie temperature is approached.

4.4.1 Spin Hall Magnetoresistance

Before investigating the magnon transport properties in detail, we study the evolution of the interfacial spin transfer properties of the YIG/Pt bilayer, in particular for the modulator electrode, utilizing the SMR as well-established tool [92, 211]. We determine the SMR at the Pt modulator strip simultaneously in angle-dependent $V_{\text{det}}^{1\omega}$ measurements for one fixed modulator current $I_{\text{mod}}^{\text{dc}}$. We use the 2-point resistance of the modulator electrode³⁵ to extract its resistance modulation as a function of the angle φ . The SMR amplitude is then defined by the ratio $\Delta R/R_0$ with ΔR the resistance modulation and R_0 the low resistance value of the SMR modulation. Similar to the current-dependent measurements, we successively increase the maximum

³⁵The resistance of the Pt strip is several 10 k Ω , while the lead resistance is only 20 Ω , such that we are always dominated by the resistance contribution from the Pt strip and can neglect the error due to the lead resistances.

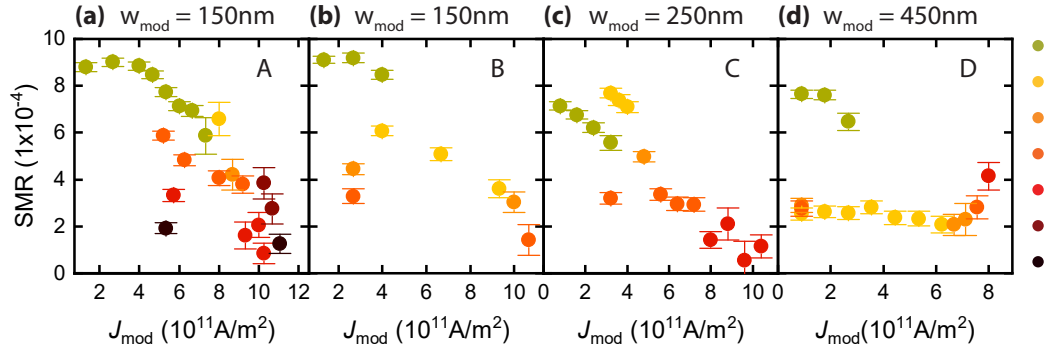


Fig. 4.19 – SMR amplitude at the Pt modulator electrode as a function of the applied current density J_{mod} . The SMR amplitude is extracted from angle-dependent measurements, which typically have been performed before the current-dependent measurements. The different colors correspond to one measurement run starting with an angle-dependent measurement at the largest current density in the corresponding run. The color scale on the right side indicates the order of the measurement runs from top to bottom. For each run the maximum applied current density was increased. Panels (a) to (d) show the results for devices A to D, respectively.

modulator current $I_{\text{mod}}^{\text{max}}$ and determine the SMR magnitude for each measurement. In our case, one measurement run consists of several angle-dependent measurements for different $I_{\text{mod}}^{\text{dc}}$ starting with the maximum modulator current $I_{\text{mod}}^{\text{max}}$ followed by smaller currents thereafter. The subsequent run is then initiated by an even larger $I_{\text{mod}}^{\text{max}}$, again followed by smaller currents. Typically, these measurements have been performed before the corresponding current-dependent measurements described above. To account for the different device geometries of the four devices in the following, we define the modulator current density $J_{\text{mod}} = I_{\text{mod}}^{\text{dc}} / (w_{\text{mod}} t_{\text{Pt}})$. The relative SMR amplitudes as a function of J_{mod} are plotted in Fig. 4.19(a) to (d) for all four devices A to D, respectively. The color scale on the right hand side of the Figure indicates the order of the measurement runs starting with the minimum $J_{\text{mod}}^{\text{max}} = I_{\text{mod}}^{\text{max}} / (w_{\text{mod}} t_{\text{Pt}})$ at the top to the maximum $J_{\text{mod}}^{\text{max}}$ at the bottom. Overall, the data reveals a significant decrease of the SMR amplitude with increasing current exposure. The only exception is device C, where the second measurement run (yellow dots) reveals a slightly larger SMR magnitude, however, all subsequent measurement runs show a decreasing SMR with increasing $J_{\text{mod}}^{\text{max}}$ again. In general, the SMR amplitude depends on different parameters such as the spin Hall angle θ_{SH} , the spin diffusion length l_{s} , the electrical conductivity σ_{e} of Pt and the spin mixing conductance $g^{\uparrow\downarrow}$ of the YIG/Pt interface [92, 211]. We discuss the changes in these parameters at large current densities below.

The most dominant effect when applying large modulator currents is the local electrical heating of the YIG/Pt interface at the modulator. Typically, the current

exposure in our samples is continuous and a few hours long, which is equivalent to annealing at large temperatures. However, in contrast to typical annealing procedures, where the whole sample is heated up, the large dc charge currents only result in a local thermal annealing at the modulator electrode. As discussed in detail in Sec. 4.4.4, we reach temperatures up to $T = 550$ K. Recent investigations of the spin transfer properties showed that both θ_{SH} as well as l_s are mostly unaffected by annealing [212], leaving only σ_e and $g^{\uparrow\downarrow}$. The electrical conductivity σ_e indeed increases with increasing $J_{\text{mod}}^{\text{max}}$ as shown in Fig. 4.21(c)-(f) in Sec. 4.4.3. This increase might also be a consequence of the annealing. As reported in Ref. [103] Fe atoms can diffuse out of the YIG/Pt interface area resulting in a slight increase of the conductivity. However, the change is not sufficient to account for the large decrease in the SMR. This means, the changes in the SMR magnitude can be traced back to a decreasing spin mixing conductance $g^{\uparrow\downarrow}$ [213]. While the decrease of the Fe atom density at the interfacial region increases σ_e , this in turn decreases the interfacial magnetic moment density at the interface, leading to a decreasing $g^{\uparrow\downarrow}$ explaining our observations on a microscopic level [103]. In contrast, the initial increase of $g^{\uparrow\downarrow}$ for device C might be related to another thermal annealing effect. In Ref. [214], an increase of the spin transfer efficiency has been observed, which the authors attributed to a better wettability of their evaporated Pt layer with the YIG surface with increasing current density and thus an increasing effective surface area through which spin current can be transmitted. Our observation of an overall decreasing SMR magnitude and thus a decreasing $g^{\uparrow\downarrow}$ can most likely be attributed to the much longer dc-type current exposure to our Pt strips, in contrast to the pulsed current scheme utilized in Ref. [214]. In the latter case, high current densities are only applied a few minutes to the Pt layer resulting in a large reduction of the heating effect compared to a few hours long exposure. It should also be noted that since our Pt strips are deposited via dc magnetron sputtering, they usually provide better spin transfer efficiencies compared to evaporated Pt layers [122]. Another effect that could influence the device performance when applying large modulator currents for a long time is electromigration. The gradual movement of ions in the Pt strip might also decrease the spin mixing conductance at the YIG/Pt interface. Over time this effect can lead to a break or gap in the strip. One would expect that such a break is most likely for the narrowest strips. However, only device D with the largest modulator width, broke before larger dc charge currents could be applied and thus we consider annealing as the dominant effect. Further investigation, such as scanning electron microscopy experiments, would be necessary to study the impact of electromigration on our Pt strips with a width in the 100 nm regime.

4.4.2 Low Modulator Current Regime

With these results in mind, we return to the modulator current dependence shown in Fig. 4.18 to discuss the impact of large modulator currents on the detector voltage amplitude $A_{\text{det}}^{1\omega}$. First, we focus on regime (i), where the magnon spin signal modulation can be described by Eq. (4.40), i.e. we only expect linear and quadratic dependencies on $I_{\text{mod}}^{\text{dc}}$. To study the impact of successively increasing current densities on the magnon transport and the magnon conductivity, we investigate the evolution of the prefactors $A_0^{1\omega}$, ΔR_{SHE} and ΔR_{th} in Eq. (4.40), which were extracted from fits to the low modulator current regime as exemplarily shown in Fig. 4.18 for device A. As introduced in Sec. 4.1.2 the prefactors correspond to the non-primed coefficients σ_{m}^0 , $\Delta\sigma_{\text{SHE}}$ and $\Delta\sigma_{\text{th}}$ in Eq. (4.14). The extracted parameters are plotted versus the maximum current density $J_{\text{mod}}^{\text{max}}$ exposed to the modulator electrode in Fig. 4.20(a) to (d) for the four devices A to D, respectively.

We first focus on the parameter $A_0^{1\omega}$ that accounts for the magnon transport amplitude without modulation for $I_{\text{mod}}^{\text{dc}} = 0$. Here, all four devices show different behaviors and no clear dependence is evident. Based on our previous discussion, where we consider a thermal annealing effect that modifies the interface spin mixing conductance [212–214], and our SMR measurements that suggest a significant decrease of $g^{\uparrow\downarrow}$ with increasing current exposure, we would expect that the magnon transport signal $A_0^{1\omega}$ increases with increasing $J_{\text{mod}}^{\text{max}}$. According to our argumentation, the modulator electrode should be less capable to absorb the diffusing magnon transport from injector to detector. Indeed, device C shows a rather monotonic increase of $A_0^{1\omega}$ over the whole current range and device A and B exhibit an increasing signal for $J_{\text{mod}}^{\text{max}} > 8 \times 10^{11} \text{ A/m}^2$, which corroborates our scenario. However, device A and B exhibit a decreasing amplitude $A_0^{1\omega}$ for intermediate currents and device D for larger current exposure. For device A, we note that after the respective measurements at $I_{\text{mod}}^{\text{max}} = 550 \mu\text{A}$ or $J_{\text{mod}}^{\text{max}} \approx 7.3 \times 10^{11} \text{ A/m}^2$, respectively, the sample was removed from and again remounted to the measurement setup. This procedure might explain the rather large jump in the non-modulated signal $A_0^{1\omega}$. A possible explanation for the observed decrease in $A_0^{1\omega}$ could be a local increase of the intrinsic magnetic Gilbert damping α_{G} beneath the modulator electrode due to the annealing process. When the electrical heating affects the crystal structure of YIG such a change in the damping could be induced. A recent work [215] demonstrated that the ferromagnetic resonance linewidth changes when the YIG layer is annealed. The authors suggest that subtle defects in thin YIG films in form of oxygen vacancies account for the change. However, a rigorous investigation of the atomic composition of the YIG/Pt interface is needed, to verify this scenario, otherwise it is a mere speculation for our samples. The aspect that our data does not

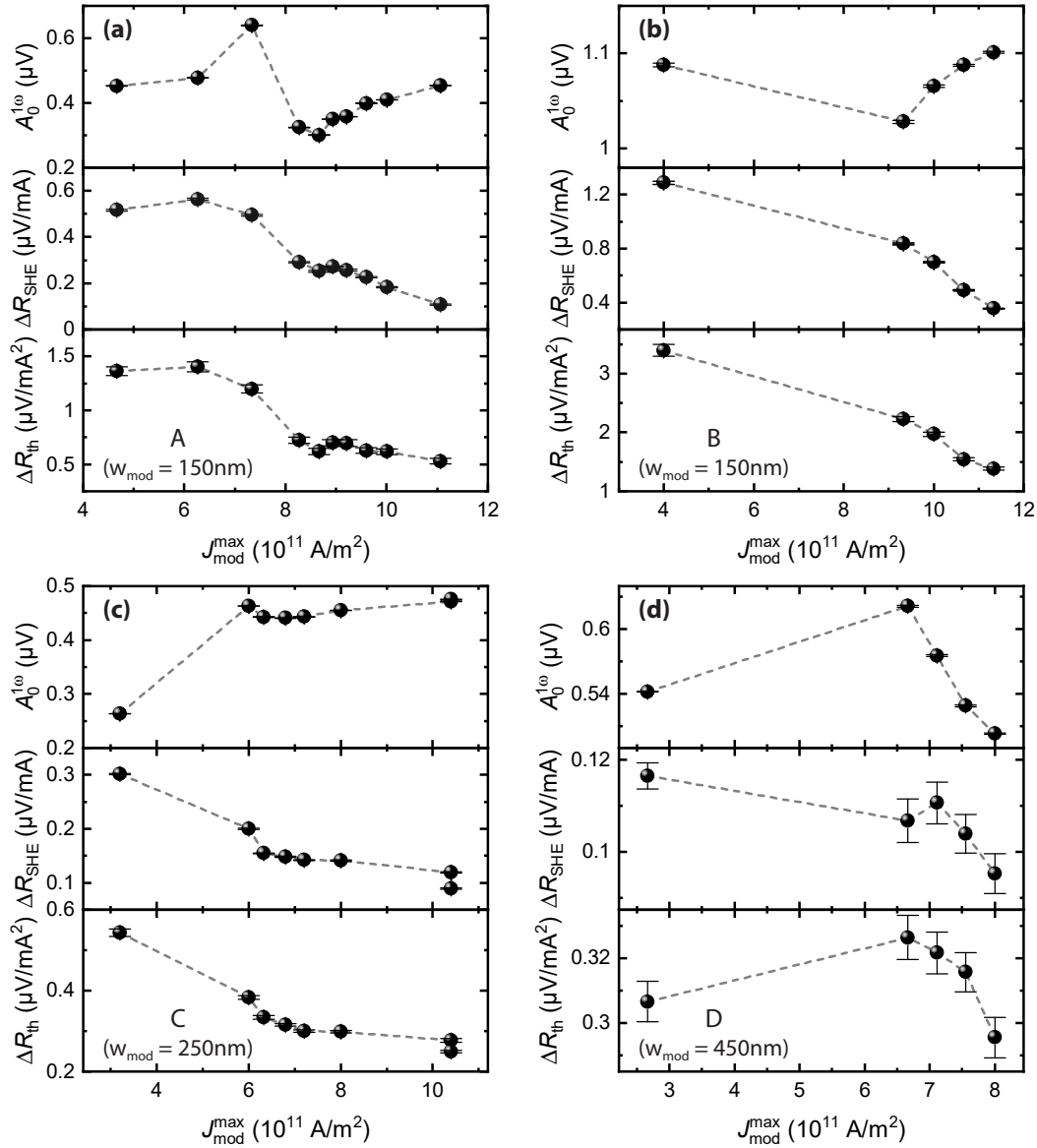


Fig. 4.20 – Extracted magnon transport parameters $A_0^{1\omega}$ for $I_{\text{mod}}^{\text{dc}} = 0$, ΔR_{SHE} the SOT-induced modulation efficiency and ΔR_{th} the thermally generated modulation as a function of the maximum applied current density $J_{\text{mod}}^{\text{max}}$ for the low bias regime. The parameters are extracted from fits to the current-dependent measurements within regime (i), as exemplarily shown in Fig. 4.18 for device A. Panels (a) to (d) show the respective parameters for devices A to D, respectively.

indicate an unambiguous increase or decrease of the magnon transport signal $A_0^{1\omega}$ within a certain current density range, suggests that this scenario is rather unlikely and that annealing induced oxygen vacancies might not be a dominant contribution. Most probably, a multitude of effects influence the behavior of the magnon transport signal, which complicates the unambiguous determination of an origin. In general, the annealing induced change of the magnon transport signal gives insight into the

interface properties of the modulator and the magnon transport properties itself. The dependence of $A_0^{1\omega}$ indicates that both of these properties are affected when large current densities are applied to the modulator electrode. In our case, we might trace it back to a decreasing spin mixing conductance $g^{\uparrow\downarrow}$ and possibly to a change in the magnetic damping of YIG at the modulator.

Next, we consider the SOT- and thermally-induced magnon transport modulation ΔR_{SHE} and ΔR_{th} in Fig. 4.20, respectively. For all four devices, we observe an overall reduced and nearly suppressed modulation effect for ΔR_{SHE} as well as ΔR_{th} on increasing the current exposure. Moreover, for each device ΔR_{SHE} and ΔR_{th} exhibit a quantitatively similar behavior. Our observations corroborate the consideration that large modulator currents result in electrical heating and thus decreasing the spin mixing conductance $g^{\uparrow\downarrow}$. Since both the SOT- and SSE-contribution of the thermally induced modulation efficiencies rely on the spin mixing conductance at the modulator interface [76, 117], the strong correlation between ΔR_{SHE} and ΔR_{th} is reasonable. Additionally, the observed decrease of both ΔR_{SHE} and ΔR_{th} can be attributed to a decrease of $g^{\uparrow\downarrow}$ with increasing modulator current densities. Only device A exhibits a slight increase of the modulation strength for the first two current densities $J_{\text{mod}}^{\text{max}}$ ³⁶. As discussed in Sec. 4.4.1, the latter might be ascribed to an increased wettability and thus an increased spin mixing conductance due to annealing as described in Ref. [214]. However, the corresponding SMR measurements for device A do not support this scenario, since they only indicate a monotonic decrease of $g^{\uparrow\downarrow}$. Moreover, a comparison among the devices shows that the absolute changes in ΔR_{SHE} and ΔR_{th} become successively smaller with increasing modulator width w_{mod} . However, comparing devices A and B, we find that the absolute changes in ΔR_{SHE} and ΔR_{th} already vary for devices with the same w_{mod} . Altogether this shows that a more systematic evaluation is necessary to obtain statistical significant results. For a better quantitative comparison, an investigation of the relative changes would be necessary. However, this is difficult in our case as $J_{\text{mod}}^{\text{max}}$ varies from device to device. The maximum current densities achieved for narrow modulator widths of device A and B are considerably larger than those of C and D, where in particular device D broke before larger values could be reached.

Note that also other effects could influence the modulation strength. For example, the thermally induced modulation of the magnon conductivity is both affected by the spin Seebeck torque at the YIG/Pt interface and the overall temperature rise in the YIG layer, leading to an increasing magnon density due to thermal excitations [141, 214]. Usually a temperature increase also modifies the temperature-dependent spin conductance $g \propto T^{3/2}g^{\uparrow\downarrow}$ at the interface [76]. However, this effect

³⁶We neglect the initial increase of ΔR_{th} for device D, since the overall change is very small compared to the other devices.

would induce higher order modulations in the low modulator current regime, which we do not observe in our experiments. Moreover, the thermally induced magnon transport modulation depends on the dissipated power in the Pt strip and thus on the resistance of the modulator electrode. For all four devices the resistivity decreases with increasing $J_{\text{mod}}^{\text{max}}$ (cf. Fig. 4.21(c)-(f)), i.e. the dissipated power is reduced. However, we can exclude this effect as a dominant contribution to the thermally induced modulation, since the changes in the resistivity are only a few 10%, while ΔR_{th} changes by a factor 2 – 3 for devices A, B and C. Another effect that might contribute to the magnon transport modulation is the change of the thermal interface resistance and therefore of the temperature profile due to the thermal annealing of the YIG/Pt interface. This in turn, could affect the magnon conductivity modulation. However, our results suggest that these effects are not the dominant contribution to the modulation strength and thus they were disregarded. Our data unambiguously shows a significant impact of large modulator current densities on the YIG/Pt interface at the modulator electrode. Due to the overall decrease of the extracted modulation magnitudes ΔR_{SHE} and ΔR_{th} , we conclude that the dominant effect is the decrease of the spin mixing conductance $g^{\uparrow\downarrow}$ due to annealing, in agreement with our SMR measurements (cf. Sec. 4.4.1).

4.4.3 Critical Modulator Current Regime

In a next step, we study the influence of large modulator currents on the critical current regime (blue region in Fig. 4.18). To better distinguish the individual curves, we plot the respective fraction of the data shown in Fig. 4.18 again in Fig. 4.21(a) with constant offsets applied to the data to avoid overlapping. Some additional curves for intermediate maximum modulator currents $I_{\text{mod}}^{\text{max}}$ were added. The dashed lines are fits to Eq. (4.39). We immediately see that the successive increase of $I_{\text{mod}}^{\text{max}}$ results in changes of the magnon transport amplitude $A_{\text{det}}^{1\omega}$ in the critical modulator current regime. On the one hand, the maximum that indicates the magnetic damping compensation shifts to larger modulator current values with increasing $I_{\text{mod}}^{\text{max}}$ and, on the other hand, the peak becomes less pronounced for each measurement. Furthermore, the sudden drop of $A_{\text{det}}^{1\omega}$ after damping compensation was reached, is strongly pronounced for low modulator current exposure, while it almost disappears for the largest applied currents. Taking into account an overall reduced spin mixing conductance as suggested by our SMR measurements as well as by the evolution of the magnon transport modulation, the vanishing peak feature indicates that the coherence of the excited magnetization dynamics is suppressed due to the increasing thermal energy. The latter (thermal energy) increases as larger currents are required for damping compensation and thus larger Joule heating is

induced (cf. Fig. 4.22). Interestingly, we observe a double-peak structure for an intermediate current regime. Such multiple peak structures indicate multiple $I_{\text{mod}}^{\text{crit}}$ and thus different conductivity peaks. This feature might result from a spatially inhomogeneous spin transparency across the Pt modulator or the magnetization dynamic parameters. The coherence between the resulting laterally distributed, SOT-induced damping compensated areas possibly decreases due to the increasing Joule heating with increasing current exposure. This, in turn destroys the spatial coherence of the excited modes, which might explain the emergence of multiple peaks. However, the spatial distribution of the interface spin transparency more likely exhibits a continuous behavior, rather than a step-like distribution. From this point of view, the magnon conductivity peak structure due to damping compensation is expected to be smeared out instead of forming multiple distinct peaks.

In order to quantify the current exposure effect in more detail, we extract η_{crit} from the fits to Eq. (4.39) (dashed lines in Fig. 4.21(a)). Since the extracted fit parameters are voltages, which are proportional to magnon conductances rather than conductivities as defined in Eq. (4.36), we have to consider the geometry of the device for the calculation of the respective magnon conductivities. With $\sigma'_{\text{m}} \propto [(d_{\text{c}} - w_{\text{mod}})/2A_{\text{YIG}}] \Delta V'$ and $\sigma_{\text{m}}^{0, \text{mod}} \propto (w_{\text{mod}}/A_{\text{YIG}}) \Delta V_{\text{mod}}^0$, we can determine the ratio η_{crit} from the experimental parameters as³⁷

$$\eta_{\text{crit}}^{\text{exp}} = \frac{d_{\text{c}} - w_{\text{mod}}}{2w_{\text{mod}}} \frac{\Delta V'}{\Delta V_{\text{mod}}^0}. \quad (4.52)$$

The results are shown as a function of $J_{\text{mod}}^{\text{max}}$ in Fig. 4.21(b) for all four devices A to D. The qualitative behavior of $\eta_{\text{crit}}^{\text{exp}}$ for all four devices clearly differs. Device C (blue data points) exhibits a rather constant behavior. In contrast, device B (red data points) only decreases with increasing modulator current density, while device D (green data points) shows an overall increasing behavior with $J_{\text{mod}}^{\text{max}}$. For device A (black data points), we observe a combination of the two observed trends, i.e. for low modulator current densities $\eta_{\text{crit}}^{\text{exp}}$ exhibits an overall increasing behavior, while the ratio decreases for $J_{\text{mod}}^{\text{max}} > 8 \times 10^{11} \text{ A/m}^2$. Devices B and D might exhibit a similar behavior as device A, however device D broke before higher current densities were reached and the data for device B is only available for large modulator current densities. According to our model, this indicates that at first a larger and then a smaller volume fraction underneath the modulator contributes to $\sigma_{\text{m}}^{0, \text{mod}}$. The observed trend $\eta_{\text{crit}}^{\text{exp}}$ increases with increasing $J_{\text{mod}}^{\text{max}}$ and thus a reduction of $\sigma_{\text{m}}^{0, \text{mod}}$ is

³⁷Note that these relations are only valid if we assume that the magnon conductivity is constant over the considered device length. However, in the context of the model introduced in Sec. 4.1.3 assuming that the modulation of the magnon conductivity is localized underneath the modulator, this is a good approximation in the critical current regime, where a zero effective damping state is expected and thus the magnon lifetime diverges and the magnon decay effectively vanishes.

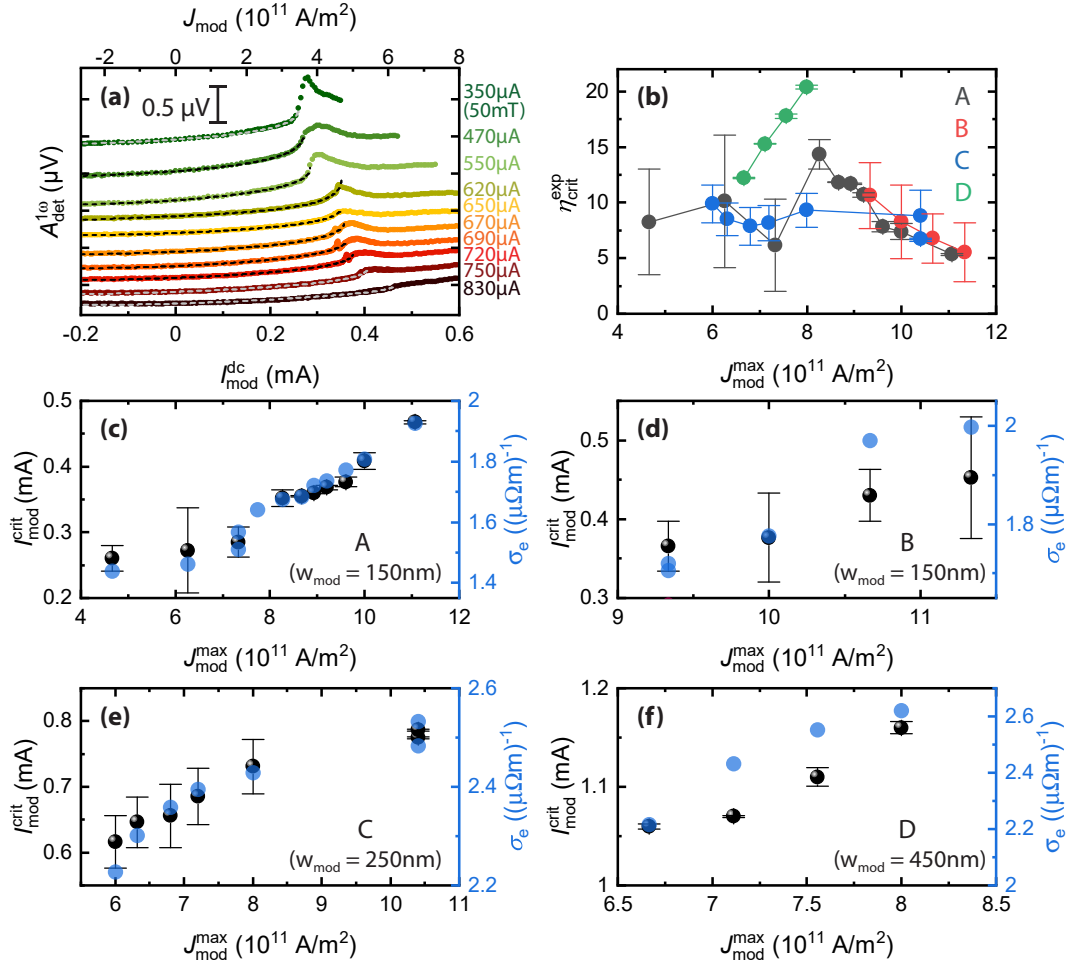


Fig. 4.21 – (a) Electrically induced magnon transport amplitude $A_{\text{det}}^{1\omega}$ as a function of $I_{\text{mod}}^{\text{dc}}$ for successively increased maximum modulator current $J_{\text{mod}}^{\text{max}}$. Compared to Fig. 4.18, the data shows a zoom-in to the regimes (i) and (ii). Note that constant vertical offsets are applied to each curve to improve the visibility of the curves in the critical current regime. The dashed lines are fits to Eq. (4.39). (b) Experimentally extracted $\eta_{\text{crit}}^{\text{exp}}$ according to Eq. (4.52) for all four devices. (c)-(f) Critical currents $I_{\text{mod}}^{\text{crit}}$ extracted from fits to Eq. (4.39), as exemplarily shown by the dashed lines in panel (a) for device A, as well as the electrical conductivity σ_e of the Pt modulator electrode as a function of the maximum applied modulator current density $J_{\text{mod}}^{\text{max}}$ for device A to D, respectively.

expected, i.e. that the area affected by the SOT of the modulator electrode becomes smaller. This is in agreement with our finding of a reduction in the spin mixing conductance $g^{\uparrow\downarrow}$, as this should also result in a decrease of $\sigma_m^{0,\text{mod}}$. In contrast, a decrease of $\eta_{\text{crit}}^{\text{exp}}$ suggests a decrease of σ_m' and an increase of $\sigma_m^{0,\text{mod}}$ with larger current exposure, which contrasts a reduction in $g^{\uparrow\downarrow}$ at first glance. There could be several reasons for this observation. The thermal annealing of the YIG/Pt interface due to large modulator currents might also lead to changes in the YIG itself. As

discussed in Sec. 4.4.2 for the low modulator current regime, a possible reduction in the damping of the magnetization dynamics underneath the modulator could improve $\sigma_m^{0, \text{mod}}$. Another explanation might be a change of the magnetic anisotropy in the YIG with increasing modulator current and thus a reshaping of the confinement conditions below the modulator, which influences the stability conditions of coherent magnon states. Moreover, the large current exposure might lead to a reshaping of the lateral distribution of $I_{\text{mod}}^{\text{crit}}$, possibly allowing a larger volume fraction to achieve damping compensation at higher $I_{\text{mod}}^{\text{crit}}$ values. Another aspect might be the decreasing coherence between the laterally distributed damping compensation areas as indicated by the emergence of multiple peaks.

Interestingly, for all devices A to D the extracted ratio $\eta_{\text{crit}}^{\text{exp}}$ is considerably larger than the expected value calculated from the geometry parameters according to Eq. (4.36), where we find $\eta_{\text{crit}} < 1$ for all cases. This indicates again that a larger area than the one covered by the Pt modulator is affected by the spin current injection. In this regard, it should be noted that while we here only investigate modulator electrode widths up to $w_{\text{mod}} = 450$ nm, a recent related study demonstrated a complete absence of a critical enhancement for $w_{\text{mod}} \geq 800$ nm [188]. Similar results were obtained for Py/Pt spin Hall oscillator devices, where the coherence and amplitude of the spin wave modes strongly decrease with increasing nanowire width [216]. In contrast to this study, here only the spin current injector (Pt) is confined via its finite width as opposed to the magnetic material (YIG), suggesting that the magnetic material does not necessarily has to be confined, but that a confined spin injector is sufficient to decrease the mode volume. Such a geometry was for example investigated by Evelt *et. al* [202] via magneto-optic techniques and has already been discussed in Sec. 4.3 with respect to $M_{\text{eff}} = 0$. In this case, damping compensation is achieved in an extended bismuth doped YIG film via a constricted Pt strip ($2 - 4 \mu\text{m}$ in length and $1 \mu\text{m}$ in width). This was found to result in a coherent emission of spin waves from the constriction into the surrounding film and strong coherent magnetization dynamics underneath the active Pt area, indicating the formation of a BEC state [202, 203]. We note that to rationalize all our observations a better understanding of the spatial profile and dimensions of the coherent magnon state and its changes, for example due to the anisotropy or dipolar effects, have to be investigated in more detail.

Apart from $\eta_{\text{crit}}^{\text{exp}}$, we can furthermore extract the critical current $I_{\text{mod}}^{\text{crit}}$ from Eq. (4.39), which we study in the following. To investigate the impact of large modulator current densities on the critical current, $I_{\text{mod}}^{\text{crit}}$ is extracted for each successive modulator current sweep from the fits (dashed lines in Fig. 4.21(a)) and plotted versus the maximum current density applied to the modulator $J_{\text{mod}}^{\text{max}}$ in Fig. 4.21(c) to (f) for device A to D, respectively. Over the whole current density range, the

critical current $I_{\text{mod}}^{\text{crit}}$ increases with increasing current exposure for all four devices, as already indicated by the current dependencies shown in panel (a) for device A. This is in agreement with our conclusions of a decreasing spin mixing conductance at the modulator interface as obtained for the behavior of the SMR and magnon transport modulation strengths. Additionally, the experimentally determined electrical conductivity σ_e of the modulator (blue data points) is shown for each plot. Similar to the critical current, σ_e increases with increasing current exposure, however the relative changes are much larger for $I_{\text{mod}}^{\text{crit}}$. Such a slight increase of the conductivity was also reported in Ref. [103] due to a possible diffusion of Fe atoms out of the YIG/Pt interface area originating from the thermal annealing effect. The qualitatively similar behavior of σ_e and $I_{\text{mod}}^{\text{crit}}$ and the seeming correlation between these two quantities might be related to this suspected Fe diffusion out of the YIG/Pt interface region. On the one hand, this scenario can explain the decreasing spin mixing conductance due to the decreasing interfacial magnetic moment density and on the other hand, the increasing conductivity can be attributed to the generation of a more pure Pt layer in contrast to the interfacial PtFe alloy. There might be further explanations for this correlation, such as a smaller thermal SSE torque due to a decreased temperature gradient at the interface originating from a reduced heating power as indicated by the increased conductivity. This scenario results in an increased $I_{\text{mod}}^{\text{crit}}$. Another possibility that leads to an increasing $I_{\text{mod}}^{\text{crit}}$ are changes to the material parameter. As demonstrated in Ref. [216], Pt with larger electrical conductivity exhibits a reduction of the spin Hall angle and an increase of the spin diffusion length. However, the two latter effects are rather unlikely, as the spin mixing conductance $g^{\uparrow\downarrow}$ in our samples decreases significantly as demonstrated in Sec. 4.4.1 via SMR measurements. While it is obvious that the large current exposure is at the origin of each of these changes, we emphasize that the correlation between σ_e and $I_{\text{mod}}^{\text{crit}}$ is only of qualitative nature and a microscopic correlation between the two quantities might not be given. In conclusion, one can state that the observed critical current increase as well as the overall impact on the critical magnon conductivity behavior is consistent with a reduction of the modulator interface quality due to current heating induced modifications.

4.4.4 Overcritical Modulator Current Regime

Finally, we investigate the overcritical modulator current regime (iii), indicated by the yellow region in Fig. 4.18. For a rigorous analysis of the modulator current far beyond $I_{\text{mod}}^{\text{crit}}$, we plot the modulator current dependence of the detector voltage amplitude $A_{\text{det}}^{1\omega}$ of device A for the largest applied maximum current $I_{\text{mod}}^{\text{max}} = 830 \mu\text{A}$ for different magnetic field magnitudes in Fig. 4.22(a). For large modulator current

magnitudes $|I_{\text{mod}}^{\text{dc}}| > 700 \mu\text{A}$, $A_{\text{det}}^{1\omega}$ rapidly decreases until the signal levels out at zero for the largest applied modulator currents. The rapid decrease shows no dependence on the magnetic field magnitude. More importantly, the behavior is symmetric under modulator current reversal, which strongly suggests a thermal origin of this effect. To verify this claim, we perform thermometry measurements to determine the temperature of the Pt modulator. To this end, we performed temperature-dependent measurements of the Pt modulator resistance and compared the data with the resistance behavior as a function of the applied current. For device A, we measured the modulator current-dependent resistance of the modulator electrode for a maximum current of $I_{\text{mod}}^{\text{max}} = 750 \mu\text{A}$ right before the resistance measurement as a function of the temperature. The resulting Pt modulator temperature versus the applied current is shown in Fig. 4.22(b). In order to determine the temperature for the largest applied current $I_{\text{mod}}^{\text{max}} = 830 \mu\text{A}$ in panel (a), we fit the data with both a parabolic $T(I_{\text{mod}}^{\text{dc}}) = T_0 + a_2(I_{\text{mod}}^{\text{dc}})^2$ and a fourth order $T(I_{\text{mod}}^{\text{dc}}) = T_0 + a_2(I_{\text{mod}}^{\text{dc}})^2 + a_4(I_{\text{mod}}^{\text{dc}})^4$ fit. While both fits well represent the temperature dependence for low modulator currents, it is obvious that the additional $(I_{\text{mod}}^{\text{dc}})^4$ -dependence models the large modulator current regime better. This higher order dependence is induced by the increased resistance as the temperature of the Pt electrode rises quadratically with the modulator current, and hence inducing a fourth order dependence.

Interestingly, the base temperature for $I_{\text{mod}}^{\text{dc}} = 0$ suggests $T \approx 300 \text{ K}$, which is considerably different to the actual base temperature of $T = 280 \text{ K}$. This deviation might stem from the current induced conductivity increase of the Pt modulator. Most likely it also changes the temperature calibration curve after the current-dependent measurement up to $I_{\text{mod}}^{\text{max}} = 750 \mu\text{A}$ and hence the temperature-dependent measurements indicate an apparent higher base temperature. Another reason for the deviation could be the larger thermal time constants in the temperature-dependent resistance measurements compared to the time intervals in the current-dependent sweeps. This means, that the sample is not able to equilibrate to the base temperature at $I_{\text{mod}}^{\text{dc}} = 0$ while the modulator current is swept from large positive to large negative current values. We consider this difference and account for the actual base temperature present in the Pt modulator by shifting the fourth order fit downwards such that $T = 280 \text{ K}$ at $I_{\text{mod}}^{\text{dc}} = 0$, as indicated by the blue line in Fig. 4.22(b). Here, an extrapolation to the maximum applied current $I_{\text{mod}}^{\text{max}} = 830 \mu\text{A}$ indicates a temperature of $T = 550 \text{ K}$, which is very close to the Curie temperature $T_C = 560 \text{ K}$ of bulk YIG [149]. Considering a negligible thermal resistance between the Pt electrode and YIG, it is reasonable to assume a local magnetic phase transition of the YIG beneath the modulator to its paramagnetic state. This results in a complete blocking of the magnon transport between injector and detector and thus a vanishing signal $A_{\text{det}}^{1\omega}$. A similar behavior was demonstrated in temperature-

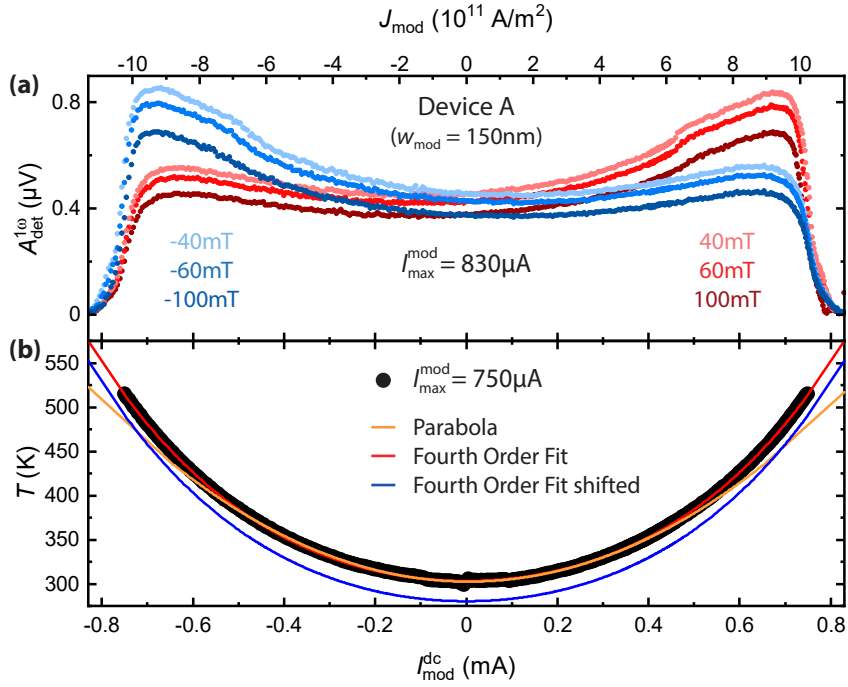


Fig. 4.22 – (a) Magnon transport amplitude $A_{\text{det}}^{1\omega}$ for device A with $w_{\text{mod}} = 150 \text{ nm}$ and a maximum current $I_{\text{mod}}^{\text{max}} = 830 \mu\text{A}$ measured at different magnetic field values. Each current dependence reveals a vanishing signal for the highest applied currents independent of the external magnetic field. (b) Thermometry measurement of the Pt modulator for device A. The data is fitted with both a parabolic fit (orange line) and a fourth order fit (red line). The blue curve correspond to a down-shifted version of the fourth order fit to account for the actual base temperature of $T = 280 \text{ K}$.

dependent studies, even for temperatures beyond T_C , in YIG/Pt samples [217]. Moreover, magnon transport measurements performed at the WMI, where Iridium (Ir) was utilized as modulator material, show a similar vanishing signal for large modulator currents [218]. Compared to Pt, Ir is characterized by a large resistance and a much smaller spin Hall efficiency, such that the thermal contribution to the modulation efficiency is significantly increased, while the SHE-induced magnon-related damping compensation is switched off [218]. Therefore, the obtained results verify the pure thermal origin of the vanishing magnon transport signal.

4.5 Summary

In this chapter, we provide an in-depth study of the manipulation of the magnon transport in three-terminal YIG/Pt devices. Via an all-electrical injection and detection scheme, magnons are induced at the injector Pt electrode via the SHE and the signal generated by diffusive magnon transport is detected via the inverse process at

the Pt detector electrode. Simultaneously, the magnon conductivity in the transport path is tuned via the additional spin current injection at a third Pt modulator electrode placed in between. Based on the model introduced in our previous work [45], we have investigated the influence of different external as well as device parameters on the modulator current dependence of the magnon conductivity. Within our discussion, we distinguish between the low modulator current regime, which is well described by a linear and quadratic $I_{\text{mod}}^{\text{dc}}$ dependence due to SOT-induced magnetization dynamics and Joule heating effects, respectively, and the critical modulator current regime, where SOT-induced nonlinear magnon conductivity contributions dominate.

First, we have compared the two measurement techniques used to access the magnon transport properties and both allow for an all-electrical generation and detection of pure spin currents in MOI/HM bilayers. For the dc-detection technique, we have introduced a modified current reversal method to take into account contributions due to the additional spin current injection at the modulator and thus enable the differentiation between the electrically (SHE) and thermally injected magnons. In contrast, the ac-readout technique employs the lock-in detection, which allows for a direct readout of these two contributions, since the first and second harmonic signal correspond to SHE- and thermally generated magnons, respectively. We have demonstrated that the dc and ac technique are both well suited to investigate the incoherent magnon transport in these three-terminal devices. Our results showed a full quantitative agreement between $V_{\text{dc}}^{\text{SHE}}$ and $V_{\text{ac}}^{1\omega}$ in the low bias regime below the critical threshold current, where the detector voltages have contributions linear and quadratic in I_{inj} . Above the critical threshold current deviations between these two detection schemes have been observed. According to our model this indicates a contribution of higher order in I_{inj} and not only in I_{mod} to the detector voltage. For the thermally generated magnons due to Joule heating, we have found a full quantitative agreement between $V_{\text{dc}}^{\text{therm}}$ and $V_{\text{ac}}^{2\omega}$ over the whole covered modulator current range. Since our model suggest that only transport coefficients up to the fifth order contribute to possible deviations between the thermal signals, the latter is not suitable to detect higher order contributions, in contrast to the SHE-induced signal.

Furthermore, we have investigated the magnon transport in YIG with strongly reduced effective magnetization M_{eff} , which has been induced by biaxial strain via epitaxial growth on YSGG substrates [205]. Characterizing the YIG thin film via broadband FMR and magnon transport measurements in two-terminal devices, we have obtained similar parameters for the Gilbert damping α_G and the magnon diffusion constant D as for high-quality YIG grown on lattice-matched GGG. In three-terminal devices, our data for small modulator currents have shown a quantitatively

similar behavior as for YIG films on GGG, while differences occur above the critical threshold when damping compensation is reached. Most importantly, we have observed an increase of the magnon induced detector signal by a factor of up to 6, which is much larger than reported in previous studies for YIG on GGG [45]. We could attribute this interesting observation to the nearly vanishing M_{eff} and the associated nearly circular magnetization precession in our film, which results in a minimization of damping effects and thus an increased spin conductivity. Extracting the critical modulator current, we could further confirm our model, as the magnetic field dependence has been associated with damping compensation [45]. The critical threshold exhibited a strictly linear dependence on the magnetic field, in contrast to YIG grown on GGG, which shows a constant behavior for small magnetic field values. This has in particular corroborated the expected scaling of $I_{\text{mod}}^{\text{dc}}$ with the saturation magnetization M_s and the magnetic anisotropy fields H_k .

Besides this intentional induced change of the device parameters, we have observed that the applied large modulator currents themselves also affect the device performance in terms of modulation efficiency and critical threshold. To this end, we have performed modulator current-dependent measurements as in the previous experiments and successively increased the maximum applied modulator current. To get insight into the underlying physics, the evolution of the interfacial spin transfer properties of the YIG/Pt bilayer with increasing maximum current via the SMR has been studied and the modulation efficiency in the low and critical modulator current regime has been modeled by appropriate fits that best describe the observed behavior in the corresponding regime. All experimental results, the decreasing SMR amplitudes as well as the significant decrease in modulation efficiencies along with an increasing threshold current with increasing current exposure, indicated the reduction of the spin mixing conductance $g^{\uparrow\downarrow}$ as the dominant effect. In addition, the critical current regime has revealed qualitative changes for large modulator current densities, suggesting an inhomogeneous distribution of the interfacial spin transfer efficiency across the Pt electrode. Last but not least, we could attribute the complete suppression of the magnon transport signal at the largest applied modulator currents to a local current-induced heating above the Curie temperature of YIG and thus a magnetic phase transition of YIG beneath the modulator to its paramagnetic state.

In summary, our investigations make an important contribution to the understanding of the manipulation of magnonic spin currents using three-terminal devices. By applying large modulator currents our experiments shed new light onto nonlinear contributions on the magnon conductance, which is essential for the implementation of devices and applications based on incoherent magnons. We are aware of the fact that we could only speculate on the physical origin of some features in the nonlinear regime. However, we are confident that our results can provide valuable

new insights for further theoretical and experimental investigations of such effects. In the outlook in Chap. 6, we discuss possible future experiments to investigate the magnetization dynamics below the modulator electrode in more detail and present first experimental results.

Magnon Spin Transport in the Antiferromagnet Hematite

As already discussed in the previous chapters, magnons are attractive for studying intriguing physical phenomena and offer a unique platform for potential technologies. Comparable to electrons, they are promising information carriers [34, 37, 182, 219] due to their solid state host and associated quantized spin. Antiferromagnetic insulators (AFIs) offer several advantages and new opportunities in this regard compared to ferro(ferri-)magnetic materials. Due to their immunity to stray fields [220, 221], high magnetic resonance frequencies in the terahertz regime [220–223], ultrafast response times [224, 225] and tunable spin [226, 227], antiferromagnetic magnons provide fast operations and robustness against thermal fluctuations. In contrast to the initial opinion that AFIs are useless for applications, there have been various theoretical proposals in the last years that exploit the diverse properties and engineerability of antiferromagnetic magnons predicting unprecedented phenomena [46, 47, 49–52, 128, 228, 229]. Experimentally, the dynamics of the spin system and transport properties of AFIs have been intensively investigated within the last decade [221, 230, 231]. However, the properties of antiferromagnetic magnons can also pose challenges. For example, in case of ferromagnetic magnons rapid experimental progress could be made by employing techniques developed in optics and optomechanics [232]. Similar approaches, however, may be challenging for antiferromagnetic magnons, as their high frequencies are not suitable for conventional GHz spectroscopy. In contrast, our all-electrical approach for the injection and detection of spin currents can overcome this drawback to a large extent. Here, the magnonic spin transport is carried by magnons with frequencies in the full frequency range [43, 76, 120, 125, 134, 164, 178, 217, 233, 234]. Moreover, for AFIs with two spatially separated HM electrodes utilized to inject and detect magnonic spin currents via the SHE, it has been demonstrated that these devices enable the study of magnon spin transport in AFIs [127, 134, 163, 164, 234]. In similar devices using an easy-axis AFI, micrometer long spin transport has been observed recently [134]. Apart from SHE-induced magnons, the transport of thermally generated magnonic spin currents via the spin Seebeck effect has also been reported [235–237].

In contrast to ferromagnetic magnons, which carry only spin with one particular direction, AFIs host pairs of spin-up and -down magnons. Superpositions of these

eigenmodes can result in circularly as well as linearly polarized oscillations of the Néel order with the latter corresponding to zero-spin excitations [226, 227]. While easy-axis AFIs exhibit right and left circularly polarized oscillations corresponding to spin-up and -down magnons, respectively, easy-plane AFIs host spin-0 magnons and therefore were considered unlikely to transport angular momentum. However, recent observations of long-distance transport of a SHE-induced magnonic spin current in easy-plane AFIs [127, 163, 164, 234] disprove this assumption. This immediately raised the question, which type of magnonic transport could support this configuration. On a theoretical level, the antiferromagnetic magnon pairs can be described within a pseudospin model in complete analogy to the two-level spin- $\frac{1}{2}$ system of electronic charge carriers [46–49]. Due to this formal equivalence between electron spin and antiferromagnetic magnon pseudospin, phenomena analogous to those occurring in spin- $\frac{1}{2}$ systems are predicted for AFIs. The corresponding antiferromagnetic pseudospin dynamics has been studied theoretically in Refs. [138, 238]. Experimentally, we previously observed for the first time the magnon Hanle effect, the magnonic analog of the electronic Hanle effect [75, 239, 240], in the easy-plane oriented AFI hematite (α -Fe₂O₃) [127]. A similar magnon-based Hanle effect has been reported in Zn-doped hematite [241]. The observation of the magnon Hanle effect opened up new opportunities. It demonstrated that the antiferromagnetic magnon pseudospin can be manipulated by an applied magnetic field and exploited in various devices, similar to the electronic spin in spintronics [239, 240]. In addition, as we also show in the following, it offers a new powerful tool for studying the rich nature of antiferromagnetic magnons described by a pseudospin formalism, and thus provides crucial information about the underlying spin interactions [43, 46, 48, 52, 238].

Since recent studies focused on thin films, which allow for a description of the results within a one-dimensional pseudospin transport model, we exploit the magnon Hanle effect to discuss the influence of the dimensionality of the AFI on the magnonic spin transport. In particular, we change the thickness of the investigated AFI films, in our case hematite (α -Fe₂O₃), and analyze the crossover characterized by the ratio of film thickness and magnon thermal wavelength. As in previous experiments [43, 127], we employ two spatially separated Pt electrodes on top of the hematite film acting as injector and detector and enabling an all-electrical injection and detection process of magnonic spin currents. For both a 15 nm and 100 nm thick thin film, we observe the Hanle signature, which can be captured by the pseudospin dynamics. However, the measured magnonic spin signal shows particular features for the thicker film that cannot be found for the thinner one. This includes an additional offset signal for low magnetic fields below the compensation field and an oscillating behavior of the magnonic spin signal around zero spin signal for high magnetic field values. We can attribute the former to the presence of finite-spin

low-energy magnons, which do not contribute to the oscillating behavior of the Hanle signal, but only lead to a constant offset signal.

Most importantly, we find a nonreciprocity in the Hanle signal when we interchange the two Pt electrodes utilized as spin injector and detector, respectively. The measured difference between the so-called forward and backward direction varies with the applied magnetic field, and thus the equilibrium Néel vector direction. Furthermore, the antisymmetric magnon spin signal shows a sign reversal when it passes the maximum of the symmetric contribution, exhibiting the characteristic Hanle curve, at the compensation field. We can explain our observations in terms of direction-dependent pseudofields which act on the magnons. The observed non-reciprocal response is a clear sign for inversion symmetry breaking in the system and, hence, opens up interesting opportunities for realizing exotic physics so far only predicted for antiferromagnets with special crystal structure.

This chapter is structured as follows: In Sec. 5.1, we first introduce the basic model describing magnons in antiferromagnets within a pseudospin picture and then expand the model in order to account for nonreciprocal effects and low-energy magnons. This model represents a convenient way to describe antiferromagnetic magnons and their transport properties in an AFI. However, it does not directly consider the injection/detection process, whose influence is also discussed in this Section. In Section 5.2, we present our experimental results for two hematite films of different thickness and discuss them in terms of our pseudospin concept. Both films show a distinct signal caused by the Hanle effect. However, there are also differences, which can partly be traced back to the presence of finite-spin low-energy magnons. In the next Sec. 5.3, we investigate the nonreciprocity of the Hanle signal, which we find to depend on the applied magnetic field. In particular, the antisymmetric signal contribution reverses sign when the signal passes the compensation field. Finally, a summary of the most important results is given in Sec. 5.4.

5.1 Theoretical Concepts

In this Section, we introduce the theoretical framework for the description of the magnonic spin transport in antiferromagnets. First, a general description of magnons in antiferromagnets within a pseudospin picture is given in Sec. 5.1.1. We note that the pseudospin description is valid for any pair of coupled bosons. Section 5.1.2 captures the time evolution of the pseudospin and its influence on the diffusive magnon spin transport in an AFI with any given anisotropies and interactions by introducing the formalism of pseudospin chemical potential together with a pseudofield. The analysis focuses on the 1D solution of the pseudospin

diffusion equation. We here only summarize the most important results of the pseudospin concept and its dynamics following the discussion in Ref. [68]. A complete description of the theoretical formalism is given by Kamra *et al.* [138]. In Sec. 5.1.3, we use this model to explain the features of the magnon Hanle effect, which first has been observed by Wimmer *et al.* [127]. In Sec. 5.1.4, we allow for an additional direction-dependent pseudofield and thus can describe also nonreciprocal effects, which have been covered in Ref. [242]. Furthermore, the influence of finite-spin low-energy magnons, which cannot be directly captured by the pseudospin chemical potential, is discussed in Sec. 5.1.5. Last but not least, we provide a general formalism in Sec. 5.1.6 that does not only account for the magnon spin transport in the AFI, but also captures the injection and detection process of our utilized nonlocal devices. The key results of the two latter sections have been published in Ref. [243].

5.1.1 Pseudospin Concept

Before we dive into the mathematical details, we would like to provide a qualitative picture of the underlying physics. The pseudospin concept is based on the fact that in AFIs the eigenmodes of the spin system appear in pairs for a given wave vector. These two eigenmodes with opposite chirality can form linear superpositions, ranging from spin-1 to spin-0 excitations [46, 48, 226]. This property reminds one of a two-level system such as the spin- $\frac{1}{2}$ of an electron. The corresponding mathematical analogy with electrons allows one to formally compare its eigenmodes to those of AFIs. However, one has to keep in mind that there is a fundamental difference between both systems due to the bosonic nature of magnons in AFIs. To describe the bosonic system some key assumptions are made in the following. We assume a Néel ordered AFI, where the exchange interaction is the dominant interaction, while others (e.g. dipolar interaction, DMI, etc.) are much smaller. This allows for a perturbative treatment of anisotropies and other nonuniversal, material-dependent interactions [138]. Secondly, the two sublattice magnetization are assumed to be antiparallel and oriented collinear, in our case along the z axis, forming the ground state. The corresponding degenerated magnon modes are typically denoted as α - and β -mode [128]. They represent spin-up (spin +1) and spin-down (spin -1) magnons that carry unit spin parallel to the Néel vector (z axis). Due to our assumptions the α - and β -modes constitute our natural basis. In a classical picture they correspond to classical moments with opposite precession direction. Now, spin-nonconserving interactions, which are treated as perturbations, can couple the basis states, and thus enable the formation of superposition states [46, 128, 226, 227, 244].

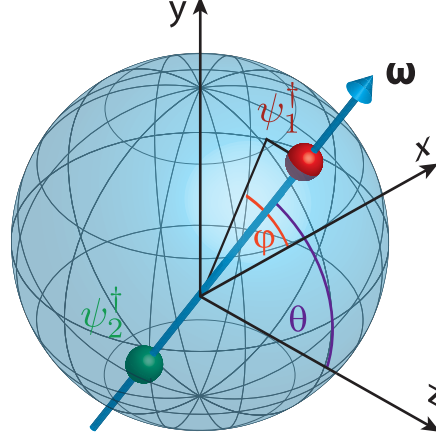


Fig. 5.1 – Schematic depiction of a magnonic two-level system on a Bloch sphere, in our case of the two antiferromagnetic eigenmodes. The intersections of the pseudofield vector ω with the Bloch sphere are indicated by red and green spheres and represent the corresponding lower- (ψ_1^\dagger) and higher-energy (ψ_2^\dagger) magnonic eigenmodes. Keep in mind that the sphere is in the creation operator space.

Mathematically, such coherently coupled bosonic modes can be described by the hamiltonian \hat{H} :

$$\begin{aligned}
 \hat{H}/\hbar &= \omega_\alpha \hat{\alpha}^\dagger \hat{\alpha} + \omega_\beta \hat{\beta}^\dagger \hat{\beta} + \frac{\Omega}{2} \hat{\alpha} \hat{\beta}^\dagger + \frac{\Omega^*}{2} \hat{\alpha}^\dagger \hat{\beta} \\
 &= \begin{pmatrix} \hat{\alpha}^\dagger & \hat{\beta}^\dagger \end{pmatrix} \begin{pmatrix} \omega_\alpha & \Omega^*/2 \\ \Omega/2 & \omega_\beta \end{pmatrix} \begin{pmatrix} \hat{\alpha} \\ \hat{\beta} \end{pmatrix} \\
 &= \underline{\hat{\alpha}^\dagger} \underline{H}_{\text{in}} \underline{\hat{\alpha}},
 \end{aligned} \tag{5.1}$$

where ω_α and ω_β characterize the frequencies of the (uncoupled) spin-up (α -mode) and spin-down (β -mode) magnons and Ω denotes the coherent coupling rate of the modes. While operators are identified with overhead tilde, matrices or vectors are indicated by an underline. In order to extract the eigenstates and -values of the coupled system, we have to diagonalize the hamiltonien $\underline{H}_{\text{in}}$ in Eq. (5.1), which can be written in the form

$$\hat{H}/\hbar = \begin{pmatrix} \hat{\psi}_1^\dagger & \hat{\psi}_2^\dagger \end{pmatrix} \begin{pmatrix} \omega_1 & 0 \\ 0 & \omega_2 \end{pmatrix} \begin{pmatrix} \hat{\psi}_1 \\ \hat{\psi}_2 \end{pmatrix} = \underline{\hat{\psi}}^\dagger \underline{H}_{\text{diag}} \underline{\hat{\psi}}, \tag{5.2}$$

with the eigenvalues $\omega_{1,2}$ and eigenvectors $\hat{\psi}_{1,2}$ of the corresponding eigenvalue equation for $\underline{H}_{\text{in}}$. Here, the diagonalized form can be expressed by $\underline{H}_{\text{diag}} = \underline{P}^\dagger \underline{H}_{\text{in}} \underline{P}$, where the transformation matrix \underline{P} is unitary with $\underline{P}^\dagger = \underline{P}^{-1}$, allowing for a standard

diagonalization procedure. The associated matrix \underline{P} is given in terms of Bloch sphere representation of the eigenvectors by

$$\underline{P} = \begin{pmatrix} \cos\left(\frac{\theta_1}{2}\right) & e^{i\varphi_2} \sin\left(\frac{\theta_2}{2}\right) \\ e^{i\varphi_1} \sin\left(\frac{\theta_1}{2}\right) & \cos\left(\frac{\theta_2}{2}\right) \end{pmatrix}. \quad (5.3)$$

Here, $\theta_{1,2}$ and $\varphi_{1,2}$ parameterize the two eigenvectors on the Bloch sphere. Since \underline{P} is unitary, we obtain the conditions $\theta_2 = \pi - \theta_1$ and $\varphi_2 = \pi + \varphi_1$ from the off-diagonal elements of Eq. (5.3). Employing these conditions, the two eigenvectors can be represented by a single pair of angles (θ, φ) , where we dropped the subscript “1”. This means, the two eigenvectors are aligned antiparallel on the Bloch sphere, as shown in Fig. 5.1, in contrast to pointing along two arbitrary directions. This results in a further simplified transformation matrix \underline{P} :

$$\underline{P} = \begin{pmatrix} \cos\left(\frac{\theta}{2}\right) & -e^{-i\varphi} \sin\left(\frac{\theta}{2}\right) \\ e^{i\varphi} \sin\left(\frac{\theta}{2}\right) & \cos\left(\frac{\theta}{2}\right) \end{pmatrix}. \quad (5.4)$$

For the relation between the eigenmodes of the coupled system and the natural basis spanned by $\hat{\alpha}^\dagger$ and $\hat{\beta}^\dagger$, we then obtain

$$\begin{pmatrix} \hat{\psi}_1^\dagger & \hat{\psi}_2^\dagger \end{pmatrix} = \begin{pmatrix} \hat{\alpha}^\dagger & \hat{\beta}^\dagger \end{pmatrix} \begin{pmatrix} \cos\left(\frac{\theta}{2}\right) & -e^{-i\varphi} \sin\left(\frac{\theta}{2}\right) \\ e^{i\varphi} \sin\left(\frac{\theta}{2}\right) & \cos\left(\frac{\theta}{2}\right) \end{pmatrix}. \quad (5.5)$$

The corresponding states $\hat{\psi}_1^\dagger$ and $\hat{\psi}_2^\dagger$ are depicted in Fig. 5.1 as a red and green sphere, respectively, for arbitrary values of θ and φ . Note that in contrast to the typical use of the Bloch sphere, which describes wavefunctions of a two-level system, the eigenvectors on the Bloch sphere in our case are given in the space of creation operators [138]. In general, the representation with a similar device, the Poincaré sphere that maps polarization states of light [245], is preferential. However, both representations share similarities and differences with our definition of the unit sphere in representing AFI modes. In this work, we utilize the Bloch sphere terminology and keep in mind that it is not a Bloch sphere in the strict sense, but rather represents excitation creation operators.

Within our considerations, we now introduce the pseudospin operator $\hat{L} = \hat{L}_x \hat{x} + \hat{L}_y \hat{y} + \hat{L}_z \hat{z}$ with its components

$$\hat{L}_x = \frac{1}{2}(\hat{\alpha}^\dagger \sigma_x \hat{\alpha}) = \frac{1}{2}(\hat{\alpha} \hat{\beta}^\dagger + \hat{\alpha}^\dagger \hat{\beta}), \quad (5.6a)$$

$$\hat{L}_y = \frac{1}{2}(\hat{\alpha}^\dagger \sigma_y \hat{\alpha}) = \frac{i}{2}(\hat{\alpha} \hat{\beta}^\dagger - \hat{\alpha}^\dagger \hat{\beta}), \quad (5.6b)$$

$$\hat{L}_z = \frac{1}{2}(\hat{\alpha}^\dagger \sigma_z \hat{\alpha}) = \frac{1}{2}(\hat{\alpha}^\dagger \hat{\alpha} - \hat{\beta}^\dagger \hat{\beta}), \quad (5.6c)$$

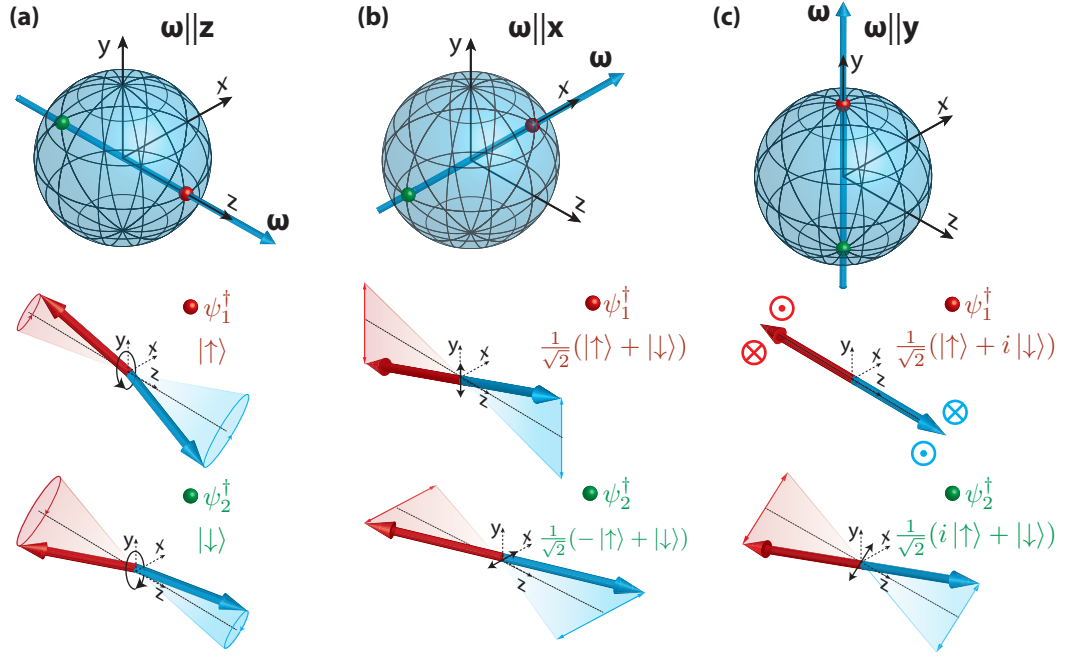


Fig. 5.2 – Illustration of the AFI eigenmodes (red and green spheres) for the pseudofield ω oriented along (a) \hat{z} , (b) \hat{x} and (c) \hat{y} . The eigenmodes correspond to (a) circular precession and (b), (c) linear oscillations of the two sublattice magnetizations in the Landau-Lifshitz description. Moreover, the eigenmodes are expressed as superpositions of the spin-up ($|\uparrow\rangle$) and -down ($|\downarrow\rangle$) basis states in the quantum picture.

where $\sigma_{x,y,z}$ are the Pauli matrices. Using these relations, we can rewrite the hamiltonian defined in Eq. (5.1) in terms of the pseudospin operator according to

$$\hat{H}/\hbar = 2\omega_0\hat{L}_0 - \omega \cdot \hat{\mathbf{L}}, \quad (5.7)$$

where $\hat{L}_0 = \frac{1}{2}(\hat{\alpha}^\dagger\sigma_0\hat{\alpha}) = \frac{1}{2}(\hat{\alpha}^\dagger\hat{\alpha} + \hat{\beta}^\dagger\hat{\beta})$ with σ_0 the 2×2 identity matrix. Furthermore, ω_0 and the components of ω are defined as [138]

$$\omega_0 = \frac{\omega_\alpha + \omega_\beta}{2}, \quad (5.8a)$$

$$\omega_z = -(\omega_\alpha - \omega_\beta), \quad (5.8b)$$

$$\omega_x + i\omega_y = -\Omega. \quad (5.8c)$$

If we compare the hamiltonian defined in Eq. (5.7) to the one of a typical spin- $\frac{1}{2}$ system, we find a close analogy between the quantity ω interacting with the pseudospin and the magnetic field coupling to an actual spin. Therefore, ω is introduced as the pseudofield. In general, the latter depends on material details, for example anisotropies, and the resulting free-energy landscape in the studied AFI and can generally be tuned via an applied magnetic field [127, 138]. More

importantly, our considerations show that the pseudofield determines the magnonic eigenmodes, since their Bloch vectors are collinear with $\boldsymbol{\omega}$ (cf. Fig. 5.1). We depict the eigenmodes and their corresponding Néel vector dynamics in the Landau-Lifshitz description for three different directions of the pseudofield in Fig. 5.2. In all cases, the pseudofield is considered along one coordinate axis. In Fig. 5.2(a), for $\boldsymbol{\omega} \parallel \hat{\mathbf{z}}$, where the coupling Ω is zero according to Eq. (5.8c), the eigenmodes are the same as our natural basis of spin-up and -down magnons representing circularly precessing Néel vectors with opposite chiralities. When $\boldsymbol{\omega} \parallel \hat{\mathbf{x}}$ in panel (b), the eigenmodes of the system are equal superpositions of the α - and β -mode corresponding to spin-zero excitations. In the Landau-Lifshitz description this corresponds to linear oscillations of the Néel vector with the linear oscillation planes perpendicular to each other. A similar situation is found in Fig. 5.2(c) for $\boldsymbol{\omega} \parallel \hat{\mathbf{y}}$, where the eigenmodes are still linearly polarized, however the two associated orthogonal planes are now rotated by 45° compared to the eigenmodes presented for $\boldsymbol{\omega} \parallel \hat{\mathbf{x}}$ and thus we still obtain spin-zero excitations as in (b).

5.1.2 Pseudospin Dynamics and Diffusive Transport

In contrast to a spin- $\frac{1}{2}$ system, for magnons in AFIs the knowledge of the eigenmodes is not sufficient to determine physical quantities, such as spin, due to their bosonic nature. In general, when we discuss dynamics in AFIs, we need to capture both the density of nonequilibrium magnons as well as their nature. Since most of the discussion so far has been based on the equilibrium description of the two coupled modes, we now consider the situation where the pseudospin is not aligned collinear with the pseudofield, allowing for the description of nonequilibrium effects. In order to account for this situation, we evaluate the expectation value of the pseudospin operator given in Ref. [138] by

$$\mathbf{L} \equiv \langle \hat{\mathbf{L}} \rangle = \frac{1}{2V} \left(- \frac{\partial n(\epsilon)}{\partial \epsilon} \Big|_{\epsilon=\hbar\omega_0} \right) (\hbar\boldsymbol{\omega} + \boldsymbol{\mu}_s) = \mathbf{L}_0 + \frac{1}{2V} \left(- \frac{\partial n(\epsilon)}{\partial \epsilon} \Big|_{\epsilon=\hbar\omega_0} \right) \boldsymbol{\mu}_s. \quad (5.9)$$

Note that the expectation value has already been divided by the volume and therefore, we refer to the quantity defined in Eq. (5.9) as pseudospin density. Furthermore, $n(\epsilon) = \left(\exp\left(\frac{\epsilon}{k_B T}\right) - 1 \right)^{-1}$ denotes the Bose-Einstein distribution function with the single magnon energy ϵ , the Boltzmann constant k_B and the temperature T . The pseudospin chemical potential is introduced as

$$\boldsymbol{\mu}_s = (\mu_1 - \mu_2)(\sin(\theta) \cos(\varphi)\hat{\mathbf{x}} + \sin(\theta) \sin(\varphi)\hat{\mathbf{y}} + \cos(\theta)\hat{\mathbf{z}}) \quad (5.10)$$

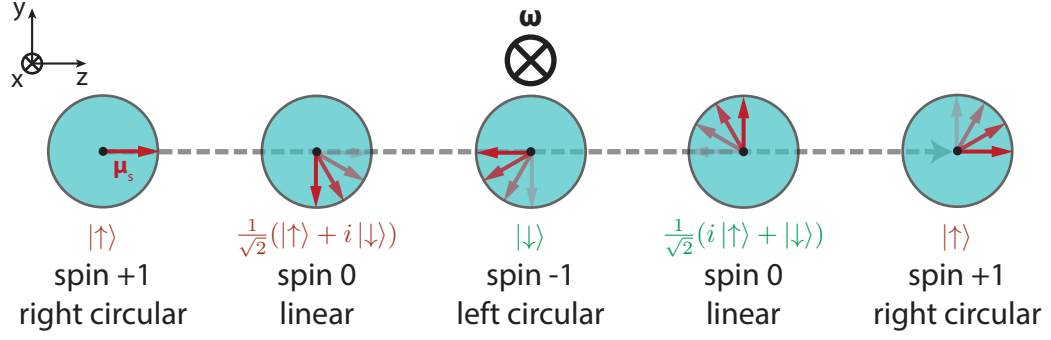


Fig. 5.3 – Precession of the pseudospin chemical potential μ_s around the pseudofield $\omega \parallel \hat{x}$. Each of the depicted directions of μ_s corresponds to an eigenmode given by the superposition of the quantum basis states.

with $\mu_{1,2}$ the chemical potentials of the respective eigenmodes [246]. The last term on the right hand side of Eq. (5.9) exhibits two contributions. $L_0 \propto \omega$ accounts for equilibrium effects originating from the energy and thus, from the occupancy difference between the two eigenmodes. The term proportional to μ_s stems from an imbalance of the eigenmodes' spin chemical potentials leading to a nonequilibrium effect. In contrast to ferromagnets, where the nonequilibrium density can be characterized by a scalar chemical potential [76] due to the presence of only one kind of magnons bearing spin-1³⁸, antiferromagnets are captured by a vectorial quantity. The pseudospin chemical potential accounts for the eigenmode information via (θ, φ) and hence, its magnitude and direction represent the density and nature of nonequilibrium antiferromagnetic magnons. It is important to mention that only the z -component of μ_s corresponds to a finite (measurable) magnon spin, while the x - and y -contributions refer to zero spin modes.

In order to describe the dynamics of the system, we have to study the time dependence of the pseudospin density L . To this end, we utilize the Heisenberg picture allowing us to set up the Heisenberg equation of motion for the pseudospin operator \hat{L} [138] and inserting Eq. (5.9) therein, we arrive at

$$\frac{d\mu_s}{dt} = \mu_s \times \omega. \quad (5.11)$$

This relation describes a precession of μ_s around the fictitious pseudofield ω . This situation resembles again that of a spin- $\frac{1}{2}$ system, where the electron spin exhibits a precession about an applied magnetic field [75, 240, 248]. However, in this case the precession sense is inverted due to the negative gyromagnetic ratio of an electron. To visualize the temporal evolution of the pseudospin chemical potential given in

³⁸Note that this is only true if the effect of spin-nonconserving interactions that yield a ferromagnetic magnon spin larger than 1 are disregarded [226, 247]. This simplification is commonly made in literature, and is furthermore typically valid for thermal magnons.

Eq. (5.11) and providing an intuitive picture, we consider an antiferromagnetic system with the pseudofield $\boldsymbol{\omega}$ aligned along the positive x -direction. Moreover, $\boldsymbol{\mu}_s$ initially points along \hat{z} . Such a situation is present in our magnon transport devices, where nonequilibrium, spin-up magnons are injected into an easy-plane AFI. Since $\boldsymbol{\mu}_s$ is not collinear with $\boldsymbol{\omega}$, the injected magnon modes are not the eigenmodes of the nonequilibrium system and hence, the chemical potential starts to precess around the pseudofield $\boldsymbol{\omega}$ in the y - z plane. In Fig. 5.3, we sketched the precessing pseudospin chemical potential as well as the corresponding quantum superposition states. We see that the initially right circularly polarized magnons transmute to linearly, to left circularly, to linearly, and back to right circularly polarized magnons for one full precession (360°) of $\boldsymbol{\mu}_s$ in the classical Landau-Lifshitz picture. In an analogous manner to the situation of an electronic spin, dephasing and decoherence processes lead to a reduction of $\boldsymbol{\mu}_s$ until the latter approaches zero and additionally aligns the pseudospin chemical potential with the pseudofield.

After having introduced the pseudospin and related quantities, we now derive the diffusion equation for an AFI in terms of the pseudospin chemical potential, enabling the discussion of diffusive transport of AFI magnons. Therefore, we have to consider the entire magnon ensemble, instead of two coupled modes at a given \mathbf{k} . Summing up over all modes from every excited wavevector, we may introduce the total pseudospin density [138]

$$\mathcal{S} \equiv \sum_{\mathbf{k}} \frac{1}{2V} \left(- \frac{\partial n(\epsilon)}{\partial \epsilon} \Big|_{\epsilon=\hbar\omega_{0\mathbf{k}}} \right) (\hbar\boldsymbol{\omega}_{\mathbf{k}} + \boldsymbol{\mu}_s) = \chi(\hbar\boldsymbol{\omega} + \boldsymbol{\mu}_s), \quad (5.12)$$

where we defined the effective susceptibility χ and the averaged pseudofield $\boldsymbol{\omega}$ as

$$\chi \equiv \int \frac{d^3k}{(2\pi)^3} \frac{1}{2} \left(- \frac{\partial n(\epsilon)}{\partial \epsilon} \Big|_{\epsilon=\hbar\omega_{0\mathbf{k}}} \right), \quad (5.13)$$

$$\boldsymbol{\omega} = \langle \boldsymbol{\omega}_{\mathbf{k}} \rangle_{\text{BZ}} \equiv \frac{\int \frac{d^3k}{(2\pi)^3} \boldsymbol{\omega}_{\mathbf{k}} \frac{1}{2} \left(- \frac{\partial n(\epsilon)}{\partial \epsilon} \Big|_{\epsilon=\hbar\omega_{0\mathbf{k}}} \right)}{\int \frac{d^3k}{(2\pi)^3} \frac{1}{2} \left(- \frac{\partial n(\epsilon)}{\partial \epsilon} \Big|_{\epsilon=\hbar\omega_{0\mathbf{k}}} \right)}. \quad (5.14)$$

Here, $\hbar\omega_{0\mathbf{k}}$ denotes the uncoupled mode energy accounting for the dispersion relation of the system when the coupling between the two modes is neglected. Following a similar procedure in deriving the diffusive transport equation as in the case of electronic spin transport [75], we can write the pseudospin density diffusion equation constituting the contributions from all occupied states as

$$\frac{\partial \mathcal{S}}{\partial t} = D_m \nabla^2 \mathcal{S} - \frac{\mathcal{S} - \mathcal{S}_0}{\tau_m} + \mathcal{S} \times \boldsymbol{\omega}, \quad (5.15)$$

where S_0 denotes the equilibrium spin density and τ_m the spin relaxation time that is assumed to be isotropic for simplicity. Moreover, we utilized the spin diffusion constant for a given \mathbf{k} -vector $D_{\mathbf{k}} = \frac{1}{3}\tau v_{\mathbf{k}}^2 = \frac{1}{3}\tau(\nabla\omega_{0\mathbf{k}})^2$ with the group velocity $v_{\mathbf{k}} = \nabla\omega_{0\mathbf{k}}$ and obtained its averaged value according to

$$D_m = \langle D_{\mathbf{k}} \rangle_{\text{BZ}} = \frac{\int \frac{d^3k}{(2\pi)^3} \frac{1}{3}\tau(\nabla\omega_{0\mathbf{k}})^2 \frac{1}{2} \left(-\frac{\partial n(\epsilon)}{\partial \epsilon} \Big|_{\epsilon=\hbar\omega_{0\mathbf{k}}} \right)}{\int \frac{d^3k}{(2\pi)^3} \frac{1}{2} \left(-\frac{\partial n(\epsilon)}{\partial \epsilon} \Big|_{\epsilon=\hbar\omega_{0\mathbf{k}}} \right)}, \quad (5.16)$$

where τ is the momentum scattering time that is also assumed to be wavevector-independent. Substituting Eq. (5.12) into Eq. (5.15), we finally obtain the diffusion equation for μ_s :

$$\frac{\partial \mu_s}{\partial t} = D\nabla^2 \mu_s - \frac{\mu_s}{\tau_m} + \mu_s \times \omega. \quad (5.17)$$

We emphasize again, that only the z -component of the pseudospin chemical potential accounts for an effective magnon spin accumulation and therefore corresponds to the finite magnon spin signal that can be detected via our device geometry. The last term on the right hand side of Eq. (5.17) takes into account the precessional behavior of the pseudospin chemical potential. If we consider that $\mu_s \parallel \omega$, the last term vanishes resulting in the well-known spin/magnon diffusion equation introduced in Sec. 2.5.2. However, when $\mu_s \not\parallel \omega$ the nonequilibrium pseudospin chemical potential does not correspond to the eigenmodes of the system and starts to precess around ω .

We can further define the pseudospin current density

$$\underline{j}_s = -D\nabla \otimes \mathcal{S} = -D\chi\nabla \otimes \mu_s. \quad (5.18)$$

The tensorial quantity accounts for the direction of the current flow as well as for the pseudospin direction.

5.1.3 Magnon Hanle Effect

In the following, we discuss the one-dimensional solution of the pseudospin chemical potential diffusion equation, as solving Eq. (5.17) in three dimensions is analytically intractable. For this reason, we consider a thin AFI film, such that μ_s does not depend on y within our chosen coordinate system (cf. Fig. 5.4). In addition, the system is considered translationally invariant along the x direction resulting in a μ_s that only depends on z . In general, using our two-terminal device geometry, where two HM electrodes are deposited on top of the AFI, magnons can be injected via a charge current driven through the injector. Note that we here work in the limit of small spin conductances of the HM/AFI interfaces [36, 45, 249]. Hence, the following boundary conditions can account for magnon spin injection [138]:

$$-D_m \chi \left. \frac{\partial \mu_{sz}}{\partial z} \right|_{z=0} = j_{s0}, \quad (5.19)$$

$$\left. \frac{\partial \mu_{sx, sy}}{\partial z} \right|_{z=0} = 0 \quad (5.20)$$

with j_{s0} the magnonic spin current density injected into the AFI by the injector electrode. This magnonic spin current density is typically proportional to the injector charge current (cf. Eq. (5.42)) at $z = 0$ (injector position), while for the x - and y -component explicitly no spin current is considered. Eq. (5.19) and Eq. (5.20) imply that only circularly polarized spin-up and -down magnons are injected into the AFI via the HM. This assumption is reasonable, since the interfacial exchange interaction at the AFI/HM interface leads to the excitation of localized spins with magnitude $+1$ or -1 in the AFI. The latter delocalize on a timescale, which is inversely proportional to the exchange energy, into a spin-up or spin-down magnon mode, respectively. On a much longer timescale that is inversely proportional to the mode coupling frequency, these delocalized spin-up and -down magnons start to precess as it is captured by our diffusion equation (5.17) as they are no longer the eigenmodes of the system, which are linearly polarized.

Without any loss of generality, we assume that $\boldsymbol{\omega} = \omega_x \hat{\mathbf{x}} + \omega_z \hat{\mathbf{z}}$, which allows us to capture the complete range of magnonic eigenmodes. As discussed above, a finite pseudofield z -component and $\omega_x = 0$ result in spin-1 magnons in the AFI corresponding to a circular precession of the Néel vector in the Landau-Lifshitz description. For $\omega_z = 0$ and $\omega_x \neq 0$ the AFI hosts spin-0 magnons and thus corresponds to linear oscillations of the Néel vector. When both components are finite ($\omega_x \neq 0, \omega_z \neq 0$), the AFI bears a spin with a magnitude between 0 and 1

that translates into an elliptical precession of the Néel vector [128, 226]. Thus, the steady state Eq. (5.17) simplifies to

$$D_m \frac{\partial^2 \boldsymbol{\mu}_s}{\partial z^2} - \frac{\boldsymbol{\mu}_s}{\tau_m} + \boldsymbol{\mu}_s \times (\omega_x \hat{\mathbf{x}} + \omega_z \hat{\mathbf{z}}) = 0. \quad (5.21)$$

Consistent with the requirement that the injected magnonic spin decays at large distances, we further assume that $\boldsymbol{\mu}_s(z \rightarrow \infty) = 0$. Finally, after some algebra, we obtain the 1D solution of the diffusion equation as

$$\mu_{sz}(z) = \mu_{\text{osc}}(z) + \mu_{\text{dec}}(z), \quad (5.22)$$

$$\begin{aligned} \mu_{\text{osc}}(z) &= \frac{\omega_x^2}{\omega_x^2 + \omega_z^2} \frac{l_m j_{s0}}{D_m \chi (a^2 + b^2)} e^{-\frac{az}{l_m}} \\ &\times \left[-b \sin\left(\frac{bz}{l_m}\right) + a \cos\left(\frac{bz}{l_m}\right) \right], \end{aligned} \quad (5.23)$$

$$\mu_{\text{dec}}(z) = \frac{\omega_z^2}{\omega_x^2 + \omega_z^2} \frac{l_m j_{s0}}{D_m \chi} e^{-\frac{z}{l_m}}, \quad (5.24)$$

where $l_m \equiv \sqrt{D_m \tau_m}$ is the magnon decay length and we have additionally defined

$$a \equiv \frac{1}{\sqrt{2}} \sqrt{1 + \sqrt{1 + \beta^2}}, \quad (5.25)$$

$$b \equiv \frac{1}{\sqrt{2}} \sqrt{-1 + \sqrt{1 + \beta^2}}, \quad (5.26)$$

$$\beta^2 \equiv \tau_m^2 (\omega_x^2 + \omega_z^2). \quad (5.27)$$

Eqs. (5.22)-(5.27) are the key result of Ref. [138] and allow for a general understanding of diffusive magnon spin transport in AFIs. Note that although our magnonic spin transport description is strictly speaking based on a low temperature approximation, it has been found to work well even at elevated temperatures [250, 251]. We see that μ_{sz} , and thus the magnon spin transport signal in the AFI consists of two distinct contributions, namely a solution μ_{dec} decaying and a solution μ_{osc} oscillating along the z -direction.

The former, described by Eq. (5.24), stems from magnonic eigenmodes that bear a finite spin or in other words the pseudospin exhibits a finite z projection. We emphasize that this contribution decays with the usual magnon decay length l_m . In easy-axis AFIs hosting spin-1 eigenexcitations [134, 163] this is the only mode of spin transport. For $\omega_x = 0$, when the AFI only hosts spin-1 magnons carrying the diffusive spin current, our results are consistent with the findings for easy-axis AFIs [36, 134, 249]. In a perfect easy-plane AFI this contribution is expected to be absent, as the eigenmodes are perfectly spinless, i.e. $\omega_z = 0, \omega_x \neq 0$. However, in general the easy-plane phase features a small but finite anisotropy within the

easy-plane [234, 252, 253] resulting in a correspondingly small spin of the magnonic eigenmodes. Within the pseudospin picture, this corresponds to $|\omega_x| \gg |\omega_z| > 0$. Overall, the decaying part can be understood as the fractional circular polarization content, which is given by the prefactor $\omega_z^2/(\omega_x^2 + \omega_z^2)$. Thus, we refer to the signal contribution μ_{dec} as the "finite-spin signal" in the discussion below.

The second contribution μ_{osc} given by Eq. (5.23) originates from the temporal evolution of the pseudospin chemical potential resulting in an oscillating behavior of the magnon spin signal. In contrast to the finite-spin signal, the oscillating behavior decays faster than l_m . The relaxation rate is additionally decreased by the factor a (cf. Eq. (5.25)). Since the magnons take different trajectories on their way from injector to detector, they arrive with different phases at the detector, and thus interfere destructively [75, 138, 240]. As discussed above, the spin-1 magnons injected by the HM injector are not the eigenmodes of the system when $\omega_x \neq 0$ and, as a result, their properties evolve with time. The latter, is captured by the pseudospin precession about the pseudofield with a precession frequency of $\omega = \sqrt{\omega_x^2 + \omega_z^2}$. The quantity ω depends on various contributions, such as anisotropy or DMI, to the magnetic free energy density. In general, the precession frequency can be tuned via an external magnetic field allowing for an experimental handle to control the magnon spin signal. In this thesis, we assume a linear dependence of the precession frequency on the applied magnetic field. We provide a more detailed discussion on this relation and the origin of the pseudofield in Sec. 5.1.4. In Eq. (5.27) we introduce the normalized pseudofield magnitude β which is proportional to the precession frequency and thus is also tuned via the applied magnetic field. In easy-plane hematite it has been shown that the detected magnon spin signal exhibits an oscillating behavior as a function of the applied magnetic field, which shares similarities with the Hanle effect and that $\omega \approx \omega_x$ vanishes at a finite compensation field H_c . Therefore, we call this oscillating contribution μ_{osc} the "Hanle signal"³⁹.

In the following, we give an intuitive picture of the magnetic field-dependent Hanle signal first introduced in Ref. [127], in which the first observation of the magnon Hanle effect has been reported. To this end, we consider a similar device that is used for the experiments consisting of a thin AFI film with an easy-plane anisotropy and two HM electrodes on top, which allow to use our all-electrical transport scheme. Furthermore, the pseudofield ω points along the positive x -direction⁴⁰. In Fig. 5.4(a)-(c) a schematic of the device as well as the evolution

³⁹In contrast to the situation for electrons, where the spin precession and Hanle effect originate from the Zeeman coupling of the electron spin to the external magnetic field, the pseudofield ω is determined by various free energy contributions describing the AFI.

⁴⁰In this work, the coordinate system of the creation operator space, where the pseudofield vector ω is defined on a Bloch sphere coincides with the one in real space, where we define the device parameters. In general, these two coordinate systems do not need to be equal.

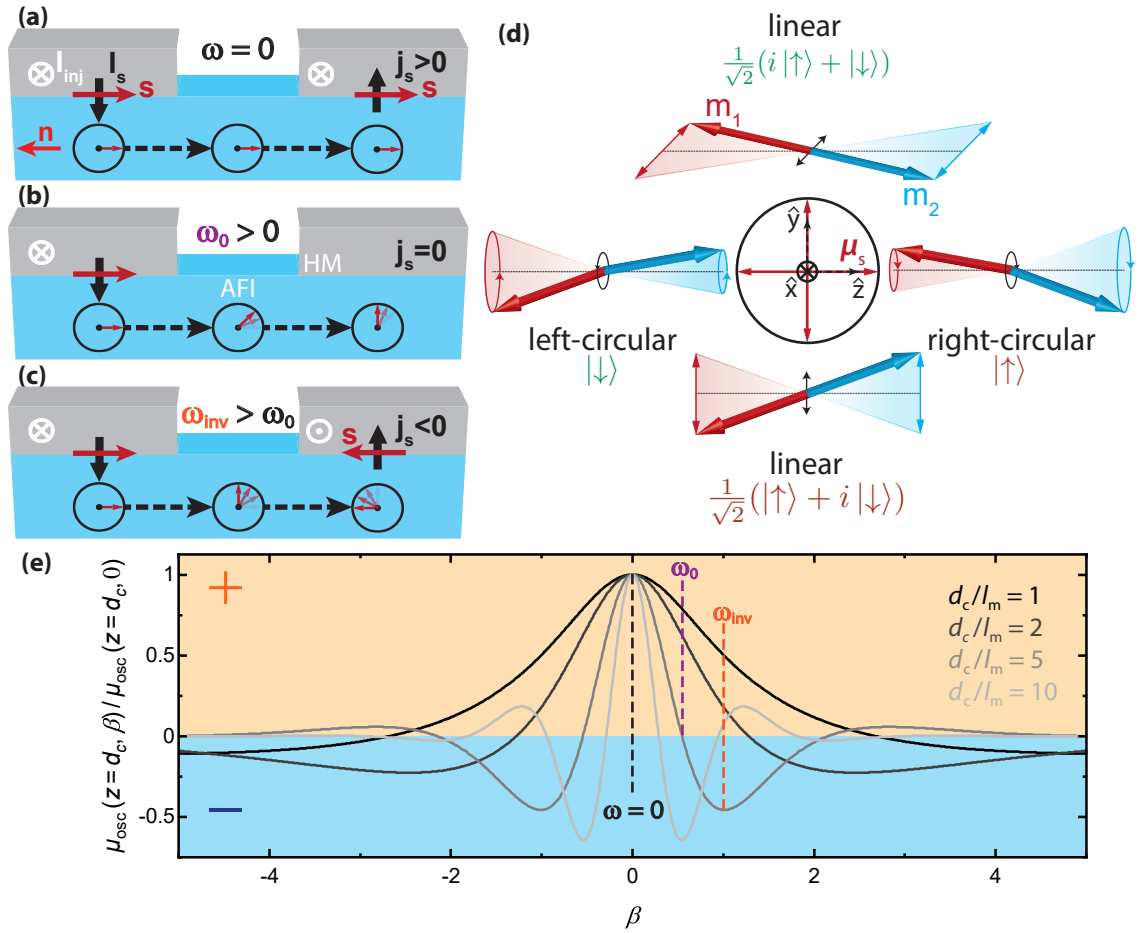


Fig. 5.4 – (a)-(c) At the injector a z -polarized magnon spin and pseudospin currents ($\mu_s \parallel \hat{z}$) are injected into the AFI corresponding to right- and left-circular precessions of the Néel vector, which are represented by spin-up and -down magnons carrying spin ± 1 . As the magnons propagate from injector to detector, the pseudospin precesses away from the z -axis and the Néel vector precession becomes increasingly elliptical resulting in a linear oscillation for $\mu_s \parallel \hat{y}$, corresponding to zero-spin excitations. The pseudospin precesses with a frequency that is controlled by the applied magnetic field. The actual magnonic spin μ_{sz} probed in our experiments is given by the projection of the pseudospin chemical potential on the z -direction and the measured magnon spin signal at the detector is (a) positive, (b) zero and (c) negative. (d) Relation between the direction of the pseudospin chemical potential μ_s and the Néel vector dynamics with the pseudofield $\omega \parallel \hat{x}$. (e) Normalized magnon chemical potential μ_{osc} (Eq. (5.23)) as a function of the normalized pseudofield magnitude β for different ratios of the distance d between injector and detector and the magnon decay length l_m . For distances significantly larger than l_m several oscillations appear. While ω_0 and ω_{inv} show a clear dependence on the ratio d_c/l_m , the position of $\omega = 0$ does not depend on the distance, since the pseudospin chemical potential does not precess in the AFI in this case, as depicted in panel (a). The upper panels (a) to (d) are adapted from Ref. [127].

of the pseudospin chemical potential μ_s for three different precession frequencies $\omega \approx \omega_x$. In experiments ω can be varied with finite applied magnetic fields. To recap, the connection between μ_s and the Néel vector dynamics is illustrated for four different directions in Fig. 5.4(d). When a charge current I_{inj} is applied to the injector electrode, a spin accumulation with polarization \mathbf{s} builds up at the AFI/HM interface due to the SHE. Due to spin-flip scattering spin-1 magnons corresponding to circularly polarized Néel vectors are injected in the AFI. In our case, this corresponds to a pseudospin chemical potential pointing along the positive z -direction. Since $\mu_s \nparallel \omega$, the pseudospin chemical potential precesses in the z - y plane with a certain precession frequency ω that depends on the magnitude of the pseudofield, while the magnons diffuse from the injector towards the detector, where μ_s has reached a finite precession angle with respect to the z -axis. The actual spin given by the z -component of μ_s leads to a spin current density j_s in the detector electrode, which is converted back into a charge current via the inverse SHE.

Figure 5.4(a) sketches the situation for a vanishing pseudofield. In experiments this can be achieved by applying a finite magnetic field that modifies the free energy landscape in such a way that the described mode coupling vanishes, leading to $\omega = 0$. We refer to this specific magnetic field value as the compensation field H_c . In the case of $\omega = 0$, μ_s does not precess in the AFI, but only varies along the z -direction. As depicted in Fig. 5.4(d), the magnonic spin transport is exclusively carried by circular polarized magnons, similar to easy-axis AFIs [134, 163]. As μ_s is fully aligned along \hat{z} (zero precession angle), we expect the magnon spin signal at the detector to be maximal. In Fig. 5.4(e), we plotted the normalized Hanle signal μ_{osc} for a fixed injector-detector spacing d_c as a function of the normalized pseudofield magnitude β (Eq. (5.27)), which is a measure for the applied magnetic field. The signal depending on the pseudofield magnitude is shown for different ratios d_c/l_m . First focusing on $d_c/l_m = 2$, we find that the maximum detector signal at H_c is perfectly represented by our theory model.

For a finite positive pseudofield, μ_s starts to precess counter-clockwise according to our definition. Hence, the precession angle increases at a fixed detector position, resulting in a smaller projection of the pseudospin chemical potential on the z -axis. This leads to the expected decreasing Hanle signal (cf. Fig. 5.4(e)). The signal decreases until it approaches zero for a pseudofield $\omega_0 > 0$ ($H_0 > H_c$) as depicted in Fig. 5.4(b). At ω_0 , the precession angle at the detector position has reached 90° and μ_s points along \hat{y} , yielding a vanishing projection on \hat{z} , and thus a vanishing Hanle signal. In the Landau-Lifshitz picture (Fig. 5.4(d)), this corresponds to a transmutation from circularly polarized magnons (spin-up) injected at the injector to linearly polarized magnons at the detector carrying zero spin.

For even larger magnitudes of the pseudofield for a fixed d_c , the precession angle becomes larger than 90° at the detector position, which represents a projection of μ_s along the negative z -direction. Besides the magnon pseudospin, also the actual spin densities have reversed directions, while propagating from injector to detector resulting in a negative Hanle signal (indicated by the orange line in Fig. 5.4(e)). The magnitude of the negative signal is largest for a precession angle of 180° which is identified with the pseudofield $\omega_{\text{inv}} > \omega_0$ ($H_{\text{inv}} > H_0$), as depicted in Fig. 5.4(c). In this case, the injected right circularly polarized magnons arrive as left circularly polarized magnons at the detector corresponding to an inversion of the magnon spin from spin $+1$ to spin -1 , as shown in Fig. 5.4(d). The signal magnitude at ω_{inv} is decreased compared to $\omega = 0$ due to the finite precession frequency. As discussed above, in this case the magnons take different trajectories on their way from injector to detector arriving with different phases at the detector, where we detect an averaged signal.

For negative pseudofield values ($\omega < 0$) or in terms of magnetic fields $H < H_c$, the precession sense of the pseudospin chemical potential is inverted and precesses clockwise. However, since only the projection of μ_s on the z -axis accounts for the measurable spin, the detected Hanle signal does not depend on the precession sense. This means, that the Hanle signal is symmetric in the vicinity of the compensation field H_c ($\omega = 0$). The various curves for different ratios d_c/l_m in Fig. 5.4(e) show that the position of the compensation field H_c is independent of the electrode spacing d_c , as the vanishing of the pseudofield depends on the free energy landscape, and thus on the properties of the investigated AFI. In contrast, the positions of ω_0 and ω_{inv} vary with the spacing d_c , as they depend on a finite precession frequency. Since the contribution μ_{osc} of the spin chemical potential decays faster than l_m the oscillations are progressively damped with increasing distance.

The theory model developed in Ref. [138] is expected to find applications in understanding magnonic spin transport in a broad range of AFIs. Due to its general validity for any coherently coupled bosonic modes, it may also trigger the development of spin-dynamics-inspired physical insights for, among others, coupled optomechanical [232] and optomagnonic systems [227, 254, 255].

5.1.4 Nonreciprocal Magnon Hanle Effect

Up to now, our theoretical model is based on materials and spatial configurations being inversion-symmetric [138]. In this section, we allow for different pseudofields in opposite directions due to inversion symmetry breaking. In particular, we assume that there is a finite nonreciprocal component of the pseudofield which is collinear with the reciprocal one, as this explains our experimental observations discussed

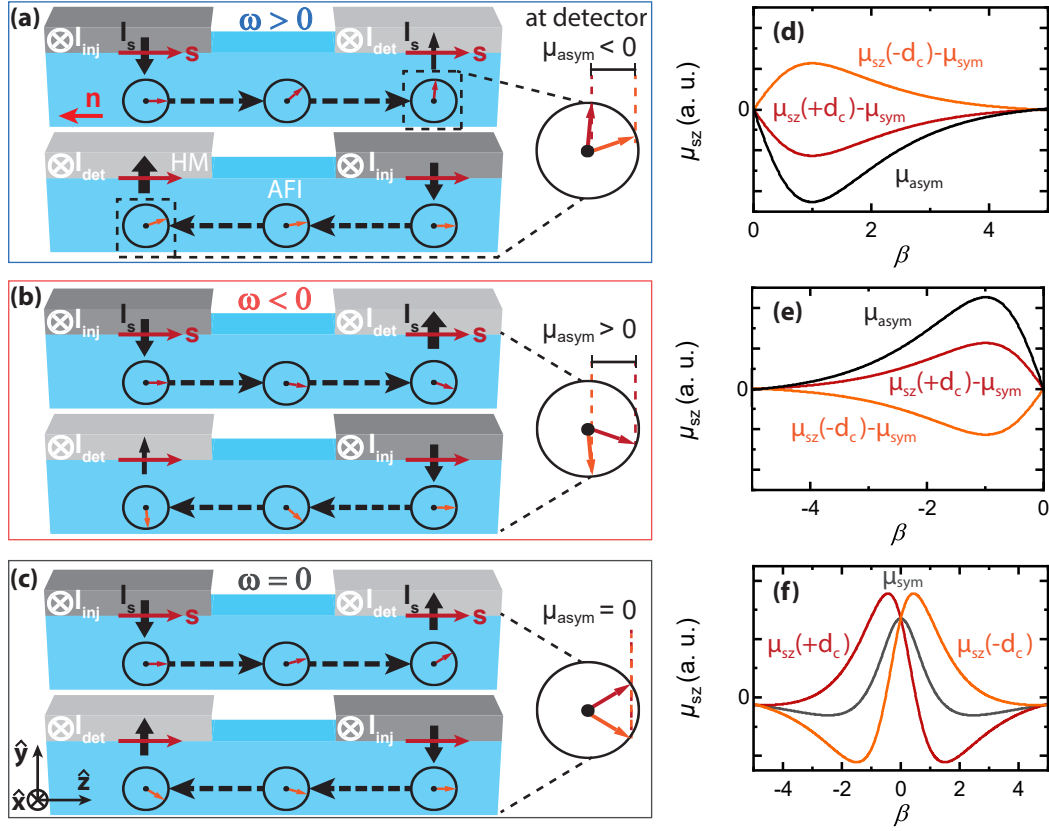


Fig. 5.5 – (a)-(c) Magnon spin and pseudospin transport in an AFI considering a nonreciprocal pseudofield directed along the x -direction. The two HM electrodes act as injector (dark gray) and detector (light gray) of the z -polarized magnonic spin. While the magnons propagate from injector to detector the pseudospin precesses around the pseudofield due to the easy-plane anisotropy in the studied AFIs. In contrast to Fig 5.4 the slightly different pseudofields in the forward (upper panels) and backward (lower panels) propagation directions result in a difference μ_{asym} in the observed magnon spin signal ($\propto \mu_{\text{sz}}$). Due to the different pseudospin precession rates a (a) negative, (b) positive and (c) zero difference μ_{asym} for the corresponding average pseudofield ω is obtained. **(d), (e)** Antisymmetric component of the pseudospin chemical potential μ_{asym} as a function of the normalized pseudofield magnitude β for an average pseudofield (d) $\omega > 0$ and (e) $\omega < 0$. The behavior is shown for the forward $z > 0$ (red line) and backward $z < 0$ (orange line) propagation direction as well as the difference of these two contributions in black. **(f)** Sum of the symmetric μ_{sym} and antisymmetric μ_{asym} component of the pseudospin chemical potential plotted versus β for the forward and backward propagation direction. For comparison, the pseudospin chemical potential is shown for $\mu_{\text{asym}} = 0$ (gray line). In all cases, a ratio of $d/l_s = 2$ has been used.

in Sec. 5.3. In our case, this means that both the reciprocal and nonreciprocal component are directed along \hat{x} . In an analogous manner as above, we first provide a qualitative picture of the underlying physics before delving into the theoretical details. We still consider the same device as before, which consists of an AFI with two spatially separated heavy metal electrodes on top to allow for an all-electrical injection and detection of magnonic spin currents due to the spin-orbit interaction in the HM. Considering the situation depicted in Fig. 5.5(a), a charge current driven through the left HM electrode injects magnon spin currents into the AFI, which corresponds to the injection of a z -polarized pseudospin current. As discussed above, the injected spin-1 magnons are not the eigenmodes of the easy-plane oriented AFI film and thus start to convert into other kinds of magnons with varying spin. This process is captured by the pseudospin precession about the pseudofield $\omega_+ \hat{x}$. Consequently, the magnon spin signal, which is given by the pseudospin z -component and is detected by the right HM electrode, depends on the pseudofield ω_+ . Remember that the latter can further be controlled via an applied magnetic field [127].

If we interchange the roles of the two HM electrodes (lower panel, Fig. 5.5(a)) and use the right electrode for spin injection, while the resulting magnon spin currents are detected at the left one, magnons in the transport channel might experience a slightly different pseudofield $\omega_- \hat{x}$ due to inversion symmetry breaking. As a result, the magnon spin signal is slightly different compared to the former configuration (upper panel, Fig. 5.5(a)). This difference is proportional to $\delta\omega \equiv (\omega_+ - \omega_-)/2$, and thus allows us to quantify the pseudofield nonreciprocity in the system. When the average pseudofield $\omega \equiv (\omega_+ + \omega_-)/2$ changes sign, i.e. the precession sense reverses direction, the difference $\delta\omega$ as well changes sign, as depicted in Fig. 5.5(b). Furthermore, the schematic in Fig. 5.5(c) emphasizes that $\delta\omega = 0$ when the pseudofield vanishes.

Considering this additional nonreciprocal pseudofield, we can describe the system via a one-dimensional diffusion equation with an extra term due to the nonreciprocal pseudofield:

$$\frac{\partial \boldsymbol{\mu}_s}{\partial t} = D_m \frac{\partial^2 \boldsymbol{\mu}_s}{\partial z^2} - \frac{\boldsymbol{\mu}_s}{\tau_m} + \boldsymbol{\mu}_s \times \omega \hat{x} - l \frac{\partial \boldsymbol{\mu}_s}{\partial z} \times \delta\omega \hat{x}. \quad (5.28)$$

Here, l is the mean free path of the AFI magnons. As discussed above, it is sufficient to consider that the pseudospin chemical potential $\boldsymbol{\mu}_s$, which describes the nonequilibrium magnons and their transport in the AFI, varies only along the z -coordinate between injector and detector. The last term on the right hand side of Eq. (5.28) is the new contribution as compared to the inversion-symmetric treatment above [138]. The additional term accounts for the different pseudofields in the forward (+) and

backward (−) direction, here within the random walk model, which describes the diffusive pseudospin transport with precession [75, 138, 256]. The magnon spin injection is again taken into account via the boundary conditions at the injector location at $z = 0$ given by Eqs. (5.19) and (5.20). Within our configuration, the direction of j_{s0} , the magnitude of the magnon spin current density driven by the electrical current through the injector electrode, is positive (negative) for transport along \hat{z} ($-\hat{z}$), leading to a + (−) sign in Eq. (5.19). To obtain the solution to Eq. (5.28) for $\mu_s(z)$ for both the forward $z > 0$ and the backward $z < 0$ case, we apply the stability requirements $\mu_s(z \rightarrow \infty) = 0$ and $\mu_s(z \rightarrow -\infty) = 0$ for the forward and backward direction, respectively. Since μ_{sz} at the detector location is directly proportional to the measured magnon spin signal, we can represent the latter by $\mu_{sz}(+d_c)$ ($\mu_{sz}(-d_c)$) for the forward (backward) transport configuration with d_c the injector-detector distance. We further define the symmetric $\mu_{\text{sym}} \equiv [\mu_{sz}(+d_c) + \mu_{sz}(-d_c)]/2$ and anti-symmetric $\mu_{\text{asym}} \equiv [\mu_{sz}(+d_c) - \mu_{sz}(-d_c)]/2$ contribution of the pseudospin chemical potential, which are evaluated as

$$\mu_{\text{sym}} = \frac{l_m j_{s0} e^{-\frac{a d_c}{l_m}}}{D_m \chi (a^2 + b^2)} \left[a \cos\left(\frac{b d_c}{l_m}\right) - b \sin\left(\frac{b d_c}{l_m}\right) \right], \quad (5.29)$$

$$\mu_{\text{asym}} = \frac{\omega \delta \omega \tau_m l}{|\omega| 2 l_m} \frac{\partial \mu_{\text{sym}}}{\partial b}. \quad (5.30)$$

Here, $a \equiv \sqrt{(1 + \sqrt{1 + \omega^2 \tau_m^2})}/2$, $b \equiv \sqrt{(-1 + \sqrt{1 + \omega^2 \tau_m^2})}/2$, and $l_m \equiv \sqrt{D_m \tau_m}$ is the magnon decay length. Note that we have retained only terms up to the first order in $l \delta \omega$, assuming $|l \delta \omega / (l_m \omega)| \ll 1$.

The expression obtained for μ_{sym} in Eq. (5.29) is the same as that in Eq. (5.23) for an inversion symmetric analysis [138]. In addition, μ_{asym} captured by Eq. (5.30) accounts for a finite nonreciprocity when the pseudofield is different for opposite directions, i.e. when $\delta \omega \neq 0$. Furthermore, Eq. (5.30) manifests the odd-in- ω behavior discussed above. To emphasize this behavior, we plot μ_{asym} (black curve) as a function of the normalized pseudofield magnitude $\beta = \omega \tau_m$ for an averaged pseudofield $\omega > 0$ in Fig. 5.5(d). The theoretical curve corresponds to the situation schematically depicted in Fig. 5.5(a). In addition, the antisymmetric components of the forward (red curve) and backward (orange curve) propagation direction are shown, representing the upper and lower panel of Fig. 5.5(a), respectively. For $\omega < 0$, shown in Fig. 5.5(e), the nonreciprocal component μ_{asym} clearly exhibits the expected sign change as motivated in Fig. 5.5(b). In Fig. 5.5(f), the total magnon spin signal for the forward $\mu_{sz}(+d_c)$ (red curve) and backward $\mu_{sz}(-d_c)$ (orange curve) propagation configuration is plotted for both precession senses of the pseudofield. For comparison, the situation for $\mu_{\text{asym}} = 0$ ($\delta \omega = 0$) is shown

in black, i.e. $\mu_{\text{sz}}(+d_c) = \mu_{\text{sz}}(-d_c) = \mu_{\text{sym}}$. This odd behavior in ω allows us to distinguish a nonreciprocal pseudofield contribution from other potential sources of nonreciprocity.

In order to apply this model to our experimental data, we introduce the following fit functions for the detected symmetric magnon spin signal amplitude $\Delta R_{\text{sym}}^{\text{el}}$:

$$\Delta R_{\text{sym}}^{\text{el}} = R_{\text{sym}}^0 + \frac{Al_{\text{m}}e^{-\frac{ad_c}{l_{\text{m}}}}}{D_{\text{m}}(a^2 + b^2)} \left[a \cos\left(\frac{bd_c}{l_{\text{m}}}\right) - b \sin\left(\frac{bd_c}{l_{\text{m}}}\right) \right]. \quad (5.31)$$

Here, $a \equiv \sqrt{(1 + \sqrt{1 + \omega^2\tau_{\text{m}}^2})}/2$, $b \equiv \sqrt{(-1 + \sqrt{1 + \omega^2\tau_{\text{m}}^2})}/2$, and $l_{\text{m}} \equiv \sqrt{D_{\text{m}}\tau_{\text{m}}}$ analog to above. As already mentioned, the pseudofield ω depends on various free energy contributions describing the AFI and is model dependent. In literature, two related but different origins have been suggested to dominate the compensation field H_c [127, 234, 238, 241]. Both models rely on the breaking of the rotational symmetry about the Néel vector that coherently couples magnons with opposing chiralities and results in a precession of pseudospin with frequency ω . However, we suggest in Ref. [127] that the compensation of the easy-plane anisotropy and the DMI are the origin of the vanishing pseudofield. In particular, we consider a constant contribution from the anisotropy and a linear applied magnetic field dependence stemming from the DMI [127]. In contrast Refs. [234, 238], suggests that at the magnetic compensation field the contributions from magnetic anisotropy and Zeeman term cancel with each other in the entire Brillouin zone. In this case, the precession frequency is composed of a magnetic anisotropy and a term that is square in the applied magnetic field stemming from the Zeeman energy [234, 238]. While the latter model considers the low k regime of the Brillouin zone, the former model focuses on the high k regime. In Ref. [241], it has been demonstrated that both models provide a good agreement with the experimentally observed Hanle peak. However, it could not be clearly determined whether the compensation field stems from either the square root of the anisotropy and exchange fields [238] or the DMI [127] and thus indicates that the full description of the magnon spin transport is probably based on a more generalized model that incorporates both models [241]. To this end, we treat the pseudofield ω as an experimentally observed field for the studied easy-plane hematite films. Here, we express the precession frequency as $\omega = c_2H - c_1$ after performing a Taylor expansion of ω around H_c . The physical origin of c_1 and c_2 is dependent on the microscopic origin of the pseudofield. For the fitting procedure, we choose D_{m} , τ_{m} , c_1 , c_2 , A and R_{sym}^0 as free fit parameters, while the center-to-center distance d_c is given by device geometry and thus is fixed. While $A = A_0j_{\text{s}0}/\chi$, where A_0 acts as a constant scaling parameter to take into account the conversion effects from the pseudospin chemical potential to the measured detector

signal $\Delta R_{\text{sym}}^{\text{el}}$, R_{sym}^0 accounts for the finite spin signal (cf. Eq. (5.24)). The fitting function for the antisymmetric magnon spin signal $\Delta R_{\text{asym}}^{\text{el}}$ reads

$$\Delta R_{\text{asym}}^{\text{el}} = R_{\text{asym}}^0 + \frac{\omega \delta \omega \tau_{\text{m}} l}{|\omega| 2l_{\text{m}}} \left[-\frac{2Al_{\text{m}} b e^{-\frac{ad_c}{l_{\text{m}}}} \left(a \cos\left(\frac{bd_c}{l_{\text{m}}}\right) - b \sin\left(\frac{bd_c}{l_{\text{m}}}\right) \right)}{D_{\text{m}}(a^2 + b^2)^2} + \frac{Al_{\text{m}} e^{-\frac{ad_c}{l_{\text{m}}}} \left(-\frac{bd_c}{l_{\text{m}}} \cos\left(\frac{bd_c}{l_{\text{m}}}\right) - \sin\left(\frac{bd_c}{l_{\text{m}}}\right) - \frac{ad_c}{l_{\text{m}}} \sin\left(\frac{bd_c}{l_{\text{m}}}\right) \right)}{D_{\text{m}}(a^2 + b^2)} \right]. \quad (5.32)$$

In general, the antisymmetric signal is fitted after the symmetric signal, as we utilize the extracted parameters from the fit to the symmetric part as fixed parameters. Consequently, this leaves only $\delta\omega l$ as a free fit parameter. Moreover, we allow for an additional offset signal R_{asym}^0 .

5.1.5 Influence of Low-energy Magnons

The introduced pseudospin chemical potential μ_s adequately describes the magnonic spin transport in an AFI for magnon wave vectors in nearly the whole Brillouin zone [138]. However, it is unable to capture the role of low-energy magnons. Although, the latter exhibit much longer scattering times or decay lengths and are excited strongly at the injector location due to their high thermal occupation probability [76, 125, 126], low-energy magnons are disregarded very often, since they constitute only a small fraction of the total magnons on the system [76]. However, many experiments demonstrated the importance and special role of these low-energy magnons [45, 248, 257]. In this section, we qualitatively discuss their role for the magnon spin transport in AFIs.

Our theoretical description is based on the assumption that the frequency difference $\Delta f_{\mathbf{k}}$ between the two eigenmodes is much smaller than their average frequency at each given wave vector \mathbf{k} [138]. Calculating the magnonic dispersion of the two eigenmodes $\omega_{\mathbf{k}}^{\pm}$ exemplarily for our system of choice, the AFI hematite, we will see that this assumption is not valid over the whole \mathbf{k} value range. In order to describe the magnon dispersion relation, we use the approach by Ka Shen [238], who addresses the magnon spectrum in an easy-plane AFI in the presence of an in-plane magnetic field. Note that we here only consider the most important results, while the details are published in Ref. [238]. In this theoretical model, the magnetic anisotropy and the antiferromagnetic exchange interaction between nearest neighbors is included. Additionally, the model accounts for the influence of DMI and an uniaxial in-plane anisotropy. Similar to our case, the model considers an external

magnetic field applied within the easy plane to control the orientation of the Néel vector. Without any loss of generality the magnetic field is set along a fixed direction, which in our case corresponds to the x -axis. As a result, the two coupled sublattice magnetizations \mathbf{M}_1 and \mathbf{M}_2 are canted and the net magnetization $\mathbf{M}_{\text{net}} = \mathbf{M}_1 + \mathbf{M}_2$ as well as the Néel vector $\mathbf{n} = \mathbf{M}_1 - \mathbf{M}_2$ are oriented along the x - and z -direction, respectively. The canting angle θ of the sublattice magnetization with respect to the z -direction is determined from the minimizing the free energy description for a system with $2N$ magnetic ions [238]:

$$E = -NS\hbar\omega_{\text{ex}} \cos(2\theta) - 2NS\hbar\omega_Z \sin(\theta) - NS\hbar\omega_{\text{DMI}} \sin(2\theta) - 2NS\hbar\omega_{\text{ani,ip}} \cos(\theta)^2, \quad (5.33)$$

where $\omega_{\text{ex}} = \gamma B_{\text{ex}}$ parameterizes the exchange energy with the gyromagnetic ratio $\gamma = g\mu_B/\hbar$ and the exchange field B_{ex} . Furthermore, $\omega_Z = \gamma B_{\text{ext}}$ is the Zeeman energy, $\omega_{\text{DMI}} = \gamma B_{\text{DMI}}$ the DMI energy, and $\omega_{\text{ani,ip}} = \gamma B_{\text{ani,ip}}$ the in-plane anisotropy energy. In addition, we define the out-of-plane (hard axis) magnetic anisotropy $\omega_{\text{ani}} = \gamma B_{\text{ani}}$, which is utilized below. Finally, we extract the canting angle by minimizing the total energy given in Eq. (5.33) with respect to θ ($\partial E/\partial\theta = 0$) and find ⁴¹

$$\theta = \frac{\omega_Z + \omega_{\text{DMI}}}{2(\omega_{\text{ex}} + \omega_{\text{ani,ip}})}. \quad (5.34)$$

A similar result has been found in Ref. [253].

In Ref. [238], the eigenfrequencies of the two linear polarized magnon modes in an easy-plane AFI are given by

$$\hbar\omega_{\mathbf{k}}^{\pm} = \sqrt{(\mathcal{A} + \mathcal{B}_{\mathbf{k}}^{\pm})(\mathcal{A} - \mathcal{B}_{\mathbf{k}}^{\pm} \pm 2C_{\mathbf{k}})}, \quad (5.35)$$

where the coefficients are defined as

$$\mathcal{A} = \hbar\omega_{\text{ex}} + \hbar\omega_{\text{ani}} + \hbar\omega_{\text{DMI}} \tan(\theta) + \hbar\omega_{\text{ani,ip}}(2 - 3\sin^2(\theta)), \quad (5.36)$$

$$\mathcal{B}_{\mathbf{k}}^{\pm} = \hbar\omega_{\text{ani}} + \hbar\omega_{\text{ani,ip}} \pm \gamma_k \hbar\omega_{\text{ex}}, \quad (5.37)$$

$$C_{\mathbf{k}} = \gamma_k \hbar\omega_{\text{ex}} \sin^2(\theta) \left(1 - \frac{\gamma'_k \omega_{\text{DMI}}}{\gamma_k \omega_{\text{ex}}} \cot(\theta) \right). \quad (5.38)$$

Here, $\gamma_k = \cos(ka/2)$ is the form factor for the exchange coupling with a the magnetic unit cell lattice constant and γ'_k the form factor for the DMI exchange coupling. In reality, only part of the exchange interacting bonds and thus number of

⁴¹Here, we assume that θ is small and only account for contributions in first order of θ , i.e., $\sin(\theta) \approx \theta$ and $\cos(\theta) \approx 1$.

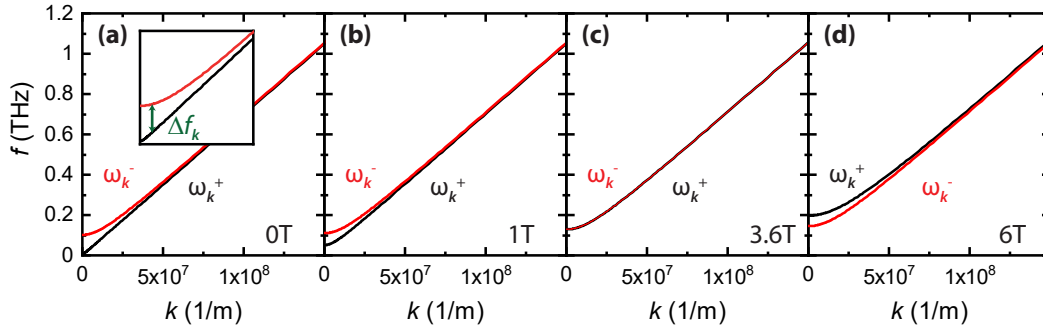


Fig. 5.6 – (a)-(d) Evolution of the magnonic dispersion of the two eigenmodes $\omega_{\mathbf{k}}^{\pm}$ in hematite [238] for increasing external magnetic field. (a) The zoom-in for zero applied magnetic field highlights the frequency difference $\Delta f_{\mathbf{k}}$ between the two eigenmodes for low k -values, where we lose the validity of linear response. (b)-(d) While $\omega_{\mathbf{k}}^{-}$ remains unchanged, $\omega_{\mathbf{k}}^{+}$ increases with energy for an increasing magnetic field strength. For (c) $\mu_0 H = 3.6$ T the frequency dependencies of two eigenmodes are identical.

neighbors are involved in the DMI. In general, this means that $\gamma_k \neq \gamma'_k$ leading to a k -dependent ratio $C_{\mathbf{k}}/\gamma_k$ [238]. However, for simplicity we assume that $\gamma_k = \gamma'_k$.

Using this assumption and Eq. (5.35), we are able to calculate the dispersion relation of hematite. The corresponding results are shown in Fig. 5.6 for different external magnetic fields. Here, we used the parameters $B_{\text{ex}} = 1000$ T, $B_{\text{ani}} = 2$ mT, $B_{\text{ani, ip}} = 0.02$ mT at room temperature [253] and $a = 0.503$ nm [158]. Without externally applied magnetic field $\mu_0 H = 0$ T, shown in Fig. 5.6(a), the two magnon modes are energetically very close at large wave vectors, fulfilling the requirement for our pseudospin transport description. However, they split up for low k values. While the $\omega_{\mathbf{k}}^{-}$ -mode approaches a finite value in a range of about 100 GHz for $k = 0$, the $\omega_{\mathbf{k}}^{+}$ -mode decreases linearly for $k \rightarrow 0$ and reaches a finite energy of about $f \approx 7$ GHz, which is in good agreement with values found in other works [252, 253]. If the frequency difference $\Delta f_{\mathbf{k}}$ between the two eigenmodes and the average frequency start to be comparable, initially we merely lose the validity of linear response, i.e., the proportionality between pseudospin and its chemical potential. But, the qualitative physics are still described adequately by the pseudospin picture. For further increasing $\Delta f_{\mathbf{k}}$, as it is the case in Fig. 5.6(a) for zero applied field, where the lower branch approaches zero at $k = 0$, while the upper branch remains finite, the pseudospin chemical potential completely fails to capture the contribution of low-energy magnons to the magnonic spin transport. The pseudospin, however, remains a well-defined and useful quantity. This means, its z projection still corresponds to the spin carried by the eigenmodes [138]. Thus, we expect that the low-energy magnons simply contribute to the finite-spin signal and hence can be captured by Eq. (5.24) as an additional offset signal that, in principle, would decay on a longer

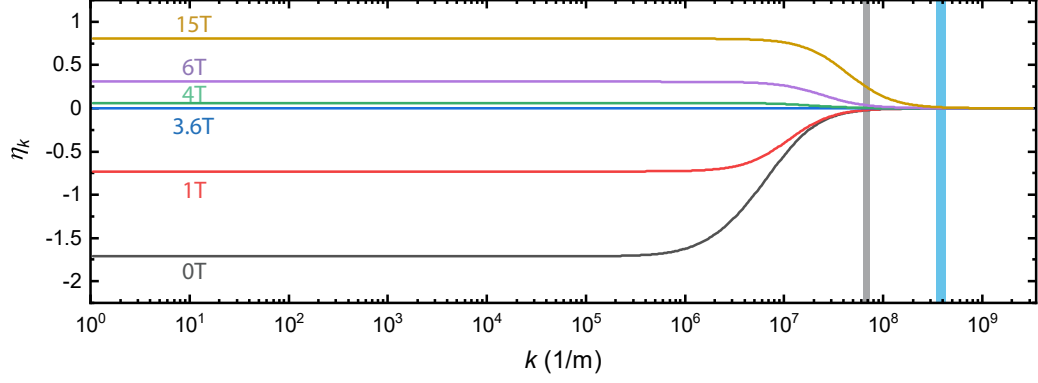


Fig. 5.7 – Ratio $\eta_{\mathbf{k}}$ as a function of the wave number k for various external magnetic fields. The shaded regions indicate typical $2\pi/t_m$ values for thick (gray region) and thin (blue region) AFI films studied in this chapter.

length scale than l_m . The pseudospin precession would be unaffected by these low-energy magnons.

Fig. 5.6 clearly shows that the splitting of the two magnon modes at small wave numbers is influenced by the external magnetic field. While $\omega_{\mathbf{k}}^-$ is nearly unaffected by changes in the applied field, $\omega_{\mathbf{k}}^+$ shifts up in energy with increasing B_{ext} for small k values. At a certain magnetic field value the splitting even vanishes (Fig. 5.6(c)) and for further increasing magnetic field the splitting is reversed (Fig. 5.6(d)). Since an increase of the applied magnetic field increases the energy of the low-energy magnons [138], we expect the occupation probability of the latter to decrease and hence also their contribution to the finite-spin signal. Nevertheless, they can be adequately described by the pseudospin chemical potential when the magnetic field is increased. In order to quantify, at which k values and magnetic fields one has to account for low-energy magnons, we define the ratio

$$\eta_{\mathbf{k}} = 2 \frac{\omega_{\mathbf{k}}^+ - \omega_{\mathbf{k}}^-}{\omega_{\mathbf{k}}^+ + \omega_{\mathbf{k}}^-}, \quad (5.39)$$

where we used $\Delta f_{\mathbf{k}} = f_{\omega_{\mathbf{k}}^+} - f_{\omega_{\mathbf{k}}^-}$. If $|\eta_{\mathbf{k}}| > 1$, i.e. when the energy difference between the two modes is no longer smaller than the average energy of the two modes at a given k value, then the pseudospin chemical potential description does no longer hold and one has to account for an additional finite-spin signal due to low-energy magnons. In Fig. 5.7, we plotted the ratio $\eta_{\mathbf{k}}$ as a function of k for different magnetic field magnitudes. We find that $|\eta_{\mathbf{k}}| > 1$ applies only for small k values. Furthermore, the calculated $\eta_{\mathbf{k}}$ shows the expected dependence on the external magnetic field.

It is important to mention that for very thin films, the density of low-energy magnons is reduced considerably. In this case, the boundary condition along the

film thickness imposes a finite and large k . In a simplified model, the out-of-plane component of the wave vector can be written as $k_{\text{oop}} \sim n\pi/t_m$ with n an integer value in range from 0 to t_m/a , where a defines the lattice constant and t_m the sample thickness. When t_m is small, $n = 0$ is the only value, which has a magnon mode energy comparable to or lower than the thermal energy. In contrast, for any nonzero n , k_{oop} becomes very large and so does the k -dependent contribution to the magnon energy, which leads to a considerable diminishing of the low-energy magnons in the system. The number n of allowed k_{oop} values increases with increasing t_m , and hence does the number of magnon modes. Consequently, a contribution of low-energy magnons is expected to become relevant in thick AFI films at low applied magnetic fields. Furthermore, when the thickness of the AFI increases, the validity of our model encounters two important length scales associated with magnons, namely the thermal wavelength l_{th} and the decay length l_m . In general, the former is much smaller than the magnon decay length. The magnon thermal wavelength determines the effective dimensionality of the AFI and thereby influences the magnon density of states and their role in the magnonic spin transport. In our experiments, we probe this transition determined by l_{th} , and thus we refer to thick films when t_m is on the order or larger than l_{th} , while thin films are characterized by $t_m \ll l_{\text{th}}$. In Fig. 5.7, we marked the corresponding k values, using the relation $2\pi/t_m$, for thin and thick AFI samples studied further below. While we do not expect an influence due to low-energy magnons in our thin films, we have to consider their contribution to the spin transport in our thick films.

5.1.6 Spin Injection and Detection

Up to now, we focused on the magnon spin propagation and dynamics in an AFI, however, we neglected to explicitly take into account the injection and detection process at the HM leads. In our pseudospin description, we assumed for the magnon spin injection a z -polarized pseudospin current density at $z = 0$, while the spin chemical potential μ_{sz} was treated as the magnon spin signal measured at the detector. However, this approach offers no direct relation between the charge current driven through the injector and the detected voltage signal in the detector electrode in our experiments. Here, we provide a broad and general theoretical framework to take this issue into account.

In order to be able to capture the essential physics, we assume that the AFI is weakly coupled to the injector and detector electrodes. Note that a complete analysis of the injection and detection process involves several parameters and becomes tedious, even for the much simpler case of a ferromagnet [76]. To describe the spin flow in our system, we consider an equivalent circuit diagram, which is depicted in

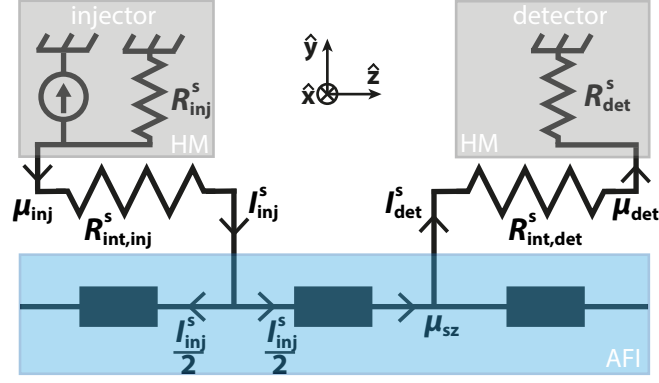


Fig. 5.8 – Sketch of an equivalent circuit diagram for magnonic spin injection and detection in our AFI/HM device. A charge current driven through the injector electrode generates a spin accumulation μ_{inj} in the HM, which in turn injects a spin current I_{inj}^s into the AFI. The injected spin current propagates and evolves as pseudospin transport. The spin current I_{det}^s detected at the detector electrode accounts for the magnon spin chemical potential $\mu_{sz}(z)$. In our case, we use the approximation that the AFI is weakly coupled to the injector and detector HM electrodes.

Fig. 5.8. Within our approximation, we consider that the interfacial spin resistances $R_{int,inj}^s$ and $R_{int,det}^s$ are much larger than the other resistances in the depicted circuit.

In our chosen configuration, a charge current density $j_{ci}\hat{x}$ is driven through the injector, which generates a z -polarized electronic spin accumulation at the HM/AFI interface that is described by [76]

$$\mu_{inj} = 2e\theta_i l_{si} \rho_i \tanh\left(\frac{t_i}{2l_{si}}\right) j_{ci} \equiv \kappa_i j_{ci}. \quad (5.40)$$

In this case, e is the elementary charge, θ_i the spin Hall angle of the injector material, l_{si} the spin decay length in the injector, ρ_i the injectors' resistivity and t_i its thickness. According to Ref. [76], the injected magnon spin current can be written as

$$I_{inj}^s = g_i w_i L (\mu_{inj} - \mu_{sz}) \approx g_i w_i L \mu_{inj} \quad (5.41)$$

with g_i the interfacial spin conductivity, w_i the injector width, and L the device length along \hat{x} , which we assume to be equal for the injector, detector, and AFI. The used approximation in Eq. (5.41) is valid in the limit of $g_i w_i L \rightarrow 0$, i.e. the entire "potential" drops across the interface. Furthermore, we have to consider that only half of the injected spin current flows κ towards the detector (positive z -direction), which leads to

$$j_{s0} = \frac{g_i \kappa_i}{2t_m t_i} I_{inj}^s, \quad (5.42)$$

where t_m is the thickness of the AFI and $I_{inj} = j_{ci}w_it_i$ defines the total charge current driven through the injector. Finally, the relation in Eq (5.42) provides a connection of the injected magnon spin current density j_{s0} , which is assumed in our pseudospin model via Eq. (5.19), to the relevant experimental variable I_{inj} .

In a similar manner, we can define the spin current injected into the detector according to [76]

$$I_{det}^s = g_d w_d L (\mu_{sz}(z) - \mu_{det}) \approx g_d w_d L \mu_{sz}(z), \quad (5.43)$$

where g_d is the interfacial spin conductivity at the detector, and w_d the detector width. Moreover, $\mu_{sz}(z)$ determines the z -component of the magnon spin chemical potential at the detector position z . Our assumption of a weak interface coupling between the AFI and the detector, results in $\mu_{det} \approx 0$. We obtain for the inverse spin Hall effect voltage under open circuit conditions [113]

$$V_{det}^{el} = \frac{\kappa_d g_d L}{\hbar t_d} \mu_{sz}(z), \quad (5.44)$$

using the interfacial spin current given by Eq. (5.43) and defining κ_d similar to κ_i in Eq. (5.40), but for the detector. In order to account for all parameters relevant to the injection/detection process, we may express Eq. (5.22) in a dimensionless form according to

$$\mu_{sz}(z) = \frac{j_{s0} l_m}{D_m \chi} \tilde{\mu}_{sz}(z). \quad (5.45)$$

Here, the dimensionless variable $\tilde{\mu}_{sz}(z)$ contains all the information on the magnon pseudospin transport and dynamics in the AFI.

Employing Eqs. (5.42), (5.44) and (5.45), we finally arrive at the experimentally measured magnetoresistance at the detector electrode:

$$\Delta R_{det}^{el} = \frac{V_{det}^{el}}{I_{inj}} = \frac{2L}{\hbar} \frac{\kappa_d g_d}{2t_d} \frac{\kappa_i g_i}{2t_i} \frac{l_m}{D_m \chi t_m} \tilde{\mu}_{sz}(z) \quad (5.46)$$

$$= \frac{2L}{\hbar} \frac{\kappa_d \kappa_i}{4t_i t_d} \frac{l_m}{D_m t_m} \left(\frac{g_i g_d}{\chi} \right) \tilde{\mu}_{sz}(z). \quad (5.47)$$

Our simplified model shows that the injector-detector separation (z) only probes the magnonic spin current transport described by $\tilde{\mu}_{sz}(z)$. However, the magnitude of the magnetoresistance signal clearly depends on several parameters, which comprise the injector, detector, AFI, as well as their interfaces. If we have a look at the temperature dependence, our model suggests that the factors in the bracket of Eq. (5.47) have the largest impact on the signal. All three quantities g_i , g_d and χ are obtained by summing over all magnons modes, and thus increase in a similar way as

the number of magnons do in an AFI with increasing temperature [76]. Consequently, the term in the bracket also increases with temperature. Previous works [92, 258] showed that the remaining parameters in Eq. (5.47) are only weakly dependent on the temperature in spin Hall magnetoresistance experiments. It is important to mention that several of these parameters, which are relevant to account for the injection/detection process, cannot be extracted from the experiments discussed below. We should further mention that our approximation that the AFI and the HM leads are weakly coupled might not be very precise, as in experiments a not too weak coupling is required to allow for a detectable signal. In particular, deviations from our model are expected when the injector-detector distance becomes comparable to the magnon decay length l_m . In this limit, we have to account directly for the boundary conditions at the injector (Eqs. (5.19) and (5.20)) and the detector when the magnon spin transport is probed in an AFI [76]. However, although the magnitude of $\Delta R_{\text{det}}^{\text{el}}$ depends on several details, the qualitative variation of the signal with the injector-detector distance or the external magnetic field is directly given by the magnonic transport in the AFI via $\tilde{\mu}_{sz}(z)$ and we find that our simple analytical model can describe most of the observed features in $\Delta R_{\text{det}}^{\text{el}}$ in a wide range of devices very well.

5.2 Influence of Dimensionality on the Magnon Spin Transport

In general, a simple intuitive understanding of the transport of electrically and thermally induced magnonic spin currents in MOIs can be achieved by assuming a variation of the magnon chemical potential along only one direction [43, 45, 76, 138]. As discussed above, this is a good approximation in magnetic layers, which are much thinner than the magnon decay length. However, this is no longer true for magnetic layer thicknesses comparable to or larger than the magnon decay length, as for instance found for the prototypical ferro(ferri)magnet YIG. In Ref. [141], the authors performed a numerical analysis, which captures the variation of the magnon chemical potential across the thickness of the YIG layer assuming the magnetic layers and the corresponding magnon density of states in three dimensions (3D). This treatment was essential for reproducing certain experimental features in films with thicknesses comparable to the magnon decay length. In contrast, when the YIG film thickness becomes larger than the magnon thermal wavelength, which is typically much smaller than the magnon decay length, no new features have been found in these magnon spin transport studies. This transition/boundary can also be associated as a change in dimensionality of the magnetic layer from quasi-2D to

quasi-3D. Another work by Kehlberger *et al.* [257], was investigating the influence of the YIG thickness in spin Seebeck measurements, providing evidence for an important role of the magnon density of states and low-energy magnons when the magnon thermal wavelength boundary is crossed. Up to now, studies in the antiferromagnet hematite focused on thin films and the experimental findings were described utilizing a 1D pseudospin transport model [127, 138]. This raises the question whether there are any features in the magnon spin transport that depend sensitively on the effective dimensionality of the magnetic layer. To this end, we investigate the magnonic spin transport in hematite films with varying thickness at different temperatures experimentally probing the transition characterized by the magnon thermal wavelength. In this section, we find, for both a $t_m = 15$ nm and a $t_m = 100$ nm thick film, a distinct signal caused by the magnon Hanle effect utilizing two-strip devices for the all-electrical injection and detection process. However, the measured magnon spin signal exhibits clear differences in both films. For the thick film, in contrast to the thinner one, we observe an oscillating behavior in the high magnetic field regime, while we find a constant offset signal in the low magnetic field regime. We use our theoretical model introduced above to discuss the data in detail and find that the latter can be attributed to the diffusive transport of low-energy finite-spin magnons.

Main parts of text and figures in this Section are reused from J. Gückelhorn, A. Kamra, T. Wimmer, M. Opel, S. Geprägs, R. Gross, H. Huebl, and M. Althammer, *Influence of low-energy magnons on magnon Hanle experiments in easy-plane antiferromagnets*, [Physical Review B 105, 094440 \(2022\)](#).

5.2.1 Experimental Details

The investigated α -Fe₂O₃ films are grown on (0001)-oriented Al₂O₃ substrates via pulsed laser deposition at the Walther-Meißner-Institut as described in Sec. 3.2. The films studied in this section have a thickness of $t_m = 15$ nm and $t_m = 100$ nm and exhibit no Morin transition, as discussed in detail in Sec. 3.1.2. Hence, both hematite films feature an out-of-plane DMI vector and an easy-plane phase over the whole temperature range [127]. As depicted in Fig. 5.9(a), the Néel vector \mathbf{n} and the two sublattice magnetizations \mathbf{M}_1 and \mathbf{M}_2 lie in the (0001)- or xz -plane. Due to the DMI the two sublattice magnetizations are slightly canted, resulting in a net magnetization $\mathbf{M}_{\text{net}} = \mathbf{M}_1 + \mathbf{M}_2$, which is oriented along the external magnetic field. Most importantly, \mathbf{M}_{net} can additionally be controlled by the magnitude of the applied magnetic field and thus we obtain a handle on the pseudofield. To allow for an all-electrical generation and detection of pure spin currents, we employ several two-strip structures with varying center-to-center distances d_c on top of the film

(cf. Fig. 5.9(a)). All Pt nanostraps have a thickness of $t_{\text{Pt}} = 5$ nm and a length of $l_{\text{inj}} = l_{\text{det}} = 100 \mu\text{m}$. The pairs of two Pt electrodes have either a width of $w_{\text{inj}} = w_{\text{det}} = 250$ nm or 500 nm. For all our measurements in hematite, we utilize the dc-detection technique. Typically, a dc charge current I_{inj} featuring current densities of $j_{\text{inj}} = I_{\text{inj}}/(w_{\text{inj}}t_{\text{Pt}}) = 2 \times 10^{11}$ A/m² is applied to the injector electrode⁴². In contrast to the experiments in YIG, the magnon spin signal measured in the hematite films is given by $R_{\text{det}}^{\text{el}} = V_{\text{det}}^{\text{el}}/I_{\text{inj}}$ in order to account for the different geometries and injector currents I_{inj} . While the angle-dependent measurements presented in the following are conducted in setup (ii), the magnetic field-dependencies are recorded in setup (iii) (cf. Sec. 3.3).

5.2.2 Thin Hematite Film

First, we focus on the $t_{\text{m}} = 15$ nm thin hematite film. The very first results on a thin easy-plane hematite film with similar thickness have been published in our previous work [127]. To investigate the magnon spin transport in our device, we apply the magnetic field along $-x$ -direction ($\varphi = 270^\circ$), which orients the Néel vector \mathbf{n} along $-\hat{z}$. This means, $\mathbf{H} \perp \mathbf{n}$ and thus, we expect a maximum magnon spin signal at the detector. In Fig. 5.9(b), we plotted the amplitude of the magnon spin signal, which is given by $\Delta R_{\text{det}}^{\text{el}} = R_{\text{det}}^{\text{el}}(\varphi = 270^\circ) - R_{\text{det}}^{\text{el}}(\varphi = 180^\circ)$, as a function of the magnetic field strength $\mu_0 H$ for two different injector-detector distances $d_c = 700$ nm (blue data points) and $d_c = 1000$ nm at a temperature of $T = 200$ K. The latter term in $\Delta R_{\text{det}}^{\text{el}}$ accounts for a constant offset originating from the experimental setup. In this configuration the magnetic field is directed along \hat{z} ($\mathbf{H} \parallel \mathbf{n}$), where no electrical magnon excitation is expected.

For both distances, the signal amplitude $\Delta R_{\text{det}}^{\text{el}}$ exhibits a pronounced peak at $\mu_0 H \approx 8$ T. The positive magnon spin signal decreases until it approaches zero signal for increasing as well as for decreasing magnetic field magnitude. For even larger or smaller magnetic field values, $\Delta R_{\text{det}}^{\text{el}}$ features a sign change, which is particularly pronounced for the structure with $d_c = 1000$ nm. This behavior of the magnon spin signal amplitude is in perfect agreement with our previous experiments [127]. Comparing the results with our theoretical model introduced in Sec. 5.1.3, we can describe our findings in terms of the "Hanle signal" (cf. Fig. 5.4). The pronounced peak can be attributed to the compensation field $\mu_0 H_c$, where the pseudofield vanishes ($\omega = 0$). As the condition for $\omega = 0$ is determined by the free energy landscape of the AFI, the peak position does not depend on the distance in accordance with our data. For $\Delta R_{\text{det}}^{\text{el}} = 0$, the pseudospin chemical potential vector

⁴²This means for injectors with $w_{\text{inj}} = 250$ nm a dc charge current of $I_{\text{inj}} = 250 \mu\text{A}$ is applied, while $I_{\text{inj}} = 500 \mu\text{A}$ is driven through injectors with $w_{\text{inj}} = 500$ nm.

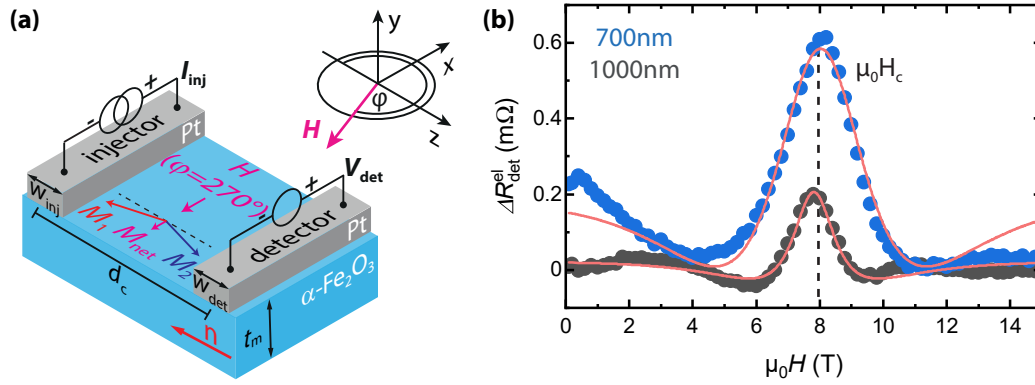


Fig. 5.9 – (a) Sketch of the sample configuration, the electrical wiring scheme, and the coordinate system with the in-plane rotation angle φ of the applied magnetic field $\mu_0 \mathbf{H}$. The two magnetic sublattices \mathbf{M}_1 and \mathbf{M}_2 are slightly canted and the resulting net magnetization \mathbf{M}_{net} is directed along the applied magnetic field $\mu_0 \mathbf{H}$. While $\mathbf{M}_{\text{net}} \parallel \mathbf{H}$, the Néel order parameter $\mathbf{n} \perp \mathbf{H}$. (b) Amplitude of the electrically induced magnon spin signal $\Delta R_{\text{det}}^{\text{el}}$ as a function of the magnetic field magnitude $\mu_0 H$ applied along the x -axis for two devices with different center-to-center distance d_c on a $t_m = 15$ nm thin hematite film for $T = 200$ K. The red lines are fits to the data via Eq. (5.31).

is rotated by 90° , which correspond to the propagation of linearly polarized magnon modes and thus zero spin is carried. The sign change of the magnon spin signal amplitude corresponds to a 180° rotation of the pseudospin chemical potential vector. Since the spin defining the pseudospin z -component is directly related to the precession sense of the corresponding magnon mode, this configuration describes an inversion of the magnon mode chirality. For the two latter cases, the pseudofield remains finite ($\omega \neq 0$) and hence the magnetic field value, where the magnon spin signal vanishes or exhibits a sign change, depends on the distance d_c , which is verified by our experimental data.

To demonstrate that the field dependence of $\Delta R_{\text{det}}^{\text{el}}$ is well described by our model, we fit the data using Eq. (5.31). The corresponding theoretical curves (red lines) shown in Fig. 5.9(b) reproduce well the measured signal around the compensation field $\mu_0 H_c$. As detailed above in Sec. 5.1.3, our model is, strictly speaking, not valid in the full investigated magnetic field range, which can be observed in the low and high magnetic field regime, where the theoretical curves deviate from the experimental data. The deviation is largest in the low magnetic field regime for the structure with $d_c = 700$ nm, where $\Delta R_{\text{det}}^{\text{el}}$ increases with decreasing magnetic field strength until it approaches a finite positive signal amplitude at $\mu_0 H = 0$ T. This behavior is in contrast to the magnetic field dependence of $\Delta R_{\text{det}}^{\text{el}}$ obtained for the structure with an electrode spacing $d_c = 1000$ nm, which reaches zero signal at zero applied magnetic field. We can explain this observation by taking into account the injection and detection process. As discussed in Sec. 5.1.5, deviations for our

model are expected when the injector-detector distance is comparable to the magnon decay length l_m . For our hematite thin films, we find $l_m \approx 500$ nm [127]. While the black data points correspond to a structure with an edge-to-edge distance of $d_e = 500$ nm, the blue data points are obtained for a structure with an electrode separation $d_e = 200$ nm, which is clearly smaller than l_m . However, obtaining a full quantitative model to account for all these contributions is complex and not within the scope of this work.

5.2.3 Thick Hematite Film

Next, we discuss the experimental data obtained for the $t_m = 100$ nm thick hematite film and compare them to the results of the $t_m = 15$ nm thin sample as well as to our theoretical model. For a comprehensive study, we first measure the magnon spin signal $R_{\text{det}}^{\text{el}}$ as a function of the in-plane magnetic field orientation φ (cf. Fig 5.9(a)) for different magnetic field strengths $\mu_0 H$ at the same temperature as for the thin film $T = 200$ K. Here, the data are shown for a structure with a center-to-center distance $d_c = 800$ nm in Fig. 5.10(a). As indicated by the gray lines, the angular dependence is well represented by a simple $\Delta R_{\text{det}}^{\text{el}} \sin^2(\varphi)$ function, where $\Delta R_{\text{det}}^{\text{el}}$ again represents the amplitude of the electrically induced magnon spin transport signal. This distinctive $\sin^2(\varphi)$ angular variation is expected for electrically induced diffusive magnon transport from injector to detector [43, 120]. Analog to the thin hematite film, the detected magnon spin signal is maximum when the magnetic field is applied along \hat{x} and thus $\mathbf{H} \perp \mathbf{n}$ in our experiments. The magnon excitation originates from the antiferromagnetic Néel order and hence is shifted by 90° compared to similar measurements in ferrimagnetic materials [43, 120, 259] in accordance with previous experiments in AFIs [127, 234].

For a more rigorous investigation, we extract the quantity $\Delta R_{\text{det}}^{\text{el}}$ from the angle-dependent data as exemplarily shown in panel (a) and plot them against the temperature in Fig. 5.10(b). We show the data for a temperature range $T = 50 - 300$ K and multiple structures with varying electrode distances d_c . Here, we chose a fixed magnetic field magnitude of $\mu_0 H = 600$ mT to be able to quantitatively compare our results to those in Ref. [164], where the authors studied the magnon spin transport in a $\alpha\text{-Fe}_2\text{O}_3$ film of similar thickness in the easy-plane phase. For all distances ranging from $d_c = 550 - 900$ nm, we find a quantitatively similar behavior with $\Delta R_{\text{det}}^{\text{el}}$ increasing for increasing temperature up to $T = 200$ K and starting to decrease again for higher temperatures. Han *et al.* [164] found a similar behavior. We can explain the initial increase of $\Delta R_{\text{det}}^{\text{el}}$ with temperature by an increase of the magnon population in the AFI. This temperature dependence has also been captured in Eq. (5.47), where we described the magnon spin signal including the injection and detection

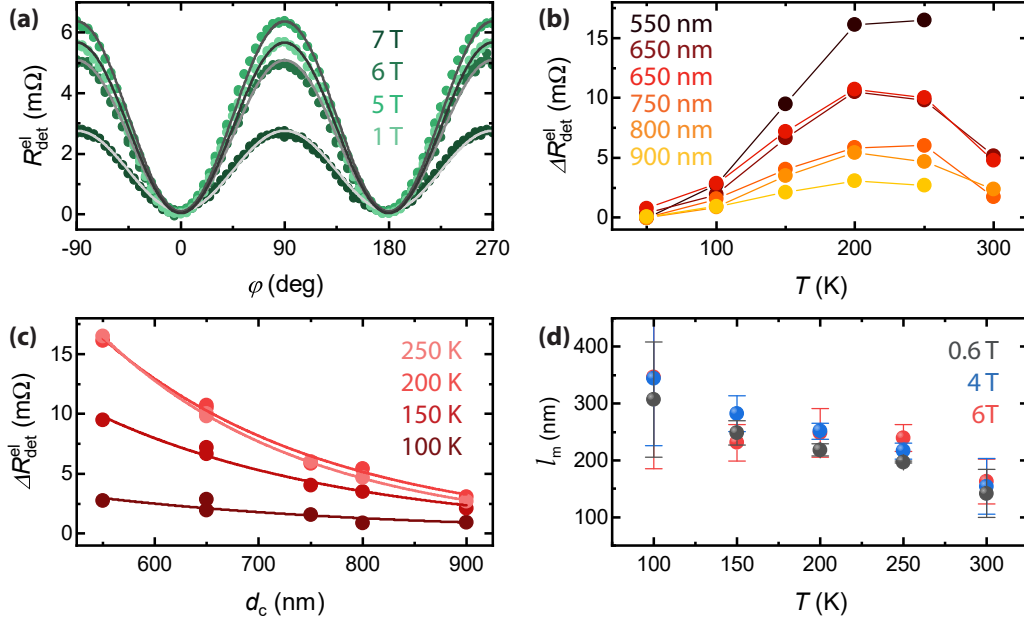


Fig. 5.10 – (a) Electrically excited magnon spin signal $R_{\text{det}}^{\text{el}}$ as a function of the in-plane angle φ for a $t_{\text{m}} = 100$ nm thick hematite film. A device with $d_{\text{c}} = 800$ nm at $T = 200$ K is investigated for various magnetic field strengths. The gray lines are fits to a simple $\Delta R_{\text{det}}^{\text{el}} \sin^2(\varphi)$ function. (b) Extracted electrically induced magnon spin signal amplitudes $\Delta R_{\text{det}}^{\text{el}}$ plotted versus the temperature for several injector-detector distances d_{c} for a fixed magnetic field magnitude $\mu_0 H = 600$ mT. The solid lines are guides to the eye. (c) Distance dependence of the amplitudes $\Delta R_{\text{det}}^{\text{el}}$ for different temperatures and $\mu_0 H = 600$ mT. The solid lines are fits to Eq. (5.48). (d) Magnon decay length l_{m} as a function of T , extracted from the data shown in panel (c), for different magnetic field strengths.

process. The dominant temperature-dependent quantities are the interfacial spin conductivities $g_{\text{inj}}, g_{\text{det}}$ and the susceptibility χ , which increase similarly with the number of magnons resulting in an enhanced magnon spin signal. In contrast, for sufficiently high temperatures, magnon scattering processes dominate the temperature dependence of $\Delta R_{\text{det}}^{\text{el}}$ and lead to a decrease of the magnon propagation length l_{m} , as shown in Fig 5.10(d). Moreover, the absolute amplitude of $\Delta R_{\text{det}}^{\text{el}}$ decreases with increasing d_{c} . This dependence is investigated in more detail in Fig. 5.10(c), where we plot $\Delta R_{\text{det}}^{\text{el}}$ versus the electrode distance d_{c} for different temperatures. As discussed in Sec. 4.1.1, we observe the expected exponential decay of $\Delta R_{\text{det}}^{\text{el}}$ for diffusive magnon transport when the distances between the Pt electrodes are larger than l_{m} and the magnon relaxation dominates [43, 141]. Furthermore, we can extract the magnon decay length l_{m} utilizing the relation

$$\Delta R_{\text{det}}^{\text{el}} = \frac{C}{l_{\text{m}}} \frac{\exp(d_{\text{c}}/l_{\text{m}})}{1 - \exp(2d_{\text{c}}/l_{\text{m}})}, \quad (5.48)$$

where C captures the distance-independent prefactors [43]. The solid lines in Fig. 5.10(c) represent fits to Eq. (5.48). The extracted l_m are shown as a function of the temperature for the fixed magnetic field magnitude $\mu_0 H = 600$ mT (black data points) in Fig. 5.10(d). Over the whole temperature range from $T = 100 - 300$ K, we find a decreasing magnon decay length with increasing temperature. A similar behavior is observed for higher magnetic field values as exemplarily shown for $\mu_0 H = 4$ T and 6 T (cf. Fig. 5.10(d)). While the temperature dependence slightly differs from the results in Ref. [164], the extracted magnon decay length $l_m \approx 150$ nm at room temperature is in good agreement. This value is about three times smaller compared to the one found in our thin hematite films ($t_m = 15$ nm) [127]. A similar magnon diffusion behavior has been found in Ref. [234], where the magnon spin transport is investigated in easy-axis as well as easy-plane configuration for a $500 \mu\text{m}$ thick (1 $\bar{1}$ 02)-oriented hematite crystal. It is encouraging that all experimental studies exhibit similar results, as it indicates that the magnon spin transport is rather dominated by the properties of the hematite than by the HM/AFI interface, which seems to be of minor concern. Moreover, this further justifies our assumption in Sec. 5.1.5 that the Pt electrodes are weakly coupled to the AFI.

Up to now, our study of the $t_m = 100$ nm thick hematite film focused on magnetic fields smaller than H_c and thus we expect that the detected magnon spin signal is dominated by the finite spin of the low-energy magnons. To verify our considerations, we perform magnetic field-dependent measurements in setup (iii), which enables us to apply magnetic field values as large as $\mu_0 H = 15$ T in contrast to $\mu_0 H = 7$ T for the angle-dependent measurements in setup (ii). In this case, the magnetic field is again applied along \hat{x} and hence $\mathbf{n} \parallel \hat{z}$, as in our hematite easy-plane films $\mathbf{H} \perp \mathbf{n}$. In Fig. 5.11, the magnon spin signal amplitude $\Delta R_{\text{det}}^{\text{el}}$ of the SHE-induced magnons is shown as a function of the magnetic field magnitude in the range of $\mu_0 H = 0 - 15$ T for two different injector-detector distances $d_c = 800$ nm and $d_c = 900$ nm at $T = 200$ K. The data is again corrected for a constant offset signal due to the experimental setup. We find clear differences between the behavior of the $t_m = 100$ nm and $t_m = 15$ nm (cf. Sec. 5.2.2) thick film.

Consistent with our previous observation, a peak in the positive magnon spin signal regime can be found for both structures at $\mu_0 H \approx 5.5$ T. We can attribute the maximum of the peak to the compensation field $\mu_0 H_c$, which is independent of the center-to-center distance d_c as the pseudofield vanishes at this magnetic field value. The Hanle peak for the thick film appears smaller due to the larger offset signal in the low magnetic field regime. We attribute this positive offset signal for $\mu_0 H < 5.5$ T to the ordinary propagation of the finite-spin low-energy magnons. The observation of the typical magnon Hanle signal support our theoretical model that the low-energy magnons do not contribute to the pseudospin precession, but

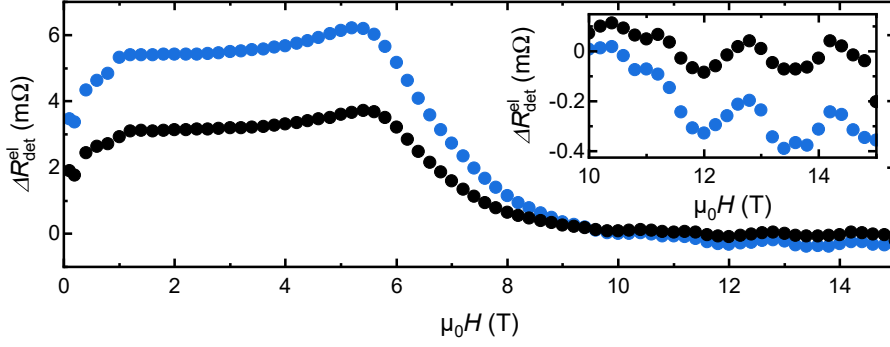


Fig. 5.11 – Electrically induced magnon spin signal amplitude $\Delta R_{\text{det}}^{\text{el}}$ as a function of the magnetic field magnitude $\mu_0 H$ for a $t_m = 100$ nm thick film. The data of two devices with different center-to-center distances d_c between the two electrodes at a temperature of $T = 200$ K are shown. The zoom-in on high magnetic fields highlights the oscillating behavior of $\Delta R_{\text{det}}^{\text{el}}$ in this regime.

rather simply to a finite-spin signal. As discussed in Sec. 5.1.5, the standing wavelike situation along the film thickness for thin films cancels out the low- k magnons. In general, the magnon spin signal stemming from low-energy magnons rapidly diminishes when the gap between the two magnon branches closes. This allows us to associate a magnetic field with this point. Recent works [238, 241] attribute this gap closing between the two magnon mode branches to the second magnetic field of relevance, the compensation field $\mu_0 H_c$. However, from our data, these two magnetic field values seem to differ slightly. This becomes particularly clear for the magnetic field dependence of $\Delta R_{\text{det}}^{\text{el}}$ for higher temperatures $T \geq 200$ K, which is shown in Fig. 5.12(a). Here, the low-energy magnon spin signal initially exhibits a rather constant behavior in the low magnetic field regime and we expect the finite-spin signal to decrease when the magnetic field approaches the compensation field. However, $\Delta R_{\text{det}}^{\text{el}}$ first starts to increase due to the Hanle signal before decreasing. With respect to previous findings, this might suggest that both characteristic magnetic fields overlap in our experiments.

For $\mu_0 H > 5.5$ T, $\Delta R_{\text{det}}^{\text{el}}$ decreases until it approaches zero, which cooperates our model/understanding of low-energy magnons, as we only expect a finite-spin signal from low-energy magnons for small external fields. When the magnetic field is further increased the energy of these magnons increases in a similar way and they can be described via the pseudospin chemical potential again. For further increasing magnetic field strength, the magnon spin signal amplitude starts to oscillate around $\Delta R_{\text{det}}^{\text{el}} = 0 \Omega$. For a better visibility, the zoom-in in Fig. 5.11 shows the data in the range $\mu_0 H = 10 - 15$ T. The signal modulation does not seem to have a clear dependence on the distance d_c . But, we find a clear temperature dependence as shown in Fig. 5.12(b). At present, we do not have a convincing explanation for the

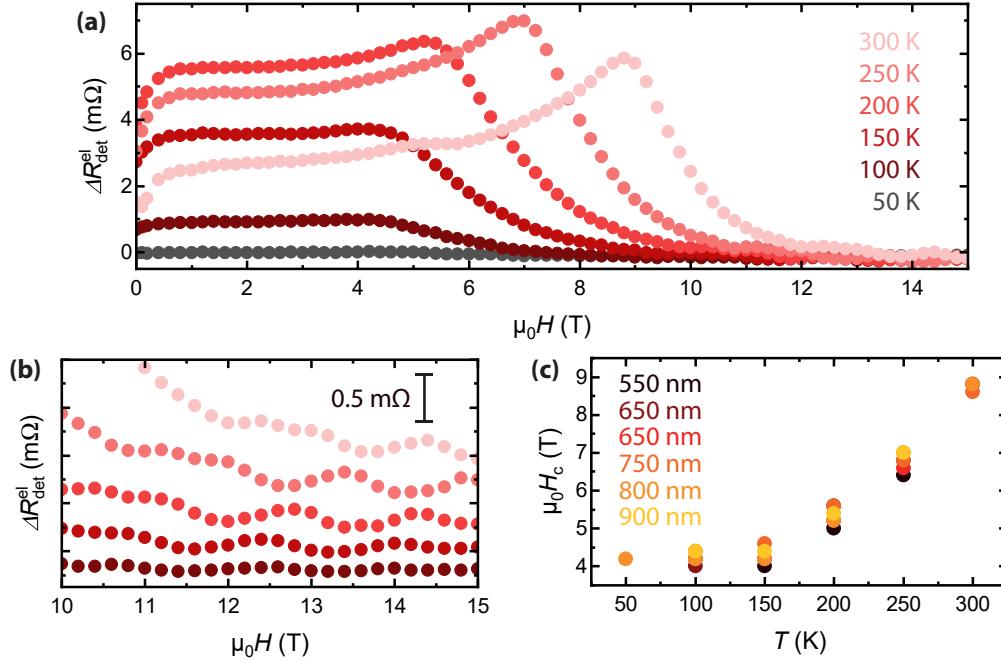


Fig. 5.12 – (a) Magnetic field dependence of the magnon spin signal amplitude $\Delta R_{\text{det}}^{\text{el}}$ due to electrically excited magnons for different temperatures and a device with a strip distance $d_c = 800$ nm. (b) Zoom-in on the oscillations for high magnetic fields for the data in (a). The curves are stacked by constant offsets for a better visibility of the minima and maxima of the oscillations. (c) Compensation field $\mu_0 H_c$ plotted versus temperature. The data has been extracted from the magnetic field dependence of $\Delta R_{\text{det}}^{\text{el}}$ measured for structures with varying d_c .

physical origin of these oscillations and more work from both theory and experiment is required to better understand this interesting finding.

Last but not least, we observe an overall increased magnon spin signal amplitude, which is about an order of magnitude larger compared to the signal measured in our thin hematite films. Comparing our data to Eq. (5.47), we would expect at a first glance that $\Delta R_{\text{det}}^{\text{el}}$ decreases with increasing hematite thickness t_m . However, this is only true if the other parameters remain unchanged. Indeed, the dominant effect in a film with increased t_m is the higher density of magnonic states resulting in a significant enhancement of the various conductances involved. For this reason, the detected magnon spin signal amplitude is increased.

As already briefly touched above, we furthermore studied the temperature dependence of the magnetic field-dependent magnon spin signal. To this end, we carried out similar measurements as for the data shown in Fig. 5.11 for various temperatures. The obtained data is shown in Fig. 5.12(a) for the structure with $d_c = 800$ nm. In the low magnetic field regime ($\mu_0 H < \mu_0 H_c$), the finite-spin signal initially increases with increasing temperature before it starts to decrease again at elevated temperatures of $T \approx 200$ K. We observe a similar behavior for $\Delta R_{\text{det}}^{\text{el}}$ at

$\mu_0 H_c$. The peak amplitude also increases with temperature, however decreases again for temperatures above $T \approx 250$ K. In the high magnetic field regime, an oscillating behavior of the signal amplitude is observed for all studied temperatures. Accounting for the two different contributions in a thick film, we can explain the observed temperature dependence well. At low temperatures, low-energy magnons dominate and hence predominantly contribute to the magnon spin transport at low magnetic fields, whereas latter is suppressed for higher magnetic fields ($\mu_0 H > \mu_0 H_c$). For increasing temperature, the higher energy magnons and the corresponding Hanle signal are more and more contributing. Thus, the Hanle peak around $\mu_0 H_c$ becomes better discernible from the finite-spin background arising due to the presence of low-energy magnons. To highlight the temperature dependence of the oscillating behavior of $\Delta R_{\text{det}}^{\text{el}}$, Fig. 5.12(b) shows a zoom-in to the data presented in panel (a) in the magnetic field range $\mu_0 H = 10 - 15$ T. We displaced the curves by constant offsets to be able to discern the minima and maxima of the high-field oscillations. Besides a clear shift in the field position with temperature of the minima and maxima, we additionally observe a decrease of the oscillation amplitude with decreasing temperature.

Finally, we extract the compensation field $\mu_0 H_c$ and plot it against the temperature for different distances in Fig. 5.12(c). For all studied distances, $\mu_0 H_c$ remains constant for a temperature range $T = 50 - 150$ K, while we find a significant increase of the values with further increasing temperatures. The observed behavior is qualitatively in perfect agreement with the results found for thinner hematite films [127] and indicates that the compensation field $\mu_0 H_c$ follows the temperature dependence of the easy-plane anisotropy [127, 241].

Due to the good agreement of our results with the ones obtained by Han *et al.* [164], we expect that the authors would have observed the Hanle signal if they would have employed higher magnetic fields. Furthermore, we would like to note that similar results have been found at the WMI by Matthias Grammer for an intermediate thick α -Fe₂O₃ film ($t_m \approx 35$ nm) [165]. Already in this thickness regime a large offset signal originating from low-energy magnons and the high-field oscillations have been observed. In addition, the study indicates that the compensation field $\mu_0 H_c$ exhibits a nonlinear decrease with decreasing film thickness. However, a more detailed study on the thickness dependence of the magnon spin signal is necessary to justify these observations.

5.3 Nonreciprocal Magnon Spin Transport

The study on the influence of the dimensionality of the magnetic layer via the magnon Hanle effect has further substantiated that the latter is a powerful tool to study the rich nature of antiferromagnetic magnons and the underlying spin interactions. Another essential aspect to be investigated in antiferromagnetic materials is the effect of inversion symmetry-breaking of the spin system. For example, several exciting theoretical predictions in quantum matter, like topological antiferromagnetic magnons [50, 51, 229, 260], are based on a broken inversion symmetry. The latter is linked to spin-orbit interaction and nonreciprocity [261], which have been the basis of exciting chiral or rectification phenomena observed across platforms [261], from supercurrents [262] to magnetoacoustic waves [263, 264]. Moreover, nonreciprocal magnonic responses in ferromagnets, which have been found in various widely used magnetic hybrids and could be employed via easily accessible detection schemes at room temperature, trigger rapid advancements [217, 261]. In AFIs, nonreciprocal magnons were observed in α - $\text{Cu}_2\text{V}_2\text{O}_7$ via neutron scattering experiments [265–272]. However, in contrast to ferromagnetic materials, antiferromagnetic materials with a broken inversion symmetry are still scarce and in general exhibit low Néel temperatures. This makes antiferromagnetic materials an interesting system for the discovery of nonreciprocity-based phenomena, especially in widely available materials and detection methods.

In this section, we experimentally demonstrate for the first time nonreciprocal magnon spin transport in an AFI. In hematite, a widely available AFI, the nonreciprocity manifests itself as direction-dependent electrically induced magnon spin transport and Hanle effect. The nonreciprocal signal varies with the equilibrium Néel vector and thus, is tunable. Within our model, we can ascribe this observation to different pseudofields, and thus different pseudofield precession rates acting on the magnons propagating in forward and backward directions. This inversion-asymmetric pseudofield is associated with an emerging magnon pseudospin-orbit interaction [48, 52, 266]. Another important aspect that our observation demonstrates, is the presence of inversion symmetry-breaking in our AFI/substrate system, since the pseudofield is directly related to the magnon eigenmodes and the underlying spin interactions.

Most parts of this Section, figures and text have been published in J. Gückelhorn, S. de-la-Peña, M. Scheufele, M. Grammer, M. Opel, S. Geprägs, J. C. Cuevas, R. Gross, H. Huebl, A. Kamra, and M. Althammer, *Observation of the Nonreciprocal Magnon Hanle Effect*, *Physical Review Letters* **130**, 216703 (2023).

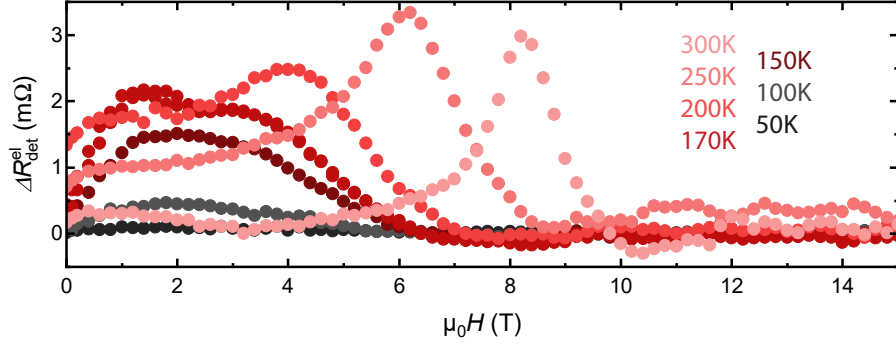


Fig. 5.13 – Electrically induced magnon spin signal $\Delta R_{\text{det}}^{\text{el}}$ as a function of the applied magnetic field magnitude $\mu_0 H$ for various temperatures. The data is obtained from a structure with $d_c = 1.2 \mu\text{m}$ on the $t_m = 89 \text{ nm}$ thick hematite film.

5.3.1 Characterization of Hematite Thin Films

In our experiments, both a $t_m = 89 \text{ nm}$ and a $t_m = 19 \text{ nm}$ thin (0001)-oriented hematite ($\alpha\text{-Fe}_2\text{O}_3$) film are investigated. Since the hematite thicknesses are comparable to the films utilized in the Sec. 5.2, we are able to study the influence of low-energy magnons on the nonreciprocal signal. One difference from the hematite films investigated above is the clearly observed Morin transition in these films, which can be traced back to slightly different growth conditions, as detailed in Sec. 3.1.2. This means the $\alpha\text{-Fe}_2\text{O}_3$ films undergo a transition from magnetic easy-axis AFIs below the Morin temperature T_M to easy-plane AFIs for $T > T_M$ [161]. In the former case, hematite hosts spin-1 magnons, which corresponds to a pseudofield pointing along the z -axis and thus the finite-spin signal is described by Eq. (5.24). However, our model for the magnon Hanle effect is based on the fact that hematite is in the easy-plane phase, where the injected spin-1 magnons are not the eigenmodes of the system, and therefore giving rise to the Hanle signal according to Eq. (5.23). For the $t_m = 89 \text{ nm}$ thick hematite film we have found a Morin transition temperature of $T_M = 205 \text{ K}$, while we obtain $T_M = 125 \text{ K}$ for the thinner film at $\mu_0 H = 100 \text{ mT}$.

To characterize the samples and justify our assumption, we first perform magnetic field-dependent electrical transport measurements at various temperatures. To this end, Pt two-strip structures are patterned on top of both films as described in Sec. 3.2. All Pt strips have a width of $w_{\text{inj}} = w_{\text{det}} = 500 \text{ nm}$, a length of $l_{\text{inj}} = l_{\text{det}} = 100 \mu\text{m}$ and a thickness of $t_{\text{Pt}} = 5 \text{ nm}$. The dc-detection technique (cf. Sec. 4.2.1) is utilized for all measurements presented in this Section to make sure that we only account for electrically induced magnons at the detector and not for thermal effects due to Joule heating. In this case, a dc charge current with a magnitude of $|I_{\text{inj}}| = 500 \mu\text{A}$ is applied to the injector electrode injecting magnons into the hematite film via the SHE. Since the Morin transition of the $t_m = 19 \text{ nm}$ thin film

is in a temperature range, where the magnon spin signal nearly vanishes and it becomes difficult to determine the transition to an easy-axis configuration, we do not expect qualitative deviations from the temperature-dependent behavior discussed in detail in Ref. [127] for a 15 nm thin hematite film. To this end, we focus on the thicker film, which exhibits a higher T_M . In an analogous manner to our previous measurements, the magnetic field \mathbf{H} is applied along the $-x$ -direction orienting the Néel vector \mathbf{n} along $-\hat{z}$ and thus $\mathbf{H} \perp \mathbf{n}$ (cf. Fig. 5.9(a)), where electrical magnon excitation is expected. The measured magnon spin signal amplitude $\Delta R_{\text{det}}^{\text{el}}$ of the $t_m = 89$ nm thick film for a structure with a center-to-center distance $d_c = 1.2 \mu\text{m}$ is shown as a function of the applied magnetic field magnitude $\mu_0 H$ in Fig. 5.13. For $T \geq 200$ K, $\Delta R_{\text{det}}^{\text{el}}$ exhibits the Hanle signature, as expected in the magnetic easy-plane configuration [127]. In accordance with our previous results [243], we additionally observe an offset signal due to low-energy magnons in the low magnetic field regime and oscillations of the magnon spin signal amplitude for high magnetic fields. The position of the compensation field $\mu_0 H_c$ clearly shifts towards smaller magnetic field values with decreasing temperature, since it follows the temperature dependence of the easy-plane anisotropy [127]. Furthermore, the peak amplitude at $\mu_0 H_c$ decreases with decreasing temperature due to the electrically excited magnon transport effect [120, 127]. From our determined Morin transition temperature for the thick film of $T_M = 205$ K, one would not expect a Hanle signal for $T = 200$ K, however our magnetometry measurements suggest that the Morin transition depends on the magnetic field strength. In our samples, T_M decreases with increasing applied magnetic field. For the thick film, the Morin transition is already below 200 K for $\mu_0 H = 0.5$ T (cf. Fig. 3.3) suggesting that the hematite film exhibits still the easy-plane configuration for $T = 200$ K. For temperatures slightly below the Morin transition temperature ($150 \text{ K} \leq T < 200 \text{ K}$), we still observe onsets of the Hanle peak, however a second peak appears at lower magnetic field values, which can be seen well for $T = 170$ K. At first glance, the position of the second peak shows no dependence on the temperature. Indeed, the additional peak exhibits a similar magnetic field dependence as found by Ross *et al.* [163] below T_M in the easy-axis configuration on (0001)-oriented $\alpha\text{-Fe}_2\text{O}_3$ films. The authors attributed this observation to a spin reorientation due to a bulk DMI vector parallel to the easy-axis, and hence perpendicular to the in-plane applied magnetic field [163]. We would expect a similar magnetic field dependence without accompanying Hanle signature in our experiments, as also our hematite films undergo a transition to the easy-axis configuration below the Morin transition temperature. The superposition of both contributions suggests that our samples do not exhibit a sharp Morin transition as a function of the applied magnetic field, but rather a magnetic field-dependent continuous transition from

an easy-plane to an easy-axis configuration with decreasing temperature. This corroborates our magnetometry measurements presented in Sec. 3.1.2, where we find a clear magnetic field dependence of the Morin transition temperature T_M . For $T < 150$ K the magnon spin signal rapidly vanishes, making a quantitative analysis of the dominant contribution difficult.

In the following, all experiments are conducted well above the Morin transition temperature, where our samples feature an easy-plane magnetic phase. Accounting for a large signal at the same time the measurements for the $t_m = 89$ nm thick film are performed at $T = 250$ K, while the ones for the $t_m = 19$ nm thin film are conducted at $T = 200$ K. This means, in accordance with our previous works [127, 243] that the DMI vector points out-of-plane and the Néel vector \mathbf{n} as well as the two sublattice magnetizations \mathbf{M}_1 and \mathbf{M}_2 lie in the (0001)- or xz -plane as depicted in Fig. 5.9(a). Both, the resulting net magnetization \mathbf{M}_{net} and \mathbf{n} can be controlled by the orientation and magnitude of the applied magnetic field \mathbf{H} .

5.3.2 Antisymmetric Magnon Spin Signal in Thick Hematite Films

In a next step, we perform angle-dependent measurements, i.e. the orientation of the external magnetic field \mathbf{H} is varied within the xz -plane and continue to focus on the thicker hematite film, where we study the same structure with $d_c = 1.2 \mu\text{m}$ at $T = 250$ K. For the investigation of the nonreciprocal transport, we will not refer to the Pt strips as injector and detector, as their roles will be interchanged in the following, but as left and right electrodes, respectively (cf. Fig. 5.14(a)). First, we apply a dc charge current I_{inj} to the left electrode and electrically inject spin into the hematite layer via the SHE. The resulting diffusive pseudospin magnon current is detected electrically via the inverse SHE as a voltage signal V_{det} at the right electrode, as depicted in Fig. 5.14(a). We refer to this as the forward transport direction $+d_c$. In a second step, the injection and detection process is interchanged between the two Pt strips. For the backward transport direction $-d_c$ sketched in Fig. 5.14(b), this means I_{inj} is applied to the right electrode leading to a spin injection there, while the corresponding voltage V_{det} is detected at the left electrode. The measured magnon spin signal $R_{\text{det}}^{\text{el}} = V_{\text{det}}/I_{\text{inj}}$ of the respective electrode acting as detector is plotted in Fig. 5.14(c) versus the angle φ of the in-plane applied magnetic field \mathbf{H} for three different magnitudes $\mu_0 H$ and both configurations. While the full circles correspond to the forward transport direction depicted in panel (a), the open circles correspond to the backward transport direction in panel (b). At first glance, all curves appear to exhibit the expected $\sin^2(\varphi)$ angular dependence for electrically induced diffusive magnon spin transport, with a factor of $\sin(\varphi)$ contributed in each case by the injection and detection process, respectively [43, 120]. However, a more careful

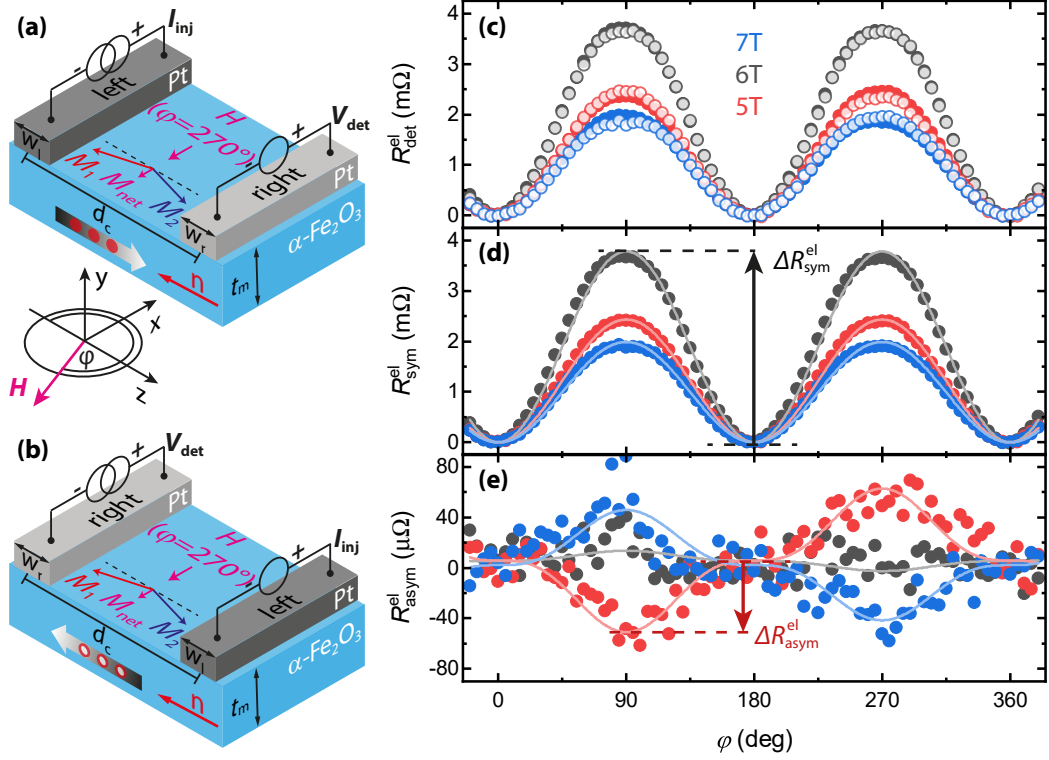


Fig. 5.14 – Sketch of the sample configuration for the (a) forward and (b) backward transport directions, the electrical wiring scheme, and the coordinate system with the in-plane rotation angle φ of the applied magnetic field $\mu_0\mathbf{H}$. Analogue to Fig. 5.9 the net magnetization \mathbf{M}_{net} is aligned along the applied magnetic field ($\mathbf{M}_{\text{net}} \parallel \mathbf{H}$), while the Néel order parameter is directed perpendicular to it ($\mathbf{n} \perp \mathbf{H}$). (c) Electrically excited magnon spin signal $R_{\text{det}}^{\text{el}}$ as a function of the in-plane angle φ measured for the structure with center-to-center distance $d_c = 1.2\mu\text{m}$ on the $t_m = 89\text{nm}$ thick hematite film at $T = 250\text{K}$. While the full circles correspond to an injection of magnons at the left electrode and a detection of $R_{\text{det}}^{\text{el}}$ at the right electrode (forward direction), the open circles account for the reversed measurement scheme (backward direction), as depicted in (a) and (b), respectively. The angle dependence is shown for different magnetic field strengths, where a constant offset arising from the experimental setup has been subtracted from each curve. (d) Symmetric contribution $R_{\text{sym}}^{\text{el}}$ of the two measurement configurations for the same magnetic field magnitudes as in (b). The lines are fits to the expected $\Delta R_{\text{sym}}^{\text{el}} \sin^2(\varphi)$ function [127, 243]. (e) Antisymmetric contribution of the shown angle dependencies in panel (b). The lines represent a $\Delta R_{\text{asym}}^{\text{el}} \sin^3(\varphi)$ fit, which indicates a $\sin(\varphi)$ dependence of the nonreciprocal pseudofield component $\delta\omega$ as discussed in the text.

examination shows that differences occur between the two propagation directions for $\mu_0 H = 5\text{T}$ and 7T , predominantly at $\varphi = 90^\circ$ and 270° . This correspond to $\mathbf{H} \parallel \hat{x}$ or $\mathbf{n} \parallel \hat{z}$, where the signal $R_{\text{det}}^{\text{el}}$ is largest, as $\mathbf{H} \perp \mathbf{n}$.

For a rigorous analysis of this observation, we define the symmetric $R_{\text{sym}}^{\text{el}} = [R_{\text{det}}^{\text{el}}(+d_c) + R_{\text{det}}^{\text{el}}(-d_c)]/2$ and antisymmetric $R_{\text{asym}}^{\text{el}} = [R_{\text{det}}^{\text{el}}(+d_c) - R_{\text{det}}^{\text{el}}(-d_c)]/2$ part of the magnon spin signal for the two measurement configurations [217]. The

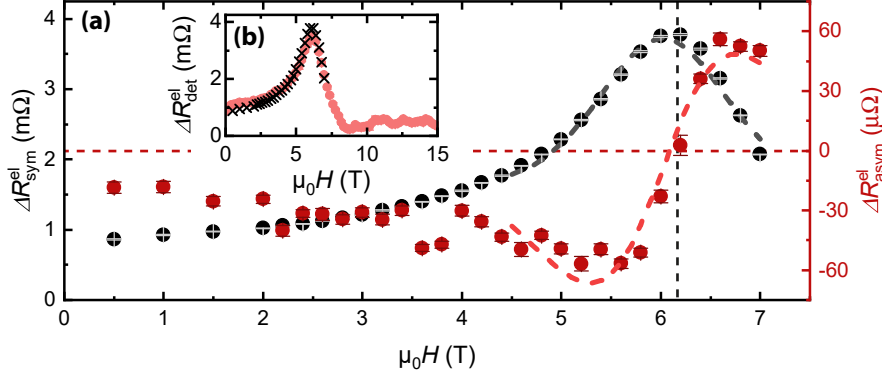


Fig. 5.15 – (a) Magnetic field dependence of the symmetric $\Delta R_{\text{sym}}^{\text{el}} \propto \mu_{\text{sym}}$ (black dots) and antisymmetric $\Delta R_{\text{asym}}^{\text{el}} \propto \mu_{\text{asym}}$ (red dots) magnon spin signal extracted from the angle dependencies shown in Fig. 5.14 (d) and (e), respectively. The error bars have been extracted from the fits to the angle-dependent data. Furthermore, the dashed lines are fits to our model using Eqs. (5.31) and (5.32). (b) Comparison of the magnon spin signal $\Delta R_{\text{det}}^{\text{el}} = \Delta R_{\text{sym}}^{\text{el}} + \Delta R_{\text{asym}}^{\text{el}}$ obtained from two different measurements setups and schemes at $T = 250$ K. The black crosses in the inset corresponds to the extracted signal amplitudes from the angle-dependent data up to $\mu_0 H = 7$ T shown in (a), while the red data points are measured for a fixed magnetic field direction $\mathbf{H} \perp \mathbf{n}$ ($\varphi = 90^\circ$) up to $\mu_0 H = 15$ T as plotted in Fig. 5.13. The latter is corrected for an offset signal measured at $\varphi = 0^\circ$ (cf. Fig. 5.14).

extracted angle dependence of the symmetric signal $R_{\text{sym}}^{\text{el}}$ is plotted in Fig. 5.14(d). The data follows a simple $\Delta R_{\text{sym}}^{\text{el}} \sin^2(\varphi)$ function as indicated by the solid lines with $\Delta R_{\text{sym}}^{\text{el}}$ the amplitude of the symmetric magnon spin signal. This behavior is in agreement with our previous reports, where we utilized an inversion-symmetric analysis [127, 243]. Fig. 5.14(e) shows the corresponding antisymmetric signal $R_{\text{asym}}^{\text{el}}$ over the same in-plane angle φ range. While $R_{\text{asym}}^{\text{el}}$ is vanishingly small over the whole angle range at $\mu_0 H = 6$ T, a clear angle dependence is found for $\mu_0 H = 5$ T and 7 T. We find that the angle dependence follows a $\Delta R_{\text{asym}}^{\text{el}} \sin^3(\varphi)$ function, where $\Delta R_{\text{asym}}^{\text{el}}$ denotes the amplitude of the antisymmetric signal. In this case, a $\sin^2(\varphi)$ dependence originates from the injection and detection process via the SHE, while the remaining factor of $\sin(\varphi)$ can be attributed to $\delta\omega$ as per Eq. (5.30). Moreover, the nonreciprocal signal $R_{\text{asym}}^{\text{el}}$ is about two orders of magnitudes smaller compared to $R_{\text{sym}}^{\text{el}}$. Another important observation, is the sign change of $\Delta R_{\text{asym}}^{\text{el}}$ for $\mu_0 H = 5$ T and 7 T. For a more quantitative analysis of the amplitudes and to explain this behavior, we now examine the magnetic field dependence of the two quantities $\Delta R_{\text{sym}}^{\text{el}}$ and $\Delta R_{\text{asym}}^{\text{el}}$.

In Fig. 5.15(a) the amplitudes $\Delta R_{\text{sym}}^{\text{el}}$ and $\Delta R_{\text{asym}}^{\text{el}}$ extracted from angle-dependent measurements performed for several magnetic field magnitudes $\mu_0 H$ as exemplarily shown in Fig. 5.14(d) and (e), respectively, are plotted versus $\mu_0 H$. Clearly, $\Delta R_{\text{sym}}^{\text{el}}$

Symbol	Unit	Fe ₂ O ₃ (19 nm)	Fe ₂ O ₃ (89 nm)
d	μm	0.75	1.2
D_m	$10^{-4}\text{m}^2/\text{s}$	1.6 ± 0.7	1.8 ± 1.3
τ_m	10^{-9}s	1.2 ± 0.3	0.8 ± 0.2
c_1	10^9l/s	8.0 ± 2.3	6.0 ± 4.0
c_2	$10^9\text{m}/(\text{As})$	1.1 ± 0.3	1.0 ± 0.6
A	$\Omega\text{m/s}$	1.3 ± 0.1	17.2 ± 3.5
R_{sym}^0	$\text{m}\Omega$	0.19 ± 0.01	2.2 ± 0.1
$\delta\omega l$	m/s	-9.9 ± 1.4	-11.2 ± 0.7
R_{asym}^0	$\mu\Omega$	-2.6 ± 1.0	-8.9 ± 2.7

Tab. 5.1 – Device dependent parameters extracted from fits to Eqs. (5.31) and (5.32) in Fig. 5.15(a) and Fig. 5.19.

(black dots) exhibits the expected Hanle curve with a compensation field of $\mu_0 H_c = 6.2\text{ T}$ [127, 243]. As expected from our inversion-symmetric approach used in previous works [127, 138, 243], we observe $\Delta R_{\text{sym}}^{\text{el}} \propto \mu_{\text{sym}}$ (Eq. (5.29)). The nonreciprocal signal $\Delta R_{\text{asym}}^{\text{el}}$ exhibits a negative amplitude for small magnetic field values until it approaches zero at $\mu_0 H_c$ and then changes sign for $\mu_0 H > \mu_0 H_c$. The behavior of the antisymmetric signal is fully consistent with the qualitative picture discussed in Sec. 5.1.4, where the precession rate of the pseudospin chemical potential is different in forward and backward direction and thus the detected magnon spin signal is slightly different. As suggested the difference changes sign together with the average pseudofield ω due to the corresponding reversal of the precession sense and vanishes with ω . Our finding that $\Delta R_{\text{asym}}^{\text{el}} \propto \mu_{\text{asym}}$ confirms the antisymmetric pseudofield as the origin of the observed nonreciprocity. To show that our experimental data is in accordance with our theory model, we fit the data via Eqs. (5.31) (gray dashed line) and (5.32) (red dashed line), respectively, as described in Sec. 5.1.4. Note that the fit range for both $\Delta R_{\text{sym}}^{\text{el}}$ and $\Delta R_{\text{asym}}^{\text{el}}$ has been restricted to $\mu_0 H = 4.5\text{ T} - 7\text{ T}$, since our model does not account for low-energy magnons [243], as demonstrated in the previous Section. Using a single set of parameters (Tab. 5.1), the magnetic field dependencies of $\Delta R_{\text{sym}}^{\text{el}}$ and $\Delta R_{\text{asym}}^{\text{el}}$ are well reproduced by the fits. Furthermore, the fitting of the data allows to estimate the degree of nonreciprocity in the pseudofield. In Tab. 5.1, the value of $\delta\omega$ can be found for the $t_m = 89\text{ nm}$ thick hematite as well as for the $t_m = 19\text{ nm}$ thin film, which is investigated in Sec. 5.3.3, both exhibiting similar values.

It is important to mention that angle-dependent measurements are mandatory to access the nonreciprocal signal given the achievable signal-to-noise ratio. However, our setup allowing for angle-dependent measurements (setup (ii)) is limited to $\mu_0 H = 7\text{ T}$. The field dependencies shown in Fig. 5.13 have been obtained in another experimental setup (setup (iii)) compared to the presented angle-dependent

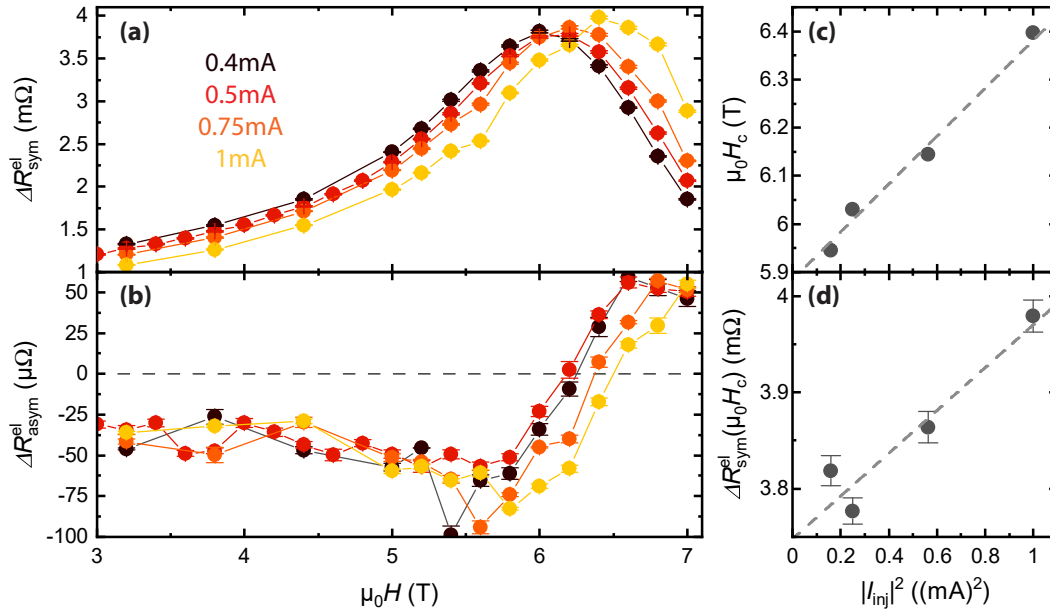


Fig. 5.16 – Magnetic field dependence of the (a) symmetric $\Delta R_{\text{sym}}^{\text{el}}$ and (b) antisymmetric $\Delta R_{\text{asym}}^{\text{el}}$ contribution to the magnon spin signal for different applied injector currents I_{inj} . The measurements were performed for the structure with $d_c = 1.2 \mu\text{m}$ on the $t_m = 89 \text{ nm}$ thick film at $T = 250 \text{ K}$. The solid lines are only guides to the eye. Extracted (c) magnetic compensation field $\mu_0 H_c$ and (d) symmetric magnon spin signal contribution $\Delta R_{\text{sym}}^{\text{el}}$ for $\mu_0 H_c$ plotted versus $|I_{\text{inj}}|^2$. The linear fit (dashed line) in panel (c) and (d) shows the linear dependence on $|I_{\text{inj}}|^2$.

measurements allowing magnetic field magnitudes up to $\mu_0 H = 15 \text{ T}$. To demonstrate that the extracted amplitudes independent of the experimental setup are in good agreement and all significant features are captured, we compare the total magnon spin transport signal $\Delta R_{\text{det}}^{\text{el}} = \Delta R_{\text{sym}}^{\text{el}} + \Delta R_{\text{asym}}^{\text{el}}$ extracted from the angle-dependent measurements (black crosses) to the data at $T = 250 \text{ K}$ obtained from the field-dependent measurements in setup (iii) (red dots) shown in Fig. 5.13. Both magnetic field dependencies are in almost perfect agreement. Note that the magnetic field dependence measured up to $\mu_0 H = 15 \text{ T}$ is corrected for an additional constant offset signal to account for the different resistance offsets in the different measurement setups. Moreover, this comparison shows that we capture all significant features with our extracted data up to $\mu_0 H = 7 \text{ T}$. For larger magnetic fields ($\mu_0 H > 7 \text{ T}$) the magnon spin signal $\Delta R_{\text{det}}^{\text{el}}$ rapidly decreases until it approaches zero and starts to oscillate around 0Ω . On the one hand, the nearly vanishing signal makes the extraction of a nonreciprocal signal $\Delta R_{\text{asym}}^{\text{el}}$ difficult. On the other hand, our model suggests that the antisymmetric signal $\Delta R_{\text{asym}}^{\text{el}}$ is maximal when the symmetric signal $\Delta R_{\text{sym}}^{\text{el}}$ reaches the point of largest slope (cf. Eq.(5.30)). For a nearly vanishing signal, we do not expect a significant nonreciprocal signal.

In order to verify our assumption of a linear response regime in our experiments, we investigate the influence of the injector current magnitude on the magnon spin transport. Up to now, only dc charge currents with an amplitude of $|I_{\text{inj}}| = 500 \mu\text{A}$ have been applied for all measurements, also in previous works a similar injector current density has been used [127, 243]. We again perform angle-dependent measurements on the same structure with $d_c = 1.2 \mu\text{m}$ at $T = 250 \text{ K}$. In this case, we first apply the dc charge current sequence for a fixed magnitude to the left electrode injecting magnons and detect the resulting voltage signal at the right electrode and after a measurements run, which covers the whole angle range, the magnitude of the applied injector current is changed. The magnitude of the applied dc charge current is varied from $|I_{\text{inj}}| = 400 \mu\text{A}$ up to 1 mA , as the measured magnon spin signal significantly decreases for smaller currents and thus is below the noise floor of our measurements. In a second step, the measurement sequence is repeated for interchanged Pt electrodes with the right electrode acting as injector and the left one as detector, while the same injector current magnitudes $|I_{\text{inj}}|$ are applied to the right electrode. We again distinguish between the symmetric $\Delta R_{\text{sym}}^{\text{el}}$ and antisymmetric $\Delta R_{\text{asym}}^{\text{el}}$ magnon spin signal. Before having a closer look at the data, it is important to emphasize that the detected voltage signal is normalized to the applied dc current. In other words, we already assumed a linear dependence of the measured voltage at the detector on the applied dc charge current driven through the injector. The extracted symmetric $\Delta R_{\text{sym}}^{\text{el}}$ and antisymmetric $\Delta R_{\text{asym}}^{\text{el}}$ magnon spin signals are plotted for different applied injector current magnitudes $|I_{\text{inj}}|$ as a function of the magnetic field strength $\mu_0 H$ in Fig. 5.16(a) and (b), respectively. Here, the red data points correspond to the results presented in Fig. 5.15(a) for $|I_{\text{inj}}| = 500 \mu\text{A}$. If we look into the extracted $\Delta R_{\text{sym}}^{\text{el}}$ values (cf. Fig. 5.16(a)), we can unambiguously identify the Hanle peak for all applied currents. Especially, the curves are in good agreement when the change in the injector current magnitude is not too large, in contrast to $|I_{\text{inj}}| = 1 \text{ mA}$, where we find a slightly different behavior. The most prominent difference, is the shift of the compensation field $\mu_0 H_c$ that corresponds to the peak of the Hanle curve to larger magnetic field values with increasing $|I_{\text{inj}}|$. These observations can be attributed to an increased device temperature due to the current induced Joule heating at the Pt electrode. This effect manifests itself in an additional $(I_{\text{inj}})^3$ contribution to the detector voltage. The antisymmetric signal $\Delta R_{\text{asym}}^{\text{el}}$ shown in Fig. 5.16(b) exhibits the expected sign change when the compensation field is crossed for all four injector currents. The very comparable behaviors and values are in good agreement with the observations for the symmetric magnon spin signal $\Delta R_{\text{sym}}^{\text{el}}$. This confirms our conjecture of a linear current dependence. The changes in the magnetic field dependence, in particular the shift of the zero signal crossing with increasing current magnitude, are associated

to the temperature increase at the two-strip structure due to Joule heating effects. Overall, the changes mirror the evolution of $\mu_0 H_c$ with $|I_{\text{inj}}|$ in accordance with our theoretical description of the magnon Hanle effect.

For a more advanced discussion of the observed changes, we extract the compensation field $\mu_0 H_c$ from the curves in Fig. 5.16(a) and plot them against the squared injector current $|I_{\text{inj}}|^2$ in Fig. 5.16(c). The rather linear dependence on $|I_{\text{inj}}|^2$ can as already discussed be interpreted as a Joule heating induced temperature increase of the investigated device. The same behavior of $\mu_0 H_c$ with $|I_{\text{inj}}|^2$ is also visible in the antisymmetric magnon spin signal when we look at the position of $\Delta R_{\text{asym}}^{\text{el}} = 0$, which shifts to larger magnetic field values with increasing current and thus temperature. Furthermore, the monotonic increase of $\mu_0 H_c$, which is represented by linear dependence on the temperature for the small temperature changes induced by Joule heating in our case, are in accordance with the observations in our previous reports [127, 243]. Last but not least, we analyze the change in the $\Delta R_{\text{sym}}^{\text{el}}$ values at the compensation field for an increasing injector current in Fig. 5.16(d). We find that $\Delta R_{\text{sym}}^{\text{el}}$ nicely follows a squared injector current $|I_{\text{inj}}|^2$ dependence. In this temperature regime, a similar increase of the detector signal amplitude with increasing temperature has been observed in our temperature-dependent measurements. Thus, the linear dependence of $\Delta R_{\text{sym}}^{\text{el}}$ on $|I_{\text{inj}}|^2$ also originates from the temperature change in our device induced by Joule heating.

For a full qualitative analysis of the nonreciprocal signal in the thick hematite film, the investigation of the temperature dependence of $\Delta R_{\text{asym}}^{\text{el}}$ is still missing. As the injector current experiments demonstrated, already small temperature changes have an impact on the nonreciprocal signal. Moreover, the temperature dependence of the total magnon spin signal or the symmetric signal, since the antisymmetric contribution is two orders of magnitude smaller and below the noise floor in our magnetic field-dependent measurements, showed significant changes of $\Delta R_{\text{det}}^{\text{el}}$ with temperature. In this case, we investigate a structure with a slightly wider center-to-center distance $d_c = 1.3 \mu\text{m}$ on the same $t_m = 89 \text{ nm}$ thick $\alpha\text{-Fe}_2\text{O}_3$ film. Before we perform angle-dependent measurements to extract the nonreciprocal signal, setup (iii) is utilized to perform magnetic field-dependent measurements up to $\mu_0 H = 15 \text{ T}$ to characterize the new structure. The magnetic field is first applied along $-\hat{x}$ and hence $\mathbf{H} \perp \mathbf{n}$ and afterwards along $-\hat{z}$ to correct for signal offsets not stemming from the magnon spin transport. For an injection at the left electrode, the detected magnon spin signal at the right electrode as a function of the magnetic field strength $\mu_0 H$ is shown in Fig. 5.17(a). For the structure with $d_c = 1.3 \mu\text{m}$, we find a similar qualitative behavior as for the structure with $d_c = 1.2 \mu\text{m}$ discussed above (cf. Fig. 5.13). For $T \geq 200 \text{ K}$, we find the expected Hanle signature, which is superimposed by a constant offset for the thick hematite

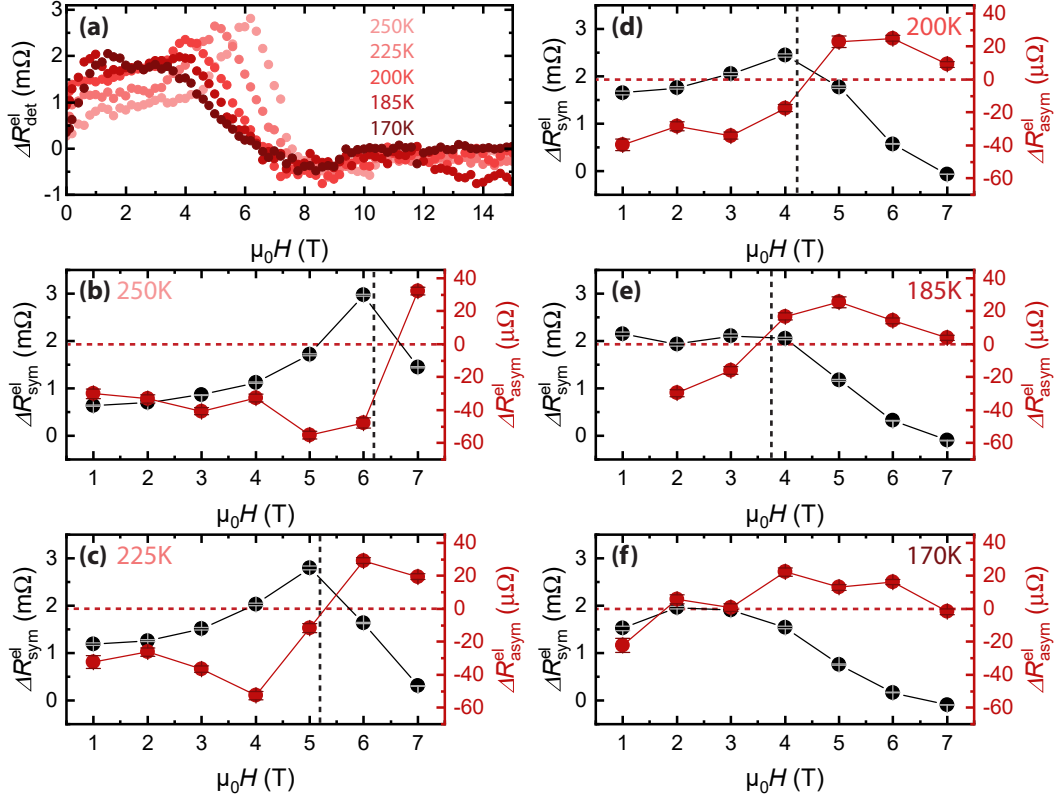


Fig. 5.17 – (a) Electrically excited magnon spin signal $\Delta R_{\text{det}}^{\text{el}} = \Delta R_{\text{sym}}^{\text{el}} + \Delta R_{\text{asym}}^{\text{el}}$ as function of $\mu_0 H$ for different temperatures for a structure with a center-to-center distance $d_c = 1.3 \mu\text{m}$ on the $t_m = 89 \text{ nm}$ thick hematite film. (b)-(f) Magnetic field dependence of the symmetric $\Delta R_{\text{sym}}^{\text{el}}$ (black dots) and antisymmetric $\Delta R_{\text{asym}}^{\text{el}}$ (red dots) contributions to the magnon spin signal, extracted from the angle-dependent measurements of the device for the same temperatures as shown in panel (a). The black dashed lines indicate the compensation field $\mu_0 H_c$ extracted from the data in (a). Note that we were not able to extract an antisymmetric signal for $\mu_0 H = 1 \text{ T}$ in panel (e). The error bars are extracted from the fits to the angle dependencies of $R_{\text{sym}}^{\text{el}}$ and $R_{\text{asym}}^{\text{el}}$, respectively.

film due to low-energy magnons in the low magnetic field regime. In contrast, for $T = 185 \text{ K}$ and 170 K , we observe contributions from both the Hanle signal and the reorientation of the spins due to the DMI present in the magnetic easy-axis phase of hematite. Moreover, the overall signal magnitude is slightly decreased compared to the structure with the smaller electrode spacing $d_c = 1.2 \mu\text{m}$ originating from the diffusive electrically induced magnon spin transport [43, 141]. For the five temperatures studied in Fig. 5.17(a), we now measure the magnon spin signal as a function of the magnetic in-plane angle φ . To extract the symmetric and antisymmetric signal, we again perform measurements in both configurations. This means, we first drive a dc charge current I_{inj} through the left electrode, while we detect the resulting voltage signal V_{det} at the right electrode and interchange the

roles of the injector and detector electrode in the next step. From the resulting angle dependencies, we extracted $\Delta R_{\text{sym}}^{\text{el}}$ (black dots) and $\Delta R_{\text{asym}}^{\text{el}}$ (red dots) and plotted them against $\mu_0 H$ in Fig. 5.17(b) to (f) for five different temperatures ranging from 170 K to 250 K, respectively. For all temperatures, the symmetric magnon spin signal $\Delta R_{\text{sym}}^{\text{el}}$ resembles the behavior of the magnetic field dependence shown in Fig. 5.17(a), which has been measured in a different experimental setup. Similar to our previous observations, the two measurement methods show a nearly perfect agreement. For decreasing temperatures, the position of the compensation field $\mu_0 H_c$ shifts towards lower magnetic field values, until it is no longer possible to unambiguously define $\mu_0 H_c$ for $T = 170$ K, where the magnetic easy-axis phase dominates and our model is no longer valid. To emphasize the compensation field, we have indicated $\mu_0 H_c$ by black dashed lines in Fig. 5.17(b)-(e), which correspond to the compensation field of the structure with $d_c = 1.2 \mu\text{m}$, since it does not depend on the electrode spacing d_c . For the antisymmetric signal $\Delta R_{\text{asym}}^{\text{el}}$, we first focus on $T = 250$ K shown in Fig. 5.17(b). We find a quantitatively similar behavior of the nonreciprocal signal as observed for the structure with $d_c = 1.2 \mu\text{m}$ presented in Fig. 5.15(a). While $\Delta R_{\text{asym}}^{\text{el}}$ exhibits negative values in the low magnetic field range ($\mu_0 H < \mu_0 H_c$), the nonreciprocal signal changes sign when it crosses the compensation field. In contrast to the symmetric component, which is slightly decreased for the structure with the larger distance between the two electrodes, the antisymmetric signal exhibits similar values for both distances. In both cases ($d_c = 1.2 \mu\text{m}$ and $1.3 \mu\text{m}$), values up to $\Delta R_{\text{asym}}^{\text{el}} \approx 60 \mu\Omega$ are reached, which indicates that the nonreciprocal signal does not sensitively depend on the electrode spacing. For decreasing temperatures (Fig. 5.17(c)-(e)), we find a quantitatively similar behavior, however the point of sign change, which is attributed to the compensation field $\mu_0 H_c$, shifts towards smaller magnetic field values in accordance with our observations for $\Delta R_{\text{sym}}^{\text{el}}$ and as expected from our theoretical model. Moreover, we find that both the symmetric $\Delta R_{\text{sym}}^{\text{el}}$ as well as the antisymmetric $\Delta R_{\text{asym}}^{\text{el}}$ magnon spin signal decrease with decreasing temperature, which is expected for electrically induced magnon spin transport [120, 127]. For $T = 170$ K depicted in Fig. 5.17(f), the behavior of the extracted antisymmetric signal clearly deviates from the curves for higher temperatures. A clear sign change in $\Delta R_{\text{asym}}^{\text{el}}$ is missing, corroborating our findings for the symmetric component, where we were not able to determine $\mu_0 H_c$. For even smaller temperatures well below the Morin transition temperature, we could not extract a nonreciprocal signal, since the antisymmetric component is expected to vanish for the magnetic easy-axis configuration. For temperatures $T < T_M$, the Hanle signal decreases and the spin reorientation due to the DMI in easy-axis configuration dominates. Thus, our model is no longer able to describe both the symmetric and antisymmetric magnon spin signal.

5.3.3 Antisymmetric Magnon Spin Signal in Thin Hematite Films

In this section, we demonstrate that the nonreciprocal signal is also present in a thin hematite film, where the contribution of low-energy magnons can be neglected [243]. To this end, we now study a two-strip device with a center-to-center distance of $d_c = 0.75 \mu\text{m}$ on top of the $t_m = 19 \text{ nm}$ thin $\alpha\text{-Fe}_2\text{O}_3$ film. To characterize the hematite film, we perform angle-dependent measurements, and thus measure the magnon spin signal as a function of the in-plane magnetic field orientation φ for the same magnetic field magnitudes $\mu_0 H$ as for the thicker film, however this time at a temperature of $T = 200 \text{ K}$. We chose this lower temperature to counteract the shift of the Hanle peak to higher magnetic field values observed in thinner hematite layers and have a sufficient large magnon spin signal at the same time [127, 243]. Similar to the thicker film, we first drive a dc charge current I_{inj} through the left electrode, while the signal of the electrically induced magnons V_{det} is measured at the right electrode (cf. Fig. 5.14(a)). In a second step, the roles of the injector and detector electrode are interchanged as depicted in Fig. 5.14(b). The detected magnon spin signal is plotted versus the angle φ in Fig. 5.18(a), where the filled dots corresponds to magnons transported from the left to the right electrode (forward propagating direction, $+d_c$) and the open circles correspond to the reversed measurement scheme (backward propagating direction, $-d_c$). While the angle dependencies exhibit very similar behaviors for both measurements configurations for $\mu_0 H = 5 \text{ T}$ and 6 T , we observe a clear difference for $\mu_0 H = 7 \text{ T}$, especially at $\varphi = 90^\circ$ and 270° , when $\mathbf{H} \perp \mathbf{n}$.

For a more rigorous discussion of this behavior, we again extract the symmetric contribution $R_{\text{sym}}^{\text{el}} = [R_{\text{det}}^{\text{el}}(+d_c) + R_{\text{det}}^{\text{el}}(-d_c)]/2$, which only contains the inversion-symmetric part, i.e. there is no difference between the pseudofields ω for the two propagation directions ($\delta\omega = 0$), and the antisymmetric contribution $R_{\text{asym}}^{\text{el}} = [R_{\text{det}}^{\text{el}}(+d_c) - R_{\text{det}}^{\text{el}}(-d_c)]/2$, where $\delta\omega \neq 0$. The angle dependence of the symmetric signal $R_{\text{sym}}^{\text{el}}$ is shown in Fig. 5.18(b). We find the expected $\sin^2(\varphi)$ dependence with an amplitude $\Delta R_{\text{sym}}^{\text{el}}$ for electrically induced magnon spin transport, as indicated by the solid lines. The corresponding antisymmetric signal $R_{\text{asym}}^{\text{el}}$ shown in Fig. 5.18(c) can be described by a $\Delta R_{\text{asym}}^{\text{el}} \sin^3(\varphi)$ function (solid lines), where $\Delta R_{\text{asym}}^{\text{el}}$ quantifies the amplitude of the nonreciprocal signal. We clearly observe the same angle dependencies for both the symmetric as well as the antisymmetric magnon spin signal as for the thicker hematite film. For the thin hematite film, the $\sin^3(\varphi)$ dependence is most pronounced for $\mu_0 H = 7 \text{ T}$ (cf. Fig 5.18(c)). In this case, the antisymmetric signal amplitude exhibits a value of $\Delta R_{\text{asym}}^{\text{el}} = -30 \mu\Omega$ at $\varphi = 90^\circ$, while we find a similar value, however with an inverted sign at $\varphi = 270^\circ$. This sign conversion resembles the one of the angle dependence of the thicker film

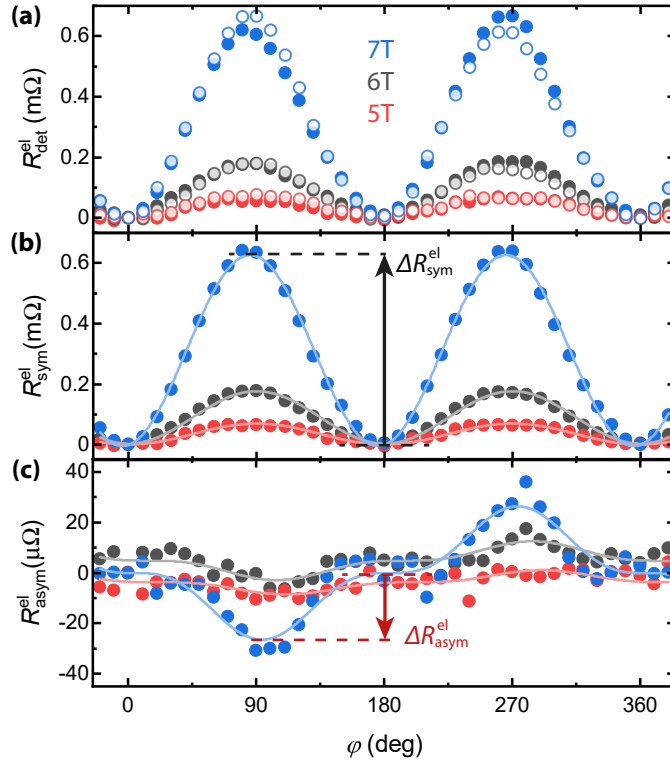


Fig. 5.18 – (a) Angle dependence of the electrically induced magnon spin signal $R_{\text{det}}^{\text{el}}$ for a structure with $d_c = 750$ nm on a $t_m = 19$ nm thin hematite film. The data is shown for the same magnetic field values as for the thick film in Fig. 5.14. The filled and open circles correspond to the measured signal in the forward and backward transport configuration, respectively. A constant offset arising from the experimental setup has been subtracted from the curves. (b) Symmetric part $R_{\text{sym}}^{\text{el}}$ extracted from the data of the two measurement configurations shown in panel (a). The lines represent a simple $\Delta R_{\text{sym}}^{\text{el}} \sin^2(\varphi)$ fit to the data, expected in the absence of a nonreciprocal contribution. (c) Antisymmetric part $R_{\text{asym}}^{\text{el}}$ of the respective angle dependencies in (a). The lines are fits to a $\Delta R_{\text{asym}}^{\text{el}} \sin^3(\varphi)$ function.

for $\mu_0 H = 5$ T. For $\mu_0 H = 6$ T, the thinner film exhibits a similar qualitative angle dependence as for $\mu_0 H = 7$ T with the same sign convention, however with a significantly decreased amplitude signal. A full vanishing of the nonreciprocal signal over the angle range is observed for $\mu_0 H = 5$ T. These observations are in contrast to the thicker $\alpha\text{-Fe}_2\text{O}_3$ film, where we found a sign change in the extracted antisymmetric amplitudes at $\varphi = 90^\circ$ and 270° when the magnetic field strength was increased from $\mu_0 H = 5$ T to 7 T.

In order to quantitatively explain this observation, we extract the amplitudes $\Delta R_{\text{sym}}^{\text{el}}$ and $\Delta R_{\text{asym}}^{\text{el}}$ from the fits in Fig. 5.18(b) and (c), respectively, and plot them as a function of the magnetic field magnitude $\mu_0 H$ in Fig. 5.19. The symmetric signal $\Delta R_{\text{sym}}^{\text{el}}$ (black dots) exhibits a slightly decreasing behavior with magnetic

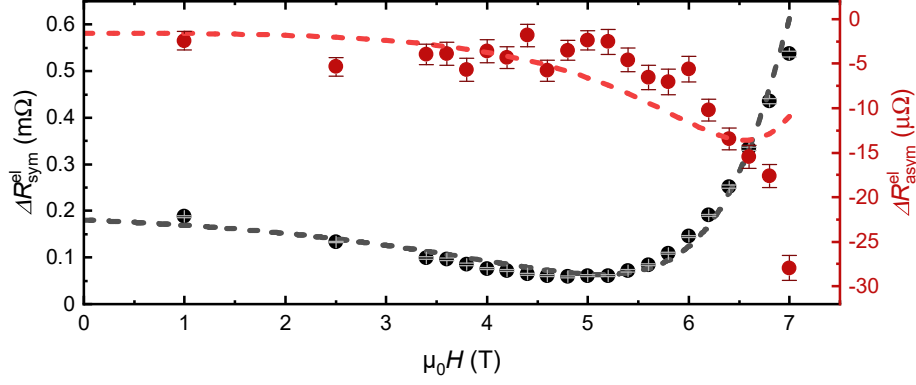


Fig. 5.19 – $\Delta R_{\text{sym}}^{\text{el}}$ and $\Delta R_{\text{asym}}^{\text{el}}$ extracted from the angle dependencies shown in Fig. 5.18 (b) and (c), respectively, plotted versus the magnetic field strength $\mu_0 H$. The dashed lines are fits to Eqs. (5.31) and (5.32), respectively. For the $t_m = 19$ nm thin film, we are limited to the $\omega < 0$ regime and thus observe no sign change in $\Delta R_{\text{asym}}^{\text{el}}$.

field strength between $\mu_0 H = 1$ T and 6 T. For $\mu_0 H > 6$ T the signal is significantly increased, which can be attributed to the onset of the Hanle peak. However, we do not reach the compensation field $\mu_0 H_c$ within the limits of our experimental setup and thus $\omega < 0$ over the whole covered magnetic field range for the thin hematite film. This effect is also reflected by the antisymmetric signal $\Delta R_{\text{asym}}^{\text{el}}$ (red dots), which shows a rather constant behavior of $\Delta R_{\text{asym}}^{\text{el}} \approx -5 \mu\Omega$ between $\mu_0 H = 1$ T and 6 T, while we find a strongly enhanced negative signal for $\mu_0 H > 6$ T, however no sign change is observed since we do not reach $\mu_0 H_c$. Analogue to the thicker film, the symmetric and antisymmetric magnon spin signal can be described by μ_{sym} and μ_{asym} , respectively. The theory curves (dashed lines) reproduce the behavior of $\Delta R_{\text{sym}}^{\text{el}}$ and $\Delta R_{\text{asym}}^{\text{el}}$ well. We utilized the same procedure as for the thicker film (cf. Sec. 5.1.4), where we first fitted the symmetric component, followed by the antisymmetric part only leaving $\delta\omega l$ and R_{asym}^0 as free fit parameter. The extracted fit parameter can be found in Tab. 5.1 together with the results of the thicker film. Overall, both films exhibit similar parameters, verifying that the low-energy magnons only contribute to a finite-spin offset signal, which does not affect the nonreciprocal signal. Note that we find a small difference between $\Delta R_{\text{asym}}^{\text{el}}$ and the corresponding theory curve (red dashed line) around $\mu_0 H = 7$ T. While the model describes the antisymmetric signal in the low magnetic field regime well, the curve suggests a decrease of the signal near the compensation field, however $\Delta R_{\text{asym}}^{\text{el}}$ continues to increase. This difference might be caused by uncertainties in the fitting procedure as we are limited to $\mu_0 H = 7$ T and hence can only fit the onset of the Hanle curve instead of the full peak. For the $t_m = 19$ nm thin $\alpha\text{-Fe}_2\text{O}_3$ film, angle-dependent measurements at higher magnetic field magnitudes are needed to verify the expected sign change in $\Delta R_{\text{asym}}^{\text{el}}$ at the compensation field of the Hanle curve.

If we further compare the results of the thin and thick hematite film in Fig. 5.19 and Fig. 5.15(a), we find that the symmetric contribution $\Delta R_{\text{sym}}^{\text{el}}$ is about an order of magnitude larger for the thicker film. In contrast, the antisymmetric signal $\Delta R_{\text{asym}}^{\text{el}}$ is on the same order of magnitude for both film thicknesses. The nonreciprocal signal of the thinner film is slightly smaller compared to the thick hematite film. However, if we take temperature effects into account, the small difference most likely originates from the temperature difference in the measurements. In Fig. 5.17(d), we see that the antisymmetric signal recorded at $T = 200$ K only reaches values up to $\Delta R_{\text{asym}}^{\text{el}} \approx 30 \mu\Omega$ similar to the thinner film. Employing our theoretical analysis via Eqs. (5.31) and (5.32) describes the data of both films almost perfectly. Thus, we deduce that the origin of our experimentally observed nonreciprocity stems from an antisymmetric pseudofield $\delta\omega$, which we find to be angle-dependent as $\sin(\varphi)$. This angle dependence is reminiscent of a related, but distinct, nonreciprocity of the magnon dispersion found in YIG/GGG heterostructures, which has been attributed to the interfacial DMI [217]. Considering that the ratio between the antisymmetric and symmetric signal in our experiments is smaller in the thicker hematite sample, our observed nonreciprocity most likely stems also from the interface between hematite and its substrate. Due to this interfacial effect, we would not expect a higher nonreciprocal signal for larger film thicknesses. Furthermore, the contribution of low-energy magnons in thick hematite films [243], which act as a finite-spin signal that superimposes the Hanle signal, complicate the extraction of the nonreciprocal signal. This means due to an increasing influence of low-energy magnons with increasing film thickness, it is unlikely to detect a nonreciprocal signal in bulk crystals. Another origin of this nonreciprocity might be the crystal structure of hematite itself, as the spin Hamiltonians used to describe hematite in the literature [127], for example in the original article by Moriya [137], could be oversimplified. To examine this potential origin, atomistic spin modeling of hematite taking into account its exact crystal structure is desirable and, hopefully, will be motivated by our findings [236, 273].

5.4 Summary

In conclusion, we have recapped the basics of the pseudospin concept, which allows to describe the magnon eigenmodes of an antiferromagnet in terms of a pseudofield determined by the free energy landscape. We also discussed the corresponding dynamics, in particular the one-dimensional solution of the pseudospin diffusion equation that describes the precessional motion of the pseudospin chemical potential. Its projection on the z -component is a measure for the diffusive magnonic spin

currents. The precession frequency, and thus the pseudofield can be tuned via an applied magnetic field. This theory has been demonstrated to capture the magnonic spin transport particularly well in thin AFI films [127]. In this work, we extend the pseudospin theory by considering a wave vector dependent pseudofield as well as by accounting for finite-spin contributions from low-energy magnons and the spin injection and detection process. This extended theoretical model is utilized to explain our recent observations found by systematically investigating the magnon pseudospin dynamics and the associated magnon Hanle effect in the AFI hematite via our two-terminal all-electrical injection and detection transport scheme.

First, we study the effect of the injector-detector distance on the magnon spin signal in a thin α -Fe₂O₃ film. An additional offset signal is found in the low magnetic field regime for edge-to-edge electrode distances in the range of a few 100 nm. This could be attributed to additional contributions caused by an injector-detector spacing smaller than the magnon decay length.

Second, the influence of the effective dimensionality of the magnetic layer on the magnon spin signal is investigated by varying the thickness of the α -Fe₂O₃ layer. To this end, we studied a 15 nm and a 100 nm thick hematite film. Characterizing the thicker film, we find good agreement with previous reports [164, 234], corroborating our model that the magnonic spin transport is dominated by the properties of hematite and that the HM/AFI interface only plays a minor role. Moreover, we measured the magnon Hanle effect in the 100 nm thick α -Fe₂O₃ film. However, the magnon spin signal of the thicker film exhibits peculiar features not observed for the thinner films. In particular, we find a pronounced offset signal in the low magnetic field range for $\mu_0 H < \mu_0 H_c$, which is attributed to contributions from low-energy magnons and their finite-spin signal. In addition, the magnon spin signal oscillates around zero signal for high magnetic fields ($\mu_0 H > 10$ T). This oscillating behavior shows no dependence on the spacing between the electrodes, but exhibits a clear temperature dependence.

In the last part of this Chapter, we demonstrate nonreciprocal magnon spin transport in both a thin and a thick hematite film. Therefore, we have injected the magnons at the left electrode and detected them at the right electrode in a first measurement run, while we interchanged their roles in a second measurement run. Angle-dependent measurements revealed that additionally to the reported symmetric signal exhibiting a $\sin^2(\varphi)$ behavior [127] with φ the in-plane rotation angle, a superimposed $\sin^3(\varphi)$ dependence can be found. A detailed investigation of this antisymmetric magnon spin signal shows that it depends on the applied magnetic field and reverses its sign when the symmetric contribution passes its nominal maximum at the compensation field H_c . Our theoretical modeling allows us to understand our observations in terms of different pseudofields, in particular due

to an antisymmetric contribution along the magnonic spin transport direction. The angle dependence indicates a $\sin \varphi$ dependence of the pseudofield nonreciprocity $\delta\omega$. Moreover, the antisymmetric pseudofield directly translates to the magnon dispersion [138] and thus, represents an observation of emergent pseudospin-orbit interaction.

Overall, our work provides an important step towards the detailed understanding of magnonic pseudospin dynamics in AFIs and highlights the rich physics in anti-ferromagnetic magnonics. In particular, the all-electrical transport scheme proves to be a powerful probe for underlying spin interactions in AFIs. Our results also demonstrate that the widely available AFI hematite is a promising candidate for realizing magnonic analogues of electron spin transport [36, 47, 138, 274] and searching for topological and nonreciprocal phenomena [49, 170, 275–277].

Summary and Outlook

This work explores the diffusive magnon-based spin transport and its control in different magnetically ordered insulators by using an all-electrical excitation and detection scheme. These magnonic spin currents share considerable similarities with conventional electronic charge transport in metals or semiconductors [43, 76] leading to analogous phenomena as they occur in electron spin systems. A major challenge in the implementation of magnonic devices is the fact that magnons are non-conserved bosonic quasiparticles, as opposed to electrons with a conserved particle number. First promising solutions to overcome this issue have been presented. For example, this electron-magnon spin transport similarity has been exploited to tune the magnon spin conductivity in the ferro(ferri-) magnet yttrium iron garnet via a charge current applied to a heavy metal electrode in a transistor-like device concept, even far beyond the linear regime [44, 45]. Furthermore, the formal equivalence between electron spin and antiferromagnetic magnon pseudospin, has been leading to the observation of the magnonic analog of the electronic Hanle effect in the antiferromagnetic insulator hematite [127, 138]. This thesis provides an important step towards the detailed understanding of magnonic spin transport and the basis for applications based on pure spin currents. In particular, we focus on systems far from equilibrium. After revisiting the basic concepts of magnon spin transport and its excitation in Chapter 2, we introduce the experimental details of our measurements in Chapter 3. Chapter 4 presents an in-depth investigation of the efficient manipulation of magnon spin currents in YIG. The magnon pseudospin dynamics and the associated magnon Hanle effect are studied systematically in hematite in Chapter 5. In the following, we give an overview of this thesis by summarizing the key findings of each chapter highlighting the rich physics in magnonics.

The implementation of a transistor-like three-terminal YIG/Pt heterostructure as introduced in Ref. [44], allows for an efficient modulation of the magnon conductivity and thus the magnon transport. Even nonlinear magnetization dynamics have been excited leading to a drastic nonlinear change of the magnon conductivity, which has been associated with a zero-effective damping state in Ref. [45], where the damping is compensated by an external drive. In this regard, one of our main results showed that apart from the nonlinear modulator current contribution, also contributions of higher order in the injector current can be found in the detector signal. This has been achieved by comparing the two most common measurement

schemes for electrically induced magnon transport, the dc-detection technique utilizing the current reversal method and the ac-readout technique based on lock-in detection. Both detection schemes have been demonstrated to be well suited to investigate incoherent magnon transport in these three-terminal devices [208]. Furthermore, we demonstrated the reduction of nonlinear damping effects by minimizing the magnetization ellipticity utilizing a biaxially strained YIG thin film, where the effective magnetization is strongly reduced [200]. This manifests itself in an increased magnon induced detector signal by a factor of about 6, corresponding to a twofold increase compared to previous experiments [45]. The main results of these experiments revealed a strictly linear magnetic field dependence of the threshold current, which defines the onset of damping compensation. This observation is attributed to the nearly vanishing effective magnetization and corroborates our present understanding of a scaling of the threshold effect with the saturation magnetization and magnetic anisotropy fields. Since all these findings are based on applying large modulator currents, we extensively discussed their influence on the magnon conductivity/transport. From our experiments successively applying larger maximum current densities, we can most likely attribute the found changes with increasing modulator current, such as a reduced modulation efficiency and SMR amplitude, to a decreasing spin mixing conductance. The complete disappearance of the transport signal could be attributed to a local heating above the Curie temperature of YIG. Overall, our in-depth investigation of the influence of different external and material parameters on the magnon transport sheds new light onto the tuning of the magnon spin conductance, especially in the critical current regime where a nonlinear modulator current dependence of the magnon conductivity dominates due to SOT-induced magnetization dynamics. Moreover, it demonstrates the great potential of magnon current based applications.

Chapter 5 systematically studies the recently discovered magnon pseudospin dynamics and the associated magnon Hanle effect [127, 138] in two-terminal α -Fe₂O₃/Pt devices. Based on our findings, we were able to expand our previous description of the measured spin transport phenomena in terms of antiferromagnetic pseudospin dynamics. Since previous studies only focused on thin films, which can be described using a one-dimensional pseudospin transport model, we addressed the role of the effective dimensionality of the magnetic layer by accounting for finite-spin low-energy magnons and included a discussion on the spin injection and detection process. For thicker hematite films, comparable or larger than the magnon thermal wavelength, we find peculiar changes in the magnetic field dependence of the magnon spin transport signal. As a main result, we found an additional offset signal in the low bias regime for the expected Hanle curve, which originates from the contribution of low-energy contributions. The latter were found to contribute simply

to a finite-spin signal, without contributing to the pseudospin precession. Another difference between thin and thick films is an oscillating behavior of the magnon spin signal that shows no dependence on the electrode spacing observed for large magnetic field values in the thick hematite film. A major result is the demonstration of nonreciprocal magnon spin transport in the antiferromagnet hematite for the first time. The antisymmetric contribution to the magnon Hanle effect was measured by interchanging the roles of the injector and detector electrode. We find that the recorded differences depend on the applied magnetic field and reverse sign when the symmetric contribution passes its nominal maximum at the compensation field. Our theoretical model allows us to assign this observation to an antisymmetric pseudofield and thus different precession rates of the pseudospin along the spin transport direction. This antisymmetric pseudofield, in turn, directly translates into a magnon dispersion and constitutes an observation of emergent pseudospin-orbit interaction. In general, the realization of electrically injected and detected spin transport in an antiferromagnetic insulator demonstrates its high potential for devices and establishes a powerful probe for magnon eigenmodes and the underlying spin interactions in the antiferromagnet.

Besides providing novel insights into the diffusive magnon spin transport and its manipulation in MOIs, our findings open up interesting new questions and opportunities for future experiments. In the following, we present preliminary experiments and discuss possible next steps within this topic.

6.1 Manipulation of Magnon Spin Transport in Three-terminal Hematite/Pt Nanostructures

In this section, we discuss the idea that the magnon spin signal in easy-plane hematite films can be manipulated in a similar manner as the magnon conductivity in YIG and in this regard present preliminary measurements conducted at the WMI. To this end, we employ three-terminal Pt structures on top of a $t_m = 35$ nm thick α -Fe₂O₃ film. Similar to other investigated films, we do not observe a Morin transition. Although this film thickness is much smaller than the studied thick films above (~ 100 nm), we have to account for the contribution of low-energy magnons [165]. The injector and detector electrode of the studied structure have a width of $w_{inj} = w_{det} = 500$ nm, a length of $l_{inj} = l_{det} = 100 \mu\text{m}$ and a thickness of $t_{Pt} = 5$ nm. The two electrodes exhibit a center-to-center distance of $d_c = 950$ nm. The modulator placed in between has a length of $l_{mod} = 116 \mu\text{m}$ and a width of $w_{mod} = 100$ nm. In order to achieve a better mechanical stability for the narrow electrode, a Pt thickness of $t_{Pt}^{mod} = 10$ nm was utilized. Note that a small edge-to-edge spacing between the electrodes of

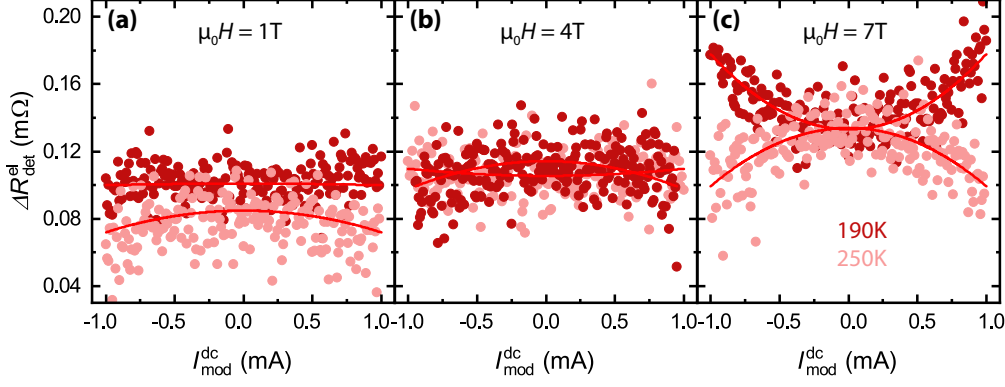


Fig. 6.1 – Electrically induced magnon spin signal amplitude $\Delta R_{\text{det}}^{\text{el}}$ as a function of the modulator current $I_{\text{mod}}^{\text{dc}}$ for a three-terminal hematite/Pt device. The measurements are conducted for two different temperatures and various magnetic field magnitudes $\mu_0 H$ with \mathbf{H} applied along the x -direction parallel to the electrodes. While for (a) $\mu_0 H = 1$ T and (b) $\mu_0 H = 4$ T a rather constant behavior is observed, the signal exhibits a quadratic dependence for (c) $\mu_0 H = 7$ T. The solid lines are fits to $\Delta R_{\text{det}}^{\text{el}} = \Delta R_0 + \Delta R_1 \cdot (I_{\text{mod}}^{\text{dc}})^2$ with ΔR_1 parameterizing the modulation strength and ΔR_0 accounting for the signal amplitude for zero applied modulator current.

$d_e = 175$ nm is chosen, to account for the smaller magnon decay length of hematite, which is on the order of some 100 nm [127, 164, 243], in contrast to YIG offering a magnon decay length larger than $1 \mu\text{m}$ [43, 182, 183].

To investigate the influence of an applied dc modulator current $I_{\text{mod}}^{\text{dc}}$ on the magnon transport properties of $\alpha\text{-Fe}_2\text{O}_3$ in the easy-plane phase, we use the dc-detection method by applying a dc charge current sequence to the injector electrode with a magnitude of $|I_{\text{inj}}| = 500 \mu\text{A}$ as introduced for the advanced current reversal method in Sec. 4.2.1. In Fig. 6.1, the detected magnon spin signal amplitude $\Delta R_{\text{det}}^{\text{el}}$ is plotted as a function of the modulator current $I_{\text{mod}}^{\text{dc}}$ for the two temperatures $T = 250$ K and 190 K for different applied magnetic fields $\mu_0 H$. In an analogous manner as for the measurements conducted on YIG samples, we first apply the magnetic field along the positive x -direction, where we expect a maximal magnon spin signal. Subsequently, the magnetic field is oriented along \hat{z} , allowing us to subtract the background signal not stemming from the magnon currents (cf. Fig. 5.9(a)). For $\mu_0 H = 4$ T (Fig. 6.1(b)), a rather constant behavior is observed for both temperatures and also for $\mu_0 H = 1$ T in Fig. 6.1(a) a modulation of the signal is absent for $T = 190$ K. In contrast, for $T = 250$ K a slight decrease of the signal for positive and negative modulator currents is observed. A even more pronounced modulation is found for $\mu_0 H = 7$ T (Fig. 6.1(c)). While the magnon spin signal decreases for $T = 250$ K with increasing applied modulator current magnitude $|I_{\text{mod}}^{\text{dc}}|$, we find an increasing behavior for $T = 190$ K. The modulation effect is about an order of magnitude smaller compared to results obtained in YIG in similar

experiments [44, 127, 208]. In all cases, the $\Delta R_{\text{det}}^{\text{el}}$ exhibits a quadratic dependence on $I_{\text{mod}}^{\text{dc}}$ as indicated by the fits to the function $\Delta R_{\text{det}}^{\text{el}} = \Delta R_0 + \Delta R_1 \cdot (I_{\text{mod}}^{\text{dc}})^2$ with ΔR_1 parameterizing the modulation efficiency and ΔR_0 accounting for the signal amplitude for zero applied modulator current. This behavior is also verified by angle-dependent measurements, where in contrast to measurements in YIG no modulation of the angle dependence is observed when a modulator current is applied, but rather a simple $\sin^2(\varphi)$ -dependence with slightly varying amplitudes [165]. This observation suggests a thermal origin of the modulation, rather than a contribution of electrically induced magnons due to the SHE, as the linear dependence on $I_{\text{mod}}^{\text{dc}}$ is negligible. However, our finding that the modulation efficiency depends on the applied magnetic field and the base temperature and not on the magnitude of the modulator current, indicates that the increased signal does not originate from an increase of the magnon conductivity in the hematite layer. Overall, we can rule out a significant influence on $\Delta R_{\text{det}}^{\text{el}}$ due to an increased magnon conductivity in the AFI caused by electrically and thermally induced magnons. Instead, thermometry measurements and the temperature dependence of the signal for a fixed magnetic field, suggest an overall increased temperature in the transport channel due to the Joule heating at the modulator electrode, leading to a change in the magnon spin signal. The thermometry measurements reveal a temperature increase of about 25 K for a maximum applied modulator current $I_{\text{mod}}^{\text{dc}} = 0.95$ mA compared to zero applied modulator current [165]. Although the temperature increase is significantly smaller compared to temperature increases in YIG thin films for similar current densities (cf. Sec. 4.4.4), this increase is large enough to shift the Hanle peak towards larger magnetic field values, as shown in Ch. 5. While the signal depends weakly on small temperature changes for $\mu_0 H = 1$ T and 4 T in Fig. 6.1(a) and (b), respectively, the influence of temperature increases near the Hanle peak at $\mu_0 H = 7$ T, where the magnons can be captured by the pseudospin dynamics. In contrast, for the lower magnetic field values, the transport is dominated by low-energy magnons.

The absence of a modulation of the magnon spin signal most likely stems from the nature of an AFI [165]. In Sec. 4.1, we restricted our discussion to a FMI, however, in AFIs the situation is more complex due to the presence of two eigenmodes with opposite chiralities. For an easy-axis AFI with the α - and β -mode as eigenmodes carrying spin+1 and spin-1, respectively, a positive applied modulator current ($I_{\text{mod}}^{\text{dc}} > 0$) results in an enhanced magnon density of α -modes and a depletion of β -modes. This means while the magnetic damping is reduced for α -mode magnons, β -mode magnons experience an enhanced damping [181]. The role of the two magnon modes is inverted for a reversed modulator current polarity.

For AFIs in the easy-plane phase, the injected spin+1 magnons are no longer the eigenmodes of the system and the pseudospin precesses with time, varying between

spin+1 to spin-0 to spin-1 excitations, which makes it rather unlikely to achieve a damping compensation. In contrast, an enhanced damping might be reached in thick hematite films for small magnetic field values, where the transport is dominated by low-energy magnons. The latter correspond to elliptically polarized eigenmodes carrying a small, but finite spin. However, a larger magnon density has to be injected compared to magnons carrying spin+1 in order to exert the same spin-orbit torque.

Another aspect that should be considered is the magnon dispersion relation of hematite. In order to reach the threshold and fulfill the condition for zero-effective damping the external spin torque has to compensate the intrinsic damping torque of the AFI system. In other words, the injected magnon accumulation with a certain spin chemical potential underneath the modulator has to be equal to the energy of the lowest lying available magnon mode, in general the magnon energy at $k = 0$ [68, 189, 196]. The latter is described in the absence of an external magnetic field by the anisotropy of the magnetic material, which defines the frequency or energy gap in the magnon dispersion relation at $k = 0$ [253]. For easy-axis AFIs, this frequency gap lies in the THz regime [253]. Such high energies can hardly be achieved by a SHE-induced damping-like spin-orbit torque via an applied modulator current $I_{\text{mod}}^{\text{dc}}$. This suggests that it is nearly impossible to reach damping compensation in this configuration.

However, we obtain a different situation for AFIs in the easy-plane phase. As shown in Fig. 5.6, the easy-plane anisotropy lifts the degeneracy between the two eigenmodes of the system, leading to a $\omega_{\mathbf{k}}^+$ -mode that decreases linearly for $k \rightarrow 0$ [238]. In this case, the magnon gap reaches energy values in the range of several GHz [252, 253], which is comparable to the magnon gap in the prototypical ferrimagnetic insulator YIG [149]. This is, however, only true for zero applied field. As we demonstrated in Sec. 5.1.5 the lower energy branch $\omega_{\mathbf{k}}^+$ shifts to higher energies with applied magnetic field. This indicates that the modulation effect is most dominant for zero applied magnetic field or rather small magnetic field values. In addition, easy-plane hematite features 120° domains and domain walls for a vanishing external magnetic field due to its three-fold symmetry (cf. Sec. 3.1.2), which leads to a significant reduction of the magnon spin signal due to domain wall scattering [163]. Moreover, an applied magnetic field enables the required control of the Néel order direction. In conclusion, a promising approach for an efficient manipulation of the magnonic spin currents in AFIs are modulator current-dependent experiments conducted for much smaller magnetic fields compared to those in the measurements presented in Fig. 6.1 and an enhanced magnon injection at the modulator electrode.

A first modulator current-dependent measurement has been conducted for $\mu_0 H = 200 \text{ mT}$ and the same nano-device as discussed above. In Fig. 6.2, the detected

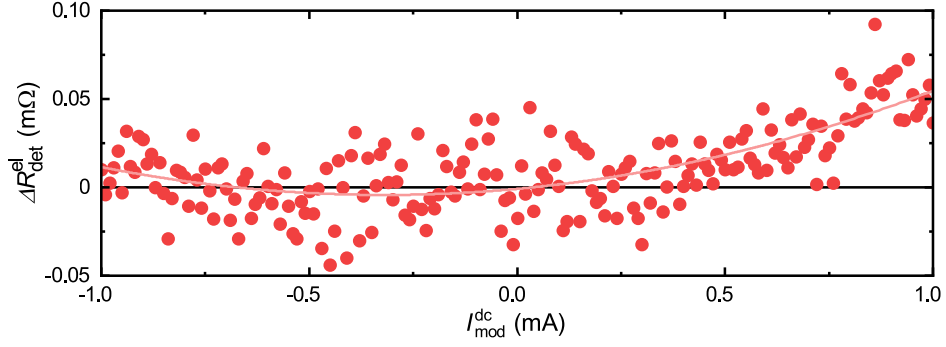


Fig. 6.2 – Electrically induced magnon spin signal amplitude $\Delta R_{\text{det}}^{\text{el}}$ as a function of the modulator current $I_{\text{mod}}^{\text{dc}}$ for a magnetic field strength of $\mu_0 H = 0.2$ T at a temperature of $T = 200$ K. The signal dependence can be described by a fit to Eq. (4.40) (solid line).

magnon spin signal is plotted versus the applied modulator current for the same current range as investigated in Fig. 6.1 at a temperature of $T = 200$ K. We find a constant and nearly vanishing $\Delta R_{\text{det}}^{\text{el}}$ for negative applied modulator currents, while we observe an increased value of $\Delta R_{\text{det}}^{\text{el}}$ with increased current magnitude in the positive regime. This asymmetric behavior indicates the contribution of a linear dependence in $I_{\text{mod}}^{\text{dc}}$ and thus, the increase of the magnon spin signal due to SHE induced magnons. This is corroborated by a fit of the results to Eq. (4.40). The magnon conductivity model introduced for ferromagnets reproduces well the measured data.

However, a better signal-to-noise ratio and a more systematic study are needed for an elaborate discussion of the results. To improve the magnon spin signal, an optimized design can be used. On the one hand, the thickness of the modulator electrode should be reduced to enable higher current densities and thus an enhanced magnon injection process. On the other hand, the separation between the electrodes or the modulator strip could be further reduced. However, this poses challenges on the fabrication process, in particular on the lift-off process. With a reduced distance, it is more likely that Pt residues remain between two strips, resulting in an electrical short. With a narrower modulator, higher current densities can be achieved, however at the expense of its mechanical stability, which is crucial during the lift-off. A further possibility would be to use a thicker hematite film, since this also increases the magnon spin signal and the generation of low-energy magnons as detailed in Sec. 5.2. At the same time, a limiting factor of this approach could be the reduced spin pumping induced damping with increasing film thickness. As shown in Sec. 4.1.1, the damping is inversely proportional to the thickness of the ferromagnetic film (cf. Eq. (4.10)) [97] and, in general, very thin films (≈ 10 nm) are required to achieve magnetic damping compensation via SHE [181]. Last but

not least, a study of the modulation efficiency in this low magnetic field regime close to zero applied magnetic field has to be conducted in future experiments [181].

6.2 Influence of Anisotropy on the Magnon Spin Transport in YIG

In Sec. 4.3, we observed an asymmetry of the modulator current-dependent magnon spin signal when the magnetic field was inverted. One possible explanation for this behavior in YIG with reduced effective magnetization was the influence of magnetic anisotropy. In contrast to our previous measurements conducted on (001)-oriented YIG thin films, where such a feature has not been observed, the YIG film with reduced effective magnetization was grown on a (111)-oriented substrate. For this reason, we give a preliminary discussion of the effects of magnetic anisotropy in this Section.

To get insight into this topic, we study the magnon transport via three-terminal nanostructures in three differently oriented YIG thin films. In an analogous manner to the measurements in Sec. 4.3, we conducted all-electrical transport measurements using the ac-readout technique with an injector current amplitude of $I_{\text{inj}} = 200 \mu\text{A}$. For all three films, we deposited injector and detector electrodes with a width of $w_{\text{inj}} = w_{\text{det}} = 500 \text{ nm}$ and a length of $l_{\text{inj}} = l_{\text{det}} = 25 \mu\text{m}$ on top of the magnetic layer. The center-to-center distance between the injector and detector $d_c = 1.5 \mu\text{m}$ is equal for all three devices. While the modulator features a length of $l_{\text{mod}} = 39 \mu\text{m}$, its width w_{mod} slightly differs. For the two YIG layers grown on (001)- and (111)-oriented GGG substrates $w_{\text{mod}} = 200 \text{ nm}$, while the modulator width is slightly increased to $w_{\text{mod}} = 300 \text{ nm}$ for the (011) orientation. The modulator width as well as the thickness of the YIG layer for all three devices are summarized in Tab. 6.1.

In Fig. 6.3, we plot the electrically induced magnon signal amplitude $A_{\text{det}}^{1\omega}$ as a function of the modulator current $I_{\text{mod}}^{\text{dc}}$ for a (a) (001)-, (b) (011)- and (c) (111)-oriented YIG thin film. The signal measured for the magnetic field applied along the $-z$ -direction ($\varphi = 0^\circ$) is corrected for a background signal not stemming from the magnonic spin transport with the magnetic field oriented along \hat{x} ($\varphi = 90^\circ$) (cf. Fig. 4.15(a)). The modulator current dependence is shown for various magnetic field values $\mu_0 H$. Note that slightly larger magnetic field values were used for the (011)- and (111)-orientation accounting for the larger anisotropy fields. In all three cases, we covered the entire modulator current range, i.e. modulator currents large enough to locally heat the magnetic layer above the Curie temperature causing a vanishing magnon transport signal were applied. In Fig. 6.3(a) for the (001)-oriented YIG film, we find a similar behavior as discussed in detail in Sec. 4.4.

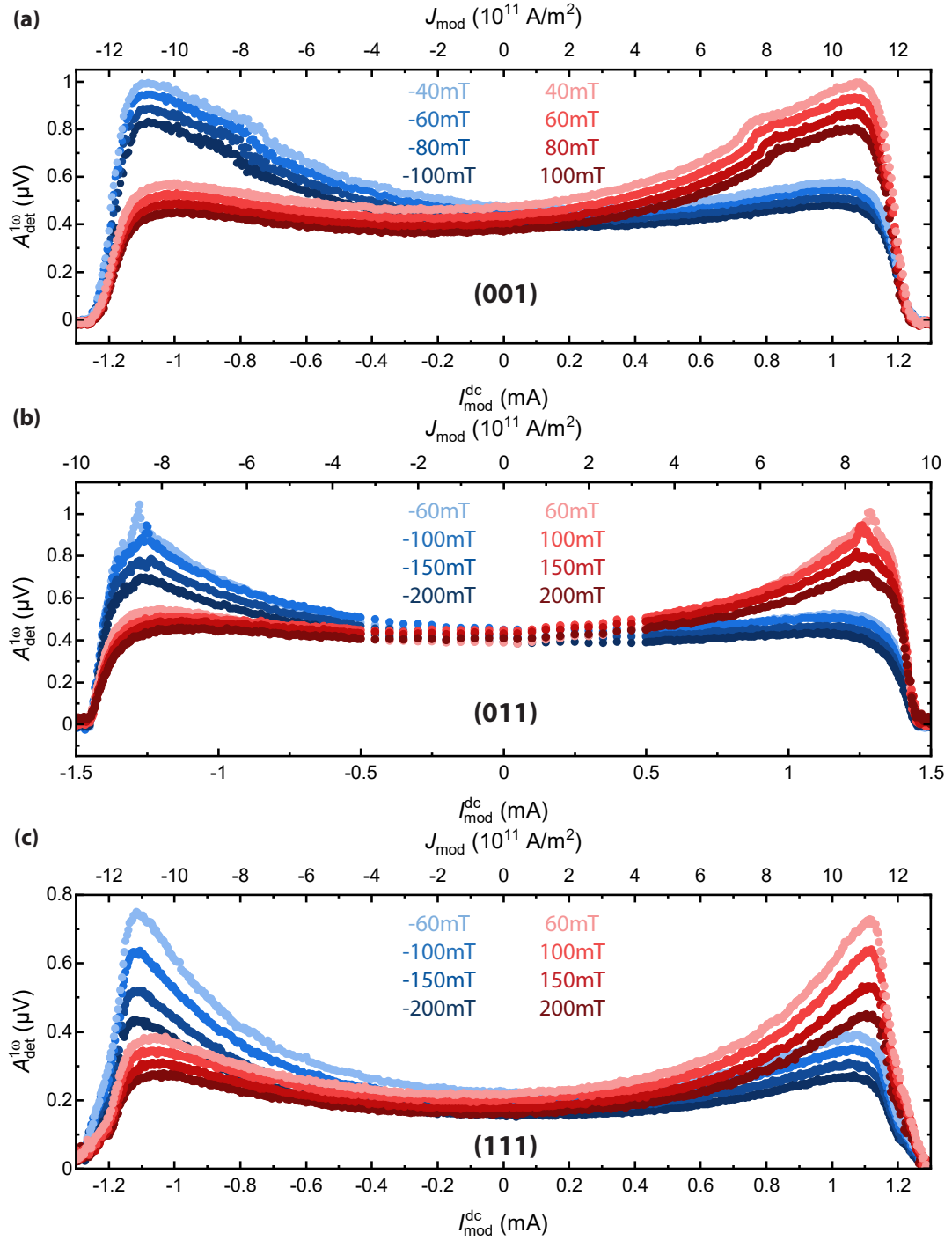


Fig. 6.3 – Electrically induced magnon signal amplitude $A_{\text{det}}^{1\omega}$ as a function of the modulator current $I_{\text{mod}}^{\text{dc}}$ for various magnetic field magnitudes $\mu_0 H$ at $T = 280$ K. The measurements were conducted on three-terminal devices attached to a (a) (001)-, (b) (011)-, and (c) (111)-oriented YIG thin film. The experimental parameters of all three films are summarized in Tab. 6.1. In all cases, the signal exhibits a superposition of a linear and quadratic dependence on $I_{\text{mod}}^{\text{dc}}$ in the low bias regime. While (001)- and (011)-oriented sample exhibit a strong increase of the signal in the critical current, which is attributed to the threshold current, the (111)-oriented film lacks of this feature. For the highest currents, the signal vanishes in all panels due to the large local temperature increase, leading to a transition of the YIG films into their paramagnetic state.

Similar dependencies are found for the two other orientations in Fig. 6.3(b) and (c), however some differences are found. In the low bias regime, all three samples exhibit the expected superposition of a linear and quadratic dependence. For further increasing modulator current values, the threshold effect can clearly be observed in Fig. 6.3(a) and (b) as a kink/peak. In contrast, such a feature is missing in panel (c) and we only observe a continuously increasing magnon spin signal with $I_{\text{mod}}^{\text{dc}}$ before it rapidly decreases and vanishes for largest applied modulator current due to a Joule heating induced temperature increase above the Curie temperature. This behavior is also found for the other two devices. An asymmetry of the magnon spin signal depending on the magnetic field orientation cannot be observed for all three devices. Interestingly, the magnon spin signal features a twofold increase compared to the signal amplitude when no current is applied for the (001)- and (011)-oriented YIG films, while it is increased by a factor of about 4 for the (111)-orientation. For the YIG films grown on (001)-oriented GGG substrates, previous works [127, 208] reported a similar enhancement.

Symbol	unit	(001)	(011)	(111)
t_{YIG}	nm	13.0	14.5	14.3
w_{mod}	nm	200	300	200
σ_{Pt}	$10^6 \text{ 1}/(\Omega \text{ m})$	3.02	2.63	2.91
α_{G}	10^{-3}	0.9 ⁴³	1.36	3.5
$\mu_0 \delta H$	mT	3.0 ⁴³	3.5	17
$\mu_0 M_{\text{eff}}$	mT	156 ⁴³	200	151
$I_{\text{mod}}^{\text{crit}}$	mA	0.53	0.96	2.38

Tab. 6.1 – YIG film dependent parameters for the three different orientations. The critical current values $I_{\text{mod}}^{\text{crit}}$ have been calculated via Eq. (4.13) utilizing the material parameters listed in this Table.

For a qualitative analysis, we investigate the critical current $I_{\text{mod}}^{\text{crit}}$ behavior, which defines the onset of a zero-effective damping state, where the injected magnons can counteract the magnetization damping resulting in an abrupt increase of the effective magnon conductivity (cf. Sec. 4.1.1). To this end, we extract $I_{\text{mod}}^{\text{crit}}$ from the data shown in Fig. 6.3(a) and (b) and plot the values against the magnetic field magnitude $\mu_0 H$ in Fig. 6.4. In addition to the orientation of the film, we indicate the crystallographic direction along which the electrodes are oriented, as the anisotropy fields within the YIG layer might also affect the magnonic spin transport. While the strips on the (001)-oriented YIG film are directed along the

⁴³This value has been extracted from broadband FMR measurements for a 12.2 nm thin YIG film grown on a (001)-oriented GGG substrate under the same conditions as the investigated 13 nm thin YIG film.

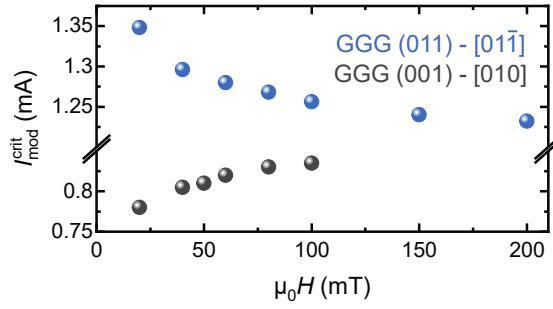


Fig. 6.4 – Extracted critical currents from Fig. 6.3(a) and (b) plotted versus the magnetic field magnitude $\mu_0 H$ for the (001)- (black dots) and (011)-oriented (blue dots) film, respectively. Note that in the former case the Pt electrodes are oriented along the [010]-direction, while they are oriented along [011] for the (011) grown film. The black dots exhibit the expected increasing dependence described by Eq. (4.13). In contrast, the blue dots show a decreasing behavior with increasing $\mu_0 H$.

[010]-direction corresponding to the hard-axis, the strips on the (011)-oriented YIG layer are deposited parallel to [011]. For the former (black dots), we find the expected increase of the threshold value with increasing magnetic field strength, which is described via Eq. (4.13). In contrast, for the (011)-oriented YIG film (blue dots), $I_{\text{mod}}^{\text{crit}}$ decreases with increasing $\mu_0 H$. Furthermore, the magnitude of the threshold current for the (011)-orientation is significantly larger than for the (001)-orientated YIG film over the whole magnetic field range. We can explain this behavior by taking into account the material parameter of the different YIG films. From broadband FMR measurements, we extracted the Gilbert damping α_G , the inhomogeneous linewidth δH and the effective magnetization M_{eff} for each film. Together with the conductivity of the Pt modulator, we utilized the derived critical current dependence described by Eq. (4.13) to estimate the expected threshold value. The extracted parameters as well as the calculated $I_{\text{mod}}^{\text{crit}}$ are listed in Tab. 6.1. Similar to our experimental results, our calculations indicate a larger critical current for (011) YIG film compared to (001) YIG. Moreover, the calculations reveal that modulator currents larger than 2 mA have to be reached for the (111)-oriented YIG film to achieve damping compensation, which is beyond the limit of the Joule heating induced temperature increase above the Curie temperature. Therefore, the material parameters of the (111)-oriented YIG thin film suggest that it is unlikely to reach the threshold effect within our measured modulator current range corroborating our observation shown in Fig. 6.3(c).

For a more quantitative comparison of the influence of the magnetic anisotropy for differently oriented YIG films on the magnon transport, the material parameters of the films have to be adjusted, so that it is possible to achieve damping compensation in each film. Furthermore, structures with equal device parameters should be com-

pared. While we here focused on differently oriented YIG films, future experiments could also explore the magnetic anisotropy contributions within the magnetic layer by orienting the electrodes along different directions. While we would not expect significant differences for structures oriented along different directions on PLD grown (111)-oriented YIG films due to its nearly isotropic behavior in-plane [278], we might expect differences for the magnon transport in (001)-oriented film featuring a small cubic anisotropy when the strips are directed along the easy- ([010]-direction) or hard-axis ([110]-direction)⁴⁴. In particular, we expect the richest effects for different magnetization orientations for (011)-oriented films [279]. In this regard, nickel ferrite (NFO) thin films might also be a good candidate. In all-electrical magnon transport experiments, NFO grown on lattice-matched substrates exhibits similar properties than YIG thin films [259, 280]. In addition, NFO features larger anisotropy fields [281], facilitating the investigation of the influence of magnetic anisotropy on the magnon transport. However, in order to investigate magnon transport larger magnetic fields have to be applied, leading to a decreased signal.

6.3 NV-Magnetometry Measurements on Three-Terminal MOI/Pt Nanostructures

In Chapter 4, we intensively studied the magnon transport manipulated via an applied dc charge current by all-electrical means, however this method does not allow to capture the dynamic response of the magnetic system. A well-established technique to measure the magnetization dynamics in a spatially resolved way, is microfocused Brillouin light scattering (BLS) [282–284]. Besides coherently excited magnetization dynamics, this method is also able to capture incoherent processes such as thermal magnons in our case [285]. Such experiments could shed further light onto the mechanisms below the modulator. For example, it could be investigated if the effect is restricted to the region below the modulator electrode or extended to a larger area. As discussed in Sec. 4.4, our magnon transport measurements suggest the latter. In particular, recent works [197, 198] provided a comprehensive study of the influence of the applied injector current magnitude on the magnon transport in two-terminal structures complemented by BLS measurements. However, in general a high intensity is only achieved in transparent samples. In opaque samples, as in our case, the scattering efficiency is strongly reduced.

To this end, we put forward another possibility in this Section to investigate the magnetization dynamics in our devices. In recent years, nitrogen-vacancy

⁴⁴For all our measurements presented in Ch. 4 the strips were oriented along the hard-axis.

(NV) defects in diamond have emerged as a powerful tool ranging from nanoscale electric and magnetic field sensing [286–291], to single-photon microscopy [292, 293] and quantum information processing [294]. Here, we exploit the electron spins associated with NV defects as a scanning probe magnetometer enabling a spatial mapping of magnetic stray fields with a sub 50 nm spatial resolution [286, 290, 295, 296]. NV magnetometry does not rely on a transparent sample and, in contrast to BLS, can be operated over a wide temperature range from cryogenic to above room temperature. Furthermore, they offer the ability to capture a large frequency range from DC to GHz and can be read out at the single-spin level using table-top photoluminescence microscopy. Recently, scanning NV magnetometry has been utilized to capture the magnetic stray fields of magnetic vortices and domain walls in ferromagnets [297–300] and antiferromagnets [301–305] as well as in several other systems such as multiferroics [306, 307], skyrmions [308–311], superconducting vortices [312–314], and two-dimensional ferromagnetism [315–317]. Most interestingly, in regards to our devices is the imaging of spin waves underneath metal electrodes [318]. This study revealed a 100-fold metal-induced increase in spin-wave damping, which was explained by a model that introduces spin-wave-induced currents into the Landau-Lifshitz-Gilbert (LLG) equation. However, this approach requires resonance between the NV electron spin resonance and the spin waves [318]. Another approach by Du *et al.* [319] demonstrated that it is possible to measure the spin chemical potential of spin waves in a 20 nm thin YIG film by detecting thermal spin fluctuations. In addition, they have shown that driving the FMR provides an efficient method for increasing the spin chemical potential. Due to the ability to measure the temperature *in-situ* [320], NV magnetometry could also be used to provide further insight into the temperature profile below the modulator electrode and verify our thermometry measurements.

In first preliminary measurements, we verify that our PLD grown thin film samples provide a large enough signal allowing for an investigation via NV magnetometry. In Fig. 6.5, we present first images of the stray field above a $t_m = 13.8$ nm thin YIG film (Fig. 6.5(a)) and a $t_m = 42.3$ nm thin hematite film (Fig. 6.5(b)) obtained by scanning NV magnetometry. Note that in both cases, the measurements have been conducted on an unstructured area of the respective film without employing our three- and two-terminal nanostructures. In this case, the NV center corresponding to a point defect in diamond with the electronic ground-state spin $S = 1$ can be initialized and read out via an optical excitation at 532 nm. The electron spin resonance is driven with a microwave field provided by a gold bonding wire to the NV center enabling its manipulation. In addition, a small magnetic field of only a few mT is applied along the NV axis (the axis that aligns with the nitrogen atom and the vacancy) utilizing a permanent magnet, which allows for a sign-

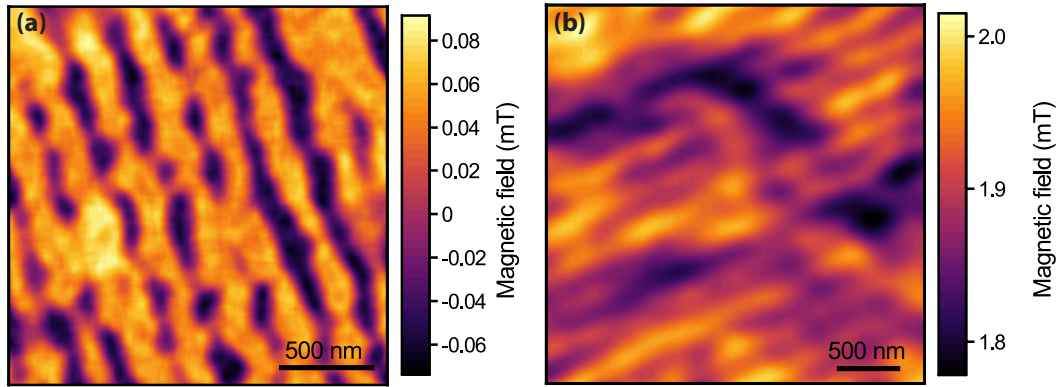


Fig. 6.5 – Magnetic stray field image of (a) a $t_m = 13.8$ nm thin $Y_3Fe_5O_{12}$ and (b) $t_m = 42.3$ nm thin $\alpha-Fe_2O_3$ film grown via PLD. (a) The stray field was measured on a structured YIG film grown on (001)-oriented GGG substrates next to a three-terminal nanostructure (not connected). (b) The NV-magnetometry measurements were performed on a bare hematite film grown on a (0001)-oriented Al_2O_3 substrate.

sensitive measurement of the stray magnetic fields. In order to allow for a scanning of the sample, latter was mounted on fine positioning units. For the ferro(ferri)-magnet YIG as well as for the antiferromagnet $\alpha-Fe_2O_3$, the image clearly shows interesting details. While the YIG sample in Fig. 6.5(a) features signals of about $300 \mu T$ (peak-to-peak), the hematite film exhibits a slightly smaller signal magnitude of about $200 \mu T$. For the latter case of hematite, slightly different results have been found in Ref. [321], where the authors investigate a 10 nm thin $\alpha-Fe_2O_3$ film grown on an Al_2O_3 substrate capped by a 5 nm thick Pt layer and a 2 nm layer of amorphous carbon. In this work, a spectrum demodulation technique relying on a periodic excitation of the electron spin resonance by fast, wide-band frequency sweeps combined with a phase-locked detection of the photo-luminescence signal is introduced to reduce the data acquisition time in scanning NV magnetometry. Room temperature measurements find a signal of $\sim 500 \mu T$ and an average domain size on the order of $1 \mu m$. This is expected for hematite featuring an easy-plane phase, where the two coupled magnetic sublattices are slightly canted in the plane [322]. In our film, we observe features with a smaller distance. This might be related to the absence of a capping in our case. However, a more in-depth investigation is needed to discuss the origin of the observed features in our PLD grown samples.

Our preliminary measurements and the recent progress in the field of NV magnetometry demonstrate that it is a well suited tool to image the spins and currents in our YIG as well as $\alpha-Fe_2O_3$ nanoscale devices, which may enable a better understanding of the underlying mechanisms.

List of Publications

- T. Wimmer, J. Gückelhorn, M. Opel, S. Geprägs, R. Gross, H. Huebl, and M. Althammer, *Analysis of Critical Behavior and Electrical Annealing of Spin Current-Controlled Magnon Transistor Devices*, In preparation (2023).
- M. Scheufele, J. Gückelhorn, M. Opel, A. Kamra, H. Huebl, R. Gross, S. Geprägs, and M. Althammer, *Impact of magnetic anisotropy on the magnon Hanle effect in α -Fe₂O₃*, [arXiv:2306.00375](https://arxiv.org/abs/2306.00375) (2023).
- J. Gückelhorn, S. de-la-Peña, M. Grammer, M. Scheufele, M. Opel, S. Geprägs, J. C. Cuevas, R. Gross, H. Huebl, A. Kamra, and M. Althammer, *Observation of the Nonreciprocal Magnon Hanle Effect*, [Physical Review Letters](https://doi.org/10.1103/PhysRevLett.130.216703) **130**, 216703 (2023).
- M. Müller, M. Scheufele, J. Gückelhorn, L. Flacke, M. Weiler, H. Huebl, S. Geprägs, R. Gross, and M. Althammer, *Reduced effective magnetization and damping by slowly-relaxing impurities in strained γ -Fe₂O₃ thin films*, [Journal of Applied Physics](https://doi.org/10.1063/1.5233905) **132**, 233905 (2022).
- J. Gückelhorn, A. Kamra, T. Wimmer, M. Opel, S. Geprägs, R. Gross, H. Huebl, and M. Althammer, *Influence of low-energy magnons on magnon Hanle experiments in easy-plane antiferromagnets*, [Physical Review B](https://doi.org/10.1103/PhysRevB.105.094440) **105**, 094440 (2022).
- J. Gückelhorn, T. Wimmer, M. Müller, S. Geprägs, H. Huebl, R. Gross, and M. Althammer, *Magnon transport in Y₃Fe₅O₁₂/Pt nanostructures with reduced effective magnetization*, [Physical Review B](https://doi.org/10.1103/PhysRevB.104.L180410) **104**, L180410 (2021).
- T. Wimmer, J. Gückelhorn, S. Wimmer, S. Mankovsky, H. Ebert, M. Opel, S. Geprägs, R. Gross, H. Huebl, and M. Althammer, *Low-temperature suppression of the spin Nernst angle in Pt*, [Physical Review B](https://doi.org/10.1103/PhysRevB.104.L140404) **104**, L140404 (2021).
- T. Wimmer, A. Kamra, J. Gückelhorn, M. Opel, S. Geprägs, R. Gross, H. Huebl, and M. Althammer, *Observation of Antiferromagnetic Magnon Pseudospin Dynamics and the Hanle Effect*, [Physical Review Letters](https://doi.org/10.1103/PhysRevLett.125.247204) **125**, 247204 (2020).
- J. Gückelhorn, T. Wimmer, S. Geprägs, H. Huebl, R. Gross, and M. Althammer, *Quantitative comparison of magnon transport experiments in three-terminal YIG/Pt nanostructures acquired via dc and ac detection techniques*, [Applied Physics Letters](https://doi.org/10.1063/1.5118240) **117**, 182401 (2020).

- M. Kremser, M. Brotons-Gisbert, J. Knörzer, J. Gückelhorn, M. Meyer, M. Barbone, A. V. Stier, B. D. Gerardot, K. Müller, and J. J. Finley, *Discrete interactions between a few interlayer excitons trapped at a MoSe_2 - WSe_2 heterointerface*, [npj 2D Materials and Applications](#) **4** (2020).

Bibliography

- [1] N. Kim, T. Austin, D. Baauw, T. Mudge, K. Flautner, J. Hu, M. Irwin, M. Kandemir, and V. Narayanan, *Leakage current: Moore's law meets static power*, *Computer* **36**, 68 (2003).
- [2] S. Gariglio, *Electric control of a spin current has potential for low-power computing*, *Nature* **580**, 458 (2020).
- [3] M. M. Waldrop, *The chips are down for moore's law*, *Nature* **530**, 144 (2016).
- [4] X. Lin, W. Yang, K. L. Wang, and W. Zhao, *Two-dimensional spintronics for low-power electronics*, *Nature Electronics* **2**, 274 (2019).
- [5] W. Liu, P. K. J. Wong, and Y. Xu, *Hybrid spintronic materials: Growth, structure and properties*, *Progress in Materials Science* **99**, 27 (2019).
- [6] V. K. Joshi, *Spintronics: A contemporary review of emerging electronics devices*, *Engineering Science and Technology, an International Journal* **19**, 1503 (2016).
- [7] J. Puebla, J. Kim, K. Kondou, and Y. Otani, *Spintronic devices for energy-efficient data storage and energy harvesting*, *Communications Materials* **1**, 24 (2020).
- [8] D. Hisamoto, W.-C. Lee, J. Kedzierski, H. Takeuchi, K. Asano, C. Kuo, E. Anderson, T.-J. King, J. Bokor, and C. Hu, *FinFET-a self-aligned double-gate MOSFET scalable to 20 nm*, *IEEE Transactions on Electron Devices* **47**, 2320 (2000).
- [9] M. Bohr, *The new era of scaling in an SoC world*, 2009 IEEE International Solid-State Circuits Conference - Digest of Technical Papers, 23-28, San Francisco, USA (2009).
- [10] S. Lin, Y.-B. Kim, and F. Lombardi, *A novel CNTFET-based ternary logic gate design*, 2009 52nd IEEE International Midwest Symposium on Circuits and Systems, 435-438, Cancun, Mexico (2009).
- [11] J. Zhang, S. Bobba, N. Patil, A. Lin, H.-S. P. Wong, G. De Micheli, and S. Mitra, *Carbon Nanotube Correlation: Promising Opportunity for CNFET Circuit Yield Enhancement*, *Proceedings of the 47th Design Automation Conference*, 889–892, Anaheim, California (2010).

- [12] A. Lungu, P. Bose, A. Buyuktosunoglu, and D. J. Sorin, *Dynamic Power Gating with Quality Guarantees*, *Proceedings of the 2009 ACM/IEEE International Symposium on Low Power Electronics and Design*, 377–382, San Francisco, USA (2009).
- [13] S. M. Yakout, *Spintronics: future technology for new data storage and communication devices*, *Journal of superconductivity and novel magnetism* **33**, 2557 (2020).
- [14] C. Chun-yen, *The highlights in the nano world*, *Proceedings of the IEEE* **91**, 1756 (2003).
- [15] B. Dieny, I. L. Prejbeanu, K. Garello, P. Gambardella, P. Freitas, R. Lehn-dorff, W. Raberg, U. Ebels, S. O. Demokritov, J. Akerman, A. Deac, P. Pirro, C. Adelman, A. Anane, A. V. Chumak, A. Hirohata, S. Mangin, S. O. Valenzuela, M. C. Onbaşlı, M. d’Aquino, G. Prenat, G. Finocchio, L. Lopez-Diaz, R. Chantrell, O. Chubykalo-Fesenko, and P. Bortolotti, *Opportunities and challenges for spintronics in the microelectronics industry*, *Nature Electronics* **3**, 446 (2020).
- [16] E. Y. Vedmedenko, R. K. Kawakami, D. D. Sheka, P. Gambardella, A. Kirilyuk, A. Hirohata, C. Binek, O. Chubykalo-Fesenko, S. Sanvito, B. J. Kirby, J. Grollier, K. Everschor-Sitte, T. Kampfrath, C.-Y. You, and A. Berger, *The 2020 magnetism roadmap*, *Journal of Physics D: Applied Physics* **53**, 453001 (2020).
- [17] V. K. Joshi, P. Barla, S. Bhat, and B. K. Kaushik, *From MTJ Device to Hybrid CMOS/MTJ Circuits: A Review*, *IEEE Access* **8**, 194105 (2020).
- [18] P. Barla, V. K. Joshi, and S. Bhat, *Spintronic devices: a promising alternative to CMOS devices*, *Journal of Computational Electronics* **20**, 805 (2021).
- [19] S. Bhatti, R. Sbiaa, A. Hirohata, H. Ohno, S. Fukami, and S. Piramanayagam, *Spintronics based random access memory: a review*, *Materials Today* **20**, 530 (2017).
- [20] W. Gerlach and O. Stern, *Das magnetische Moment des Silberatoms*, *Zeitschrift für Physik* **9**, 353 (1922).
- [21] W. Gerlach and O. Stern, *Der experimentelle Nachweis der Richtungsquantelung im Magnetfeld*, *Zeitschrift für Physik* **9**, 349 (1922).
- [22] P. A. M. Dirac and R. H. Fowler, *The quantum theory of the electron*, *Proceedings of the Royal Society of London A* **117**, 610 (1928).

- [23] M. N. Baibich, J. M. Broto, A. Fert, F. N. Van Dau, F. Petroff, P. Etienne, G. Creuzet, A. Friederich, and J. Chazelas, *Giant Magnetoresistance of (001)Fe/(001)Cr Magnetic Superlattices*, *Physical Review Letters* **61**, 2472 (1988).
- [24] G. Binasch, P. Grünberg, F. Saurenbach, and W. Zinn, *Enhanced magnetoresistance in layered magnetic structures with antiferromagnetic interlayer exchange*, *Physical Review B* **39**, 4828 (1989).
- [25] S. S. P. Parkin, *Giant Magnetoresistance in Magnetic Nanostructures*, *Annual Review of Materials Science* **25**, 357 (1995).
- [26] M. Julliere, *Tunneling between ferromagnetic films*, *Physics Letters A* **54**, 225 (1975).
- [27] J. S. Moodera, L. R. Kinder, T. M. Wong, and R. Meservey, *Large Magnetoresistance at Room Temperature in Ferromagnetic Thin Film Tunnel Junctions*, *Physical Review Letters* **74**, 3273 (1995).
- [28] T. Miyazaki and N. Tezuka, *Giant magnetic tunneling effect in Fe/Al₂O₃/Fe junction*, *Journal of Magnetism and Magnetic Materials* **139**, L231 (1995).
- [29] S. S. Parkin, C. Kaiser, A. Panchula, P. M. Rice, B. Hughes, M. Samant, and S.-H. Yang, *Giant tunnelling magnetoresistance at room temperature with MgO (100) tunnel barriers*, *Nature Materials* **3**, 862 (2004).
- [30] S. Yuasa, T. Nagahama, A. Fukushima, Y. Suzuki, and K. Ando, *Giant room-temperature magnetoresistance in single-crystal Fe/MgO/Fe magnetic tunnel junctions*, *Nature Materials* **3**, 868 (2004).
- [31] S. Datta and B. Das, *Electronic analog of the electro-optic modulator*, *Applied Physics Letters* **56**, 665 (1990).
- [32] K. S. Das, F. Feringa, M. Middelkamp, B. J. van Wees, and I. J. Vera-Marun, *Modulation of magnon spin transport in a magnetic gate transistor*, *Physical Review B* **101**, 054436 (2020).
- [33] A. Hoffmann, *Pure spin-currents*, *Physica Status Solidi C* **4**, 4236 (2007).
- [34] G. E. Bauer, E. Saitoh, and B. J. Van Wees, *Spin caloritronics*, *Nature Materials* **11**, 391 (2012).
- [35] M. Althammer, *Pure spin currents in magnetically ordered insulator/normal metal heterostructures*, *Journal of Physics D: Applied Physics* **51**, 313001 (2018).

- [36] K. Shen, *Pure spin current in antiferromagnetic insulators*, *Physical Review B* **100**, 094423 (2019).
- [37] A. V. Chumak, V. I. Vasyuchka, A. A. Serga, and B. Hillebrands, *Magnon spintronics*, *Nature Physics* **11**, 453 (2015).
- [38] M. Dyakonov and V. Perel, *Current-induced spin orientation of electrons in semiconductors*, *Physics Letters A* **35**, 459 (1971).
- [39] J. E. Hirsch, *Spin Hall Effect*, *Physical Review Letters* **83**, 1834 (1999).
- [40] V. E. Demidov, S. Urazhdin, H. Ulrichs, V. Tiberkevich, A. Slavin, D. Baither, G. Schmitz, and S. O. Demokritov, *Magnetic nano-oscillator driven by pure spin current*, *Nature Materials* **11**, 1028 (2012).
- [41] R. Cheng, D. Xiao, and A. Brataas, *Terahertz Antiferromagnetic Spin Hall Nano-Oscillator*, *Physical Review Letters* **116**, 207603 (2016).
- [42] T. Chen, R. K. Dumas, A. Eklund, P. K. Muduli, A. Houshang, A. A. Awad, P. Dürrenfeld, B. G. Malm, A. Rusu, and J. Åkerman, *Spin-Torque and Spin-Hall Nano-Oscillators*, *Proceedings of the IEEE* **104**, 1919 (2016).
- [43] L. Cornelissen, J. Liu, R. Duine, J. B. Youssef, and B. Van Wees, *Long-distance transport of magnon spin information in a magnetic insulator at room temperature*, *Nature Physics* **11**, 1022 (2015).
- [44] L. J. Cornelissen, J. Liu, B. J. van Wees, and R. A. Duine, *Spin-Current-Controlled Modulation of the Magnon Spin Conductance in a Three-Terminal Magnon Transistor*, *Physical Review Letters* **120**, 097702 (2018).
- [45] T. Wimmer, M. Althammer, L. Liensberger, N. Vlietstra, S. Geprägs, M. Weiler, R. Gross, and H. Huebl, *Spin Transport in a Magnetic Insulator with Zero Effective Damping*, *Physical Review Letters* **123**, 257201 (2019).
- [46] R. Cheng, M. W. Daniels, J.-G. Zhu, and D. Xiao, *Antiferromagnetic spin wave field-effect transistor*, *Scientific Reports* **6**, 1 (2016).
- [47] M. W. Daniels, R. Cheng, W. Yu, J. Xiao, and D. Xiao, *Nonabelian magnonics in antiferromagnets*, *Physical Review B* **98**, 134450 (2018).
- [48] K. Shen, *Magnon Spin Relaxation and Spin Hall Effect Due to the Dipolar Interaction in Antiferromagnetic Insulators*, *Physical Review Letters* **124**, 077201 (2020).
- [49] M. Kawano and C. Hotta, *Thermal Hall effect and topological edge states in a square-lattice antiferromagnet*, *Physical Review B* **99**, 054422 (2019).

- [50] R. Cheng, S. Okamoto, and D. Xiao, *Spin Nernst Effect of Magnons in Collinear Antiferromagnets*, [Physical Review Letters](#) **117**, 217202 (2016).
- [51] V. A. Zyuzin and A. A. Kovalev, *Magnon Spin Nernst Effect in Antiferromagnets*, [Physical Review Letters](#) **117**, 217203 (2016).
- [52] M. Kawano, Y. Onose, and C. Hotta, *Designing Rashba–Dresselhaus effect in magnetic insulators*, [Communications Physics](#) **2**, 1 (2019).
- [53] I. M. Miron, K. Garello, G. Gaudin, P.-J. Zermatten, M. V. Costache, S. Auffret, S. Bandiera, B. Rodmacq, A. Schuhl, and P. Gambardella, *Perpendicular switching of a single ferromagnetic layer induced by in-plane current injection*, [Nature](#) **476**, 189 (2011).
- [54] C. O. Avci, A. Quindeau, C.-F. Pai, M. Mann, L. Caretta, A. S. Tang, M. C. Onbasli, C. A. Ross, and G. S. Beach, *Current-induced switching in a magnetic insulator*, [Nature Materials](#) **16**, 309 (2017).
- [55] C. Safranski, I. Barsukov, H. K. Lee, T. Schneider, A. Jara, A. Smith, H. Chang, K. Lenz, J. Lindner, Y. Tserkovnyak, M. Wu, and I. N. Krivorotov, *Spin caloritronic nano-oscillator*, [Nature Communications](#) **8**, 117 (2017).
- [56] S. Mühlbauer, B. Binz, F. Jonietz, C. Pfleiderer, A. Rosch, A. Neubauer, R. Georgii, and P. Böni, *Skyrmion Lattice in a Chiral Magnet*, [Science](#) **323**, 915 (2009).
- [57] A. Neubauer, C. Pfleiderer, B. Binz, A. Rosch, R. Ritz, P. G. Niklowitz, and P. Böni, *Topological Hall Effect in the A Phase of MnSi*, [Physical Review Letters](#) **102**, 186602 (2009).
- [58] W. Jiang, P. Upadhyaya, W. Zhang, G. Yu, M. B. Jungfleisch, F. Y. Fradin, J. E. Pearson, Y. Tserkovnyak, K. L. Wang, O. Heinonen, S. G. E. te Velthuis, and A. Hoffmann, *Blowing magnetic skyrmion bubbles*, [Science](#) **349**, 283 (2015).
- [59] A. Fert, N. Reyren, and V. Cros, *Magnetic skyrmions: advances in physics and potential applications*, [Nature Reviews Materials](#) **2**, 17031 (2017).
- [60] K. Everschor-Sitte, J. Masell, R. M. Reeve, and M. Kläui, *Perspective: Magnetic skyrmions – Overview of recent progress in an active research field*, [Journal of Applied Physics](#) **124**, 240901 (2018).
- [61] J. Zázvorka, F. Jakobs, D. Heinze, N. Keil, S. Kromin, S. Jaiswal, K. Litzius, G. Jakob, P. Virnau, D. Pinna, K. Everschor-Sitte, L. Rózsa, A. Donges, U. Nowak, and M. Kläui, *Thermal skyrmion diffusion used in a reshuffler device*, [Nature Nanotechnology](#) **14**, 658 (2019).

- [62] C. Back, V. Cros, H. Ebert, K. Everschor-Sitte, A. Fert, M. Garst, T. Ma, S. Mankovsky, T. L. Monchesky, M. Mostovoy, N. Nagaosa, S. S. P. Parkin, C. Pfleiderer, N. Reyren, A. Rosch, Y. Taguchi, Y. Tokura, K. von Bergmann, and J. Zang, *The 2020 skyrmionics roadmap*, [Journal of Physics D: Applied Physics](#) **53**, 363001 (2020).
- [63] E. Fermi, *Sulla quantizzazione del gas perfetto monoatomico*, [Rendiconti Lincei \(in Italian\)](#) **3**, 145 (1926).
- [64] P. A. M. Dirac and R. H. Fowler, *On the theory of quantum mechanics*, [Proceedings of the Royal Society of London A](#) **112**, 661 (1926).
- [65] S. N. Bose, *Plancks Gesetz und Lichtquantenhypothese*, [Zeitschrift für Physik](#) **26**, 178 (1924).
- [66] A. Einstein, *Quantentheorie des einatomigen idealen Gases. Zweite Abhandlung*, in [Albert Einstein: Akademie-Vorträge](#), 245-257, John Wiley & Sons, Ltd (2005).
- [67] D. rer. nat. Matthias Althammer, *Pure Spin Currents In Magnetic Insulators*, Habilitation, Technische Universität München (2020).
- [68] T. Wimmer, *Control and Manipulation of Magnonic Spin Currents in Magnetic Insulators*, [Dissertation](#), Technical University of Munich (2021).
- [69] Y.-T. Chen, S. Takahashi, H. Nakayama, M. Althammer, S. T. B. Goennenwein, E. Saitoh, and G. E. W. Bauer, *Theory of spin Hall magnetoresistance*, [Physical Review B](#) **87**, 144411 (2013).
- [70] Y.-T. Chen, S. Takahashi, H. Nakayama, M. Althammer, S. T. B. Goennenwein, E. Saitoh, and G. E. W. Bauer, *Theory of spin Hall magnetoresistance (SMR) and related phenomena*, [Journal of Physics: Condensed Matter](#) **28**, 103004 (2016).
- [71] G. E. Uhlenbeck and S. Goudsmit, *Ersetzung der Hypothese vom unmechanischen Zwang durch eine Forderung bezüglich des inneren Verhaltens jedes einzelnen Elektrons*, [Die Naturwissenschaften](#) **13**, 953 (1925).
- [72] W. Pauli, *Zur Quantenmechanik des magnetischen Elektrons*, [Zeitschrift für Physik](#) **43**, 601 (1927).
- [73] R. Gross and A. Marx, *Festkörperphysik*, [De Gruyter](#) (2022).

- [74] P. C. van Son, H. van Kempen, and P. Wyder, *Boundary Resistance of the Ferromagnetic-Nonferromagnetic Metal Interface*, [Physical Review Letters](#) **58**, 2271 (1987).
- [75] J. Fabian, A. Matos-Abiague, C. Ertler, P. Stano, and I. Žutić, *Semiconductor spintronics*, [Acta Physica Slovaca](#) **57**, 565 (2007).
- [76] L. J. Cornelissen, K. J. H. Peters, G. E. W. Bauer, R. A. Duine, and B. J. van Wees, *Magnon spin transport driven by the magnon chemical potential in a magnetic insulator*, [Physical Review B](#) **94**, 014412 (2016).
- [77] L. P. Kadanoff and P. C. Martin, *Hydrodynamic equations and correlation functions*, [Annals of Physics](#) **24**, 419 (1963).
- [78] H. S. Bennett and P. C. Martin, *Spin Diffusion in the Heisenberg Paramagnet*, [Physical Review](#) **138**, A608 (1965).
- [79] I. J. Lowe and S. Gade, *Density-Matrix Derivation of the Spin-Diffusion Equation*, [Physical Review](#) **156**, 817 (1967).
- [80] A. Hoffmann, *Spin Hall Effects in Metals*, [IEEE Transactions on Magnetics](#) **49**, 5172 (2013).
- [81] J. Sinova, S. O. Valenzuela, J. Wunderlich, C. H. Back, and T. Jungwirth, *Spin Hall effects*, [Reviews of Modern Physics](#) **87**, 1213 (2015).
- [82] V. Edelstein, *Spin polarization of conduction electrons induced by electric current in two-dimensional asymmetric electron systems*, [Solid State Communications](#) **73**, 233 (1990).
- [83] J. R. Sánchez, L. Vila, G. Desfonds, S. Gambarelli, J. Attané, J. De Teresa, C. Magén, and A. Fert, *Spin-to-charge conversion using Rashba coupling at the interface between non-magnetic materials*, [Nature Communications](#) **4**, 2944 (2013).
- [84] S. Sangiao, J. M. De Teresa, L. Morellon, I. Lucas, M. C. Martinez-Velarte, and M. Viret, *Control of the spin to charge conversion using the inverse Rashba-Edelstein effect*, [Applied Physics Letters](#) **106**, 172403 (2015).
- [85] A. Manchon, H. C. Koo, J. Nitta, S. M. Frolov, and R. A. Duine, *New perspectives for Rashba spin-orbit coupling*, [Nature Materials](#) **14**, 871 (2015).
- [86] Q. Shao, G. Yu, Y.-W. Lan, Y. Shi, M.-Y. Li, C. Zheng, X. Zhu, L.-J. Li, P. K. Amiri, and K. L. Wang, *Strong Rashba-Edelstein Effect-Induced Spin-Orbit*

Torques in Monolayer Transition Metal Dichalcogenide/Ferromagnet Bilayers, *Nano Letters* **16**, 7514 (2016).

- [87] N. Nagaosa, J. Sinova, S. Onoda, A. H. MacDonald, and N. P. Ong, *Anomalous Hall effect*, *Reviews of Modern Physics* **82**, 1539 (2010).
- [88] T. Taniguchi, J. Grollier, and M. D. Stiles, *Spin-Transfer Torques Generated by the Anomalous Hall Effect and Anisotropic Magnetoresistance*, *Physical Review Applied* **3**, 044001 (2015).
- [89] A. Davidson, V. P. Amin, W. S. Aljuaid, P. M. Haney, and X. Fan, *Perspectives of electrically generated spin currents in ferromagnetic materials*, *Physics Letters A* **384**, 126228 (2020).
- [90] Y. K. Kato, R. C. Myers, A. C. Gossard, and D. D. Awschalom, *Observation of the Spin Hall Effect in Semiconductors*, *Science* **306**, 1910 (2004).
- [91] Y. Tserkovnyak and S. A. Bender, *Spin Hall phenomenology of magnetic dynamics*, *Physical Review B* **90**, 014428 (2014).
- [92] M. Althammer, S. Meyer, H. Nakayama, M. Schreier, S. Altmannshofer, M. Weiler, H. Huebl, S. Geprägs, M. Opel, R. Gross, D. Meier, C. Klewe, T. Kuschel, J.-M. Schmalhorst, G. Reiss, L. Shen, A. Gupta, Y.-T. Chen, G. E. W. Bauer, E. Saitoh, and S. T. B. Goennenwein, *Quantitative study of the spin Hall magnetoresistance in ferromagnetic insulator/normal metal hybrids*, *Physical Review B* **87**, 224401 (2013).
- [93] D. Ralph and M. Stiles, *Spin transfer torques*, *Journal of Magnetism and Magnetic Materials* **320**, 1190 (2008).
- [94] A. Manchon, J. Železný, I. M. Miron, T. Jungwirth, J. Sinova, A. Thiaville, K. Garello, and P. Gambardella, *Current-induced spin-orbit torques in ferromagnetic and antiferromagnetic systems*, *Review of Modern Physics* **91**, 035004 (2019).
- [95] S. A. Bender and Y. Tserkovnyak, *Interfacial spin and heat transfer between metals and magnetic insulators*, *Physical Review B* **91**, 140402 (2015).
- [96] A. Brataas, Y. V. Nazarov, and G. E. W. Bauer, *Finite-Element Theory of Transport in Ferromagnet–Normal Metal Systems*, *Physical Review Letters* **84**, 2481 (2000).
- [97] Y. Tserkovnyak, A. Brataas, and G. E. W. Bauer, *Enhanced Gilbert Damping in Thin Ferromagnetic Films*, *Physical Review Letters* **88**, 117601 (2002).

- [98] Y. Tserkovnyak, A. Brataas, and G. E. W. Bauer, *Spin pumping and magnetization dynamics in metallic multilayers*, *Physical Review B* **66**, 224403 (2002).
- [99] M. Büttiker, *Four-Terminal Phase-Coherent Conductance*, *Physical Review Letters* **57**, 1761 (1986).
- [100] B. J. van Wees, H. van Houten, C. W. J. Beenakker, J. G. Williamson, L. P. Kouwenhoven, D. van der Marel, and C. T. Foxon, *Quantized conductance of point contacts in a two-dimensional electron gas*, *Physical Review Letters* **60**, 848 (1988).
- [101] X. Jia, K. Liu, K. Xia, and G. E. W. Bauer, *Spin transfer torque on magnetic insulators*, *Europhysics Letters* **96**, 17005 (2011).
- [102] M. Weiler, M. Althammer, M. Schreier, J. Lotze, M. Pernpeintner, S. Meyer, H. Huebl, R. Gross, A. Kamra, J. Xiao, Y.-T. Chen, H. Jiao, G. E. W. Bauer, and S. T. B. Goennenwein, *Experimental Test of the Spin Mixing Interface Conductivity Concept*, *Physical Review Letters* **111**, 176601 (2013).
- [103] L. Liu, Y. Li, Y. Liu, T. Feng, J. Xu, X. R. Wang, D. Wu, P. Gao, and J. Li, *Interfacial modulation of spin pumping in YIG/Pt*, *Physical Review B* **102**, 014411 (2020).
- [104] M. Johnson and R. H. Silsbee, *Interfacial charge-spin coupling: Injection and detection of spin magnetization in metals*, *Physical Review Letters* **55**, 1790 (1985).
- [105] M. Johnson and R. H. Silsbee, *Coupling of electronic charge and spin at a ferromagnetic-paramagnetic metal interface*, *Physical Review B* **37**, 5312 (1988).
- [106] S. Maekawa, S. Valenzuela, E. Saitoh, and T. Kimura, *Spin Current*, OUP Oxford (2012).
- [107] X. Waintal, E. B. Myers, P. W. Brouwer, and D. C. Ralph, *Role of spin-dependent interface scattering in generating current-induced torques in magnetic multilayers*, *Physical Review B* **62**, 12317 (2000).
- [108] P. M. Haney, H.-W. Lee, K.-J. Lee, A. Manchon, and M. D. Stiles, *Current induced torques and interfacial spin-orbit coupling: Semiclassical modeling*, *Physical Review B* **87**, 174411 (2013).
- [109] T. Gilbert, *A phenomenological theory of damping in ferromagnetic materials*, *IEEE Transactions on Magnetics* **40**, 3443 (2004).

- [110] L. Landau and E. Lifshitz, *On the theory of the dispersion of magnetic permeability in ferromagnetic bodies*, in *Perspectives in Theoretical Physics*, 51-65, Elsevier (1992).
- [111] Y. Tserkovnyak, A. Brataas, G. E. W. Bauer, and B. I. Halperin, *Nonlocal magnetization dynamics in ferromagnetic heterostructures*, *Review of Modern Physics* **77**, 1375 (2005).
- [112] M. V. Costache, M. Sladkov, S. M. Watts, C. H. van der Wal, and B. J. van Wees, *Electrical Detection of Spin Pumping due to the Precessing Magnetization of a Single Ferromagnet*, *Physical Review Letters* **97**, 216603 (2006).
- [113] O. Mosendz, V. Vlaminck, J. E. Pearson, F. Y. Fradin, G. E. W. Bauer, S. D. Bader, and A. Hoffmann, *Detection and quantification of inverse spin Hall effect from spin pumping in permalloy/normal metal bilayers*, *Physical Review B* **82**, 214403 (2010).
- [114] K. Ando, S. Takahashi, J. Ieda, Y. Kajiwara, H. Nakayama, T. Yoshino, K. Harii, Y. Fujikawa, M. Matsuo, S. Maekawa, and E. Saitoh, *Inverse spin-Hall effect induced by spin pumping in metallic system*, *Journal of Applied Physics* **109**, 103913 (2011).
- [115] B. Heinrich, C. Burrowes, E. Montoya, B. Kardasz, E. Girt, Y. Y. Song, Y. Sun, and M. Wu, *Spin Pumping at the Magnetic Insulator (YIG)/Normal Metal (Au) Interfaces*, *Physical Review Letters* **107**, 066604 (2011).
- [116] C. Hahn, G. de Loubens, M. Viret, O. Klein, V. V. Naletov, and J. Ben Youssef, *Detection of Microwave Spin Pumping Using the Inverse Spin Hall Effect*, *Physical Review Letters* **111**, 217204 (2013).
- [117] J. Xiao, G. E. W. Bauer, K. Uchida, E. Saitoh, and S. Maekawa, *Theory of magnon-driven spin Seebeck effect*, *Physical Review B* **81**, 214418 (2010).
- [118] K. Uchida, J. Xiao, H. Adachi, J. Ohe, S. Takahashi, J. Ieda, T. Ota, Y. Kajiwara, H. Umezawa, H. Kawai, G. E. W. Bauer, S. Maekawa, and E. Saitoh, *Spin Seebeck insulator*, *Nature Materials* **9**, 894 (2010).
- [119] H. Nakayama, M. Althammer, Y. T. Chen, K. Uchida, Y. Kajiwara, D. Kikuchi, T. Ohtani, S. Geprägs, M. Opel, S. Takahashi, R. Gross, G. E. W. Bauer, S. T. B. Goennenwein, and E. Saitoh, *Spin Hall Magnetoresistance Induced by a Nonequilibrium Proximity Effect*, *Physical Review Letters* **110**, 206601 (2013).

- [120] S. T. B. Goennenwein, R. Schlitz, M. Pernpeintner, K. Ganzhorn, M. Althammer, R. Gross, and H. Huebl, *Non-local magnetoresistance in YIG/Pt nanostructures*, [Applied Physics Letters](#) **107**, 172405 (2015).
- [121] X. Wang, Z. Zhou, Y. Nie, Q. Xia, and G. Guo, *Self-consistent study of local and nonlocal magnetoresistance in a YIG/Pt bilayer*, [Physical Review B](#) **97**, 094401 (2018).
- [122] N. Vlietstra, J. Shan, V. Castel, B. J. van Wees, and J. Ben Youssef, *Spin-Hall magnetoresistance in platinum on yttrium iron garnet: Dependence on platinum thickness and in-plane/out-of-plane magnetization*, [Physical Review B](#) **87**, 184421 (2013).
- [123] S. Meyer, R. Schlitz, S. Geprägs, M. Opel, H. Huebl, R. Gross, and S. T. B. Goennenwein, *Anomalous Hall effect in YIG|Pt bilayers*, [Applied Physics Letters](#) **106**, 132402 (2015).
- [124] J. M. Gomez-Perez, X.-P. Zhang, F. Calavalle, M. Ilyn, C. González-Orellana, M. Gobbi, C. Rogero, A. Chuvilin, V. N. Golovach, L. E. Hueso, F. S. Bergeret, and F. Casanova, *Strong Interfacial Exchange Field in a Heavy Metal/Ferromagnetic Insulator System Determined by Spin Hall Magnetoresistance*, [Nano Letters](#) **20**, 6815 (2020).
- [125] S. S.-L. Zhang and S. Zhang, *Magnon Mediated Electric Current Drag Across a Ferromagnetic Insulator Layer*, [Physical Review Letters](#) **109**, 096603 (2012).
- [126] S. S.-L. Zhang and S. Zhang, *Spin convertance at magnetic interfaces*, [Physical Review B](#) **86**, 214424 (2012).
- [127] T. Wimmer, A. Kamra, J. Gückelhorn, M. Opel, S. Geprägs, R. Gross, H. Huebl, and M. Althammer, *Observation of Antiferromagnetic Magnon Pseudospin Dynamics and the Hanle Effect*, [Physical Review Letters](#) **125**, 247204 (2020).
- [128] S. M. Rezende, A. Azevedo, and R. L. Rodríguez-Suárez, *Introduction to antiferromagnetic magnons*, [Journal of Applied Physics](#) **126**, 151101 (2019).
- [129] J. Barker and G. E. W. Bauer, *Thermal Spin Dynamics of Yttrium Iron Garnet*, [Physical Review Letters](#) **117**, 217201 (2016).
- [130] S. Geprägs, A. Kehlberger, F. D. Coletta, Z. Qiu, E.-J. Guo, T. Schulz, C. Mix, S. Meyer, A. Kamra, M. Althammer, H. Huebl, G. Jakob, Y. Ohnuma, H. Adachi, J. Barker, S. Maekawa, G. E. W. Bauer, E. Saitoh, R. Gross, S. T. B. Goennenwein, and M. Kläui, *Origin of the spin Seebeck effect in compensated ferrimagnets*, [Nature Communications](#) **7**, 10452 (2016).

- [131] J. Cramer, E.-J. Guo, S. Geprägs, A. Kehlberger, Y. P. Ivanov, K. Ganzhorn, F. Della Coletta, M. Althammer, H. Huebl, R. Gross, J. Kosel, M. Kläui, and S. T. B. Goennenwein, *Magnon Mode Selective Spin Transport in Compensated Ferrimagnets*, *Nano Letters* **17**, 3334 (2017).
- [132] Y. Ohnuma, H. Adachi, E. Saitoh, and S. Maekawa, *Spin Seebeck effect in antiferromagnets and compensated ferrimagnets*, *Physical Review B* **87**, 014423 (2013).
- [133] C. Kim, S. Lee, H. G. Kim, J. H. Park, K. W. Moon, J. Y. Park, J. M. Yuk, K. J. Lee, B. G. Park, S. K. Kim, K. J. Kim, and C. Hwang, *Distinct handedness of spin wave across the compensation temperatures of ferrimagnets*, *Nature Materials* **19**, 980 (2020).
- [134] R. Lebrun, A. Ross, S. Bender, A. Qaiumzadeh, L. Baldrati, J. Cramer, A. Brataas, R. Duine, and M. Kläui, *Tunable long-distance spin transport in a crystalline antiferromagnetic iron oxide*, *Nature* **561**, 222 (2018).
- [135] S. M. Wu, W. Zhang, A. KC, P. Borisov, J. E. Pearson, J. S. Jiang, D. Lederman, A. Hoffmann, and A. Bhattacharya, *Antiferromagnetic Spin Seebeck Effect*, *Physical Review Letters* **116**, 097204 (2016).
- [136] I. Dzyaloshinsky, *A thermodynamic theory of “weak” ferromagnetism of antiferromagnetics*, *Journal of Physics and Chemistry of Solids* **4**, 241 (1958).
- [137] T. Moriya, *Anisotropic Superexchange Interaction and Weak Ferromagnetism*, *Physical Review* **120**, 91 (1960).
- [138] A. Kamra, T. Wimmer, H. Huebl, and M. Althammer, *Antiferromagnetic magnon pseudospin: Dynamics and diffusive transport*, *Physical Review B* **102**, 174445 (2020).
- [139] K. S. Olsson, K. An, G. A. Fiete, J. Zhou, L. Shi, and X. Li, *Pure Spin Current and Magnon Chemical Potential in a Nonequilibrium Magnetic Insulator*, *Physical Review X* **10**, 021029 (2020).
- [140] K. Ganzhorn, T. Wimmer, J. Cramer, R. Schlitz, S. Geprägs, G. Jakob, R. Gross, H. Huebl, M. Kläui, and S. T. B. Goennenwein, *Temperature dependence of the non-local spin Seebeck effect in YIG/Pt nanostructures*, *AIP Advances* **7**, 085102 (2017).
- [141] J. Shan, L. J. Cornelissen, N. Vlietstra, J. Ben Youssef, T. Kuschel, R. A. Duine, and B. J. van Wees, *Influence of yttrium iron garnet thickness and heater opacity*

- on the nonlocal transport of electrically and thermally excited magnons, *Physical Review B* **94**, 174437 (2016).
- [142] M. Schreier, N. Roschewsky, E. Dobler, S. Meyer, H. Huebl, R. Gross, and S. T. B. Goennenwein, *Current heating induced spin Seebeck effect*, *Applied Physics Letters* **103**, 242404 (2013).
- [143] S. M. Rezende, R. L. Rodríguez-Suárez, R. O. Cunha, A. R. Rodrigues, F. L. A. Machado, G. A. Fonseca Guerra, J. C. Lopez Ortiz, and A. Azevedo, *Magnon spin-current theory for the longitudinal spin-Seebeck effect*, *Physical Review B* **89**, 014416 (2014).
- [144] P. Drude, *Zur Elektronentheorie der Metalle*, *Annalen der Physik* **306**, 566 (1900).
- [145] P. Drude, *Zur Elektronentheorie der Metalle; II. Teil. Galvanomagnetische und thermomagnetische Effecte*, *Annalen der Physik* **308**, 369 (1900).
- [146] S. Geller and M. Gilleo, *The crystal structure and ferrimagnetism of yttrium-iron garnet, $Y_3Fe_2(FeO_4)_3$* , *Journal of Physics and Chemistry of Solids* **3**, 30 (1957).
- [147] M. A. Gilleo and S. Geller, *Magnetic and Crystallographic Properties of Substituted Yttrium-Iron Garnet, $3Y_2O_3 \cdot xM_2O_3 \cdot (5 - x)Fe_2O_3$* , *Physical Review* **110**, 73 (1958).
- [148] C. Suchomski, *Strukturelle, optische und magnetische Eigenschaften von Nanokristallinen Metalloxid-Dünnschichten mit mesoporöser Morphologie*, *Dissertation, Justus-Liebig-Universität Giessen* (2012).
- [149] V. Cherepanov, I. Kolokolov, and V. L'vov, *The saga of YIG: Spectra, thermodynamics, interaction and relaxation of magnons in a complex magnet*, *Physics Reports* **229**, 81 (1993).
- [150] N. Miura, I. Oguro, and S. Chikazumi, *Computer simulation of temperature and field dependences of sublattice magnetizations and spin-flip transition in gallium-substituted yttrium iron garnet*, *Journal of the Physical Society of Japan* **45**, 1534 (1978).
- [151] K. E. P. Hansen, G. Winkler, *Landolt-Börnstein Group III: Condensed Matter Vol. 12A (Part A: Garnets and Perovskites)*, *Springer-Verlag* (1978).
- [152] H. Maier-Flaig, S. Klingler, C. Dubs, O. Surzhenko, R. Gross, M. Weiler, H. Huebl, and S. T. B. Goennenwein, *Temperature-dependent magnetic damping of yttrium iron garnet spheres*, *Physical Review B* **95**, 214423 (2017).

- [153] C. Dubs, O. Surzhenko, R. Linke, A. Danilewsky, U. Brückner, and J. Dellith, *Sub-micrometer yttrium iron garnet LPE films with low ferromagnetic resonance losses*, *Journal of Physics D: Applied Physics* **50**, 204005 (2017).
- [154] S. Klingler, H. Maier-Flaig, C. Dubs, O. Surzhenko, R. Gross, H. Huebl, S. T. B. Goennenwein, and M. Weiler, *Gilbert damping of magnetostatic modes in a yttrium iron garnet sphere*, *Applied Physics Letters* **110**, 092409 (2017).
- [155] M. Haertinger, C. H. Back, J. Lotze, M. Weiler, S. Geprägs, H. Huebl, S. T. B. Goennenwein, and G. Woltersdorf, *Spin pumping in YIG/Pt bilayers as a function of layer thickness*, *Physical Review B* **92**, 054437 (2015).
- [156] O. d'Allivy Kelly, A. Anane, R. Bernard, J. Ben Youssef, C. Hahn, A. H. Molpeceres, C. Carrétéro, E. Jacquet, C. Deranlot, P. Bortolotti, R. Lebourgeois, J.-C. Mage, G. de Loubens, O. Klein, V. Cros, and A. Fert, *Inverse spin Hall effect in nanometer-thick yttrium iron garnet/Pt system*, *Applied Physics Letters* **103**, 082408 (2013).
- [157] A. V. Chumak, A. A. Serga, M. B. Jungfleisch, R. Neb, D. A. Bozhko, V. S. Tiberkevich, and B. Hillebrands, *Direct detection of magnon spin transport by the inverse spin Hall effect*, *Applied Physics Letters* **100**, 082405 (2012).
- [158] A. H. Morrish, *Canted Antiferromagnetism: Hematite*, **WORLD SCIENTIFIC** (1995).
- [159] E. J. Samuelsen and G. Shirane, *Inelastic neutron scattering investigation of spin waves and magnetic interactions in α -Fe₂O₃*, *physica status solidi (b)* **42**, 241 (1970).
- [160] C. G. Shull, W. A. Strauser, and E. O. Wollan, *Neutron Diffraction by Paramagnetic and Antiferromagnetic Substances*, *Physical Review* **83**, 333 (1951).
- [161] F. J. Morin, *Magnetic Susceptibility of α -Fe₂O₃ and α -Fe₂O₃ with Added Titanium*, *Physical Review* **78**, 819 (1950).
- [162] P. J. Besser, A. H. Morrish, and C. W. Searle, *Magnetocrystalline Anisotropy of Pure and Doped Hematite*, *Physical Review* **153**, 632 (1967).
- [163] A. Ross, R. Lebrun, O. Gomonay, D. A. Grave, A. Kay, L. Baldrati, S. Becker, A. Qaiumzadeh, C. Ulloa, G. Jakob, F. Kronast, J. Sinova, R. Duine, A. Brataas, A. Rothschild, and M. Kläui, *Propagation Length of Antiferromagnetic Magnons Governed by Domain Configurations*, *Nano Letters* **20**, 306 (2020).

- [164] J. Han, P. Zhang, Z. Bi, Y. Fan, T. S. Safi, J. Xiang, J. Finley, L. Fu, R. Cheng, and L. Liu, *Birefringence-like spin transport via linearly polarized antiferromagnetic magnons*, [Nature Nanotechnology](#) **15**, 563 (2020).
- [165] M. Grammer, *Controlling Magnon Transport in the Antiferromagnetic Insulator Hematite*, [Master's thesis, Technical University of Munich](#) (2022).
- [166] J. Ahopelto, G. Ardila, L. Baldi, F. Balestra, D. Belot, G. Fagas, S. D. Gendt, D. Demarchi, M. Fernandez-Bolaños, D. Holden, A. Ionescu, G. Meneghesso, A. Mocuta, M. Pfeffer, R. Popp, E. Sangiorgi, and C. S. Torres, *NanoElectronics roadmap for Europe: From nanodevices and innovative materials to system integration*, [Solid-State Electronics](#) **155**, 7 (2019).
- [167] R. Jansen, *Silicon spintronics*, [Nature Materials](#) **11**, 400 (2012).
- [168] M. Coll, J. Fontcuberta, M. Althammer, M. Bibes, H. Boschker, A. Calleja, G. Cheng, M. Cuoco, R. Dittmann, B. Dkhil, I. E. Baggari], M. Fanciulli, I. Fina, E. Fortunato, C. Frontera, S. Fujita, V. Garcia, S. Goennenwein, C.-G. Granqvist, J. Grollier, R. Gross, A. Hagfeldt, G. Herranz, K. Hono, E. Houwman, M. Huijben, A. Kalaboukhov, D. Keeble, G. Koster, L. Kourkoutis, J. Levy, M. Lira-Cantu, J. MacManus-Driscoll, J. Mannhart, R. Martins, S. Menzel, T. Mikolajick, M. Napari, M. Nguyen, G. Niklasson, C. Paillard, S. Panigrahi, G. Rijnders, F. Sánchez, P. Sanchis, S. Sanna, D. Schlom, U. Schroeder, K. Shen, A. Siemon, M. Spreitzer, H. Sukegawa, R. Tamayo, J. [van den Brink], N. Pryds, and F. M. Granozio, *Towards Oxide Electronics: a Roadmap*, [Applied Surface Science](#) **482**, 1 (2019).
- [169] A. V. Chumak, A. A. Serga, and B. Hillebrands, *Magnonic crystals for data processing*, [Journal of Physics D: Applied Physics](#) **50**, 244001 (2017).
- [170] K. Nakata, P. Simon, and D. Loss, *Spin currents and magnon dynamics in insulating magnets*, [Journal of Physics D: Applied Physics](#) **50**, 114004 (2017).
- [171] K. An, D. R. Birt, C.-F. Pai, K. Olsson, D. C. Ralph, R. A. Buhrman, and X. Li, *Control of propagating spin waves via spin transfer torque in a metallic bilayer waveguide*, [Physical Review B](#) **89**, 140405 (2014).
- [172] O. Gladii, M. Collet, K. Garcia-Hernandez, C. Cheng, S. Xavier, P. Bortolotti, V. Cros, Y. Henry, J.-V. Kim, A. Anane, and M. Bailleul, *Spin wave amplification using the spin Hall effect in permalloy/platinum bilayers*, [Applied Physics Letters](#) **108**, 202407 (2016).

- [173] V. E. Demidov, S. Urazhdin, E. R. J. Edwards, M. D. Stiles, R. D. McMichael, and S. O. Demokritov, *Control of Magnetic Fluctuations by Spin Current*, [Physical Review Letters](#) **107**, 107204 (2011).
- [174] V. E. Demidov, S. Urazhdin, A. B. Rinkevich, G. Reiss, and S. O. Demokritov, *Spin Hall controlled magnonic microwaveguides*, [Applied Physics Letters](#) **104**, 152402 (2014).
- [175] T. Fischer, M. Kewenig, D. A. Bozhko, A. A. Serga, I. I. Syvorotka, F. Ciubotaru, C. Adelmann, B. Hillebrands, and A. V. Chumak, *Experimental prototype of a spin-wave majority gate*, [Applied Physics Letters](#) **110**, 152401 (2017).
- [176] A. V. Chumak, A. A. Serga, and B. Hillebrands, *Magnon transistor for all-magnon data processing*, [Nature Communications](#) **5**, 1 (2014).
- [177] M. Krawczyk and D. Grundler, *Review and prospects of magnonic crystals and devices with reprogrammable band structure*, [Journal of Physics: Condensed Matter](#) **26**, 123202 (2014).
- [178] S. Vélez, A. Bedoya-Pinto, W. Yan, L. E. Hueso, and F. Casanova, *Competing effects at Pt/YIG interfaces: Spin Hall magnetoresistance, magnon excitations, and magnetic frustration*, [Physical Review B](#) **94**, 174405 (2016).
- [179] B. L. Giles, Z. Yang, J. S. Jamison, and R. C. Myers, *Long-range pure magnon spin diffusion observed in a nonlocal spin-Seebeck geometry*, [Physical Review B](#) **92**, 224415 (2015).
- [180] M. I. Dyakonov and V. I. Perel, *Possibility of Orienting Electron Spins with Current*, [Journal of Experimental and Theoretical Physics Letters](#) **13** (1971).
- [181] M. Althammer, *All-Electrical Magnon Transport Experiments in Magnetically Ordered Insulators*, [physica status solidi \(RRL\) – Rapid Research Letters](#) **15**, 2100130 (2021).
- [182] Y. Kajiwara, K. Harii, S. Takahashi, J. Ohe, K. Uchida, M. Mizuguchi, H. Umezawa, H. Kawai, K. Ando, K. Takanashi, S. Maekawa, and E. Saitoh, *Transmission of electrical signals by spin-wave interconversion in a magnetic insulator*, [Nature](#) **464**, 262 (2010).
- [183] H. Yu, O. d’Allivy Kelly, V. Cros, R. Bernard, P. Bortolotti, A. Anane, F. Brandl, F. Heimbach, and D. Grundler, *Approaching soft X-ray wavelengths in nanomagnet-based microwave technology*, [Nature Communications](#) **7**, 11255 (2016).

- [184] C. Liu, J. Chen, T. Liu, F. Heimbach, H. Yu, Y. Xiao, J. Hu, M. Liu, H. Chang, T. Stueckler, S. Tu, Y. Zhang, Y. Zhang, P. Gao, Z. Liao, D. Yu, K. Xia, n. Lei, W. ZHAO, and M. Wu, *Long-distance propagation of short-wavelength spin waves*, [Nature Communications](#) **9**, 738 (2018).
- [185] K. Ganzhorn, S. Klingler, T. Wimmer, S. Geprägs, R. Gross, H. Huebl, and S. T. B. Goennenwein, *Magnon-based logic in a multi-terminal YIG/Pt nanostructure*, [Applied Physics Letters](#) **109**, 022405 (2016).
- [186] J. Cramer, L. Baldrati, A. Ross, M. Vafae, R. Lebrun, and M. Kläui, *Impact of electromagnetic fields and heat on spin transport signals in $Y_3Fe_5O_{12}$* , [Physical Review B](#) **100**, 094439 (2019).
- [187] S. Takei, *Spin transport in an electrically driven magnon gas near Bose-Einstein condensation: Hartree-Fock-Keldysh theory*, [Physical Review B](#) **100**, 134440 (2019).
- [188] J. Liu, X.-Y. Wei, G. E. W. Bauer, J. B. Youssef, and B. J. van Wees, *Electrically induced strong modulation of magnon transport in ultrathin magnetic insulator films*, [Physical Review B](#) **103**, 214425 (2021).
- [189] L. Berger, *Emission of spin waves by a magnetic multilayer traversed by a current*, [Physical Review B](#) **54**, 9353 (1996).
- [190] A. Hamadeh, O. d'Allivy Kelly, C. Hahn, H. Meley, R. Bernard, A. H. Molpeceres, V. V. Naletov, M. Viret, A. Anane, V. Cros, S. O. Demokritov, J. L. Prieto, M. Muñoz, G. de Loubens, and O. Klein, *Full Control of the Spin-Wave Damping in a Magnetic Insulator Using Spin-Orbit Torque*, [Physical Review Letters](#) **113**, 197203 (2014).
- [191] M. Collet, X. De Milly, O. d. Kelly, V. V. Naletov, R. Bernard, P. Bortolotti, J. B. Youssef, V. Demidov, S. Demokritov, J. L. Prieto, M. Muñoz, V. Cros, A. Anane, G. de Loubens, and O. Klein, *Generation of coherent spin-wave modes in yttrium iron garnet microdiscs by spin-orbit torque*, [Nature Communications](#) **7**, 10377 (2016).
- [192] B. Hillebrands and A. Thiaville, *Spin Dynamics in Confined Magnetic Structures III*, [Springer](#) (2006).
- [193] A. Prabhakar and D. D. Stancil, *Spin waves*, [Springer](#) (2009).
- [194] W. Zhang, W. Han, X. Jiang, S.-H. Yang, and S. Parkin, *Role of transparency of platinum-ferromagnet interface in determining intrinsic magnitude of spin Hall effect*, [Nature Physics](#) **11**, 496 (2015).

- [195] S. A. Bender, R. A. Duine, and Y. Tserkovnyak, *Electronic Pumping of Quasiequilibrium Bose-Einstein-Condensed Magnons*, [Physical Review Letters](#) **108**, 246601 (2012).
- [196] S. A. Bender, R. A. Duine, A. Brataas, and Y. Tserkovnyak, *Dynamic phase diagram of dc-pumped magnon condensates*, [Physical Review B](#) **90**, 094409 (2014).
- [197] R. Kohno, N. Thiery, E. Clot, R. Schlitz, K. An, V. V. Naletov, L. Vila, N. Beaulieu, J. B. Youssef, H. Merbouche, V. Cros, M. Anane, T. Hauet, V. E. Demidov, S. O. Demokritov, G. de Loubens, and O. Klein, *Non-local magnon transconductance in extended magnetic insulating films. Part I: spin diode effect*, [arXiv:2210.08304](#) (2022).
- [198] R. Kohno, N. Thiery, E. Clot, R. Schlitz, K. An, V. V. Naletov, L. Vila, N. Beaulieu, J. B. Youssef, H. Merbouche, V. Cros, M. Anane, T. Hauet, V. E. Demidov, S. O. Demokritov, G. de Loubens, and O. Klein, *Non-local magnon transconductance in extended magnetic insulating films. Part II: two-fluid behavior*, [arXiv:2210.08283](#) (2022).
- [199] N. Thiery, A. Draveny, V. V. Naletov, L. Vila, J. P. Attané, C. Beigné, G. de Loubens, M. Viret, N. Beaulieu, J. Ben Youssef, V. E. Demidov, S. O. Demokritov, A. N. Slavin, V. S. Tiberkevich, A. Anane, P. Bortolotti, V. Cros, and O. Klein, *Nonlinear spin conductance of yttrium iron garnet thin films driven by large spin-orbit torque*, [Physical Review B](#) **97**, 060409 (2018).
- [200] J. Gückelhorn, T. Wimmer, M. Müller, S. Geprägs, H. Huebl, R. Gross, and M. Althammer, *Magnon transport in $Y_3Fe_5O_{12}/Pt$ nanostructures with reduced effective magnetization*, [Physical Review B](#) **104**, L180410 (2021).
- [201] H. Suhl, *The theory of ferromagnetic resonance at high signal powers*, [Journal of Physics and Chemistry of Solids](#) **1**, 209 (1957).
- [202] M. Evelt, L. Soumah, A. Rinkevich, S. Demokritov, A. Anane, V. Cros, J. Ben Youssef, G. de Loubens, O. Klein, P. Bortolotti, and V. Demidov, *Emission of Coherent Propagating Magnons by Insulator-Based Spin-Orbit-Torque Oscillators*, [Physical Review Applied](#) **10**, 041002 (2018).
- [203] B. Divinskiy, S. Urazhdin, S. O. Demokritov, and V. E. Demidov, *Controlled nonlinear magnetic damping in spin-Hall nano-devices*, [Nature Communications](#) **10**, 1 (2019).
- [204] E. Popova, N. Keller, F. Gendron, L. Thomas, M.-C. Brioso, M. Guyot, M. Tessier, and S. S. P. Parkin, *Perpendicular magnetic anisotropy in ultrathin*

- yttrium iron garnet films prepared by pulsed laser deposition technique*, *Journal of Vacuum Science & Technology A* **19**, 2567 (2001).
- [205] C. Y. Guo, C. H. Wan, M. K. Zhao, H. Wu, C. Fang, Z. R. Yan, J. F. Feng, H. F. Liu, and X. F. Han, *Spin-orbit torque switching in perpendicular $Y_3Fe_5O_{12}/Pt$ bilayer*, *Applied Physics Letters* **114**, 192409 (2019).
- [206] H. Maier-Flaig, S. T. B. Goennenwein, R. Ohshima, M. Shiraishi, R. Gross, H. Huebl, and M. Weiler, *Note: Derivative divide, a method for the analysis of broadband ferromagnetic resonance in the frequency domain*, *Review of Scientific Instruments* **89**, 076101 (2018).
- [207] Y. Lin, L. Jin, D. Zhang, H. Zhang, and Z. Wang, *Magnetic Anisotropy of Yttrium Iron Garnet from Density Functional Theory*, *The Journal of Physical Chemistry C* **127**, 689 (2023).
- [208] J. Gückelhorn, T. Wimmer, S. Geprägs, H. Huebl, R. Gross, and M. Althammer, *Quantitative comparison of magnon transport experiments in three-terminal YIG/Pt nanostructures acquired via dc and ac detection techniques*, *Applied Physics Letters* **117**, 182401 (2020).
- [209] A. Vansteenkiste, J. Leliaert, M. Dvornik, M. Helsen, F. Garcia-Sanchez, and B. Van Waeyenberge, *The design and verification of MuMax3*, *AIP Advances* **4**, 107133 (2014).
- [210] H. Ulrichs, *From chaotic spin dynamics to noncollinear spin textures in YIG nanofilms by spin-current injection*, *Physical Review B* **102**, 174428 (2020).
- [211] Y.-T. Chen, S. Takahashi, H. Nakayama, M. Althammer, S. T. B. Goennenwein, E. Saitoh, and G. E. W. Bauer, *Theory of spin Hall magnetoresistance*, *Physical Review B* **87**, 144411 (2013).
- [212] L. J. Zhu, D. C. Ralph, and R. A. Buhrman, *Irrelevance of magnetic proximity effect to spin-orbit torques in heavy-metal/ferromagnet bilayers*, *Physical Review B* **98**, 134406 (2018).
- [213] L. Zhu, D. C. Ralph, and R. A. Buhrman, *Effective Spin-Mixing Conductance of Heavy-Metal-Ferromagnet Interfaces*, *Physical Review Letters* **123**, 057203 (2019).
- [214] R. Kohno, N. Thiery, K. An, P. Noel, L. Vila, V. V. Naletov, N. Beaulieu, J. B. Youssef, G. de Loubens, and O. Klein, *Enhancement of YIG|Pt spin conductance by local Joule annealing*, *Applied Physics Letters* **118**, 032404 (2021).

- [215] H. Bai, X. Z. Zhan, G. Li, J. Su, Z. Z. Zhu, Y. Zhang, T. Zhu, and J. W. Cai, *Characterization of YIG thin films and vacuum annealing effect by polarized neutron reflectometry and magnetotransport measurements*, *Applied Physics Letters* **115**, 182401 (2019).
- [216] E. Sagasta, Y. Omori, M. Isasa, M. Gradhand, L. E. Hueso, Y. Niimi, Y. Otani, and F. Casanova, *Tuning the spin Hall effect of Pt from the moderately dirty to the superclean regime*, *Physical Review B* **94**, 060412 (2016).
- [217] R. Schlitz, S. Granovsky, D. Pohl, A. Thomas, B. Rellinghaus, and S. T. B. Goennenwein, *Nonlocal magnon-based transport in yttrium-iron-garnet–platinum heterostructures at high temperatures*, *Physical Review B* **103**, 214434 (2021).
- [218] E. Karadza, *Disentangling Electrical and Thermal Modulations of Magnon Conductivity in Yttrium Iron Garnet*, *Master’s thesis*, Technical University of Munich (2021).
- [219] V. V. Kruglyak, S. O. Demokritov, and D. Grundler, *Magnonics*, *Journal of Physics D: Applied Physics* **43**, 260301 (2010).
- [220] T. Jungwirth, X. Marti, P. Wadley, and J. Wunderlich, *Antiferromagnetic spintronics*, *Nature Nanotechnology* **11**, 231 (2016).
- [221] V. Baltz, A. Manchon, M. Tsoi, T. Moriyama, T. Ono, and Y. Tserkovnyak, *Antiferromagnetic spintronics*, *Reviews of Modern Physics* **90**, 015005 (2018).
- [222] J. Li, C. B. Wilson, R. Cheng, M. Lohmann, M. Kavand, W. Yuan, M. Aldosary, N. Agladze, P. Wei, M. S. Sherwin, and J. Shi, *Spin current from sub-terahertz-generated antiferromagnetic magnons*, *Nature* **578**, 70 (2020).
- [223] P. Vaidya, S. A. Morley, J. van Tol, Y. Liu, R. Cheng, A. Brataas, D. Lederman, and E. del Barco, *Subterahertz spin pumping from an insulating antiferromagnet*, *Science* **368**, 160 (2020).
- [224] P. Němec, M. Fiebig, T. Kampfrath, and A. V. Kimel, *Antiferromagnetic optospintronics*, *Nature Physics* **14**, 229 (2018).
- [225] K. Olejník, T. Seifert, Z. Kašpar, V. Novák, P. Wadley, R. P. Campion, M. Baumgartner, P. Gambardella, P. Němec, J. Wunderlich, J. Sinova, P. Kužel, M. Müller, T. Kampfrath, and T. Jungwirth, *Terahertz electrical writing speed in an antiferromagnetic memory*, *Science Advances* **4**, eaar3566 (2018).
- [226] A. Kamra, U. Agrawal, and W. Belzig, *Noninteger-spin magnonic excitations in untextured magnets*, *Physical Review B* **96**, 020411 (2017).

- [227] L. Liensberger, A. Kamra, H. Maier-Flaig, S. Geprägs, A. Erb, S. T. B. Goennenwein, R. Gross, W. Belzig, H. Huebl, and M. Weiler, *Exchange-Enhanced Ultrastrong Magnon-Magnon Coupling in a Compensated Ferrimagnet*, *Physical Review Letters* **123**, 117204 (2019).
- [228] J. Lan, W. Yu, and J. Xiao, *Antiferromagnetic domain wall as spin wave polarizer and retarder*, *Nature Communications* **8**, 178 (2017).
- [229] A. Mook, J. Henk, and I. Mertig, *Edge states in topological magnon insulators*, *Physical Review B* **90**, 024412 (2014).
- [230] D. Hou, Z. Qiu, and E. Saitoh, *Spin transport in antiferromagnetic insulators: progress and challenges*, *NPG Asia Materials* **11**, 35 (2019).
- [231] M. B. Jungfleisch, W. Zhang, and A. Hoffmann, *Perspectives of antiferromagnetic spintronics*, *Physics Letters A* **382**, 865 (2018).
- [232] M. Aspelmeyer, T. J. Kippenberg, and F. Marquardt, *Cavity optomechanics*, *Reviews of Modern Physics* **86**, 1391 (2014).
- [233] J. Li, Y. Xu, M. Aldosary, C. Tang, Z. Lin, S. Zhang, R. Lake, and J. Shi, *Observation of magnon-mediated current drag in Pt/yttrium iron garnet/Pt (Ta) trilayers*, *Nature Communications* **7**, 10858 (2016).
- [234] R. Lebrun, A. Ross, O. Gomonay, V. Baltz, U. Ebels, A.-L. Barra, A. Qaiumzadeh, A. Brataas, J. Sinova, and M. Kläui, *Long-distance spin-transport across the Morin phase transition up to room temperature in ultra-low damping single crystals of the antiferromagnet α -Fe₂O₃*, *Nature Communications* **11**, 6332 (2020).
- [235] G. R. Hoogeboom and B. J. van Wees, *Nonlocal spin Seebeck effect in the bulk easy-plane antiferromagnet NiO*, *Physical Review B* **102**, 214415 (2020).
- [236] A. Ross, R. Lebrun, M. Evers, A. Deák, L. Szunyogh, U. Nowak, and M. Kläui, *Exceptional sign changes of the nonlocal spin Seebeck effect in antiferromagnetic hematite*, *Physical Review B* **103**, 224433 (2021).
- [237] T. Wimmer, J. Gückelhorn, S. Wimmer, S. Mankovsky, H. Ebert, M. Opel, S. Geprägs, R. Gross, H. Huebl, and M. Althammer, *Low-temperature suppression of the spin Nernst angle in Pt*, *Physical Review B* **104**, L140404 (2021).
- [238] K. Shen, *Magnon spin transport around the compensation magnetic field in easy-plane antiferromagnetic insulators*, *Journal of Applied Physics* **129**, 223906 (2021).

- [239] J. Kikkawa and D. Awschalom, *Lateral drag of spin coherence in gallium arsenide*, [Nature](#) **397**, 139 (1999).
- [240] F. Jedema, H. Heersche, A. Filip, J. Baselmans, and B. Van Wees, *Electrical detection of spin precession in a metallic mesoscopic spin valve*, [Nature](#) **416**, 713 (2002).
- [241] A. Ross, R. Lebrun, L. Baldrati, A. Kamra, O. Gomonay, S. Ding, F. Schreiber, D. Backes, F. Maccherozzi, D. A. Grave, A. Rothschild, J. Sinova, and M. Kläui, *An insulating doped antiferromagnet with low magnetic symmetry as a room temperature spin conduit*, [Applied Physics Letters](#) **117**, 242405 (2020).
- [242] J. Gückelhorn, S. de-la Peña, M. Scheufele, M. Grammer, M. Opel, S. Geprägs, J. C. Cuevas, R. Gross, H. Huebl, A. Kamra, and M. Althammer, *Observation of the Nonreciprocal Magnon Hanle Effect*, [Physical Review Letters](#) **130**, 216703 (2023).
- [243] J. Gückelhorn, A. Kamra, T. Wimmer, M. Opel, S. Geprägs, R. Gross, H. Huebl, and M. Althammer, *Influence of low-energy magnons on magnon Hanle experiments in easy-plane antiferromagnets*, [Physical Review B](#) **105**, 094440 (2022).
- [244] A. Kamra, E. Thingstad, G. Rastelli, R. A. Duine, A. Brataas, W. Belzig, and A. Sudbø, *Antiferromagnetic magnons as highly squeezed Fock states underlying quantum correlations*, [Physical Review B](#) **100**, 174407 (2019).
- [245] J. A. Jones, A. J. D’Addario, B. L. Rojec, G. Milione, and E. J. Galvez, *The Poincaré-sphere approach to polarization: Formalism and new labs with Poincaré beams*, [American Journal of Physics](#) **84**, 822 (2016).
- [246] B. Flebus, *Chemical potential of an antiferromagnetic magnon gas*, [Physical Review B](#) **100**, 064410 (2019).
- [247] A. Kamra and W. Belzig, *Super-Poissonian Shot Noise of Squeezed-Magnon Mediated Spin Transport*, [Physical Review Letters](#) **116**, 146601 (2016).
- [248] T. Kikkawa, K.-i. Uchida, S. Daimon, Z. Qiu, Y. Shiomi, and E. Saitoh, *Critical suppression of spin Seebeck effect by magnetic fields*, [Physical Review B](#) **92**, 064413 (2015).
- [249] R. E. Troncoso, S. A. Bender, A. Brataas, and R. A. Duine, *Spin transport in thick insulating antiferromagnetic films*, [Physical Review B](#) **101**, 054404 (2020).

- [250] F. Keffer and R. Loudon, *Simple Physical Theory of Spin Wave Interactions*, *Journal of Applied Physics* **32**, S2 (1961).
- [251] M. Bloch, *Magnon Renormalization in Ferromagnets Near the Curie Point*, *Physical Review Letters* **9**, 286 (1962).
- [252] H. Wang, Y. Xiao, M. Guo, E. Lee-Wong, G. Q. Yan, R. Cheng, and C. R. Du, *Spin Pumping of an Easy-Plane Antiferromagnet Enhanced by Dzyaloshinskii–Moriya Interaction*, *Physical Review Letters* **127**, 117202 (2021).
- [253] I. Boventer, H. T. Simensen, A. Anane, M. Kläui, A. Brataas, and R. Lebrun, *Room-Temperature Antiferromagnetic Resonance and Inverse Spin-Hall Voltage in Canted Antiferromagnets*, *Physical Review Letters* **126**, 187201 (2021).
- [254] D. MacNeill, J. T. Hou, D. R. Klein, P. Zhang, P. Jarillo-Herrero, and L. Liu, *Gigahertz Frequency Antiferromagnetic Resonance and Strong Magnon-Magnon Coupling in the Layered Crystal CrCl₃*, *Physical Review Letters* **123**, 047204 (2019).
- [255] H. Huebl, C. W. Zollitsch, J. Lotze, F. Hocke, M. Greifenstein, A. Marx, R. Gross, and S. T. B. Goennenwein, *High Cooperativity in Coupled Microwave Resonator Ferrimagnetic Insulator Hybrids*, *Physical Review Letters* **111**, 127003 (2013).
- [256] S. de-la-Peña, R. Schlitz, S. Vélez, J. C. Cuevas, and A. Kamra, *Theory of drift-enabled control in nonlocal magnon transport*, *Journal of Physics: Condensed Matter* **34**, 295801 (2022).
- [257] A. Kehlberger, U. Ritzmann, D. Hinzke, E.-J. Guo, J. Cramer, G. Jakob, M. C. Onbasli, D. H. Kim, C. A. Ross, M. B. Jungfleisch, B. Hillebrands, U. Nowak, and M. Kläui, *Length Scale of the Spin Seebeck Effect*, *Physical Review Letters* **115**, 096602 (2015).
- [258] S. Meyer, M. Althammer, S. Geprägs, M. Opel, R. Gross, and S. T. B. Goennenwein, *Temperature dependent spin transport properties of platinum inferred from spin Hall magnetoresistance measurements*, *Applied Physics Letters* **104**, 242411 (2014).
- [259] J. Shan, P. Bougiatioti, L. Liang, G. Reiss, T. Kuschel, and B. J. van Wees, *Nonlocal magnon spin transport in NiFe₂O₄ thin films*, *Applied Physics Letters* **110**, 132406 (2017).
- [260] S. A. Owerre, *A first theoretical realization of honeycomb topological magnon insulator*, *Journal of Physics: Condensed Matter* **28**, 386001 (2016).

- [261] Y. Tokura and N. Nagaosa, *Nonreciprocal responses from non-centrosymmetric quantum materials*, [Nature Communications](#) **9**, 3740 (2018).
- [262] F. Ando, Y. Miyasaka, T. Li, J. Ishizuka, T. Arakawa, Y. Shiota, T. Moriyama, Y. Yanase, and T. Ono, *Observation of superconducting diode effect*, [Nature](#) **584**, 373 (2020).
- [263] M. Küß, M. Heigl, L. Flacke, A. Hörner, M. Weiler, M. Albrecht, and A. Wixforth, *Nonreciprocal Dzyaloshinskii–Moriya Magnetoacoustic Waves*, [Physical Review Letters](#) **125**, 217203 (2020).
- [264] M. Küß, M. Albrecht, and M. Weiler, *Chiral Magnetoacoustics*, [Frontiers in Physics](#) **10** (2022).
- [265] G. Gitgeatpong, Y. Zhao, P. Piyawongwatthana, Y. Qiu, L. W. Harriger, N. P. Butch, T. J. Sato, and K. Matan, *Nonreciprocal Magnons and Symmetry-Breaking in the Noncentrosymmetric Antiferromagnet*, [Physical Review Letters](#) **119**, 047201 (2017).
- [266] F. J. dos Santos, M. dos Santos Dias, and S. Lounis, *Modeling spin waves in noncollinear antiferromagnets: Spin-flop states, spin spirals, skyrmions, and antiskyrmions*, [Physical Review B](#) **102**, 104436 (2020).
- [267] J.-H. Moon, S.-M. Seo, K.-J. Lee, K.-W. Kim, J. Ryu, H.-W. Lee, R. D. McMichael, and M. D. Stiles, *Spin-wave propagation in the presence of interfacial Dzyaloshinskii–Moriya interaction*, [Physical Review B](#) **88**, 184404 (2013).
- [268] J.-V. Kim, R. L. Stamps, and R. E. Camley, *Spin Wave Power Flow and Caustics in Ultrathin Ferromagnets with the Dzyaloshinskii–Moriya Interaction*, [Physical Review Letters](#) **117**, 197204 (2016).
- [269] H. T. Nembach, J. M. Shaw, M. Weiler, E. Jué, and T. J. Silva, *Linear relation between Heisenberg exchange and interfacial Dzyaloshinskii–Moriya interaction in metal films*, [Nature Physics](#) **11**, 825 (2015).
- [270] M. Garst, J. Waizner, and D. Grundler, *Collective spin excitations of helices and magnetic skyrmions: review and perspectives of magnonics in non-centrosymmetric magnets*, [Journal of Physics D: Applied Physics](#) **50**, 293002 (2017).
- [271] H. Wang, J. Chen, T. Liu, J. Zhang, K. Baumgaertl, C. Guo, Y. Li, C. Liu, P. Che, S. Tu, S. Liu, P. Gao, X. Han, D. Yu, M. Wu, D. Grundler, and H. Yu, *Chiral Spin-Wave Velocities Induced by All-Garnet Interfacial Dzyaloshinskii–Moriya*

- Interaction in Ultrathin Yttrium Iron Garnet Films*, [Physical Review Letters](#) **124**, 027203 (2020).
- [272] T. Yu, C. Wang, M. A. Sentef, and G. E. W. Bauer, *Spin-Wave Doppler Shift by Magnon Drag in Magnetic Insulators*, [Physical Review Letters](#) **126**, 137202 (2021).
- [273] V. Brehm, M. Evers, U. Ritzmann, and U. Nowak, *Magnonic proximity effect in insulating ferromagnetic and antiferromagnetic trilayers*, [Physical Review B](#) **105**, 104408 (2022).
- [274] A. Mook, B. Göbel, J. Henk, and I. Mertig, *Taking an electron-magnon duality shortcut from electron to magnon transport*, [Physical Review B](#) **97**, 140401 (2018).
- [275] M. Malki and G. S. Uhrig, *Topological magnon bands for magnonics*, [Physical Review B](#) **99**, 174412 (2019).
- [276] M. Malki and G. S. Uhrig, *Topological magnetic excitations*, [Europhysics Letters](#) **132**, 20003 (2020).
- [277] J. Liu, L. Wang, and K. Shen, *Dipolar spin waves in uniaxial easy-axis antiferromagnets: A natural topological nodal-line semimetal*, [Physical Review Research](#) **2**, 023282 (2020).
- [278] A. Krysztofik, H. Głowiński, P. Kuświk, S. Ziętek, L. E. Coy, J. N. Rychły, S. Jurga, T. W. Stobiecki, and J. Dubowik, *Characterization of spin wave propagation in (111) YIG thin films with large anisotropy*, [Journal of Physics D: Applied Physics](#) **50**, 235004 (2017).
- [279] B. A. Kalinikos, M. P. Kostylev, N. V. Kozhus, and A. N. Slavin, *The dipole-exchange spin wave spectrum for anisotropic ferromagnetic films with mixed exchange boundary conditions*, [Journal of Physics: Condensed Matter](#) **2**, 9861 (1990).
- [280] J. Shan, A. V. Singh, L. Liang, L. J. Cornelissen, Z. Galazka, A. Gupta, B. J. van Wees, and T. Kuschel, *Enhanced magnon spin transport in NiFe₂O₄ thin films on a lattice-matched substrate*, [Applied Physics Letters](#) **113**, 162403 (2018).
- [281] A. V. Singh, B. Khodadadi, J. B. Mohammadi, S. Keshavarz, T. Mewes, D. S. Negi, R. Datta, Z. Galazka, R. Uecker, and A. Gupta, *Bulk Single Crystal-Like Structural and Magnetic Characteristics of Epitaxial Spinel Ferrite Thin Films with Elimination of Antiphase Boundaries*, [Advanced Materials](#) **29**, 1701222 (2017).

- [282] V. E. Demidov, S. O. Demokritov, B. Hillebrands, M. Laufenberg, and P. P. Freitas, *Radiation of spin waves by a single micrometer-sized magnetic element*, *Applied Physics Letters* **85**, 2866 (2004).
- [283] V. E. Demidov and S. O. Demokritov, *Magnonic Waveguides Studied by Microfocus Brillouin Light Scattering*, *IEEE Transactions on Magnetics* **51**, 4 (2015).
- [284] T. Sebastian, K. Schultheiss, B. Obry, B. Hillebrands, and H. Schultheiss, *Micro-focused Brillouin light scattering: imaging spin waves at the nanoscale*, *Frontiers in Physics* **3** (2015).
- [285] S. O. Demokritov, V. E. Demidov, O. Dzyapko, G. A. Melkov, A. A. Serga, B. Hillebrands, and A. N. Slavin, *Bose–Einstein condensation of quasi-equilibrium magnons at room temperature under pumping*, *Nature* **443**, 430 (2006).
- [286] G. Balasubramanian, I. Chan, R. Kolesov, M. Al-Hmoud, J. Tisler, C. Shin, C. Kim, A. Wojcik, P. R. Hemmer, A. Krueger, T. Hanke, A. Leitenstorfer, R. Bratschitsch, F. Jelezko, and J. Wrachtrup, *Nanoscale imaging magnetometry with diamond spins under ambient conditions*, *Nature* **455**, 648 (2008).
- [287] J. R. Maze, P. L. Stanwix, J. S. Hodges, S. Hong, J. M. Taylor, P. Cappellaro, L. Jiang, M. G. Dutt, E. Togan, A. S. Zibrov, A. Yacoby, R. L. Walsworth, and M. D. Lukin, *Nanoscale magnetic sensing with an individual electronic spin in diamond*, *Nature* **455**, 644 (2008).
- [288] J. M. Taylor, P. Cappellaro, L. Childress, L. Jiang, D. Budker, P. Hemmer, A. Yacoby, R. Walsworth, and M. Lukin, *High-sensitivity diamond magnetometer with nanoscale resolution*, *Nature Physics* **4**, 810 (2008).
- [289] F. Dolde, H. Fedder, M. W. Doherty, T. Nöbauer, F. Rempp, G. Balasubramanian, T. Wolf, F. Reinhard, L. C. Hollenberg, F. Jelezko, and J. Wrachtrup, *Electric-field sensing using single diamond spins*, *Nature Physics* **7**, 459 (2011).
- [290] C. L. Degen, *Scanning magnetic field microscope with a diamond single-spin sensor*, *Applied Physics Letters* **92**, 243111 (2008).
- [291] F. Casola, T. Van Der Sar, and A. Yacoby, *Probing condensed matter physics with magnetometry based on nitrogen-vacancy centres in diamond*, *Nature Reviews Materials* **3**, 1 (2018).
- [292] S. Sekatskii and V. Letokhov, *Nanometer-resolution scanning optical microscope with resonance excitation of the fluorescence of the samples from a single-atom*

excited center, *Journal of Experimental and Theoretical Physics Letters* **63**, 319 (1996).

- [293] A. Cuche, A. Drezet, Y. Sonnefraud, O. Faklaris, F. Treussart, J.-F. Roch, and S. Huant, *Near-field optical microscopy with a nanodiamond-based single-photon tip*, *Optics Express* **17**, 19969 (2009).
- [294] P. Neumann, R. Kolesov, B. Naydenov, J. Beck, F. Rempp, M. Steiner, V. Jacques, G. Balasubramanian, M. L. Markham, D. J. Twitchen, S. Pezzagna, J. Meijer, J. Twamley, F. Jelezko, and J. Wrachtrup, *Quantum register based on coupled electron spins in a room-temperature solid*, *Nature Physics* **6**, 249 (2010).
- [295] L. Rondin, J.-P. Tetienne, P. Spinicelli, C. Dal Savio, K. Karrai, G. Dantelle, A. Thiaville, S. Rohart, J.-F. Roch, and V. Jacques, *Nanoscale magnetic field mapping with a single spin scanning probe magnetometer*, *Applied Physics Letters* **100**, 153118 (2012).
- [296] P. Maletinsky, S. Hong, M. S. Grinolds, B. Hausmann, M. D. Lukin, R. L. Walsworth, M. Loncar, and A. Yacoby, *A robust scanning diamond sensor for nanoscale imaging with single nitrogen-vacancy centres*, *Nature Nanotechnology* **7**, 320 (2012).
- [297] L. Rondin, J.-P. Tetienne, S. Rohart, A. Thiaville, T. Hingant, P. Spinicelli, J.-F. Roch, and V. Jacques, *Stray-field imaging of magnetic vortices with a single diamond spin*, *Nature Communications* **4**, 2279 (2013).
- [298] J.-P. Tetienne, T. Hingant, J.-V. Kim, L. H. Diez, J.-P. Adam, K. Garcia, J.-F. Roch, S. Rohart, A. Thiaville, D. Ravelosona, and V. Jacques, *Nanoscale imaging and control of domain-wall hopping with a nitrogen-vacancy center microscope*, *Science* **344**, 1366 (2014).
- [299] J.-P. Tetienne, T. Hingant, L. J. Martínez, S. Rohart, A. Thiaville, L. H. Diez, K. Garcia, J.-P. Adam, J.-V. Kim, J.-F. Roch, I. M. Miron, G. Gaudin, L. Vila, B. Ocker, D. Ravelosona, and V. Jacques, *The nature of domain walls in ultrathin ferromagnets revealed by scanning nanomagnetometry*, *Nature Communications* **6**, 6733 (2015).
- [300] S. Vélez, J. Schaab, M. S. Wörnle, M. Müller, E. Gradauskaite, P. Welter, C. Gutgsell, C. Nistor, C. L. Degen, M. Trassin, M. Fiebig, and P. Gambardella, *High-speed domain wall racetracks in a magnetic insulator*, *Nature Communications* **10**, 4750 (2019).

- [301] P. Appel, B. J. Shields, T. Kosub, N. Hedrich, R. Hübner, J. Faßbender, D. Makarov, and P. Maletinsky, *Nanomagnetism of magnetoelectric granular thin-film antiferromagnets*, [Nano Letters](#) **19**, 1682 (2019).
- [302] M. Wörnle, P. Welter, Z. Kašpar, K. Olejník, V. Novák, R. Campion, P. Wadley, T. Jungwirth, C. Degen, and P. Gambardella, *Current-induced fragmentation of antiferromagnetic domains*, [arXiv:1912.05287](#) (2019).
- [303] M. S. Wörnle, P. Welter, M. Giraldo, T. Lottermoser, M. Fiebig, P. Gambardella, and C. L. Degen, *Coexistence of Bloch and Néel walls in a collinear antiferromagnet*, [Physical Review B](#) **103**, 094426 (2021).
- [304] N. Hedrich, K. Wagner, O. V. Pylypovskiy, B. J. Shields, T. Kosub, D. D. Sheka, D. Makarov, and P. Maletinsky, *Nanoscale mechanics of antiferromagnetic domain walls*, [Nature Physics](#) **17**, 574 (2021).
- [305] A. Finco, A. Haykal, R. Tanos, F. Fabre, S. Chouaieb, W. Akhtar, I. Robert-Philip, W. Legrand, F. Ajejas, K. Bouzehouane, N. Reyren, T. Devolder, J.-P. Adam, J.-V. Kim, V. Cros, and V. Jacques, *Imaging non-collinear antiferromagnetic textures via single spin relaxometry*, [Nature Communications](#) **12**, 767 (2021).
- [306] I. Gross, W. Akhtar, V. Garcia, L. Martínez, S. Chouaieb, K. Garcia, C. Carrétéro, A. Barthélémy, P. Appel, P. Maletinsky, J.-V. Kim, J. Y. Chauleau, N. Jaouen, M. Viret, M. Bibes, S. Fusil, and V. Jacques, *Real-space imaging of non-collinear antiferromagnetic order with a single-spin magnetometer*, [Nature](#) **549**, 252 (2017).
- [307] J.-Y. Chauleau, T. Chirac, S. Fusil, V. Garcia, W. Akhtar, J. Tranchida, P. Thibaudeau, I. Gross, C. Blouzon, A. Finco, M. Bibes, B. Dkhil, D. D. Khalyavin, P. Manuel, V. Jacques, N. Jaouen, and M. Viret, *Electric and antiferromagnetic chiral textures at multiferroic domain walls*, [Nature Materials](#) **19**, 386 (2020).
- [308] Y. Dovzhenko, F. Casola, S. Schlotter, T. Zhou, F. Büttner, R. Walsworth, G. Beach, and A. Yacoby, *Magnetostatic twists in room-temperature skyrmions explored by nitrogen-vacancy center spin texture reconstruction*, [Nature Communications](#) **9**, 2712 (2018).
- [309] I. Gross, W. Akhtar, A. Hrabec, J. Sampaio, L. J. Martínez, S. Chouaieb, B. J. Shields, P. Maletinsky, A. Thiaville, S. Rohart, and V. Jacques, *Skyrmion morphology in ultrathin magnetic films*, [Physical Review Materials](#) **2**, 024406 (2018).

- [310] A. Jenkins, M. Pelliccione, G. Yu, X. Ma, X. Li, K. L. Wang, and A. C. B. Jayich, *Single-spin sensing of domain-wall structure and dynamics in a thin-film skyrmion host*, [Physical Review Materials](#) **3**, 083801 (2019).
- [311] S. Vélez, S. Ruiz-Gómez, J. Schaab, E. Gradauskaite, M. S. Wörnle, P. Welter, B. J. Jacot, C. L. Degen, M. Trassin, M. Fiebig, and P. Gambardella, *Current-driven dynamics and ratchet effect of skyrmion bubbles in a ferrimagnetic insulator*, [Nature Nanotechnology](#) **17**, 834 (2022).
- [312] L. Thiel, D. Rohner, M. Ganzhorn, P. Appel, E. Neu, B. Müller, R. Kleiner, D. Koelle, and P. Maletinsky, *Quantitative nanoscale vortex imaging using a cryogenic quantum magnetometer*, [Nature Nanotechnology](#) **11**, 677 (2016).
- [313] M. Pelliccione, A. Jenkins, P. Ovartchaiyapong, C. Reetz, E. Emmanouilidou, N. Ni, and A. C. Bleszynski Jayich, *Scanned probe imaging of nanoscale magnetism at cryogenic temperatures with a single-spin quantum sensor*, [Nature Nanotechnology](#) **11**, 700 (2016).
- [314] P. J. Scheidegger, S. Diesch, M. L. Palm, and C. L. Degen, *Scanning nitrogen-vacancy magnetometry down to 350 mK*, [Applied Physics Letters](#) **120**, 224001 (2022).
- [315] L. Thiel, Z. Wang, M. A. Tschudin, D. Rohner, I. Gutiérrez-Lezama, N. Ubrig, M. Gibertini, E. Giannini, A. F. Morpurgo, and P. Maletinsky, *Probing magnetism in 2D materials at the nanoscale with single-spin microscopy*, [Science](#) **364**, 973 (2019).
- [316] Q.-C. Sun, T. Song, E. Anderson, A. Brunner, J. Förster, T. Shalomayeva, T. Taniguchi, K. Watanabe, J. Gräfe, R. Stöhr, X. Xu, and J. Wrachtrup, *Magnetic domains and domain wall pinning in atomically thin CrBr₃ revealed by nanoscale imaging*, [Nature Communications](#) **12**, 1989 (2021).
- [317] F. Fabre, A. Finco, A. Purbawati, A. Hadj-Azzem, N. Rougemaille, J. Coraux, I. Philip, and V. Jacques, *Characterization of room-temperature in-plane magnetization in thin flakes of CrTe₂ with a single-spin magnetometer*, [Physical Review Materials](#) **5**, 034008 (2021).
- [318] I. Bertelli, B. G. Simon, T. Yu, J. Aarts, G. E. W. Bauer, Y. M. Blanter, and T. van der Sar, *Imaging Spin-Wave Damping Underneath Metals Using Electron Spins in Diamond*, [Advanced Quantum Technologies](#) **4**, 2100094 (2021).
- [319] C. Du, T. van der Sar, T. X. Zhou, P. Upadhyaya, F. Casola, H. Zhang, M. C. Onbasli, C. A. Ross, R. L. Walsworth, Y. Tserkovnyak, and A. Yacoby, *Control*

and local measurement of the spin chemical potential in a magnetic insulator, *Science* **357**, 195 (2017).

- [320] V. M. Acosta, E. Bauch, M. P. Ledbetter, A. Waxman, L.-S. Bouchard, and D. Budker, *Temperature Dependence of the Nitrogen-Vacancy Magnetic Resonance in Diamond*, *Physical Review Letters* **104**, 070801 (2010).
- [321] P. Welter, B. A. Josteinsson, S. Josephy, A. Wittmann, A. Morales, G. Puebla-Hellmann, and C. L. Degen, *Fast scanning nitrogen-vacancy magnetometry by spectrum demodulation*, [arXiv:2205.06579](https://arxiv.org/abs/2205.06579) (2022).
- [322] F. P. Chmiel, N. Waterfield Price, R. D. Johnson, A. D. Lamirand, J. Schad, G. van der Laan, D. T. Harris, J. Irwin, M. S. Rzchowski, C.-B. Eom, and P. G. Radaelli, *Observation of magnetic vortex pairs at room temperature in a planar α -Fe₂O₃/Co heterostructure*, *Nature Materials* **17**, 581 (2018).

Acknowledgements - Danksagung

Auch wenn es in den letzten vier Jahren manchmal stressige Zeiten gab, in denen man gute Nerven beweisen musste, möchte ich die schöne Zeit am WMI nicht missen. Das Gelingen dieser Doktorarbeit wäre ohne die Unterstützung und Hilfe in verschiedenen Bereichen von zahlreichen Menschen nicht möglich gewesen. Diesen bin ich zu großem Dank verpflichtet und möchte mich insbesondere bei den folgenden Personen bedanken:

- Meinem Doktorvater *Prof. Dr. Rudolf Gross* für die Möglichkeit meine Doktorarbeit am Walther-Meißner-Institut durchführen zu können, das immer wieder eine solide Plattform und eine tollen Arbeitsatmosphäre geboten hat. Danke für die wertvollen Kommentare zu verschiedensten Manuskripten sowie zu dieser Doktorarbeit und die interessanten Gespräche/Diskussionen, bei denen Sie immer ein einfaches Bild parat hatten, um komplexe Fragestellungen zu beantworten.
- Meinem Betreuer *Dr. Matthias Althammer* für die ausgezeichnete Betreuung während meiner gesamten Promotionszeit. Ich habe immer wieder eine offene Tür vorgefunden für Angelegenheiten jeglicher Art, sei es die Unterstützung im Labor, deine Expertise und wertvollen Hinweise zu physikalischen Fragen, als auch die Hilfe bei organisatorischen Fragen. Darüber hinaus vielen Dank für all die Zeit, die du dir genommen hast für die Diskussion und Interpretation von Messdaten und das Korrekturlesen von Manuskripten und der vorliegenden Doktorarbeit. Ich habe auch immer die entspannte Arbeitsatmosphäre sehr genossen, die du geschaffen hast, auch durch deine Ermutigung, sich in stressigeren Zeiten auch mal eine kurze Auszeit zu nehmen.
- *Dr. Stephan Geprägs* für die Einführung in die Dünnschichtfilmtechnologie, sowie die Hilfe und das Teilen deiner Expertise beim Wachstumsprozess von Filmen an der PLD bis hin zur Charakterisierung durch Röntgen- und SQUID-Messungen. Allgemein möchte ich mich für deine positive und entspannte Art bedanken, auch dann noch, wenn man mal wieder zu unmöglichen Zeiten Mist an der PLD baut. Das hat auch immer die Tutorübungsvorbesprechun-

gen sehr angenehm gemacht, danke dafür und deine Bemühungen bei der Übungsorganisation.

- *PD Dr. Hans Hübl* für die wertvollen Diskussionen über meinen Messdaten und vor allem für deine kritischen Hinterfragungen und Denkanstöße zu Interpretationen von Daten und Manuskripten, die mich in neue Richtungen haben denken lassen und zu einem besseren Verständnis führten.
- *Dr. Matthias Opel* für deine ständige Hilfsbereitschaft, sei es nun bei EDV Problemen, bei den Kryostaten oder anderen Dingen. Ich möchte mich auch für deine wichtigen Beiträge und Hinweise zu Messdaten und Manuskripten bedanken. Nicht zuletzt möchte ich mich noch einmal ausdrücklich dafür bedanken, dass du meinen Vortrag bei der DPG-Frühjahrstagung 2023 übernommen hast.
- Meinem "Vorgänger" *Dr. Tobias Wimmer*, der mich in das Thema eingeführt, mir alle wichtigen Vorgänge beigebracht und mir die Feinheiten der Messtechnik gezeigt hat. Ich habe enorm von deinem Wissen und deinen ausführlichen Erklärungen zu Fragen zum Thema Magnonentransport profitiert.
- *Dr. Akashdeep Kamra* for continuing the great collaboration on the antiferromagnetic pseudospin project. I would also like to thank you for your intuitive and understandable explanations and insights into the theory model, which were always easy to understand even as an experimentalist.
- *Dr. Kai Wagner* und *Prof. Dr. Patrick Maletinsky* für die gute Zusammenarbeit und das Näherbringen der NV-Magnetometrie. Sie haben es mir ermöglicht, nach Basel zu kommen, um an den Experimenten teilzunehmen und meine ersten Erfahrungen mit NV-Magnetometermessungen zu sammeln. Es war eine nervenaufreibende (danke Bonder) aber auch schöne Zeit in Basel. Hier ein besonderer Dank an Kai für deine Hilfe jeglicher Art. Ich hoffe, dass ein zweiter Versuch von mehr Erfolg gekrönt sein wird.
- Meinen Doktorandenkollegen der Magnetikergruppe *Dr. Luis Flacke*, *Dr. Lukas Liensberger*, *Thomas Luschmann*, *Manuel Müller*, *Patricia Oehrl*, *Korbinian Rubenbauer*, *Monika Scheufele*, *Dr. Daniel Schwienbacher* und *Dr. Tobias Wimmer*, die mich über kürzere oder längere Zeit begleitet haben, für den produktiven Austausch und die gegenseitige schnelle und unkomplizierte Hilfe bei Problemen. Besonders bedanken möchte ich mich hier auch bei Manu für die FMR-Charakterisierung unzähliger PLD Filme, deinen Einsatz beim Superbowl und deine Ausdauer bei meinen Masteranden, die dich mal mehr, mal

weniger Nerven gekostet haben. Auch Moni danke ich für das Weiterführen der Hämatit-Experimente und das Durchforsten sehr großer Origin-Files.

- Meinen Bürokollegen *Daniil Bazulin, Maria-Teresa Handschuh, Dr. Lukas Liensberger, Yuki Nojiri, Leander Peis* und *Gabriele Rager* für die schöne und produktive Zeit und die Gespräche jeglicher Art, die immer wieder eine schöne Ablenkung von der Arbeit waren.
- Meinem ersten Masterstudenten *Matthias Grammer* für das Vorantreiben der Hämatit-Experimente, dein Einsatz bei der Fabrikation von sehr kleinen Strukturen und deine Bemühungen beim Piezo-Rotator-Stab. Ich habe mich immer wieder über deine gute Laune gefreut, die man schon von weitem mitbekommen hat. Ich habe unsere Diskussionen immer sehr geschätzt und habe selber durch die ein oder andere Frage noch etwas dazulernen können.
- *Franz Weidenhiller* als Masterstudent für deine großartige Hilfe bei einem wichtigen Projekt und für deinen unermüdlichen Einsatz und deine Ausdauer, die Microwave pumping Strukturen zum Funktionieren zu bringen. Ich freue mich, dass du dich dafür noch rechtzeitig belohnt wurdest und danke dir für die schöne Zusammenarbeit.
- *Maria Sigl* als Masterstudentin, die ich leider nur noch am Anfang ihrer Arbeit begleiten konnte, für deine Hilfe bei der Charakterisierung unserer Proben und das Fortführen der Kooperation mit Kaiserslautern zu BLS-Messungen an unseren Strukturen. Ich habe unsere Zusammenarbeit sehr genossen und wünsche dir noch viel Erfolg für die restliche Zeit deiner Masterarbeit.
- Der Verwaltung *Andrea Person, Martina Meven, Carola Siegmayer*, und insbesondere *Emel Dönertas* für die unkomplizierte und immer hilfsbereite Art bei jeglichen administrativen Angelegenheiten.
- Der technischen Belegschaft des WMI, sprich allen Mitarbeitern der Helium-Halle, der Werkstatt und den Labortechnikern für eure Hilfsbereitschaft bei Problemen aller Art und dem damit verbundenem wichtigem Beitrag zum Aufrechterhalten des wissenschaftlichen Betriebs, sei es nun die kurzfristige Bereitstellung von Helium oder Stickstoff, Abhilfe bei elektronischen Problemen am Messequipment oder der Nachschub wichtiger Materialien für die Chemie. Hier möchte ich mich besonders bei *Tom Brenninger* für die große Unterstützung bei der exakten Konstruktion des Rotatorstabes bedanken.
- Allgemein allen Kollegen und Kolleginnen, sowie Masterstudenten und Masterstudentinnen des WMI für die angenehme Arbeitsatmosphäre und die gute Zeit

bei festlichen Anlässen des WMI oder Aktivitäten außerhalb der Arbeitszeit, wie unter anderem gemütliche Abende im HongHong in Garching.

- Meinem *Karate Team* des ESV Freimann, das immer wieder für den nötigen Ausgleich gesorgt hat.
- Meiner Familie *Ute, Christian* und *Daniel* für euren großen Rückhalt und Unterstützung in allen Lebenslagen. Danke für eure aufbauenden Worte und dafür, dass ihr immer an mich glaubt!